UNIVERSITÉ
LAVAL

NANOSTRUCTURED CATALYSTS FOR THE DEVELOPMENT OF THE HYDROGEN ECONOMY

Thèse

YEN HOANG

Doctorat en chimie
Philosophiae Doctor (Ph.D)

Québec, Canada

Résumé

La catalyse joue un rôle essentiel dans de nombreuses applications industrielles telles que les industries pétrochimique et biochimique, ainsi que dans la production de polymères et pour la protection de l'environnement. La conception et la fabrication de catalyseurs efficaces et rentables est une étape importante pour résoudre un certain nombre de problèmes des nouvelles technologies de conversion chimique et de stockage de l'énergie. L'objectif de cette thèse est le développement de voies de synthèse efficaces et simples pour fabriquer des catalyseurs performants à base de métaux non nobles et d'examiner les aspects fondamentaux concernant la relation entre structure/composition et performance catalytique, notamment dans des processus liés à la production et au stockage de l'hydrogène.

Dans un premier temps, une série d'oxydes métalliques mixtes (Cu/CeO$_2$, CuFe/CeO$_2$, CuCo/CeO$_2$, CuFe$_2$O$_4$, NiFe$_2$O$_4$) nanostructurés et poreux ont été synthétisés grâce à une méthode améliorée de nanocasting. Les matériaux Cu/CeO$_2$ obtenus, dont la composition et la structure poreuse peuvent être contrôlées, ont ensuite été testés pour l'oxydation préférentielle du CO dans un flux d'hydrogène dans le but d'obtenir un combustible hydrogène de haute pureté. Les catalyseurs synthétisés présentent une activité et une sélectivité élevées lors de l'oxydation sélective du CO en CO$_2$.

Concernant la question du stockage d'hydrogène, une voie de synthèse a été trouvée pour le composét mixte CuO-NiO, démontrant une excellente performance catalytique comparable aux catalyseurs à base de métaux nobles pour la production d'hydrogène à partir de l'ammoniaborane (aussi appelé borazane). L'activité catalytique du catalyseur étudié dans cette réaction est fortement influencée par la nature des précurseurs métalliques, la composition et la température de traitement thermique utilisées pour la préparation du catalyseur.

Enfin, des catalyseurs de Cu-Ni supportés sur silice colloïdale ou sur des particules de carbone, ayant une composition et une taille variable, ont été synthétisés par un simple procédé d'imprégnation. Les catalyseurs supportés sur carbone sont stables et très actifs à la fois dans l'hydrolyse du borazane et la décomposition de l'hydrazine aqueuse pour la

production d'hydrogène. Il a été démontré qu'un catalyseur optimal peut être obtenu par le contrôle de l'effet bi-métallique, l'interaction métal-support, et la taille des particules de métal.

Abstract

Catalysis plays an essential role in many industrial applications such as petrochemical and biochemical industries, as well as in the production of polymers and in environmental protection. Design and fabrication of efficient catalysts in a cost-effective way is an important milestone to address a number of unresolved issues in the new generation of chemical and energy conversion technologies. The objective of the studies in this thesis is the development of facile synthetic routes to prepare efficient catalysts based on non-noble metals, and elucidate fundamental aspects regarding the relationship between structure/composition and catalytic performance, in particular in the case of processes related to production and storage of hydrogen fuel.

At first, a series of nanostructured porous mixed metal oxides (Cu/CeO_2, $CuFe/CeO_2$, $CuCo/CeO_2$, $CuFe_2O_4$, $NiFe_2O_4$) have been synthesized via an improved nanocasting method. The porous structure of the nanocast products was tailored by tuning the mesostructure of the mesoporous silica phases used as templates. The obtained Cu/CeO_2 materials with controlled composition and porous structure were then tested in preferential oxidation of CO in a hydrogen stream to achieve high purity hydrogen fuel. The synthesized catalysts exhibit high activity and selectivity in selective oxidation of CO to CO_2.

Regarding hydrogen storage, we reported a cost-effective synthetic way towards bi-component CuO-NiO catalyst showing excellent catalytic performance, which is comparable to noble metal catalysts, in the hydrogen generation from ammonia-borane. Moreover, we demonstrate that the interaction between Cu and Ni species is essential in accelerating hydrogen evolution of ammonia borane. The catalytic activity of the obtained catalyst investigated in this reaction is strongly influenced by the nature of the metal precursors, the composition and the thermal treatment temperature employed for the catalyst preparation.

Finally, silica- and carbon-supported Cu-Ni nanocatalysts, with tunable composition and metal particle size, were synthesized by simple incipient wetness method. The carbon supported catalysts are stable, highly active and selective in both ammonia-borane

hydrolysis and the decomposition of hydrous hydrazine for hydrogen evolution. We showed that optimal catalysts can be achieved through manipulation of bimetallic effect, metal-support interaction, and adequate metal particle size.

Table of Contents

List of Figures

List of Tables

List of Abbreviations

1-D	1-dimensional
2-D	2-dimensional
3-D	3-dimensional
AAS	Atomic absorption spectroscopy
AB	Ammonia-borane
BBC	Body-centered cubic
BET	Brunauer–Emmett–Teller
BJH	Barrett–Joyner–Halenda
CTAB	Cetyltrimethylammonium bromide
CMK-1	Carbon mesostructures Korea Advanced Institute of Science and Technology number 1
EDX	Energy-dispersive X-ray spectroscopy
FCC	Face-centered cubic
HAADF	High angle annular dark field
HRTEM	High-resolution transmission electron microscopy
IUPAC	International Union of Pure and Applied Chemistry
KIT-6	Mesoporous silica Korean Institute of Technology number 6
MCM-48	Mobil Composition of Mater number 48
NLDFT	Nonlocal density functional theory
PEO	Poly(ethylene oxide), -(CH_2CH_2O)-
Pluronic F127	Triblock copolymer, $PEO_{106}PPO_{70}PEO_{106}$
Pluronic P123	Triblock copolymer, $PEO_{20}PPO_{70}PEO_{20}$

PPO	Poly(propylene oxide), -[CH$_2$CH(CH$_3$)O]-
PROX	Preferential oxidation
QSDFT	Quenched solid density functional theory
SBA-15	Mesoporous silica Santa Barbara number 15
SBA-16	Mesoporous silica Santa Barbara number 16
SI	Supporting information
STEM	Scanning transmission electron microscopy
TEM	Transmission electron microscopy
TOF	Turnover frequency
TPR	Temperature-programmed reduction
XRD	X-ray diffraction
XPS	X-ray photoelectron spectroscopy

Acknowledgements

First and foremost, I would like to thank my supervisor, Professor Freddy Kleitz for his guidance and support throughout the work to make this thesis possible. I also would like to give sincere gratitude to my co-supervisor, Professor Serge Kaliaguine, for his continual mentoring and infectious enthusiasm. I am deeply grateful towards both my supervisors for giving me the opportunity to explore the interesting world of material science and catalysis.

Great appreciation goes to the professors who served on my thesis committee board: Prof. Cathleen M. Crudden, Prof. Anna Ritcey, and Prof. Frédéric-G. Fontaine.

I need to thank many dedicated administrative and technician assistants for all the help during the entire period of my study. I would like to thank Richard Janvier for his help with electron microscopes. Thanks to Alain Adnot for XPS analysis, and Jean Frenette for XRD measurement. Thanks to Mr. Gilles Lemay and Dr. Bendaoud Nohair for their tremendous help with reaction setups, AAS analysis, and TPR measurement. I would like to thank Yongbeom Seo and Prof. Ryong Ryoo (KAIST, Korea) for access to high-resolution TEM microscopy data.

During my third year of PhD study, I received the Bourses du Fonds Arthur-Labrie fellowship administered by the Department of Chemistry. I would like to thank the Department of Chemistry for supporting this fellowship.

I am also thankful to many past and current members in the Kleitz group for providing a rich working experience, intellectual stimulation and friendship. There are a few Kleitz group members that I would like to thank in particular. I thank Dr. Rémy Guillet-Nicolas and Nima Masoumifard for all their help in the laboratory. Nima, you are always willing to help and I really admire your diligence and patience in doing research. I have to thank Dr. Mahesh Muraleedharan Nair, one of the first people I met in the Kleitz group and worked with on nanocasting. I would like thank Fanny Silencieux for her great help in completing the abstracts in French of the thesis. I will never forget the memory of the "girl office" which was filled with sharing and laughter. I wish you Meryem, Binh, Maëla, humorous and loving girls all the best in the future. Thanks to Estelle, a gentle girl, for your friendship. I wish you the best of luck with your research. My life in Laval has

been also enriched by many exchange students. Thanks to Yen Chua, an adventurous student coming from Australia, for your friendship. I learned a lot about life from her and I wish her the best of luck with PhD study and life ahead.

I need to thank all my Vietnamese friends for their friendship who made my time of graduate school more memorable and a lot of fun. Particularly, I would like to thank Dr. Vinh-Thang Hoang, Dr. Gia-Thanh Vuong for all the help I received from the beginning days in Laval.

Most importantly, none of this would have been possible without the love and patience of my family, which I am very grateful for. Thanks to my parents, my younger sister and parents in law for their love and support for me at all time. Above all, a huge thank to my husband, Dinh Cao Thang for providing inspiration, encouragement and sharing all difficulties in research work as well as in daily life. My dearest little son, Dinh Hoang Tung, is the greatest thing that has happened in my life. I am greatly indebted to him, for he has made so many sacrifices to make my research to be accomplished. I am lucky to have such a wonderful family.

Finally, I would like to take this opportunity to thank you all in Laval and wish you all the best in your lives.

To my dear parents, my loving husband, Cao Thang, and my wonderful son, Hoang Tung

Preface

This thesis is divided in eight chapters. Four of them were written in the form scientific papers that have been published or submitted. The candidate is the primary author of all these papers.

Chapter 4 has been published as Hoang Yen, Yongbeom Seo, Rémy Guillet-Nicolas, Serge Kaliaguine and Freddy Kleitz, "One-step-impregnation hard templating synthesis of high-surface-area nanostructured mixed metal oxides ($NiFe_2O_4$, $CuFe_2O_4$ and Cu/CeO_2)", Chem. Commun. **2011**,*47*, 10473-10475.

Chapter 5 has been published as Hoang Yen, Yongbeom Seo, Serge Kaliaguine and Freddy Kleitz, "Tailored Mesostructured Copper/Ceria Catalysts with Enhanced Performance for Preferential Oxidation of CO at Low Temperature", *Angew. Chem. Int. Ed.* **2012**, *5*, 12032 –12035.

Chapter 6 has been published as Hoang Yen and Freddy Kleitz, "High-performance solid catalysts for H_2 generation from ammonia borane: progress through synergetic Cu–Ni interaction", *J. Mater. Chem. A*, **2013**,*1*, 14790-14796.

Chapter 7 has been submitted as Hoang Yen, Yongbeom Seo, Serge Kaliaguine and Freddy Kleitz, "On the Role of Metal-Support Interactions, Particle size, and Metal-Metal Synergy in CuNi Nanocatalysts for H_2 Generation".

In these works, the candidate performed all of the synthetic experiments with the supervision of Prof. Freddy Kleitz and Prof. Serge Kaliaguine. The characterization of the synthesized materials was carried out partly with the help of technicians and the high resolution TEM data were collected by Yongbeom Seo, who was also coauthor or acknowledged. The candidate collected and interpreted the data, and wrote the first drafts of all manuscripts. All the authors revised the manuscripts prior to publication.

Chapter 1:

Introduction

In this chapter, the issues related to clean hydrogen fuel are briefly highlighted. The scope and organization of the thesis are also detailed.

1.1 The hydrogen economy: Issues and perspectives

The problems of energy crisis and global warming have led to an intensive search for new fuels, particularly for transportation applications. Hydrogen is considered to be the best alternative to hydrocarbon fuels due to its high energy content and environmentally benign nature. Hydrogen is a sustainable energy carrier, emitting only water during combustion or oxidation process, which can be used for transportation and stationary power generation. It can be derived from diverse sources such as biomass, water as well as fossil fuels via different technologies.[1-4] There are essentially two ways to run a road vehicle on hydrogen. In the first one, hydrogen in an internal combustion engine is burnt rapidly with oxygen from air. In the second way, hydrogen is combined with oxygen in a simple electrochemical device that directly converts chemical energy into electrical energy. The efficiency of the direct process of electron transfer from oxygen to hydrogen is not limited by the thermodynamic aspects of traditional combustion energy; it can reach 50–60%, twice as much as the thermal process. In this regard, hydrogen fueled proton-exchange membrane (PEM) fuel cells to power the automobile promise an alternative to the internal combustion engine and its use of liquid petroleum fuel. [1,2,5]

However, the implementation of a hydrogen economy is suffering from several unresolved problems. The first critical question involves hydrogen sources. The ultimate hydrogen economy predicts that it will be generated from water via electrolysis with the power provided by the sun or wind. However, these technologies are still being developed and more technical progress as well as cost reduction needs to occur for them to be competitive with current hydrogen production processes from fossil fuels. The majority of the world's hydrogen supply is currently obtained by reforming hydrocarbons, followed by the water-gas shift reaction. This 'reformate' hydrogen contains significant quantities of CO (0.5-2%). It is essential to further remove CO to a parts-per-million level from the hydrogen stream to make fuel cell quality hydrogen. During the past decades, great efforts have been devoted towards the development of advanced catalytic processes for selective removal of CO from H_2-rich reformate while minimizing the loss of H_2. .[1,2,5,6]

Furthermore, when clean hydrogen can be produced either from renewable sources or fossil fuels, hydrogen storage remains a major problem for a complete transition towards

the hydrogen economy. It is necessary to store hydrogen safely, and at high gravimetric/volumetric capacities. On a weight basis, the chemical energy per unit mass of hydrogen is nearly three times larger than that of gasoline (142 MJ/kg for H_2 versus 47 MJ/kg for gasoline). However, on a volume basis hydrogen has only about a quarter of the energy content of gasoline (8 MJ/L for liquid H_2 versus 32 MJ/L for gasoline).[7,8] Several solutions have been explored and found promising, including physical storage (high pressure, low temperature, and adsorption) and chemical storage (hydrides, amine–borane adducts, and amides/imides).[7-9] However, none of these solutions is mature enough to be implemented, and drastic improvement is still needed. Safe and efficient hydrogen storage methods which allow a convenient release of hydrogen under mild conditions are desired urgently. In this context, catalyst-assisted hydrogen generation from hydrogen storage materials (e.g., ammonia-borane, hydrous hydrazine, formic acid and so forth) has been one of the most studied and desired approaches towards a hydrogen-powered society.[9-12]

1.2 Nanostructured catalysts as a viable solution

The establishment of a sustainable hydrogen-based energy future calls for new catalytic processes, with more active and more selective catalysts, and preferably made from earth-abundant elements. The catalytic properties of a material are determined by several complex factors including composition, physical structure, the interface between active catalyst phase and an oxide support, etc.[13-19] Advances in nanoscience are bringing new opportunities for developing catalytic systems with high activities for energetically challenging reactions, high selectivity to valuable products, and extended life times. The exceptional catalytic performance of nanocatalysts has been demonstrated in numerous catalytic reactions owing to the fact that nanostructured materials may possess many novel chemical and physical properties.[20-27] In particular, searching for novel nanocatalysts useful for the production of clean hydrogen fuel and efficient hydrogen evolution reactions has attracted substantial research efforts. However, finding cost effective and high performance catalysts remains a major challenge.[4,9,20,28,29]

4

1.3 Scope of the thesis

Preferential oxidation (PROX) of CO in excess hydrogen currently attracts significant attention for removing CO from hydrogen, in particular for PEM fuel cell applications.[6,30,31] It is essential, because CO is highly poisonous to the electro-catalysts generally used in fuel cells. The objective of the PROX reaction is to achieve high CO conversion to CO_2 without excessive hydrogen oxidation (to water), i.e., to decrease the CO concentration to less than 100 ppm. An efficient catalyst must be not only highly selective but also highly active at the operating temperature of the fuel cell (which is around 80ºC). On the other hand, among the potential candidates for efficient chemical hydrogen storage, ammonia borane (AB; NH_3BH_3) and hydrous hydrazine ($N_2H_4.H_2O$), both compounds with high hydrogen contents, were shown to be promising hydrogen carriers for storage and transportation. Catalyst-assisted hydrogen generation from hydrogen storage compounds via hydrolysis of AB or selective decomposition of hydrous hydrazine are interesting pathways to release H_2.[9-12] Noble metal-based catalysts are known to be effective in all these reactions.[32-40] However, precious metals lack the selectivity that is required for the PROX process and the high cost hampers their wider application. Therefore, considerable efforts are devoted to explore the synthesis of efficient catalysts based on non-noble metals for the development of clean hydrogen fuel and new energy storage materials.[41-54] Besides the practical potential, these reactions are also excellent probe reactions to study the properties of novel catalysts.

The focus of the work presented in this thesis is the development of cost effective and high performance catalysts for 1) the preferential oxidation of CO in excess H_2 and 2) hydrogen generation from AB and hydrous hydrazine. Our strategy consists in developing efficient synthesis pathways to produce novel nanostructured materials showing exceedingly high specific surface area and precisely tailored compositions and structures. In addition, the purpose of this work is also to gain better understanding of the relationship existing between catalytic properties and physicochemical characteristics of the synthesized nanostructured materials and to achieve deeper insights into possible synergy effects within such nanoscale catalysts.

1.4 Thesis organization

The thesis is organized as a story that consists of introduction, background, experimental methods, results and discussion.

The current chapter, Chapter 1 explains briefly the motivation and the scope of the research work in this thesis.

Chapter 2 introduces the fundamentals of heterogeneous catalysis, and then summarizes key factors determining the catalytic properties of a material. This chapter also describes the concepts and principles behind the synthetic methods used in this thesis for the preparation of various supported mesoporous metal oxide catalysts.

Chapter 3 presents the experimental techniques applied in the thesis for the characterization of the synthesized materials, as well as the techniques used to determine the catalytic performance.

In Chapter 4, a facile approach based on the so-called "nanocasting" method is described in detail for the synthesis of a series of mixed mesoporous metal oxide materials (Cu/CeO_2, $CuFe_2O_4$, $NiFe_2O_4$,) exhibiting high surface area and various pore structures.

In Chapter 5, the synthetic approach developed in Chapter 4 was employed to prepare different metal oxide hybrid compositions (Cu/CeO_2, $CuFe/CeO_2$, $CuCo/CeO_2$). The influence of the composition and texture of the synthesized catalysts are then studied in the PROX reaction.

In Chapter 6, exceedingly high catalytic performance of the bi-component CuO–NiO catalysts is demonstrated for the H_2 evolution from AB in aqueous solution. Parameters such as metal precursors, composition, and heat treatment conditions, have a profound influence on the synergetic interaction existing between Cu and Ni, which plays a critical role in accelerating hydrogen evolution from AB.

Chapter 7 proposes a simple method for the synthesis of highly dispersed CuNi supported on mesoporous carbon and silica nanospheres effective for hydrogen generation from both AB and hydrous hydrazine. Chemical composition and size of the metal particles, which show significant effects on catalytic properties of bimetallic CuNi

supported catalysts, can be readily controlled by varying the metal loading and feed ratio of metal precursors.

The thesis ends with Chapter 8 where conclusions and recommendations for future work are presented.

Chapter 2:

Nanostructured catalysts

This chapter introduces the basic concepts of heterogeneous catalysis as well as the main factors influencing the catalytic properties of the catalysts. The synthetic strategies to prepare the nanostructured porous catalysts are also discussed.

2.1 Fundamentals of heterogeneous catalysis

Catalysis is a phenomenon by which chemical reactions are accelerated by small quantities of foreign substances, called catalysts. A catalyst can accelerate the rate of a thermodynamically feasible reaction but cannot affect the position of the thermodynamic equilibrium. Heterogeneous catalysis involves systems in which catalyst and reactants are in different physical phases. Typical heterogeneous catalysts are inorganic solids such as metals, oxides, sulfides, acids, carbides, salts.[55,56]

Heterogeneous catalysis is a tremendously challenging and highly multi-disciplinary area requiring knowledge from chemistry (physical, organic and inorganic), physics (solid state, condensed matter), and engineering (materials processing, reactor design, modeling). It deals not only with fundamental principles or mechanisms of catalytic reactions but also with preparation, properties, and applications of the catalysts. Heterogeneous catalysts are the workhorses of the chemical, pharmaceutical and petrochemical industries as well as oil refining and environmental protection. It has been estimated that about 90% of all chemical processes use heterogeneous catalysts.[57,58]

During a heterogeneously catalyzed reaction, the reactants and products undergo a series of steps over the solid catalyst, including the diffusion of the reactants to the catalyst surface, adsorption of the reactants on the active sites, surface reaction of the adsorbed intermediates, and then the desorption and diffusion of the products away from the catalyst. In heterogeneous catalysis, chemisorption of the reactants and products on the catalyst surface is of central importance. To see how the catalyst accelerates the reaction, we need to look at the potential energy diagram of a reaction influenced by the presence of the catalyst (Figure 2.1). For the uncatalyzed reaction, the reaction proceeds when reactants collide with sufficient energy to overcome an appreciable activation barrier. For the catalyzed reaction, the reactants undergo chemisorption on the catalyst surface to form active phases by which the reaction can readily occur. The interaction between catalyst and reacting species should neither be too weak nor too strong. If the adsorption is too weak the catalyst has little effect, and will, for example, be unable to dissociate a bond. If the interaction is too strong, the adsorbates will be unable to desorb from the surface. Both extremes result in small rates of reaction. In other words, the most active catalyst is often

neither a very reactive nor a very noble surface, but rather a compromise between these extremes. This is the concept of Sabatier's principle in heterogeneous catalysis.[55,57]
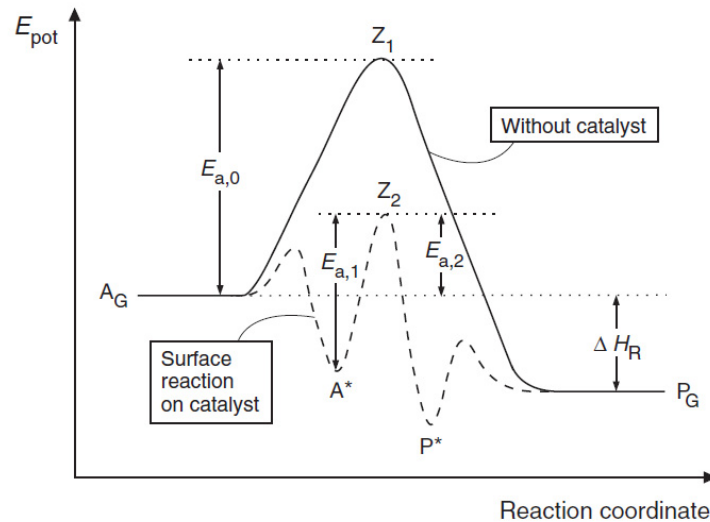
Figure 2.1. Course of a heterogeneously catalyzed gas-phase reaction $A_G \rightarrow P_G$.[57]

$E_{a,0}$ = activation energy of the homogeneous uncatalyzed gas-phase reaction

$E_{a,1}$ = true activation energy

$E_{a,2}$ = apparent activation energy of the catalyzed reaction

Z_1 = transition state of the gas-phase reaction

Z_2 = transition state of the surface reaction

ΔH_R = reaction enthalpy

These different steps are associated with an activation energy which is significantly lower than that of the uncatalyzed reaction. The activation for an overall reaction is defined as *apparent* activation energy. In principle, the activation energy E_a can be derived from the Arrhenius plot of the rate constant against the reciprocal temperature according to the equation (2.1):

$$\ln k(T) = \ln \nu - E_a/RT \qquad (2.1)$$

where ν is the pre-exponential factor (sometimes called prefactor), k is rate constant, R is gas constant.

The performance of a catalyst can be measured in terms of three main properties: activity, selectivity, and stability. Activity is a measure of how fast a reaction proceeds in the presence of the catalyst. Activity can be defined in terms of kinetics or from a more practically-oriented viewpoint. For comparative measurements, such as catalyst screening and optimization of catalyst production conditions, conversion under constant reaction conditions or temperature required for a given conversion can be used to determine the activity. The turnover frequency, TOF, which is defined as the number of molecules converted per active site and per unit of time for a reaction at given reaction conditions and extent of reaction, is commonly used as a measure of catalyst activity. This definition permits an easy comparison between the works of different researchers. When more than one reaction is taking place, catalyst selectivity is defined as the fraction of the starting material that is converted to the desired product. In comparative selectivity studies, the reaction conditions of temperature and conversion must be kept constant.

Finally, the chemical, thermal, and mechanical stability of a catalyst determines its lifetime in industrial reactors. A good catalyst should exhibit high selectivity towards the desired product (the most important property), high activity and sufficiently long life time.

2.2 Factors determining the properties of the catalysts

Metals and metal oxides constitute a wide class of heterogeneous catalysts and are the center of interest of our research in this thesis. Thus, in the present section we will discuss the factors that generally influence the catalytic properties of a catalyst, with emphasis on transition metal materials. A solid catalyst surface is complicated with the occurrence of various defects (e.g., vacancies and adatoms), and the specific position of an atom on the surface can be referred to by one of several names, as illustrated in Figure 2.2. For nanoparticles, the surface atoms or surface sites are often defined in terms of their coordination numbers and they also can be named according to their position on the particle surface (T: terrace, C: corner, E: edge). Each kind of surface atom could have different reactivity due to their different electronic structure.[15,55,57,59-61]
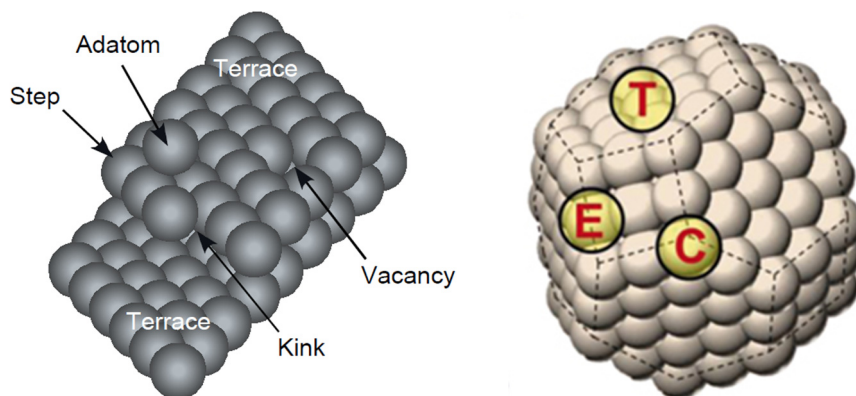
Figure 2.2. Schematic representation of a single crystal surface (left) and of a nanocrystal (right)

Therefore, the catalytic performance can be changed substantially by tuning the surface composition and surface structure which can be tailored through particle size and shape, alloying, metal-support interactions as well as support texture.

2.2.1 Facet effect

Metal/metal oxide particles exhibit different crystallographic facets (e.g. fcc (111) and fcc (100) (Figure 2.3), i.e. different atomic structures.
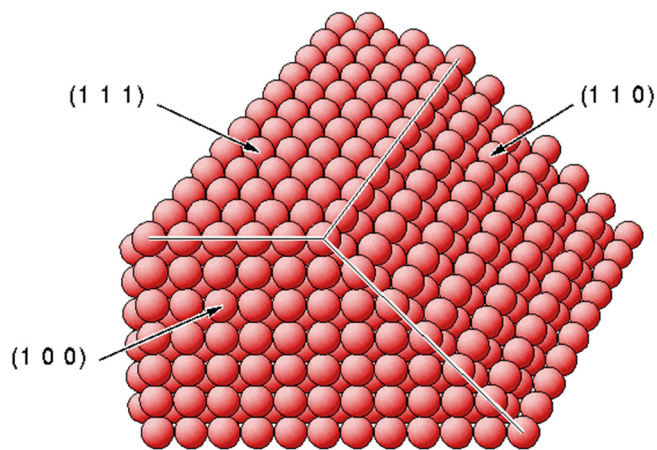
Figure 2.3. The fcc lattice with different plane surface structures.

There are two ways in which the geometric structure can affect the stability of reaction intermediates and the activation energy of a chemical reaction: electronic and geometrical effects.[15,62-68] The electronic effect is caused by surface metal atoms in different

environments having slightly different local electronic structures and hence, they interact differently with molecules both when adsorbing and reacting. Change in the atomic structure causes the modification of the electronic structure. For example, atoms in the most close-packed (111) surface of face-centered cubic lattice (fcc: Ni, Cu, Rh, Pd, Ag, Ir, Pt, Au) have a coordination number of 9. This number is 8 for the more open (100) surface and for a step or for the (110) surface it is 7. As a general rule of thumb, the more open the surface (i.e., lower coordination number), the more reactive it is. The fact that, for instance, steps bind CO stronger than the flat surfaces is in excellent agreement with experiments.[55,60]
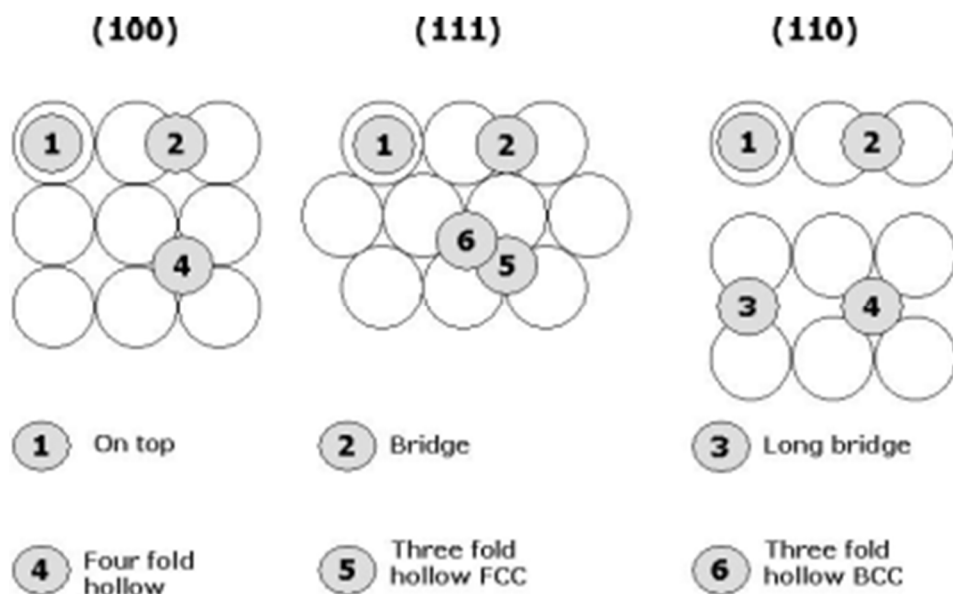
Figure 2.4. Adsorption sites on various surfaces.[55]

The purely geometric effect arises from different surface geometries which provide different configurations to a molecule for bonding. The number and type of adsorption sites on a surface depend on its geometry. The most common adsorption sites are presented in Figure 2.4. The geometric effects could become prominent over electronic effects in some processes that need more than one surface atom to proceed or when a specific arrangement between surface atoms with proper interatomic distances will be required to generate the active site. Geometric structure affects the reactivity based on the atomic arrangement and may include compressed or expanded arrangements of atoms (compressive or tensile

strain). Strain effect can be induced by the incorporation of the foreign (hetero) atoms with different lattice constant, the tuning of the particle size or interactions with the support.[59,60,69-71]

The chemistry of oxide surfaces is even more complicated because they are made up of positive metal cations and negative oxygen anions. Figure 2.5 shows the different terminations of NiO in the cubic rock-salt structure. The low-energy (100) and (110) facets present a non-polar surface containing equal numbers of metal cations and oxygen anions. There are two different unstable polar (111) surfaces, namely those terminated by nickel or by oxygen. For metal oxides, three key concepts applicable to the surface chemistry are the coordination environment, oxidation state, and redox properties.[55,72-74]
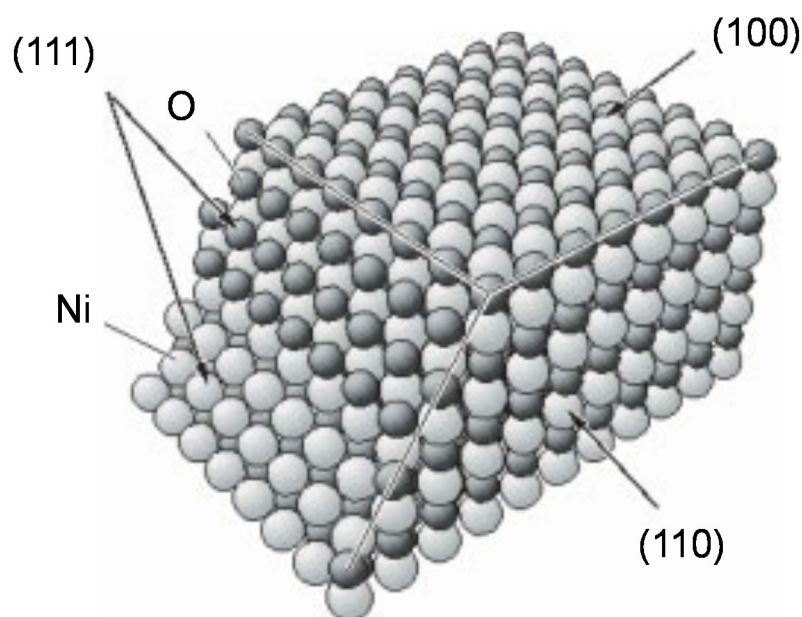
Figure 2.5. Hypothetical particle of cubic NiO, exhibiting three crystallographic surfaces. The (100) and (110) surfaces are nonpolar, implying that Ni and O ions are present in equal numbers, but the polar (111) surface can be terminated either by Ni cations or O anions. In practice, NiO crystals predominantly show (100) terminated surfaces.[55]

Advances in nanoscience enable the synthesis of well-defined nanocrystals with tunable exposed facets, which further boosted research on the catalytic properties of well-defined surfaces.[20,27,64,75-80] An example is shown in Figure 2.6, where the selectivity of pyrrole hydrogenation over Pt nanoparticles exhibits the so-called *shape dependence*. The dominant product over Pt nanocubes was n-butylamine. Over Pt nanopolyhedra of similar

size, a mixture of pyrrolidine and n-butylamine formed. To further understand this shape sensitivity, sum-frequency generation (SFG) surface vibrational spectra of pyrrole adsorbed onto Pt single crystals were compared. The study showed that n-butylamine formation is enhanced on the Pt(100) surface, the dominant surface of the nanocubes, relative to the Pt (111) surface. The results demonstrate that the underlying mechanism responsible for the shape selectivity dependence is here the difference in the nature of exposed facets of Pt particles.[20,81]
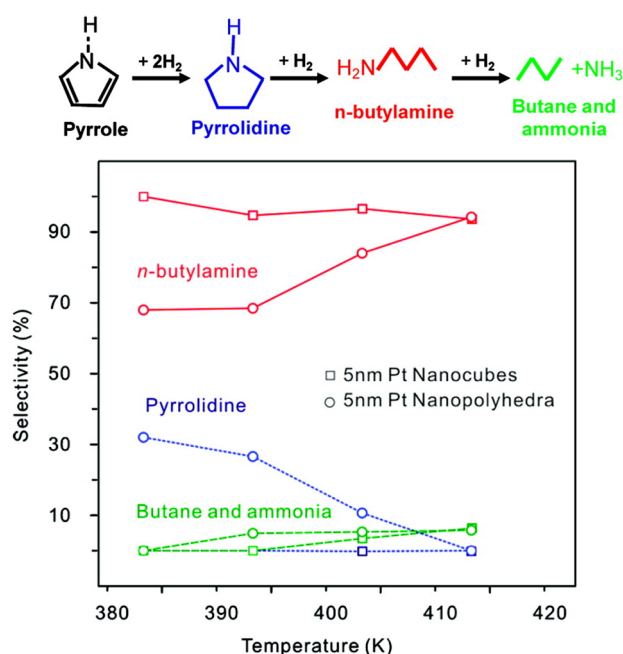
Figure 2.6. The nanoparticle shape dependence of the selectivity of pyrrole hydrogenation.[20]

In summary, the catalytic performance of a given catalyst can be tuned by changing the exposed facets. Clearly, for each application, optimization of the catalyst preparation is needed in order to obtain the desired surface structure.

2.2.2 Size effect

Because catalysis occurs on the surface, the initial incentive to obtain the active phase in the form of small particles was to maximize the surface area exposed to the reactants. However, particles in the nanosize range inherently expose edges, kinks, corners, steps and other sites involving coordinatively unsaturated atoms, whose reactivity may differ

significantly from that of the corresponding bulk metal surfaces.[14,56,59,82-87] Reactions can be classified into four categories depending on how the rate of the reaction, expressed in TOF, varies as a function of the particle size (Figure 2.7). The TOF of reactions described as *structure-insensitive* does not depend on particle size (curve 1). On the other hand, the reaction is said to be *structure-sensitive* if the TOF varies with particle size, and this may happen in several cases: it may decrease when the particle size decreases (curve 2), i.e. larger particles are more active than small ones (curve 3); it may increase for decreasing particle size, i.e. smaller particles are more active than larger ones; or it may go through a maximum (curve 4).[56,82,85]
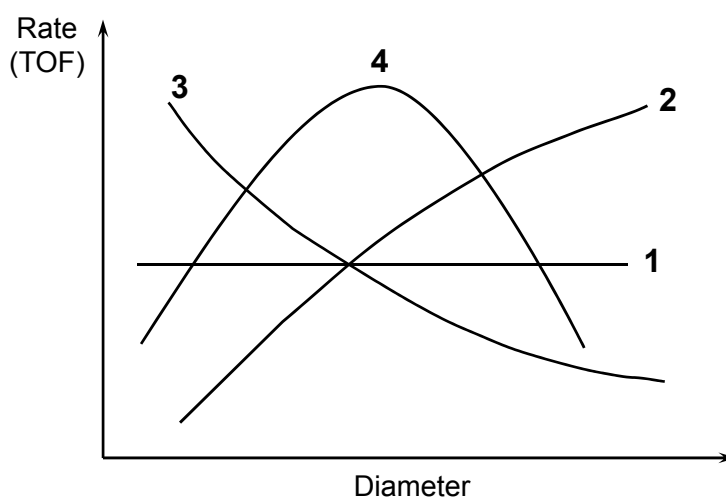
Figure 2.7. The different types of reaction rate-particle size relationship.

Understanding the particle size-catalytic properties relationship of metallic nanoparticles is not a simple task and is of intense research interest. The best example for demonstrating the exceptional catalytic activity of nanomaterials is a catalyst consisting of gold nanoparticles ranging in diameter from 1 to 6 nm dispersed on a titania support (Figure 2.8). This catalyst exhibits high activities for CO oxidation at room temperature. It has been suggested that quantum confinement effects alter the electronic structure of this noble metal and lead to the unusual catalytic activities observed.[23] Another interesting example is the variation in activity and selectivity of Co-based catalysts as a function of Co particle size in the Fischer-Tropsch reaction – the industrial process that converts CO and H_2 (syngas) into hydrocarbons. It was observed that the TOF decreased from 23×10^{-3} to

1.4×10^{-3} s^{-1}, while the C_{5+} selectivity decreased from 85 to 51 wt% when the cobalt particle size was reduced from 16 to 2.6 nm.[88]
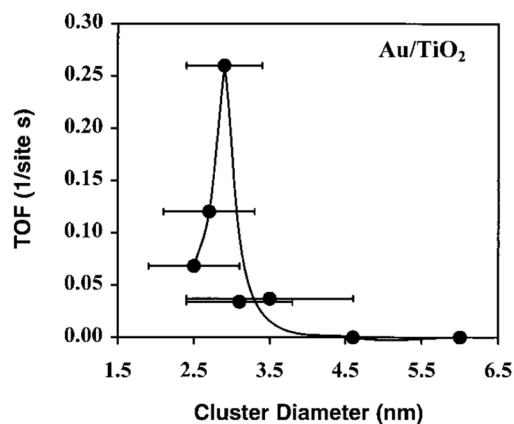
Figure 2.8. CO oxidation turnover frequencies (TOFs) at 300 K as a function of the average size of the Au clusters supported on a high surface area TiO_2 support.[23]

In short, decreasing particle size may have positive, negative or no influence on the activity and selectivity of a given catalytic system. The possible explanations of particle size effects originates from electronic or/and geometric factors. Thus, it is of practical interest to optimize the particle size of given metal particles for a specific reaction system.

2.2.3 Bimetallic systems

Bimetallic catalysts, which often exhibit electronic and chemical properties that are distinct from those of their corresponding individual metal constituents, offer the opportunity to obtain new catalysts with enhanced selectivity, activity, and stability.[22,24,89,90] Several reasons have been put forward to explain the promotion of the catalytic properties of bimetallic catalysts: (i) Ligand effects are caused by the interactions of a specific kind of metal atom with the surroundings (or ligands) of the relevant metal atoms that induces electronic charge transfer between the atoms, and thus affects their electronic structure. (ii) Ensemble effects whereby the addition of a metal alters the ensemble size of the active sites. (iii) Stabilizing effects whereby the addition of a metal improves the stability of the catalytically active metal (e.g., by inhibiting sintering or suppressing poisoning phenomena). (iv) Bifunctional effects where each metal component could promote different elementary reaction steps. These effects often co-exist and impact simultaneously the observed catalytic behavior.[22,91-97]

There are many examples for bimetallic catalysts that are applied in industrial processes.[57,58] Recently, this field has been revolutionized by the emergence of rational catalyst design at the nanoscale. With advances in density functional theory and nanoscience, it is now possible to design and synthesize nanocatalysts as well as describe catalytic reactions at the atomic scale. Many bimetallic catalysts have been investigated in search of innovative nanocatalysts for important catalytic reactions, such as CO_2 reduction, biomass upgrade to chemicals and fuels, catalytic hydrogen generation from chemical storage materials.[22,32,39,49,91,93-99] An excellent example is the stable, highly active and selective Raney-NiSn catalyst for H_2 production by aqueous phase reforming of biomass-derived hydrocarbons.[22] The performance of this non-precious catalyst compares favorably with that of platinum-based catalysts. The addition of tin to nickel decreases the rate of methane formation resulting from C-O bond cleavage while maintaining the high rates of C-C bond cleavage required for hydrogen formation. The beneficial effect of Sn on the selectivity for the production of H_2 may be due to the presence of Sn at Ni-defect sites and by the formation of Ni-Sn alloy surfaces, such as a Ni_3Sn alloy. Another interesting example is using Au-Cu bimetallic nanoparticles for electrochemical reduction of CO_2.[96] It has been suggested that two important factors related to intermediate binding, the electronic effect and the geometric effect, dictate the activity of gold–copper bimetallic nanoparticles. Au_3Cu, which has the highest mass activity for CO, outperforms conventional Au nanoparticle catalysts by more than an order of magnitude. Another recent example is the great activity enhancement observed for AuNi alloy nanoparticles supported on mesoporous MIL-101 in the catalytic hydrolysis of AB.[36] It is revealed that the AuNi@MIL-101 catalysts are more active for the hydrolysis of AB than the monometallic counterparts, thus demonstrating a synergistic effect between Au and Ni, as shown in Figure 2.9. The Au/Ni atomic ratio of 7:93 is the most active, in which the AB hydrolysis reaction is completed in 2.67 min with a 70 ml H_2 release, corresponding to H_2/AB = 3 ((Au + Ni)/AB = 0.017 in molar ratio), giving a turnover frequency (TOF) value of 66.2 $mol_{H2}mol_{cat}^{-1}min^{-1}$.
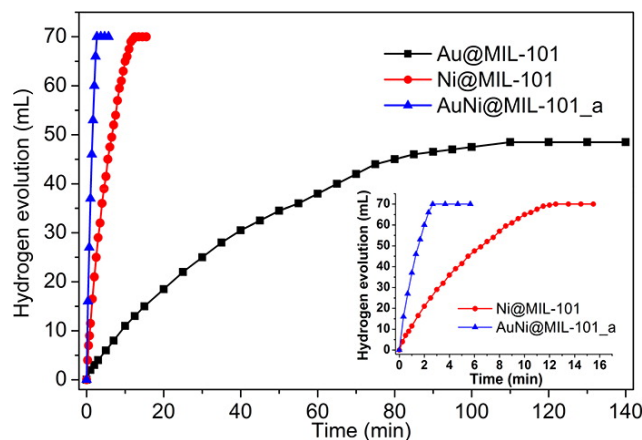
Figure 2.9. Plots of time vs volume of hydrogen generated from AB (1mmol in 5 mL water) hydrolysis at room temperature catalyzed by the Au@MIL-101, Ni@MIL-101, and AuNi@MIL-101_a catalysts (50mg, (Au+Ni)/AB (molar ratio) = 0.017).[36]

The use of bimetallic catalysts will be crucial for developing many important applications in catalysis and energy conversion. A good knowledge of theory may help with understanding and predicting new properties associated with bimetallic catalysts, but in the end, experimental studies under realistic conditions will be always central to create and implement technical catalysts.

2.2.4 Metal-support interaction

Most catalysts consist of nanometer-sized particles dispersed on a high-surface-area micro/mesoporous oxide or carbon support. These support materials stabilize metal catalysts against sintering under harsh reaction conditions such as strong reduction media and high temperature.[100-102] In addition, the support can strongly affect the intrinsic activity and selectivity of a catalyst. This can originate from the presence of special sites at the perimeter of the metal particles, where the electronic properties of both metal and support atoms influence the adsorbed species. In other cases, the surface properties of metal particles modified by strong interaction with the support directly affect the strength of the metal-adsorbate bonding.[16,103-112]

The choice of the appropriate catalyst support for a particular active component and reaction system is important. For instance, silver nanoparticles have much higher stability on reduced $CeO_2(111)$ than on $MgO(100)$. This effect is the consequence of the very large adhesion energy (~2.3 joules per square meter) of Ag nanoparticles to reduced $CeO_2(111)$,

21

which was found to be a result of strong bonding to both defects and CeO_2 (111) terraces, localized by lattice strain.[102] In another example, it has been proven that the temperature and efficiency for NO reduction with hydrocarbons over a gold supported catalyst depend on the nature of the metal oxide support and vary as ZnO (523 K, 49%), α-Fe_2O_3 (523 K, 12%), MgO (623 K, 42%), TiO_2 (623 K, 30%), Al_2O_3 (673-723 K, 80%).[113] A further illustration for electronic metal-support interaction is a significant enhancement in the catalytic activity, by the factor of 20-fold, for the water-gas shift reaction ($H_2O + CO \rightarrow H_2 + CO_2$) over the peculiar platinum-ceria interactions compared with platinum catalysts. The results of valence photoemission measurements and DFT calculations revealed that the Pt-ceria interactions lead to much smaller density of Pt 5d states near the Fermi level than that expected for bulk metallic Pt, which consequently greatly decreases the activation barrier for the water dissociation; this step is thought to be rate-limited in the water gas shift reaction. Moreover, the authors also show that an even more active Pt/CeO_2 catalyst is obtained when the ceria support is itself supported in the form of tiny nanoparticles on bulk TiO_2(111), rather than in the form of an extended bulk CeO_2(111) surface. This highlights an exciting new type of two-phase support material, in which two nanostructured oxide phases serve as a better support.[110] Moreover, catalyst support can provide additional functions for the reactions.[57,85,91,114-116] For example, if the reaction requires a bifunctional catalyst (e.g. metal and acid functions), acidic supports such as silica-alumina materials could be used. On the other hand, if the reaction occurs only on the metal, a more inert support such as silica or carbon is suitable.

2.2.5 Support structure

The pore structure of the support can influence the performance of the active components, since the course of the reaction is often dependent on the rate of diffusion of the reactants and products.[55-57] According to International Union of Pure and Applied Chemistry (IUPAC), the pores of materials are classified by their size: pore sizes in the range of 2 nm and below are called micropores, those in the range of 2 nm to 50 nm are named mesopores, and those above 50 nm are macropores.[117] The pore size distribution, pore connectivity and morphology were shown to directly impact the catalytic properties of porous materials.[57,118-125] For example, microporous materials such as zeolites can

selectively convert molecules on the basis of their size. Here, starting materials of a certain size and shape can penetrate into the interior of the zeolite pores and undergo reaction at the catalytically active sites. Substrate molecules that are larger than the pore apertures cannot react. In addition, the porous structure of the support material has proven to be a crucial factor for catalyst stability. Loss of active surface area by metal particle growth is a major cause of deactivation for supported catalysts. Generally, narrow pores mitigate particle growth, an effect which likely relates to lower particle mobility when the size of the growing nanoparticles becomes similar to that of the pore host. In addition to pore size, pore connectivity and morphology can also play a role on the particle growth by influencing the pathways for the transport of metal species under reaction conditions.[118,121] Many innovations were made in designing nanostructured support materials. Ordered mesoporous materials with large pore size, large pore volume and tailored pore architecture are outstanding candidates for investigating the pore structure-catalytic property relationship of supported catalysts.[126-131] In this regard, it was suggested, for instance, that one-dimensional (1D) pore structure limit growth of metal particles as compared to highly interconnected three-dimensional (3D) pore systems. However, 3D interconnected porosities are strongly preferred to avoid mass transport limitations and pore blockage. In addition, the metal-support interface may also be influenced by the nature and degree of concave or convex pore surface.

2.2.6 Conclusions

In this section, a brief introduction about the major factors influencing the catalytic properties of solid catalysts was presented. One of the principal objectives of modern research in heterogeneous catalysis is the development of methods for further control and manipulation of the activity, selectivity and stability of such catalytic systems. This can be achieved by different approaches, including (i) selection of catalyst composition, (ii) manipulations of the atomic structure (e.g., by controlling the size and morphology of the catalyst), (iii) choice of the support (composition, structure), or any combination thereof. The ultimate goal is to acquire enough knowledge on the factors determining catalytic properties to be able to tailor catalysts for a particular application. However, in the real catalytic processes, the complex interplay between all the factors makes it difficult to

distinguish the influence of each parameter. For example, decreasing particle size not only increases surface area but also changes the fractions of corner, edge and terrace atoms. The smaller the particle, the more affected it is likely to be by metal-support interaction and reaction medium. Moreover, the structure of heterogeneous catalysts is dynamic and depends on the composition of the surrounding environment. Some structures and active phases may only exist under reaction conditions rendering more difficulties to identify the attributes responsible for the catalytic behavior of the catalyst.

2.3 Synthesis of nanostructured catalysts

Nanoparticles of transition metals dispersed on high-surface-area oxides or carbon form the basis for many catalysts that are important in energy technology, pollution prevention as well as environmental clean-up. Ordered mesoporous materials with tunable pore structure, controllable pore size distribution, high surface area, large pore volume and thermal stability are very suitable catalyst supports or can be used as catalysts themselves, because they provide high dispersion of metal nanoparticles and facilitate the access of the substrates to the active sites. [126-133] The following sub-sections intend to briefly describe the approaches used in the present thesis for the synthesis of mesoporous materials and metal-supported mesoporous materials as catalysts.

2.3.1 Mesoporous materials via soft-templating method

Soft-templating is defined as a process in which organic molecules serve as a 'mold', or template, and around which a framework is built up. The removal of these organic molecules via calcination or solvent extraction results in a cavity which retains the same morphology and structure as the organic molecule assembly.[134,135] Figure 2.10 presents a schematic illustration of the general sol-gel-type synthesis generally used to construct mesostructured materials. In this method, the surfactant (cationic, anionic or non-ionic surfactant, some typical surfactants are listed in Table 2.1) serves as the organic template or structure-directing agent (SDA). Charged inorganic species strongly interact with charged surfactant head groups (or block-copolymer hydrophilic components), either directly or through counter-ion and hydrogen bond-mediated pathways.
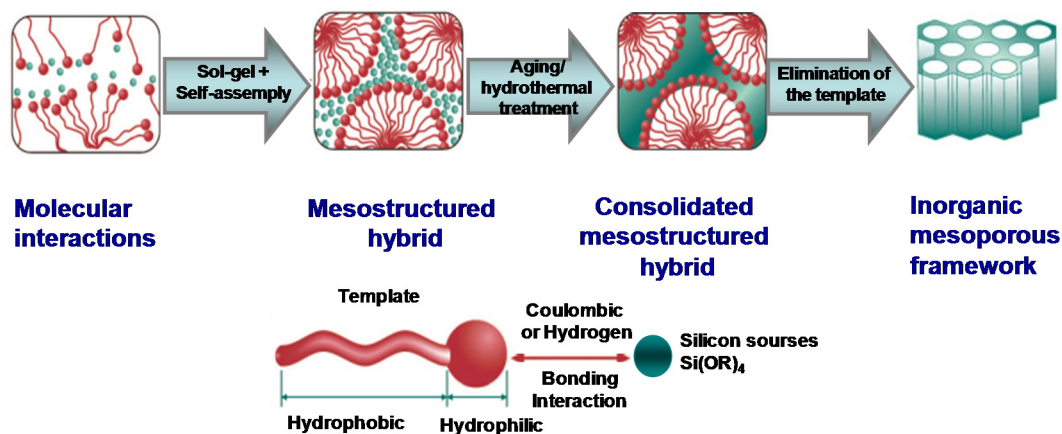
Figure 2.10. General soft-templating approach for mesostructure assembly.[136]

Soluble inorganic species and surfactant molecules combine to eventually form a hybrid mesophase that is the precursor of the final mesostructured hybrid. Among the surfactants, non-ionic surfactants and block copolymers (e.g., Pluronic-type, PEO-PPO-PEO) having a wide range of ordered microdomain morphologies are widely used in the synthesis of mesostructured materials owing to their low cost, low toxicity and biodegradability.[137,138]

Table 2.1. Examples of some common surfactants.

This route is suitable for the preparation of mesoporous silica, because the hydrolysis and condensation rates of silicates can easily be controlled by adjusting reaction parameters such as pH value and temperature. The derived mesostructures are influenced by a rational

control of the organic-inorganic interactions and the cooperative-assembly of silica species and surfactants. A large variety of mesoporous silicas with different pore structures including two-dimensional hexagonal (*p6mm*) and three-dimensional cubic (*Im*3*m*, *Ia*3*d*, *Fm*3*m,* etc.) have been synthesized (Figure 2.11).
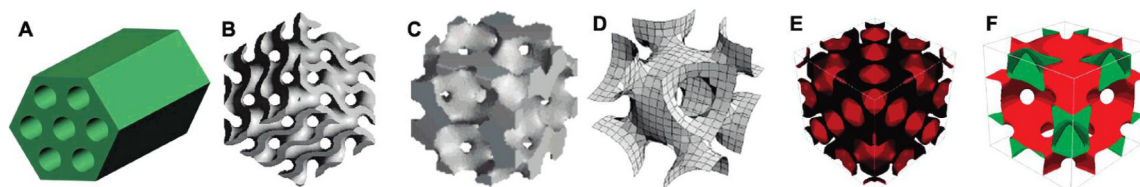
Figure 2.11. Pore models of mesostructures with symmetries of (A) *p6mm*, (B) *Ia*3*d*, (C) *Pm*3*n*, (D) *Im*3*m*, (E) *Fd*3*m*, and (F) *Fm*3*m*.[135]

Examples of different mesoporous structures are illustrated by electron microscopy images in Figure 2.12
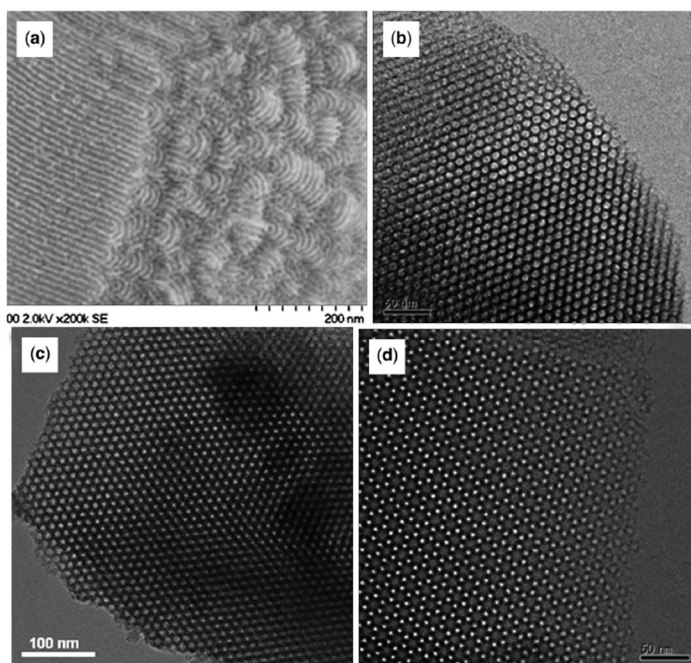
Figure 2.12 (a) High-resolution SEM image revealing the pore network organization of SBA-15 silica. (b) TEM image showing the 2-D hexagonal arrangement (*p6mm*) of the mesopores in SBA-15. (c) TEM image of cage-like (*Im3m*) SBA-16 silica, viewed along the [111] direction. (d) Typical TEM image of the bicontinuous (*Ia3d*) KIT-6 silica structure, viewed along the [111] direction.[139]

The texture properties and pore morphologies can be controlled by varying synthesis conditions (pH, time, temperature) and gel compositions, by use of organic additives or added electrolytes, and by the nature of surfactants used. In particular, a fine control of the mesopore size is desirable because of potential applications as catalysts, selective sorbents, and hosts for quantum size effect materials. Several methods can be applied to adjust the pore sizes of such mesoporous molecular sieves.[58,134,139-143] Some of the synthetic tools used for tailoring pore size are described below.

Surfactant chain length: The pore diameter of mesoporous materials depends on the length of hydrophobic groups in the surfactant molecules or polymers. For non-ionic surfactants and block copolymers, the adjustment of pore size can also be achieved by varying the concentration of the templating agent, and by changing the ratio of block size in the copolymers.[58,140,144,145]

Time and temperature: The reaction solution containing inorganic species and surfactants are most often hydrothermally aged at temperatures ranging from 40°C to 150°C for a period of time varying from hours to days in order to enhance the polymerization degree of inorganic species.

Hydrothermal treatment temperature or time
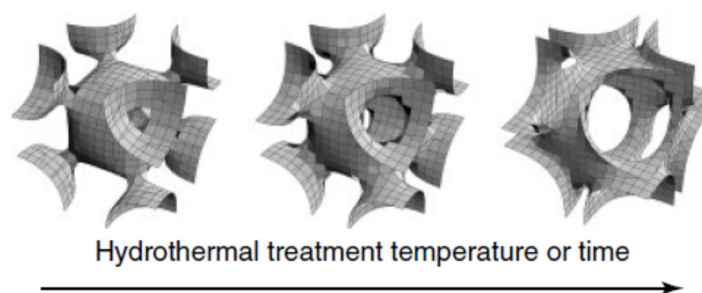
Figure 2.13. Structure tailoring of SBA-16 by increasing the hydrothermal treatment time or temperature.[58]

Changing hydrothermal treatment time and temperature can tailor pore size. In case of block copolymer especially, increasing the synthesis temperature leads to micelles with a larger hydrophobic core volume which in turn results in an increase in pore size of the materials.[142,143] A similar effect of pore size increase occurs upon longer hydrothermal

treatment time. For example, the pore openings and the main mesocage sizes of SBA-16 silica can be enlarged systematically by increasing the time and/or temperature of the hydrothermal treatment (Figure 2.13)

Organic additives: Adding organic swelling agents is a significant way to expand pore sizes. Hydrophobic organic species can be solubilized inside the hydrophobic regions of surfactant micelles, which leads to a swelling of the micelles. The pore sizes are most efficiently expanded by the addition of large organic hydrocarbons to the synthesis mixture, such as dodecane, trimethylbenzene, triisopropylbenzene, tertiary amines, and poly(propylene glycol) .[134,140,141]

Unlike mesoporous silica, synthesis of non-siliceous mesoporous materials is definitely not as straightforward because of the different chemical behavior of the metal precursors used.[134,136] Metal precursors (generally chlorides or alkoxides) are much more reactive than silica-based analogues; uncontrolled condensation yields macroscopic phase segregation. In addition, synthesis procedures are extremely sensitive to many external parameters, leading in some cases to irreproducible results. In particular, redox reactions, possible phase transitions, and crystallization processes are often accompanied by the collapse of the structure. Strategies for controlling the hydrolysis–condensation rates of metal precursors include utilizing specific pH ranges, stabilizing ligands, nonaqueous media, pre-formed nanoclusters, controlled hydrolysis, or some combination thereof. The first porous transition metal oxide was reported by Antonelli et al. in 1995 based on titania.[146] Since then, a large number of mesoporous metals and metal oxides have been synthesized.[147-149]

The soft-templating method is versatile, but it is also complicated and unpredictable. The obtained mesostructures from the self-assembly process are strongly dependent on temperature, solvent, concentration, hydrophobic/hydrophilic properties, interface interaction, ionic strength and many other parameters. This makes prediction of the resulting final mesostructure more difficult. In particular, this method is considered unsuitable for the synthesis of materials with composition and structure requiring high-temperature treatments such as carbon, some spinels or perovskites, which are sensitive to thermal treatment and redox reactions. It thus remains a challenge to simultaneously obtain

highly crystalline transition metal oxides while retaining the nanostructure control as directed from the surfactant templates.

The soft templating method was used in this work to synthesize different mesoporous carbon and silicas designated as KIT-6, SBA-15, MCM-48.

2.3.2 Mesoporous materials via hard templating (nanocasting) method

The hard-templating process (i.e., *nanocasting*) is a powerful method to create mesoporous materials that are difficult to synthesize by processes utilizing cooperative assembly between surfactants and inorganic species. Rigid templates may be very diverse, but a relatively general procedure for nano-replication can be given. In the first step of a structure replication process, the pores of the matrix are filled with the precursor for the desired product, for example, metal salts such as nitrates for metal oxides. This is usually realized by impregnation with a precursor solution, either by a "wet impregnation" or by the "incipient wetness" technique. The interaction of the precursor species with the pore walls is crucial, and it may involve hydrogen bonding, coordination of metal ions (e.g., on silanol groups), Coulomb interactions, and van der Waals forces, which facilitate the migration of metal ions. Other approaches to efficiently infiltrate the precursor species into the pores of the matrix include vapor-phase infiltration and infiltration in the liquid/molten state in absence of solvent. After the infiltration of the precursors and, if needed, the subsequent removal of the solvent, the formation of the wanted product is typically accomplished at elevated temperatures.[150]
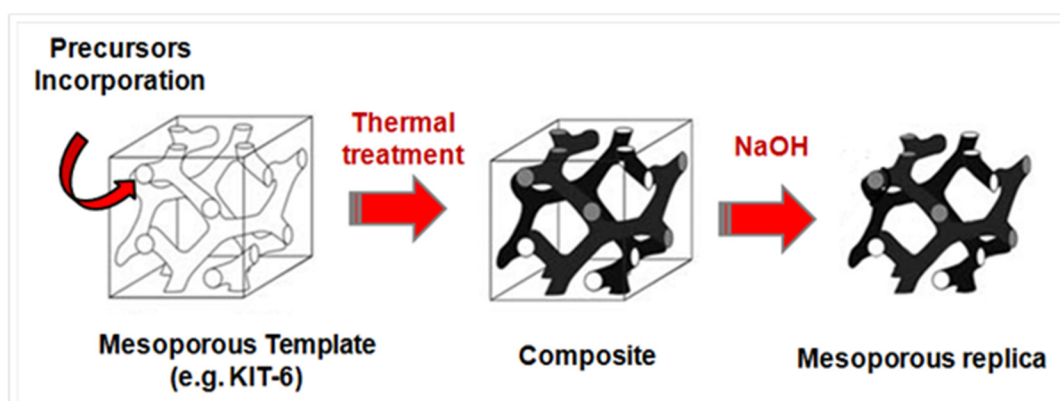
Figure 2.14. Schematic representation of hard templating method for the synthesis of non-siliceous mesostructured materials.

In short, this synthetic pathway involves four main steps as illustrated schematically in Figure 2.14): 1) choosing and generating the original template (mesoporous silica or carbon are usually used), 2) filling the mesopores with the precursors of the target composition, 3) converting these precursors into an continuous solid (i.e., formation of a composite consisting of the original template and a target inorganic/polymeric solid), and finally, 4) removing selectively the original template by a chemical or a thermal treatment.

The great advantage of this approach is the possibility of replication of complex mesophases and mesopore topologies with a precise level of structural and compositional control. Furthermore, morphology and particle shape of the template may be conserved for the nanocast replicas (e.g., spheres, thin films, monoliths).[151-154]

The target material is usually not incorporated in the pore system of the template as such, but under the form of a precursor (often in solution) that has to be converted subsequently into the final material. This precursor needs to meet several requirements. First, as it must enter the template structure, it must either be gaseous, highly soluble, or liquid at moderate conditions, so that it can be infiltrated into the voids of the template while achieving high loadings;[58,150,155,156] Second, conversion to the desired composition should be simple and with as little volume shrinkage as possible. Finally, in most of the cases, it should not react chemically with the solid template. Metal nitrate salts are attractive precursors due to their high solubility, and availability at low cost. Moreover, pure oxides can be obtained because of the facile and complete removal of nitrates via thermal decomposition. Then, when choosing the original template, two important points must be considered. One is whether the template can maintain its ordered mesostructure during the conversion process in the third step. The other is whether the template can be easily removed without disrupting the mesoporous structure in the resulting replica. One of the most versatile hard templates is ordered mesoporous silica, since it can be prepared in diverse pore structures and morphologies.[135] Note that, these silica materials dissolve rather easily in HF or NaOH solutions, but multiple treatments are often needed to ensure optimal removal of silica. Though, it is not unusual to detect residual silicon (a few %) in the nanocast oxides when silica is removed using NaOH.

The infiltration of the precursor into the pore channels is one of the most important factors in nanocasting. The wet impregnation technique is commonly used,[155-157] in which the solid template is dispersed in a dilute solution of precursors in order for the solute species to migrate and to be adsorbed on the pore surface upon solvent evaporation. This method often results in low level of loading of the pores with the precursors. Another widely used technique is the dry impregnation, also called incipient wetness.[158-160] In this method, a saturated solution of the precursor is used and the volume of the solution is restricted to the pore volume of the hard template used. Although the incipient wetness technique usually leads to a higher precursor loading, multiple impregnation steps are often required for optimized filling of the pores. Alternatively, a solid-liquid route, which is based on using molten nitrate salts for infiltrating the mesoporous silica without of the need of a solvent, has been applied to increase oxide loadings in the mesoporous tempalte.[161,162] In all these cases, however, the unique driving force for accelerating the movement of the precursor solution into the mesopore channels is capillary effects. Therefore, improving capillary force could facilitate the migration of the precursor species. Generally, the metal precursors used in nanocasting are hydrophilic. It is believed that enhancing the hydrophilic character of the pore walls can increase the incorporation of the precursor with a high filling degree. For this purpose, surface functionalization of mesoporous silicas by certain organic groups (e.g., $-NH_2$, $-CH=CH_2$) was attempted in order to improve the interaction between the pore walls of the template and the metal precursors.[160,163,164] Another way is to maintain a high surface silanol concentration by performing acidic solvent extraction or oxidation under microwave treatment to remove the structure-directing agents used in the synthesis of the parent mesoporous silica template, instead of calcination at high temperature.[150,155,156,165] These above strategies can indeed improve the interactions between the pore walls of the templates and the precursors through hydrogen and/or coordination bonding. However, these surface interactions are in fact mostly effective for the first layer of adsorbed precursor species. As the amount of precursor loading needed to obtain a stable mesostructure replica is far higher than the amount of a monolayer adsorption, the interactions between the precursors themselves are therefore also critical to reach high loading. In addition, too strong interactions between precursors and pore

surfaces may hinder the migration of the precursors throughout the structure and, consequently, block the channels.

Beside these chemical aspects, the physical aspects should not be underestimated in the infiltration process. The impregnation process may be viewed as the replacement of a solid-gas interface by a solid-liquid interface.[58,166] Here, the pressure developed in the nanopores upon impregnation caused by compressed air bubbles may reach several MPa depending on the liquid-gas interfacial tension and pore size of the mesoporous template. The higher the surface tension of the precursor solution and smaller the size of the template selected, the higher is the pressure in the air bubbles inside the pores.[58,167] The development of high pressure could impose large forces on the portions of the pore walls in contact with these bubbles, which may degrade the mesopore framework of the support upon impregnation. Moreover, replacement of the solid-gas interface by a solid-liquid interface generally causes a substantial heat release which may alter the quality of impregnation when using high concentration of precursor solution. Some methods for preventing or limiting the degradation of the mesoporous template can be employed, such as operating impregnation in vacuum, using fairly volatile solvents (alcohols or acetone are widely used in nanocasting), or adding a surfactant to the solution. However, these solutions either are difficult for practical application or lead to a lower precursor filling because of the presence of additives or the use of less polar solvents (i.e., lower solubility of metal precursors in the solution). One interesting alternative method called the "bi-solvent technique" was proposed to overcome precursor infiltration issues.[168,169] In this method, the support is first dispersed in a pure less wetting solvent prior to being placed in the impregnation solution. Here, the characteristics of exothermic effects and high pressure development are no longer valid in the step of impregnation. The driving force for the infiltration of the metal precursors into the pore channels is a concentration gradient. In connection to that, we recently developed a versatile one-step-impregnation synthesis method, which was shown particularly suitable for preparation of nanocast mixed metal oxide compositions using nitrate salts as precursors. This method is based on using molten nitrate salts in the presence of an organic solvent (e.g., n-hexane or cyclohexane) under refluxing conditions, to infiltrate different mesoporous silicas as typical solid templates (see details in Chapter 4).

After the impregnation step, subsequent drying and thermal treatment(s) to convert the precursor into the desired metals/metal oxides are also important steps in the course of the replication process. Here, diffusion, nucleation, particle growth and phase transformations take place during drying and thermal treatments. In multi-component systems, the uniformity of the replicated composite may be influenced by the choice of metal precursors, and the presence of chelating agents (e.g., citric acid) may be needed to achieve homogeneous precursor distributions as it is, for instance, the case for the nanocast synthesis of perovskites.[170,171] In turn, the physical and chemical properties of resulting material can be linked to several parameters inherent to the treatment conditions used. For instance, the size of the replica particles was shown to be strongly affected by the environment atmosphere during thermal treatment.[172]

The hard templating method was implemented in the present thesis to synthesize various high-surface-area mesoporous single and mixed metal oxides.

2.3.3 Metal-supported mesoporous materials

There are different routes, such as co-condensation, ion-exchanging, surface grafting, chemical vapor condensation, spreading and wetting etc., to prepare supported metal catalysts as schematically shown in Figure 2.15.[58,85,166,173] The choice of method is not always trivial and depends a lot on specific applications. The methods most frequently used to achieve the deposition of the active component precursor in the form of nanoparticles onto a preformed porous support are impregnation, deposition–precipitation, and metal colloid deposition. Both impregnation and deposition-precipitation involve the dissolution of the metal precursor in an appropriate solvent, followed then by drying in the case of impregnation; for deposition–precipitation the next step is pH adjustment, changing the valence of a dissolved active precursor, or decreasing the concentration of a compound forming soluble complexes with the active precursor. The resulting solid composite is subsequently subjected to direct reduction or calcination-reduction steps to decompose the metal precursor to yield the active final metallic state as well as metal-support bonding. The disadvantage of these two techniques is the difficulty of well controlling the particle structure, the distribution of metal particle size and the location of metal nanoparticles in the support pores. Variables which are important include the concentration of the precursor

salt, type of salt, solvent, nature of the support, time of contact with the support and the presence of other compounds, thermal treatment conditions (e.g., temperature, heating rate, gas composition).[174-180]In the metal colloid deposition, the preformed metal particles are adsorbed onto a support, both suspended in a solvent. The size and structure of the metal particles are well controlled using the numerous methods known for nanoparticle synthesis. However, the metal-support interaction is usually weak. In addition, by-products of the nanoparticle preparation which are present in the liquid medium and some nanoparticle protective agents may interfere with the catalytic performance of the resulting catalysts.[78,79,181-184]
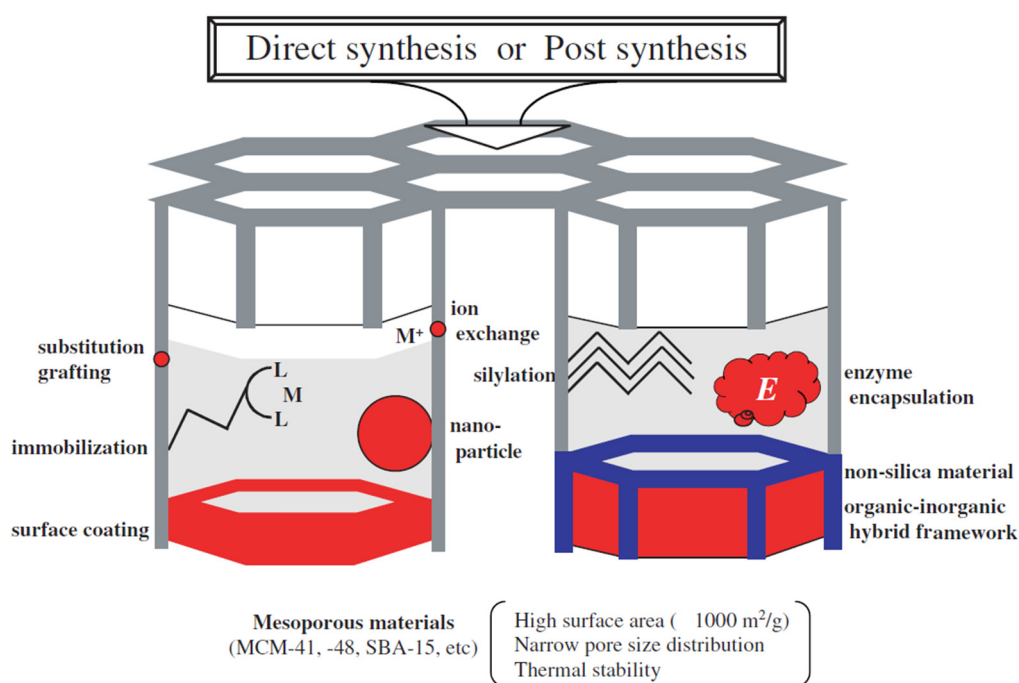
Figure 2.15. Schematic sketch of the various methods for the functionalization of mesoporous material. There are many possible strategies and pathways to introduce novel functions in mesoporous materials.[173]

In this thesis, the impregnation is the method of choice to prepare supported metal catalysts owing to its synthetic simplicity. The simplicity of the preparation method enables large quantities of catalysts to be prepared. In addition, this procedure can be used to achieve predetermined metal loadings on the catalyst.

34

Chapter 3:
Characterization techniques

A variety of techniques were used for the characterization of the materials, which were synthesized in this thesis. The complexity of the materials requires a number of combined physical and chemical characterizations to fully understand the physicochemical properties and catalytic chemistry of such materials. Please note that the experimental details for the characterizations of the materials in this thesis and the instruments information are detailed in the different Results and Discussion chapters.

3.1 Physical adsorption

Gas adsorption can be used for the characterization of specific surface area, pore size, pore size distribution and pore volume of nanoporous materials.[58,139,185] Adsorption is a general phenomenon which occurs every time that a gas or liquid (fluid) comes in contact with a solid. Physisorption is the result of van der Waals forces, and the accompanying heat of adsorption is comparable in magnitude to the heat of evaporation of the adsorbate. This technique is based on the measurement of adsorbed amount as a function of pressure (or relative pressure P/P_0, where P_0 is the saturation pressure of the adsorptive) at a given temperature. The resulting relationship, usually presented in graphical form, between the amount adsorbed and the pressure, is known as sorption isotherms. The measurement of nitrogen, argon and krypton adsorption at cryogenic temperatures (77 K and 87 K) is mainly used for surface area and pore size characterization. Nitrogen at 77 K is considered to be a standard adsorptive for surface area and pore size analysis.
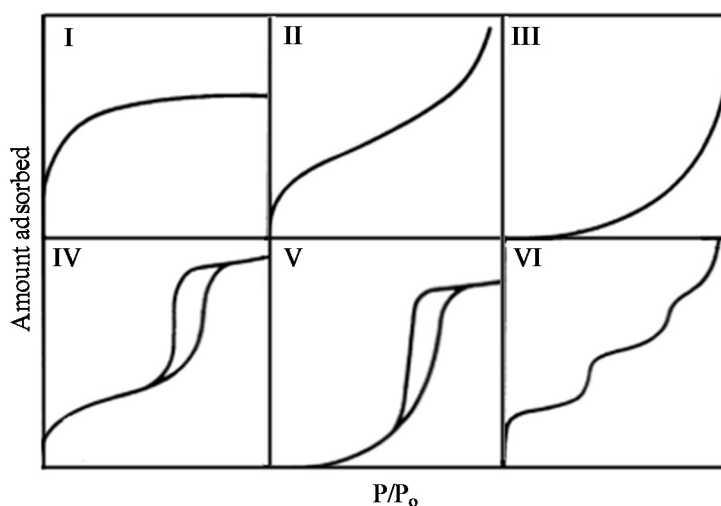
Figure 3.1. IUPAC classification of the physisorption isotherms.

The first step in the interpretation of a physisorption isotherm is inspection of its shape, because the shape of the isotherms strongly depends on the interplay between the strength of attractive fluid-wall and fluid-fluid interactions as well as the porous structure of the adsorbent. Within this context, the International Union of Pure and Applied Chemistry (IUPAC) has published a classification of six types of adsorption isotherms and proposed to classify pores by their internal pore width. Micropores: pores of internal width

less than 2 nm; mesopores: pores of internal width between 2 and 50 nm; macropores: pores of internal width greater than 50 nm. It has become popular to refer to micropores and mesopores as nanopores. The classification of physisorption isotherms and associated hysteresis loops is shown in Figure 3.1. Type I isotherms are characteristic of microporous materials such as zeolites or activated carbons. Type II and III isotherms are given by the physisorption of gases on most non-porous or macroporous adsorbents. Type IV and V isotherms are representative for mesoporous adsorbents. Type VI isotherms represent layer-by-layer adsorption on a highly uniform surface.

The sorption behavior in micropores is dominated almost entirely by the interactions between fluid molecules and the pore walls, therefore micropores fill through a continuous process (i.e., no phase transition). In contrast, the sorption behavior in mesopores depends not only on the fluid-wall attraction, but also on the attractive interactions between the fluid molecules. This leads to the occurrence of multilayer adsorption and capillary (pore) condensation (at $P/P_0 \geq 0.2$). Pore condensation is the phenomenon whereby a gas condenses to a liquid-like phase in a pore at a pressure P less than the saturation pressure P_0 of the bulk liquid.
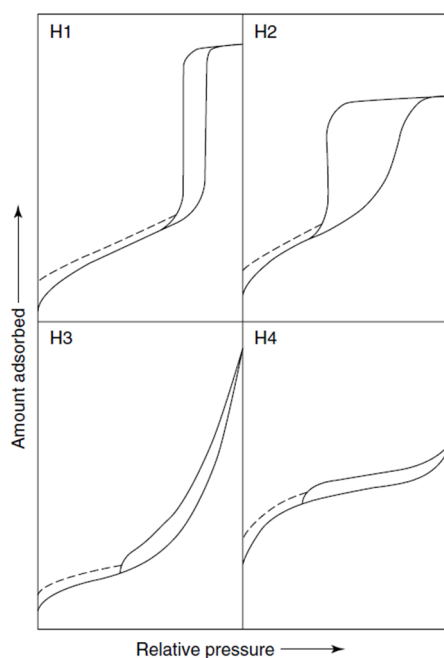
Figure 3.2. Types of hysteresis loops.

38

Capillary condensation is very often accompanied by hysteresis. The shapes of the adsorption hysteresis loop classified by IUPAC (see Figure 3.2) have been attributed to particular pore structures/networks. Type H1 loop is associated with adsorbents with a narrow distribution of uniform (cylindrical-like) pores. Materials that give rise to H2 hysteresis contain a more complex pore structure in which network effects (e.g., pore blocking/percolation) are important. Type H3 and type H4 do not terminate in a plateau at high relative pressures, and thus, the limiting desorption boundary curve is not easy to define. This behavior can for instance be caused by the existence of non-rigid aggregates of plate-like particles or assemblages of slit-shaped pores. The mechanism and origin of sorption hysteresis is still under investigation. In general, evaporation occurs without nucleation, via a receding meniscus, whereas condensation occurs delayed due to the metastabilities associated with the nucleation of liquid bridges, causing capillary condensation and capillary evaporation in mesopores. Both capillary effects occur most often at different relative pressures which lead to the appearance of hysteresis loops.[186-191]

The BET equation, proposed by Brunauer, Emmett, and Teller in 1938, is commonly used for the evaluation of specific surface area. Usually, two stages are involved in the evaluation of the BET area. First, it is necessary to transform a physisorption isotherm into the 'BET plot' and from there to derive the value of the BET monolayer capacity, n_m. The second stage is the calculation of the specific surface area, S, which requires knowledge of the molecular cross-sectional area. The monolayer capacity n_m is calculated from the adsorption isotherm using the BET equation (Eq. 3.1)

$$\frac{P/P_o}{n(1-P/P_o)} = \frac{1}{n_m c} + \frac{c-1}{n_m c} \times \frac{P}{P_o}$$
(3.1)

Where n is the amount adsorbed at the relative pressure P/P_0, n_m is the monolayer capacity, c is a constant related exponentially to the heat of adsorption in the first adsorbed layer. The surface area can thus be calculated from the monolayer capacity on the assumption of close packing as:

$$S = n_m \sigma L$$
(3.2)

Where σ is the molecular cross-sectional area, n_m is the monolayer capacity, L is the Avogadro constant. The BET equation is applicable for surface area analysis of nonporous and mesoporous materials, but in a strict sense should not be applicable in case of microporous adsorbents.

The Barett-Joyner Halenda method (BJH) is widely used for mesopore analysis based on the modified Kelvin equation (Eq. 3.3):

$$\ln (P/P_0) = -2\gamma\cos\theta /RT\rho(r_p - t_c) \qquad (3.3)$$

Where R is the universal gas constant, γ is surface tension of the liquid condensate and ρ is its density, θ is contact angle of the liquid meniscus against the pore wall, r_p the pore radius and t_c the thickness of an adsorbed multilayer film, which is formed prior to pore condensation. The Kelvin equation provides a relationship between the pore diameter and the pore condensation pressure, and predicts that pore condensation shifts to a higher relative pressure with increasing pore diameter and temperature.

However, methods based on the modified Kelvin equation do not take into account the influence of the adsorption potential on the position of the pore condensation transition. It is further assumed that the pore fluid has essentially the same thermophysical properties as the correspondent bulk fluid. It is found that the BJH- and related approaches based on the modified Kelvin equation underestimate the pore size up to 25 % for pores smaller than 10 nm.

The alternative and more accurate way to determine pore size distributions is therefore to apply density functional theory methods. Nonlocal density functional theory (NLDFT) describes the configuration of adsorbed molecules in pores on a molecular level and thus provides detailed information about the local fluid structure near curved solid walls as compared to the bulk fluid. The DFT methods were developed for pore size analysis taking into account the particular characteristics of the hysteresis, that is, the pore shape. Correspondingly, pore size distributions are calculated for a given pore geometry, using a series of theoretical isotherms (kernels) for pores of the respective geometry with different diameters. In principle, the NLDFT method may be applied over the complete range of nanopore sizes when suitable kernels are available. A drawback of the standard NLDFT is that they do not take sufficiently into account the chemical and geometrical

heterogeneity of the pore walls. Recently, the NLDFT method was modified to take into account the molecular level surface roughness that is typical to most carbonaceous and siliceous materials as well as other materials including hybrid organic–inorganic hierarchical structures. This technique, named the quenched solid density functional theory (QSDFT), was shown to be more practical than NLDFT for the analysis of microporous and mesoporous silicas and carbons.[185,190,192,193]

Nitrogen physical adsorption was used throughout our research to characterize the mesostructure and porosity of the synthesized materials.

3.2 X-Ray diffraction (XRD)

X-ray diffraction is one of the most widely applied techniques in catalyst characterization. It is used to identify bulk phases inside solid catalysts, characterize defects, and estimate crystal sizes.[58,69,194] X-ray diffraction is the reinforced elastic scattering of X-ray photons by atoms in a periodic lattice. In principle, if the incident plane wave hits the crystal at an arbitrary angle, the interference of the reflected waves can be constructive (in phase), destructive or partially destructive (out of phase) (Figure 3.3).
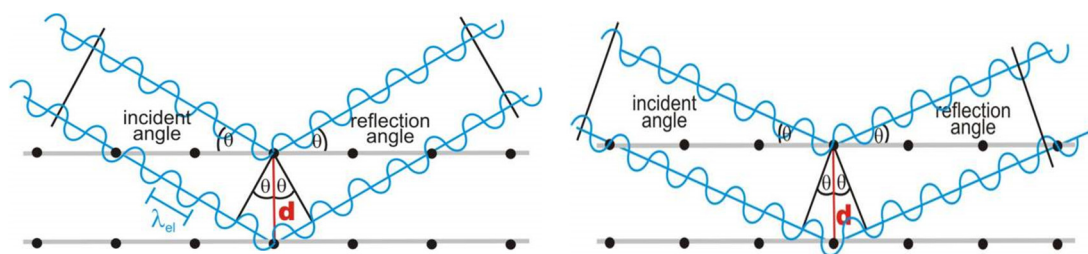
Figure 3.3. (Left) Constructive interference of reflected waves (reflected waves in phase, i.e., maxima are superimposed). (Right) Destructive interference of reflected waves (in the two reflected waves, maximum and minimum of the respective wave amplitude are superimposed).

A diffraction peak will be produced for an incident angle θ if the interference is constructive. In order to generate constructive interference, the path difference of the two or more rays scattered at the same direction is an integer of the wavelength of the X-rays (1.54 Å for CuK_α radiation). Figure 3.3 demonstrates how diffraction of X-rays by crystal planes allows one to derive lattice spacing by using the Braggs law:

$$n\lambda = 2d\sin\theta \qquad (3.4)$$

Where λ is the wavelength of the X-rays, d is the distance between two lattice planes, θ is the angle between the incoming X-rays and the normal to the reflecting lattice plane, and n is an integer called the order of the reflection. In the derivation of Braggs law, a perfect crystal and a perfectly parallel incident beam as well as a strictly monochromatic radiation was assumed. In fact, these conditions never exist because only an infinite crystal is really perfect and no radiation is strictly monochromatic.
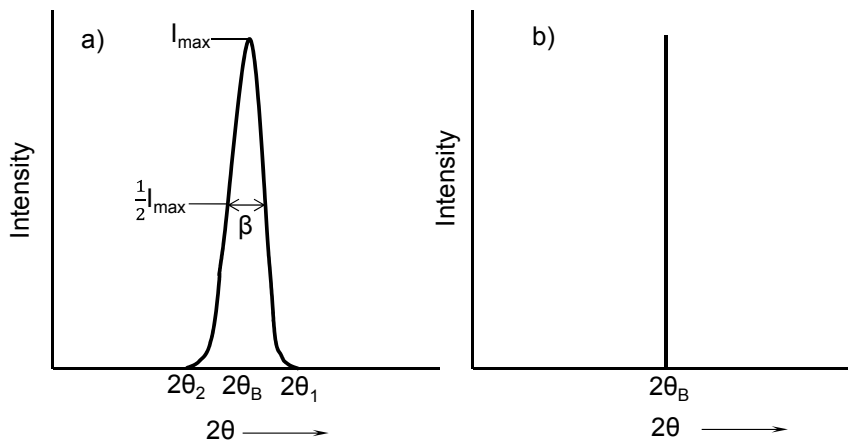
Figure 3.4. Effect of finite particle size on diffraction curves, (a) Influence of crystallite size on width of diffraction peak, (b) hypothetical case of diffraction occurring only at the exact Bragg angle.[194]

Deviations from Braggs law are important when dealing with particles of crystallite sizes below 100 nm, i.e., nanoparticles, for small size can be considered an imperfect crystal because it is not infinite. The finite crystallite sizes lead to peak broadening due to incomplete destructive interference in scattering directions where the X-rays are out of phase. If the path difference between rays scattered by the first two planes differs only slightly from an integral number of wavelengths, then the plane scattering a ray exactly out of phase with the ray from the first plane will lie deep within the crystal. If the crystal is so small that this plane does not exist, then complete cancellation of all the scattered rays will not result. We will find that very small crystals cause broadening of the diffracted beam, i.e., diffraction (scattering) at angles near to, but not equal to, the exact Bragg angle. Figure 3.4a demonstrates the effect of finite particle size on a diffraction curve, while Figure 3.4b

illustrates the hypothetical case of diffraction occurring only at the exact Bragg angle. The Scherrer formula relates crystal size to peak width:

$$D = k \, \lambda / \beta \cos\theta \qquad (3.5)$$

Where D is the crystallite size, λ the wavelength, β the peak width, k a correction factor (often taken as 0.9-1) and the θ Bragg angle. X-ray peak broadening provides a quick but not always reliable estimate of the particle size. Better procedures to determine particle sizes from X-ray diffraction are based on line profile analysis with Fourier transform methods.

From an XRD experiment, information about the lattice strain of the sample can be obtained. Lattice strain or microstrain ε is defined as a variation in d-spacing $\delta d/d$ and is usually given as a percentage. Lattice strain will affect the diffraction pattern and can be derived by line profile analysis. The variation may be uniform, that is, compressive or tensile, which leads to a shift of a Bragg peak, but not necessarily to broadening (Figure 3.5a).
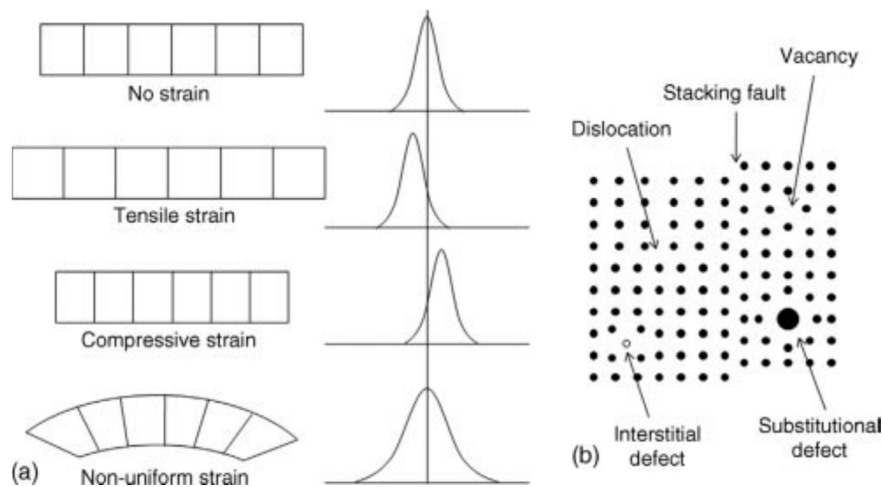
Figure 3.5. Schematic representation of different kinds of lattice strain as a result of external stress and their effects on Bragg diffraction peaks (a), and different kinds of defects that contribute to nonuniform lattice strain (b).[69]

This type of strain may result from external stress, lattice mismatch at epitaxial phase boundaries, or lattice atom substitution. The shift of Bragg peaks reflects a significant change in the lattice parameter and the interatomic distances. This may have a significant

impact on the electronic structure, for example, in the form of a d-band shift in the case of transition metals, and affect the adsorptive and catalytic properties of a material.[59,69,71,195-197] Nonuniform strain may be due to defects such as vacancies or interstitials. Dislocations and planar faults also induce a strain field in their surroundings. A schematic representation of how different kinds of lattice defects may locally change the interatomic distances without affecting the average d-spacing is given in Figure 3.5b.

In a crystal, the periodicities of atom layers with the distances of atom layers normally less than 0.2 nm result in XRD patterns in a wide range of 2 theta values (10-90º) In the case of ordered mesoporous materials. The long-range ordering of periodic mesoporous materials (the inter-plane distance between mesopores being about several nanometers) can be evidenced using low angle powder XRD, whereby Bragg reflections can be detected at low values of the 2 theta angle (less than 10º). From the positions of these reflections, the spacing between lattice planes can be determined and information about the size and symmetry of the mesoscopic lattice are obtained. In analogy with liquid crystal phases, mesostructured materials exhibit hexagonal, lamellar, or cubic phases.

In summary, XRD is a basic characterization technique for solid-state analysis. It provides basic structure information on particles that are sufficiently large, along with an estimate of their crystal domain size. Deeper analysis reveals particle anisotropy, and information on stress and strain. The limitation of XRD is that it cannot detect particles that are either too small or amorphous.

X-ray diffraction was used in our research for the determination of phases, crystal size, lattice strain, and the mesostructure of the synthesized materials.

3.3 Transmission electron microscopy (TEM)

Transmission electron microscopes are very powerful and versatile research tools with which one can obtain accurate data on the morphology, size, and spatial distribution of small particles on supports. They are essential in the study of crystallography, defects, surfaces, and interfaces in a wide variety of solids.[69,198,199]

In principle, electron microscopes use a beam of highly energetic electrons to examine objects on a very fine scale. The wealth of very different information that is

44

obtainable by various methods is caused by the multitude of signals that arise when an electron interacts with a specimen, and the fact that the strength of the various interactions is very dependent on the morphology, crystallography and chemical composition of the sample.

When an electron hits onto a material, different interactions can occur, as summarized in Figure 3.6. For a systemization, the interactions can be classified into two different types, namely elastic and inelastic interactions. In the former case, no energy is transferred from the electron to the sample. Furthermore, elastic scattering happens if the electron is deflected from its path by Coulomb interaction with the positive potential inside the electron cloud. By this, the primary electron loses no energy or – to be accurate –only a negligible amount of energy. In the inelastic interaction, energy is transferred from the incident electrons to the sample. The energy transferred to the specimen can cause different signals such as X-rays, Auger or secondary electrons, plasmons, UV quanta or cathodoluminescence.
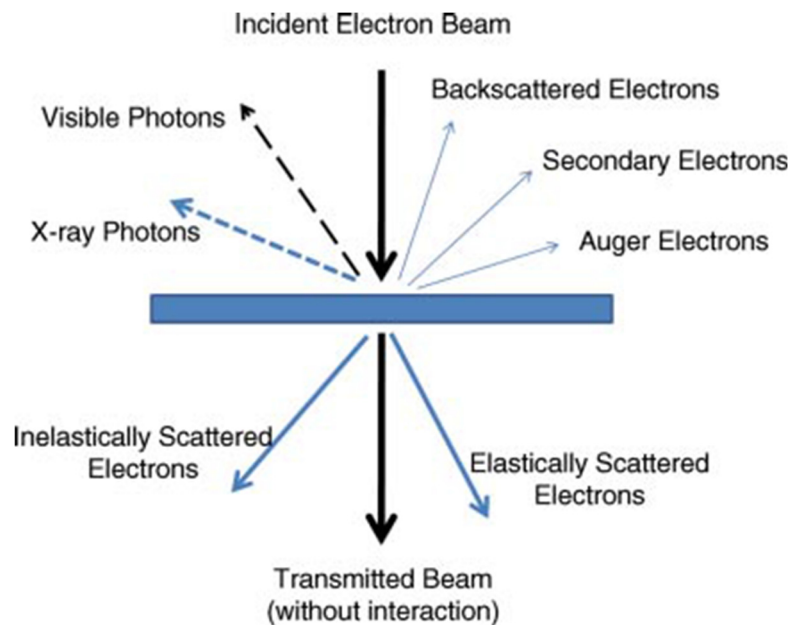
Figure 3.6. The main types of signal generated in the electron beam–specimen interaction.[199]

TEM exploits three different interactions of electron beam-specimen: unscattered electrons (transmitted beam), elastically scattered electrons (diffracted beam) and inelastically scattered electrons. The transmitted beam is used for morphology analysis

while the diffracted beam and inelastically scattered electrons are used respectively for crystalline and composition characterizations. In TEM, a primary electron beam of high energy (100-300 keV) and intensity passes through a condenser to produce parallel rays which impinge on the sample. Electrons have characteristic wavelengths of less than 1Å, and come close to monitoring atomic details; magnification in TEM instruments is ~10^5 - 10^6. When incident electrons are transmitted through the thin specimen without any interaction occurring inside the specimen, then the beam of these electrons is called transmitted. As the attenuation of the beam depends on the density and the thickness of the sample, the transmitted electrons form a two-dimensional projection of the sample mass, which is subsequently magnified by the electron optics to produce a so-called bright field image. Image contrast in TEM operating in bright field mode is based on mass thickness and diffraction effects. The contrast of areas in which heavy atoms are localized will appear darker than that of those comprising light atoms and thick areas appear darker than thin areas of the same material as demonstrated in the TEM image of CuNi supported on mesoporous carbon nanospheres (Figure 3.7). The effect of thickness can be seen as the areas at the intersections of carbon nanospheres appear darker than those of separated nanospheres, while the effect of large differences in mass is observed as the bimetallic CuNi particles, with a size of about 10 nm, and appear with a black contrast (Cu and Ni are by far heavier than carbon support). Furthermore, the Cu-Ni particles are crystalline, and as a result, diffraction contrast contributes to the dark contrast as well. TEM is one of the only catalyst characterization techniques which enable the determination of particle size distributions.

Furthermore, elastic scattering happens if the electron is deflected from its path by Coulomb interaction with the positive potential of nuclei of the atoms. By this, the primary electron loses no energy or to be accurate only a negligible amount of energy. If the specimen is a crystalline material, the spacing between the scattering centers (atoms) is regular, constructive interference of the scattered electrons in certain directions can happen and thereby diffracted beams are generated. The crystallographic information could be obtained by the technique of high-resolution TEM (HRTEM) which is performed using an objective aperture that allows several diffracted beams to interfere with the axial transmitted beam to form the image.

46

Composition analysis in the electron microscope by the various processes of inelastic scattering of electrons during the beam–sample interactions is particularly effective in studies of micro- and mesoporous catalysts and molecular sieves. Energy-dispersive X-ray spectroscopy (EDX), where X-ray intensities are measured as a function of the X-ray energy, is the most convenient method to use. This technique is often coupled with electron microscopy.

TEM, HRTEM and EDX techniques were used in the present thesis for the determination of mesostructure, crystalline phases, elemental analysis, as well as particle size distributions.
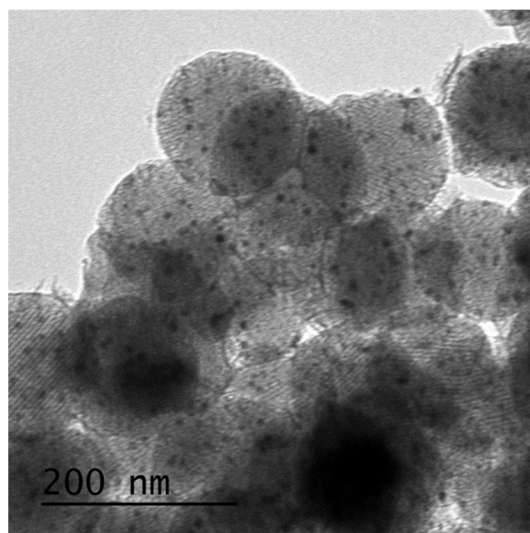
Figure 3.7. TEM image of bimetallic CuNi nanoparticles supported on mesoporous carbon nanospheres.

3.4 X-ray photoelectron spectroscopy

X-ray Photoelectron Spectroscopy (XPS) is among the most frequently used techniques for the characterization of catalysts, as it provides information on the elemental composition in the surface region, and the oxidation state of the elements. Photoelectron spectroscopy is based on the photoelectric effect: a sample which is irradiated with light of sufficiently small wavelength emits electrons.[58,69,199] In XPS, an atom absorbs a photon of energy, hv, after which a core or valence electron with a certain binding energy E_b is ejected with kinetic energy E_k (Figure 3.8):

$$E_k = h\nu - E_b - \varphi \qquad (3.6)$$

Where h is Planck's constant; ν is the frequency of the exciting radiation; E_b is the binding energy of the photoelectron with respect to the Fermi level of the sample; φ is the work function of the spectrometer.
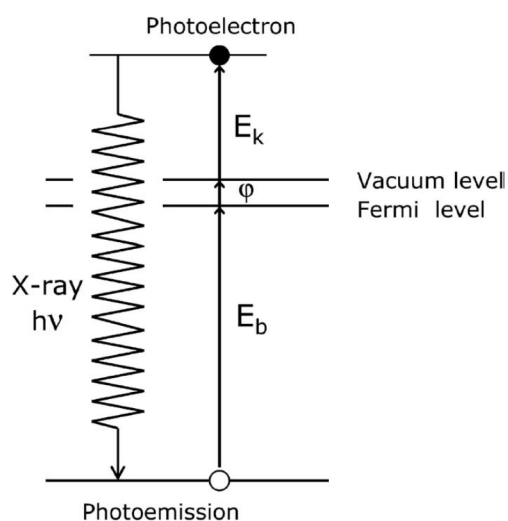
Figure 3.8. Schematic energy level diagram for photoemission.

In XPS, the intensity of photoelectrons is measured as a function of their kinetic energy. By using equation (3.6), one converts kinetic energy into binding energy which is usually the property assigned to the x-axis of a spectrum. Photoelectron peaks are labeled according to the quantum numbers of the level from which the electron originates. An electron with orbital momentum l (0; 1; 2; 3; indicated as s; p; d; f;) and spin momentum s has a total momentum $j = l + s$. As the spin may be either up $s = 1/2$ or down $s = -1/2$, each level with $l \geq 1$ has two sublevels, with an energy difference called the spin-orbit splitting. Thus, the Cu 3p level gives two photoemission peaks, $3p_{3/2}$ (with $l = 1$ and $j = 1 + 1/2$) and $3p_{1/2}$ ($l = 1$ and $j = 1 - 1/2$) as shown in Figure 3.9.
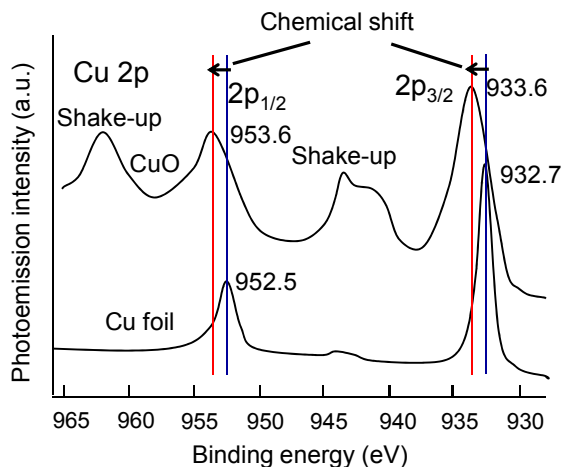
Figure 3.9. Cu(2p) spectra of different oxidation states in CuO and Cu.

Binding energies of electrons are characteristic of the element from which the photoelectron originates, thus XPS can be used to analyze the composition of samples. Binding energies also contain chemical information, because the energy levels of core electrons depend slightly on the chemical state of the atom. Chemical shifts are typically in the range of 0 to 3 eV. In general, the binding energy increases usually with increasing oxidation state, and for a fixed oxidation state with the electronegativity of the ligands. In other words, energy required to remove a core electron from an atom should increase with increasing positive net atomic charge and decrease with increasing negative net atomic charge. Almost all photoelectrons used in XPS have kinetic energies in the range of 0.2 to 1.5 keV. The inelastic mean free path of an electron depends on its kinetic energy, thus the probing depth of XPS (usually taken as 3λ) varies between 1.5 and 6 nm.

Photoelectrons may impart energy to other electrons in the atom leading to kinetic energy losses and the corresponding shake-up peaks (also called satellites) appear at higher binding energies in the spectrum. Discrete shake-up peaks are prominently present in the spectra of several oxides of nickel, copper, iron, and cobalt. They are highly useful features as their properties depend on the oxidation state of the emitting atom (Figure 3.9).

In our study, XPS was used in Chapter 5, 6, 7 to investigate the chemical state and surface composition of different metal oxide catalysts.

3.5 Raman Spectroscopy

Raman spectroscopy has been used to investigate oxide catalysts. It provides insight into the structure of oxides, their crystallinity, and the coordination of metal oxide sites. Raman spectroscopy is based on the inelastic scattering of photons, which lose energy by exciting vibrations in the sample. When a monochromatic light of frequency v_0 hits a sample, Rayleigh scattering of quanta with energy hv_0 occurs in an elastic scattering process. The Raman scattering of quanta with energy smaller or larger by the amount of the vibrational energy hv_{vib} occurs in an inelastic scattering process. Stocks lines are recorded as the Raman spectrum.[58,69,199,200]

CeO$_2$ and CeO$_2$-based materials are of interest for their utilization in three-way catalysts, in environmental catalysis, and as catalyst supports. Raman spectroscopy has been widely used to characterize the nature of the CeO$_2$ support and the oxygen species formed on it. For example, it is well established that the Raman band near 464 cm^{-1} in CeO$_{2-x}$ nanoparticles, which is assigned to the vibrational metal-oxygen mode of the F2g symmetry in a cubic fluorite lattice, shifts to lower energies, and the line shape of this feature gets broader as the particle size gets smaller. The source of shifting and broadening is associated with the strain coming from the presence of Ce^{3+} ions and oxygen vacancies.[201-205]

In our research, this technique was especially employed to characterize the presence of oxygen vacancies and defects in the Metal/CeO$_2$ catalysts which play important roles in CO oxidation studied in Chapter 5.

3.6 Temperature-programmed reduction (TPR)

TPR is a highly useful technique which enables a quick characterization of metallic catalysts.[57,58,69] In TPR, one follows the degree of reduction of the catalyst as a function of time, while the temperature increases at a linear rate. In TPR, a reducible catalyst or catalyst precursor is exposed to a flow of a reducing gas mixture (typically H$_2$ or CO in inert gas) while the temperature is increased linearly. The rate of reduction is continuously followed by measuring the composition (H$_2$ or CO content) of the reducing gas mixture at the outlet of the reactor. In our case, the temperature-programmed reduction experiments

were carried out using Advanced Scientific Designs, RXM-100 as shown simplified in Figure 3.10. The reactor was connected to a thermal conductivity detector (TCD).
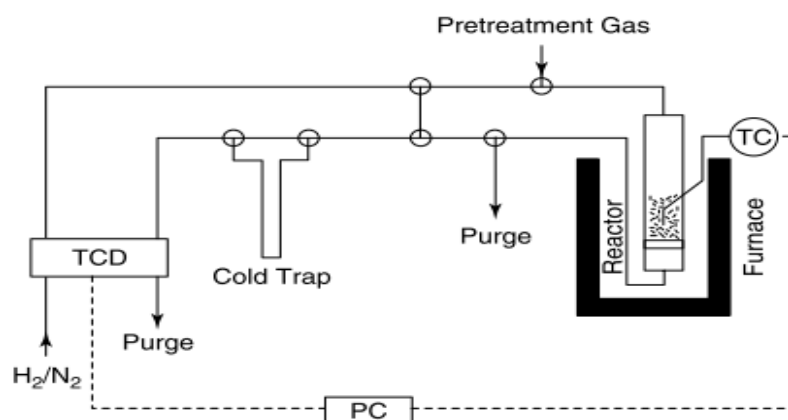
Figure 3.10. Scheme of a typical TPR apparatus (TCD, thermal conductivity detector; TC, thermocouple; PC, computer).

TPR provides information on the temperature needed for the reduction of a catalyst. For bimetallic catalysts, TPR profiles often indicate whether the two metals are in contact or not.[105,206-216] The TPR of supported metallic catalysts can reveal evidence of metal-support interaction.
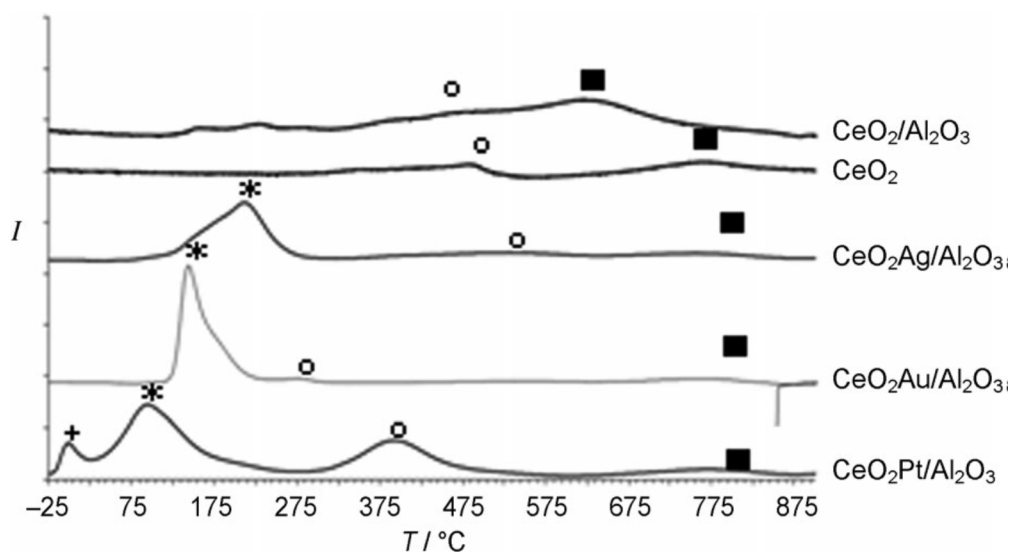
Figure 3.11. TPR profile of $CeO_2/PM/Al_2O_3$ (PM: Pt, Au, and Ag). +: PM oxide reduction); * reduction of surface ceria in contact with PM; ○ reduction of surface ceria not in contact with PM; ■ reduction of bulk ceria.[105]

For example, in the case of precious metals (Ag, Au, Pt) supported on CeO_2 metal incorporation promotes the reduction of CeO_2 at much lower temperature compared to reduction of pure CeO_2 (Figure 3.11). Furthermore, it was suggested that metal incorporation promotes both hydrogen spillover and an electronic modification, with the latter providing the driving force and the cause of the hydrogen spillover. The reduction mechanism is as follows: As soon as a precious metal oxide becomes metallic it dissociates hydrogen; atomic hydrogen migrates to ceria in contact with metals and reduces the oxide instantaneously.[105]

In the present study, TPR was used to investigate the reducibility and the interaction between catalyst constituents, properties which are closely associated with the catalytic properties of the catalysts.

3.7 Atomic absorption spectroscopy

The bulk composition can be analyzed by means of Atomic Absorption Spectroscopy (AAS). In AAS, electronic transitions between the energy levels of atoms into excited states are generated by the absorption of photons in the visible frequency range (about 200–1000 nm). The change in intensity of the light beam is measured and correlated with the concentration relative to the absorbance of a calibration standard. The absorption lines are characteristic for each element. The instrumentation consists of a hollow-cathode light source of the element to be measured, a flame (usually an air–acetylene or air–propane flame)–into which a sample solution is dosed, a monochromator for the analysis of the wavelength of the radiation of the element under study and a detector. For AAS, a solid catalyst sample has to be dissolved by an acid such as HCl, HNO_3 or HF.[58]

3.8 Catalytic reaction studies

3.8.1. Preferential oxidation of CO

The catalysts were pretreated and tested using a stainless-steel continuous fixed-bed flow micro-reactor (BTRS –Jr PC, Autoclave Engineers) shown schematically in Figure 3.12. Electronic mass flow controllers were used for regulation of the gas feed streams. The reactor was constructed of stainless-steel tubing with 3 mm wall thickness and dimension

of 4.5 mm I.D. by 300 mm length. The reactor was heated using a tubular furnace that was regulated using a proportional temperature controller. The temperature of the catalyst bed was monitored using a 1.2 mm O.D thermocouple that extended along the center of reactor into the bed. Prior to the tests, 100mg of sample was treated under a flowing 20% O_2/He mixture at 300°C for 60min. The feed contained 1.64% CO, 1.62% O_2, 90.25% H_2, and balance He. Products and reactants were analysed using a gas chromatograph equipped with TC-detector. No products other than those resulting from CO or H_2 combustion (i.e., CO_2 and H_2O) were observed under the applied reaction conditions. Basically, values of percentage conversion and selectivity in the CO-PROX process are defined as:

$$\chi_{CO} = \frac{F^{in}_{CO} - F^{out}_{CO}}{F^{in}_{CO}} \times 100 \qquad \chi_{O_2} = \frac{F^{in}_{O_2} - F^{out}_{O_2}}{F^{in}_{O_2}} \times 100$$

$$S_{CO_2} = \frac{\chi_{CO} F^{in}_{CO}}{2 \chi_{O_2} F^{in}_{O_2}} \times 100$$

Where χ and S are percentage conversion and selectivity, respectively, and F is (inlet or outlet) molar flow of the indicated gas.
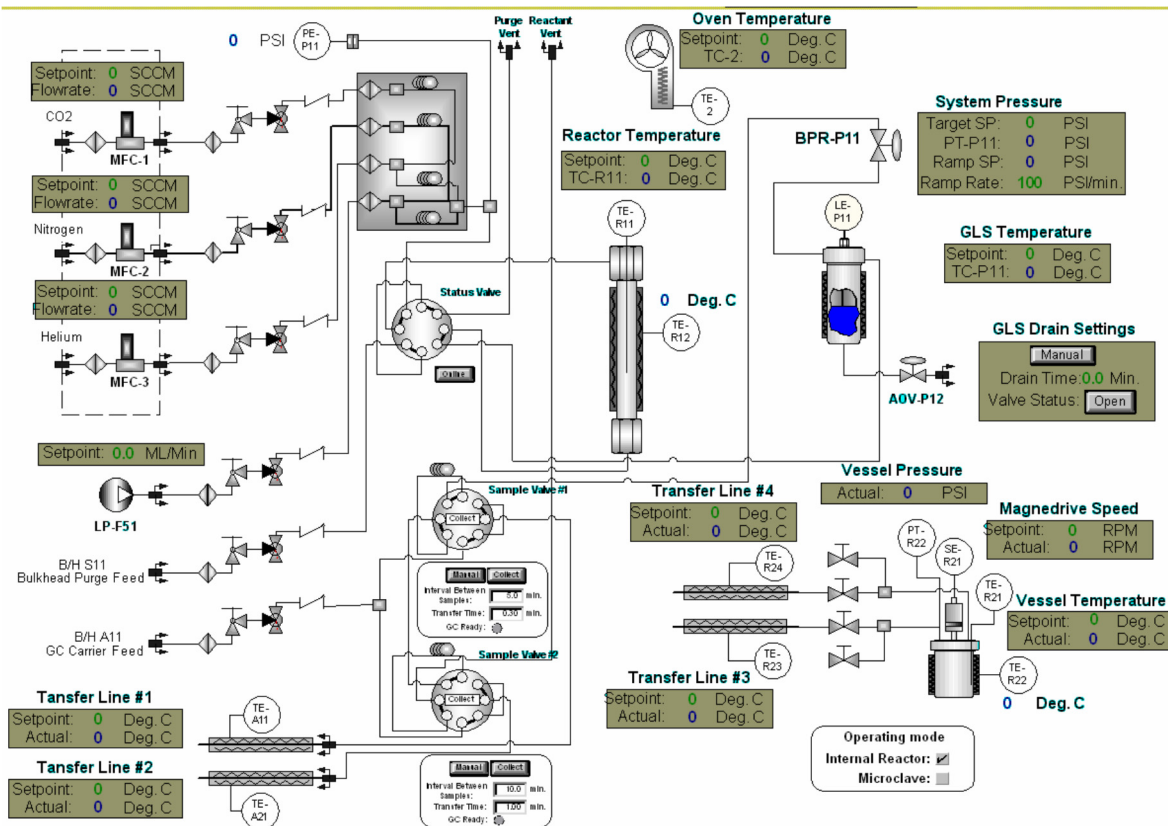
Figure 3.12. Scheme of catalyst testing system BTRS-Jr PC

3.8.2. Catalytic hydrogen generation

a) Catalytic hydrolysis of ammonia-borane (AB): The catalytic activity of the prepared catalysts toward hydrolysis of AB ($H_3NBH_3 + 2H_2O \rightarrow NH_4^+ + BO_2^- + 3H_2$) was determined by measuring the rate of hydrogen generation in a typical water-filled gas burette system. A 5 ml aqueous dispersion of catalyst was transferred into the reaction flask and a 5 ml aqueous solution of AB (0.73-2.92 mmol) was injected into the catalyst solution under stirring. The volume of hydrogen gas evolved was measured by recording the displacement of water level in an inverted and graduated water-filled burette.

b) Catalyst reusability in the hydrolysis of AB: After the hydrogen generation reaction was completed, the catalysts were kept in the reaction solution under ambient conditions, and another equivalent of AB in 2 ml H_2O was added to the reaction system. The process was repeated for several cycles.

54

c) Hydrous hydrazine decomposition reaction: The catalytic tests were carried out at $60^{\circ}C$ in three-necked round bottom flask. The reaction was initiated by introducing 0.3 ml diluted $N_2H_4.H_2O$ (16 ml $N_2H_4.H_2O$ in 100 ml aqueous solution) into the flask containing 100 mg of catalyst dispersed in 8 ml NaOH solution (0.5 M). The gaseous product was passed through a trap containing 0.1M hydrochloric acid to ensure the adsorption of ammonia (if generated), and was then volumetrically monitored using the gas burette.

The hydrogen of hydrazine could be released by the desired complete decomposition through the reaction:

$$H_2NNH_2 \rightarrow N_2 + 2H_2 \text{ (pathway 1)}$$
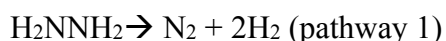
or the undesired incomplete decomposition to ammonia:

$$3H_2NNH_2 \rightarrow 4NH_3 + N_2 \text{ (pathway 2)}$$
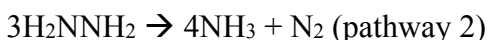
The selectivity towards hydrogen (x) was determined based on the following equation: $3N_2H_4 \rightarrow 4(1\text{-}x) NH_3 + 6xH_2 + (1+2x) N_2$, which could be derived from the above two pathways. The selectivity could be calculated as follows: $x=(3\lambda\text{-}1)/8$ where $\lambda=n(N_2 + H_2)/n(N_2H_4)$ $(1/3 \leq \lambda \leq 3)$.

In order to further confirm the selectivity to hydrogen obtained from volumetric measurement, the amount of ammonia in the HCl trap was determined by acid-base titration.

d) Acid-base test of the ammonia gas: the gas evolved from the catalytic hydrolysis of AB and hydrazine decomposition was passed through a 50 ml standard solution of 0.1M HCl at room temperature. After the reaction was completed, the resulting HCl solution was titrated with a standard solution of 0.1M NaOH by using phenolphthalein as an indicator. The presence of released ammonia was probed by comparing the difference in the amount of NaOH consumed for the blank HCl solution and the HCl solution after AB hydrolysis reaction.

Chapter 4:

One-step-impregnation hard templating synthesis of high-surface-area nanostructured mixed metal oxides (NiFe$_2$O$_4$, CuFe$_2$O$_4$ and Cu/CeO$_2$)

Hoang Yen[a], Yongbeom Seo[b], Rémy Guillet-Nicolas[a], Serge Kaliaguine[c] and Freddy Kleitz [a]

[a]Department of Chemistry and Centre de Recherche sur les Matériaux Avancés (CERMA), Université Laval, Quebec GIV 0A6, Canada.

[b]Center for Functional Nanomaterials, Department of Chemistry and Graduate School of Nanoscience & Technology (WCU), KAIST, Daejeon, Korea

[c]Department of Chemical Engineering, Université Laval, Canada

Résumé

Dans ce chapitre, une méthode en une seule étape d'imprégnation efficace pour synthétiser des oxydes bimétalliques mésoporeux et cristallins (par exemple $NiFe_2O_4$, $CuFe_2O_4$, Cu/CeO_2) a été développée en utilisant de la silice mésoporeuse comme matrice rigide dans des conditions optimisées de mélange. Ce nouveau procédé permet l'obtention d'une réplique fidèle de la mésostructure avec un rendement élevé et une grande pureté de phase, tout en conservant la morphologie des particules de la matrice.

Abstract

We report here on an efficient one-step-impregnation method to synthesize crystalline mesoporous bimetal oxides (e.g.$NiFe_2O_4$, $CuFe_2O_4$, Cu/CeO_2) using mesoporous silicas as hard templates under optimized mixing conditions. This new procedure enables a true replication of the mesostructure with high yield and phase purity, while retaining particle morphology of the template.

4.1. Introduction

The templated synthesis of porous non-siliceous compositions via the nanocasting pathway is a method based on using mesoporous silica or carbon materials, in most cases, as solid templates, in which suitable precursors are first infiltrated and then converted/solidified while being confined within the host matrix. This method has emerged as a highly powerful strategy for producing a wide range of amorphous or crystalline nanoporous materials having vast potential for applications in catalysis, sensing, or batteries.[77,217-221] However, the nanocast synthesis of multi-metal oxides,[158,222-224] e.g. mixed metal oxides, perovskites or spinels, has been far less explored compared to single metal oxides, most likely due to their more difficult preparation requiring accurate stoichiometry, miscible precursors and high crystallization temperatures. As representative examples, $NiFe_2O_4$ and $CuFe_2O_4$ are among the most extensively studied materials in the fields of electronics, magnetics and catalysis.[176,225,226] Also, Cu/CeO_2 is a promising candidate for CO gas sensing or preferential CO oxidation in the presence of H_2 for proton-exchange membrane fuel cell technology.[54,227] However, thus far, the synthesis of such mesoporous mixed metal oxides in high purity and high yield remains difficult. Moreover, in the standard nanocasting procedure, multiple impregnation steps or surface modification of the template is often needed for optimized filling of the pores, which could represent a severe drawback for expanding the use of nanocasting. Clearly, progress to improve the nanocasting synthesis is urgently needed.

Herein, we thus report a versatile one-step synthesis method suitable for nanoporous mixed metal oxides (e.g.$NiFe_2O_4$, $CuFe_2O_4$, Cu/CeO_2) using nitrate salts as precursors, and different mesoporous silicas as typical solid templates. In this new procedure, mesostructured crystalline bimetal oxide replicas showing a very high surface area are obtained in one single impregnation step, which is performed under reflux, followed by calcination at given temperatures and template dissolution. These conditions are shown not only to be suitable for easy preparation of phase-pure mesoporous mixed metal oxides in high yields, but also allow proper replication of the particle morphology of the template, as demonstrated by the example of MCM-48 nanospheres.

4.2. Experimental section

4.2.1. Synthesis of mesoporous silica SBA-15

The synthesis was performed with the following initial molar gel composition: 0.99 TEOS/0.54 HCl/0.016 P123/100H$_2$O. In a typical synthesis, 6.0 g of Pluronic P123 was dissolved in 114 g of deionized water and 3.5 g of hydrochloric acid (37%) at 35°C under magnetic stirring. Then, 13.0 g of TEOS was rapidly added to the initial homogeneous solution. The resulting mixture was stirred for 24 h at 35°C and subsequently hydrothermally treated for an additional 24 h at 100°C to ensure further framework condensation. The solid product was filtered without washing and dried for 24h at 100°C. For template removal, the as-synthesized silica powders were first shortly slurried in ethanol and subsequently calcined at 550°C for 3 h.[228]

4.2.2. Synthesis of mesoporous silica KIT-6

Briefly, 9.0 g of Pluronic P123 (EO$_{20}$PO$_{70}$EO$_{20}$, Sigma-Aldrich) was dissolved in 325 g of distilled water and 17.40 g of HCl (37%) under vigorous stirring. After complete dissolution, 9.0 g of 1-butanol was added. The mixture was left under stirring at 35°C for 1 h, after which 19.35 g of tetraethyl orthosilicate (TEOS) was added to the homogeneous clear solution. The synthesis is carried out in a closed polypropylene bottle. The molar composition of the starting reaction mixture is TEOS/P123/HCl/H$_2$O/BuOH =1/0.017/1.9/195/1.31. This mixture was left under stirring at 35°C for 24 h, followed by an aging step at 100°C for 24 h under static. The resulting solid products were then filtered and dried for 24 h at 100°C. The solid product was then filtered, dried, and finally calcined at 550°C.[229]

4.2.3. Synthesis of mesoporous silica MCM-48 nanospheres:

The MCM-48 nanospheres were synthesized using a mixture of cetyltrimethylammonium bromide (CTAB) and ethanol as a structure-directing mixture. Tetraethyl orthosilicate (TEOS) and triblock copolymer F127 (Pluronic F127, EO$_{106}$PO$_{70}$EO$_{106}$) were applied as a silica source and a particle dispersion agent, respectively. The molar composition of the reaction mixture was of 1TEOS:0.16CTAB:21.4NH$_3$:85EtOH:676H$_2$O:0.017F127. A typical preparation of MCM-48 nanosphere is as follows: 1 g of CTAB and 4g of F127 are

dissolved in 212 ml of distilled water, 85 g of EtOH, and 21.28 g of 29 wt% ammonium hydroxide solution at room temperature. After complete dissolution, 3.6 g of TEOS is added into the mixture at once. After 1 min of mechanical stirring at 1000 rpm, the mixture was kept at a static condition for 24 h at RT for further silica condensation. The white solid product is recovered by ultrahigh speed centrifuge, washed with water, and dried at 70°C in air. The final template free MCM-48 nanosphere materials are obtained after calcination 550°C for 5 h in air.[230]

4.2.4. Synthesis of mixed metal oxides by hard templating

Hydrated metal nitrates $Cu(NO_3)_2.3H_2O$, $Ce(NO_3)_3.6H_2O$, $Ni(NO_3)_2.6H_2O$, $Fe(NO_3)_3.9H_2O$ (Aldrich) were used as the metal precursors. Typically, 2.5 g of the nitrate salts in stoichiometric proportion were pre-mixed together with 1g of mesoporous silica powder and ground in an agate mortar in the presence of 10 ml non-polar organic solvent (e.g. n-hexane, cyclohexane) to form homogeneous mixture. Note here that the metal nitrate hydrate salts can be liquefied at lower temperature on the surface of the solid than in the bulk when they are pressed and ground. Therefore, this wet grinding step could serve as a driving force for reducing melting point and thus increasing homogeneity of the mixture. The resulting mixture was subsequently dispersed in 30 ml of the respective solvent and stirred overnight under reflux (70-80°C). Under these conditions, the salt hydrate precursors melt to form a highly concentrated salt solution and thus preferentially adsorbed into the pores due to the surface polarity of silica matrix. The solid products were then obtained via filtration, dried in air at 70-80°C and calcined at 500°C (for Cu/CeO_2 and $NiFe_2O_4$) or 600°C (in the case of $CuFe_2O_4$) for 5h with heating ramp of 1°C/min. The silica template was then selectively removed by treating the powders with NaOH (2M) solution at room temperature 3 times for 24 h. Finally, the nanocast products were washed with water and ethanol, and then dried at 70°C.

4.2.5. Characterization

Transmission electron microscopy (TEM) images and selected area electron diffraction (SAED) of TiO_2 NPs were obtained on a JEOL JEM 1230 operated at 120 kV. Samples were prepared by placing a drop of a dilute toluene dispersion of nanocrystals onto a 200 mesh carbon coated copper grid and evaporated immediately at ambient temperature. High-

resolution transmission electron microscopy (HRTEM) images were obtained on a using Philips F20 Tecnai instrument microscope operated at 160 kV.

X-ray diffraction (XRD): The quality of 2D hexagonal SBA-15 and 3D cubic KIT-6 was checked by low-angle X-ray diffraction (XRD) recorded on a Rigaku Multiplex, operated at 2 kW, using Cu Kα radiation. The long range order of mesoporous materials produces distinct diffraction patterns at angles in the range of $0º < 2\theta < 5º$. The wide X-ray diffraction patterns of the samples were obtained on a Bruker SMART APEXII X-ray diffractometer operated at 1200 W power (40 kV, 30 mA) and equipped with a CuK$_\alpha$ radiation source (λ=1.5418 Å).

Nitrogen physisorption experiments were measured on a Micromeritics ASAP 2010 system at liquid nitrogen temperature (-196ºC) with prior degassing of the calcined silica samples under vacuum at 200ºC and nanocast materials at 150ºC overnight. Total pore volumes were determined using the adsorbed volume at a relative pressure of 0.95. The Brunauer-Emmett-Teller (BET) equation was used to calculate the surface area S_{BET} from adsorption data obtained at P/P_0 between 0.05 and 0.2. The pore size distributions were obtained by the non-local density functional theory (NLDFT) method and calculated using the Autosorb-1 software, supplied by Quantachrome Instruments. The NLDFT kernel selected considers sorption of N_2 on silica at -196ºC assuming cylindrical pore geometry and the model based on the adsorption branch.

4.3. Results and discussion

4.3.1. Structural characterization of mesoporous silicas (SBA-15, KIT-6, and MCM-48)

The quality of the mesostructures of the different materials was judged from TEM, powder X-ray diffraction (XRD) and N_2 physisorption (Figure 4.1 and S4.1, S4.2). First, all of the silica templates showed the expected highly ordered mesoporous structures, in agreement with the literature. The present series of mesoporous silica materials under study were first characterized by XRD in order to confirm the nature of the mesophase. All XRD diffraction patterns of the template-free materials indicate long range order with the symmetry of the mesophase being commensurate with the body-centered cubic *Ia3d* space group of KIT-6,

MCM-48 and hexagonal symmetry *P6mm* of SBA-15. The TEM images further confirm the mesostructure of all mesoporous silicas, particularly, the MCM-48 nanospheres exhibit uniform diameter of about 120 nm.
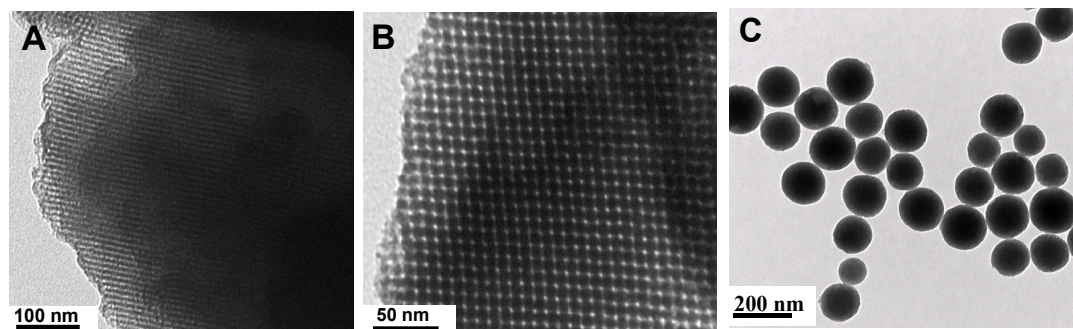
Figure 4.1. TEM images of mesoporous silicas: (A) SBA-15 aged at 100°C, (B) KIT-6 aged at 100°C, (C) MCM-48 nanospheres.

The high structural order of the mesopore SBA-15, KIT-6 and MCM-48 materials is also evident from the gas adsorption data. As can be seen, all the isotherms are typical type IV exhibiting a steep capillary condensation step characteristic of narrow distribution of mesopores. The specific surface area, pore size and pore volume of the synthesized mesoporous silica materials deduced from nitrogen sorption were presented in table S4.1.

4.3.2. Nanostructured mixed metal oxides (Cu/CeO$_2$, NiFe$_2$O$_4$, CuFe$_2$O$_4$)

Figure 4.2 (A1, A2 and A3) show TEM images of NiFe$_2$O$_4$, CuFe$_2$O$_4$ and Cu(20)/CeO$_2$ (molar ratio of Cu to Ce is of 0.2) obtained from the replication of 3-D cubic KIT-6 silica. All of these replicas clearly present extended domains of the ordered 3-D pore structure. Moreover, TEM investigations of the nanocast replicas generated with MCM-48 nanospheres (Figure 4.2 B1, B2 and B3) evidently confirmed the formation of mesoporous NiFe$_2$O$_4$, CuFe$_2$O$_4$ and Cu(20)/CeO$_2$ materials with retention of the spherical particle morphology of the template.
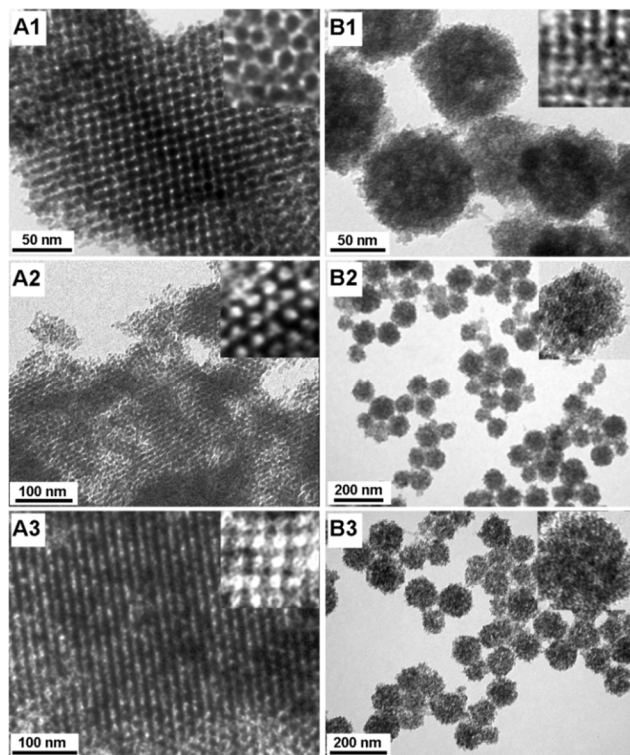
Figure 4.2. TEM images of mesoporous bimetal oxide replicas prepared using KIT-6 (A1, A2, A3) silica and MCM-48 silica nanospheres (B1, B2, B3): (A1, B1) $NiFe_2O_4$, (A2, B2) $CuFe_2O_4$, (A3, B3) Cu(20)/CeO_2. Insets show high magnification images of the corresponding materials.

The large extent of network replication through the one-step impregnation process was further evidenced when using SBA-15 silica as the template. As shown in Figure 4.3, TEM images of the resulting nanocasts displayed wide arrays of mesoscopically ordered $NiFe_2O_4$, $CuFe_2O_4$ and Cu(20)/CeO_2. High-resolution TEM investigations (Figure 4.3 and Figure S4.4, SI) revealed that the framework walls of the samples consist of nanocrystalline domains of ferrite-type spinels. The lattice fringes corresponding to the (311), (200) planes of face-centered cubic spinels are clearly visible and connecting bridges between two nanowires can be observed (Figure 4.3E and 4.3F). Elemental EDX mapping combined with HAADF-STEM conducted on nanowire array samples ($CuFe_2O_4$, $NiFe_2O_4$) confirmed the occurrence of homogeneous distributions of Cu, Fe, Ni and O. It is noteworthy that isolated nanowires of $NiFe_2O_4$, with a diameter of 6–7 nm, were obtained in the case of a SBA-15 template aged at 80°C, with a metal precursor loading of 1.5 g/1 g silica. Such 1-D spinel structures (e.g. individual elongated $NiFe_2O_4$ nanowires) could be of special interest owing to their magnetic and electronic properties.[231-233] We also observed that

68

nanostructures varying from short nanorods to nanowire arrays were produced as the loading of nitrate precursors was increased from 1.5 to 2.5 g/1 g silica (Figure 4.3B and S4.5, SI), confirming the nanocast structure dependence on precursor loading.[156]
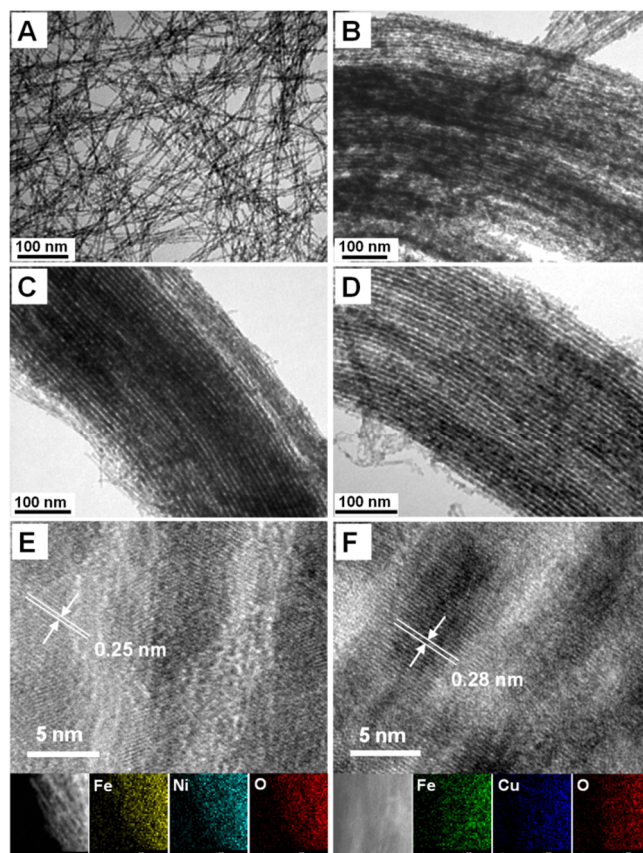
Figure 4.3. TEM and HRTEM images of the oxide replicas using SBA-15 template: (A, C, E) $NiFe_2O_4$, (D, F) $CuFe_2O_4$, (B) $Cu(20)/CeO_2$.

Wide-angle XRD patterns of the mixed metal oxides obtained from the KIT-6 and MCM-48 templates (Figure 4.4B and Figure S4.6, SI) all indicated pure crystalline phase with a face-centered cubic structure for both CeO_2 and the ferrite spinels. The diffraction peaks are relatively broad, reflecting the nanocrystalline nature of the walls of the replicas. The average crystal sizes calculated according to the Scherrer equation were about 6 nm for $Cu(20)/CeO_2$ and $CuFe_2O_4$, and 9 nm for $NiFe_2O_4$ (all from KIT-6), values which are in line with previous reports on nanocast metal oxides templated from similar silica materials.[161,222,223] The absence of the CuO phase in the wide-angle XRD pattern of $Cu(20)/CeO_2$ proved that Cu species are highly dispersed or incorporated in the ceria lattice, and the presence of Cu was confirmed by atomic absorption. As shown in Figure

4.4A (see also Figure S4.7 and S4.8, SI), the low angle XRD patterns of the mesoporous mixed metal oxide samples (Cu(20)/CeO$_2$, NiFe$_2$O$_4$, CuFe$_2$O$_4$) prepared using different templates (MCM-48, KIT-6, SBA-15) showed weak diffraction peaks at low 2-theta values associated with the mesoscopic structure of the mixed metal oxides.
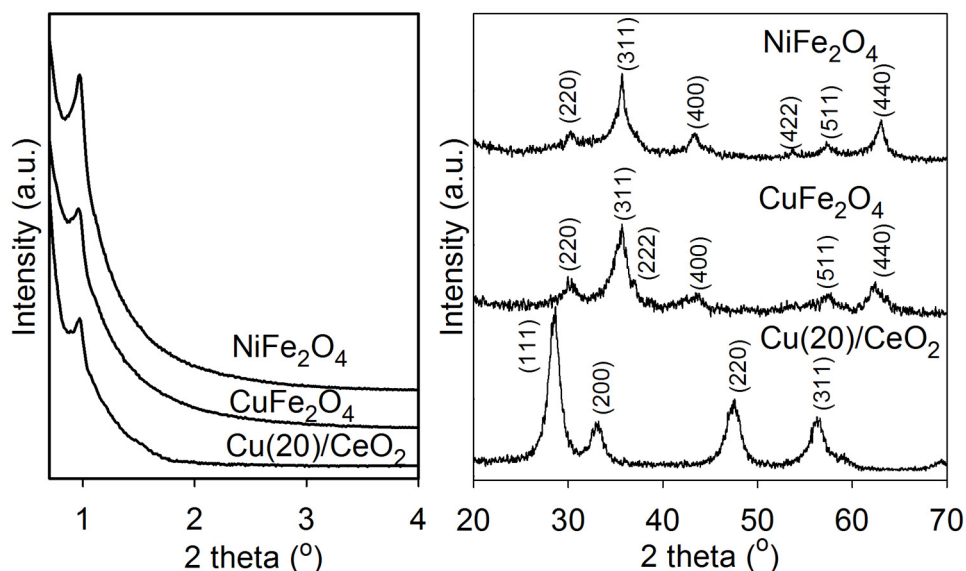
Figure 4.4. Low-angle (left) and wide-angle (right) XRD patterns of nanocast materials using KIT-6 as the template.

In terms of porosity, the nanocast samples showed high nitrogen sorption capacity at −196°C with isotherms being characteristic of well-developed mesoporous nanocast metal oxides (Figure S4.9).[156,223,230] In particular, the mesoporous bimetal oxide samples from MCM-48 nanospheres possess a very high surface area and high pore volume, among the highest reported to date:[234,235] 219 m^2 g^{-1} and 0.57 cm^3 g^{-1} for Cu(20)/CeO$_2$, 296 m^2 g^{-1} and 0.52 cm^3 g^{-1} for CuFe$_2$O$_4$, and 250 m^2 g^{-1} and 0.32 cm^3 g^{-1} for NiFe$_2$O$_4$, respectively (see Table S4.2). Here, NLDFT pore size distributions of CuFe$_2$O$_4$ and NiFe$_2$O$_4$ indicated mesopores of ~2.5–3.5 nm (Fig. S4.10, SI).

To compare with previous nanocasting procedures, we also synthesized mesoporous Co$_3$O$_4$ (using KIT-6 template), an important anti-ferromagnetic material which had been prepared previously by nanocasting.[156,163,236] In most cases, it was reported that multi-impregnation steps or vinyl functionalization of the silica surface is necessary to obtain

such a highly ordered mesostructure of Co_3O_4.[156,163] In our case, the results revealed that cobalt oxide replicated perfectly the *Ia3d* pore structure of un-modified KIT-6, in one single impregnation step (Figure S4.11 and S4.12, SI), yielding a surface area of 118 m^2 g^{-1}, pore volume of 0.28 cm^3 g^{-1} and narrow pore size distribution of 4 nm.

Methods such as melt infiltration of mesoporous silica with nitrate salts have been applied to increase oxide loading in the porous host framework.[161,237] However, these efforts were limited to single metal oxides and the use of highly viscous molten salts may degrade the mesopore framework of the support upon impregnation. To explain this, the impregnation process may be viewed as the replacement of a solid–gas interface by a solid–liquid interface. Here, the pressure developed in the nanopores upon impregnation caused by compressed air bubbles may reach several MPa depending on the liquid–gas interfacial tension. The molten metal salts are highly viscous with high surface tension, which could limit diffusion in pores and induce high pressure during the infiltration process. Such drawbacks of directly using molten metal salts can be overcome if the pore space of the silica support is first filled with alkane solvents, which have much lower surface tension than highly concentrated salt solutions, prior to being placed in contact with the metal precursors. In our case, nonpolar organic solvents were used to pre-wet the silica surface. Then, to gain additional insight into the process of precursor infiltration under our reflux conditions, the effects of solvent and reflux temperature on the structure of $Cu(20)/CeO_2$ were studied using a SBA-15 template. As can be seen in Figure S4.13 (SI), bundles of nanowires were obtained when using a variety of solvents (n-hexane, n-heptane and cyclohexane) under refluxing at 70°C and 80°C. However, bulk particles were formed with increasing the reflux temperature up to 100°C. This effect may be due to weaker interactions between the metal precursors and the parent silica surface at higher temperature, resulting in limited infiltration of the precursors into the pore channels. Most importantly, $Cu(20)/CeO_2$ samples prepared without applying the reflux process, with other parameters remaining the same, consist of short disordered nanorods (Figure S4.14), suggesting insufficient pore filling. Similarly, $Cu(20)/CeO_2$ was also prepared by conventional wet impregnation using ethanol with same loading of precursors and annealing conditions as before. In that case, bulk oxide particles were observed (Figure

S4.15). These results plainly establish that the reflux process in organic solvent facilitates the infiltration of the pores with the metal precursors.

4.4. Conclusions

In conclusion, we have described an efficient and simple synthetic procedure for improving the nanocasting preparation of crystalline nanostructured porous metal oxides. The method based on using molten nitrate salts in the presence of an organic solvent (e.g. n-hexane or cyclohexane) under refluxing conditions is adapted for a large variety of compositions, especially high-surface-area mixed metal oxides, which are difficult to prepare otherwise. The following chapter will present catalytic performances of the $Cu-CeO_2$-based materials prepared by this improved nanocasting method. To study the catalytic properties of these new materials, the CO-preferential oxidation in excess of H_2 (i.e., PROX process) was chosen as a representative and important catalytic reaction.

4.5. Supporting information
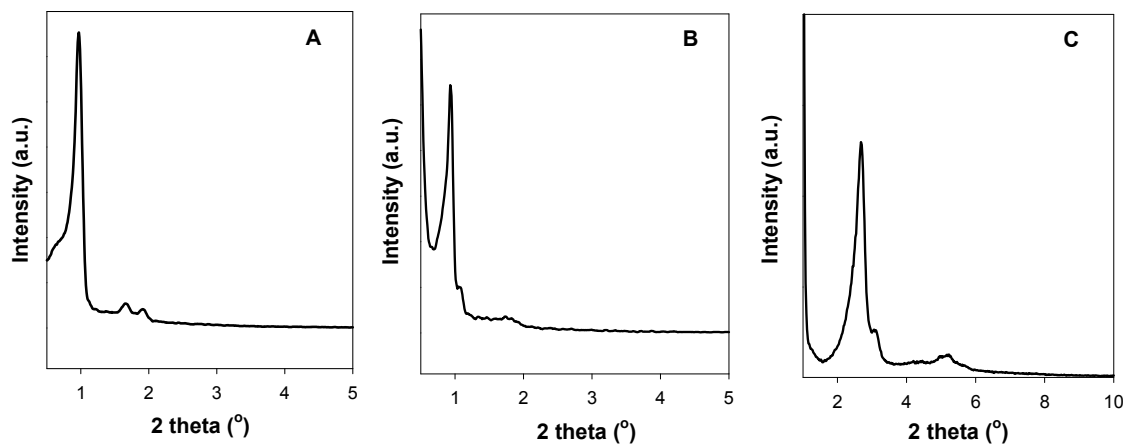
Figure S4.1. Low angle XRD patterns of mesoporous silicas: (A) SBA-15 aged at 100°C, (B) KIT-6 aged at 100°C, (C) MCM-48 nanospheres (Rigaku Multiplex, operated at 2 kW, using Cu Kα radiation).
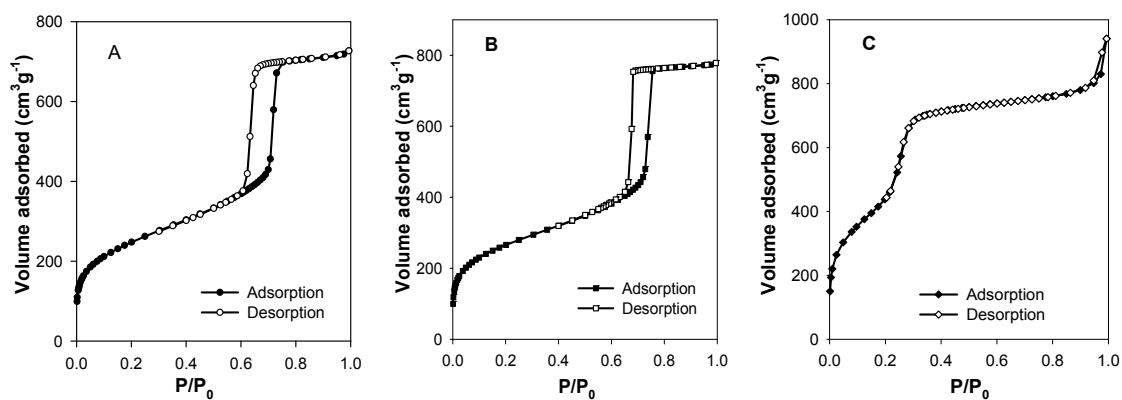
Figure S4.2. N$_2$ adsorption-desorption isotherms at -196°C of mesoporous silicas: (A) SBA-15 silica aged at 100°C, (B) KIT-6 silica aged at 100°C, (C) MCM-48 silica nanospheres (Micromeretics ASAP 2010).

Table S4.1. Structural parameters of the mesoporous silica materials

Sample	Surface area S_{BET} (m²/g)	Pore volume (cm³/g)	Pore size (nm)
KIT-6	904	1.16	7.6
SBA-15	713	0.88	7.0
MCM-48	1650	1.31	3.5
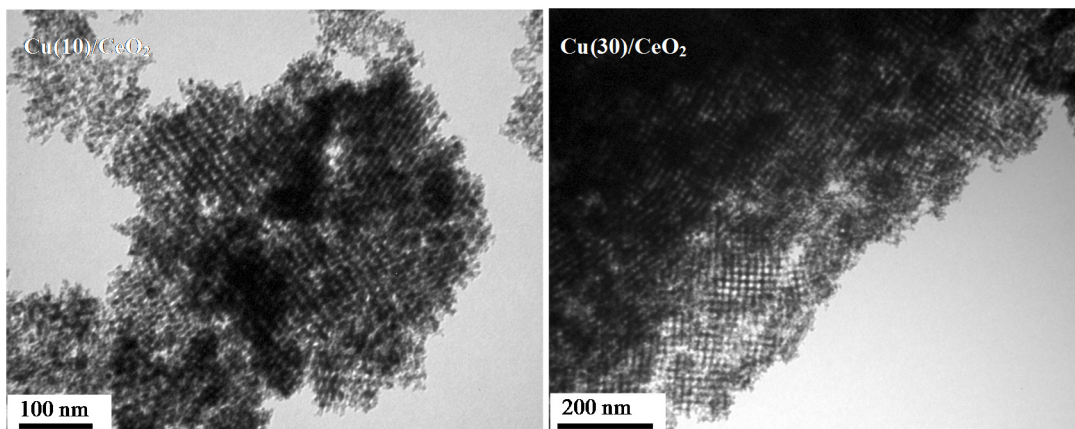
Figure S4.3. TEM images of Cu(10)/CeO₂ and Cu(30)/CeO₂ prepared using KIT-6 as a template (as indicated).
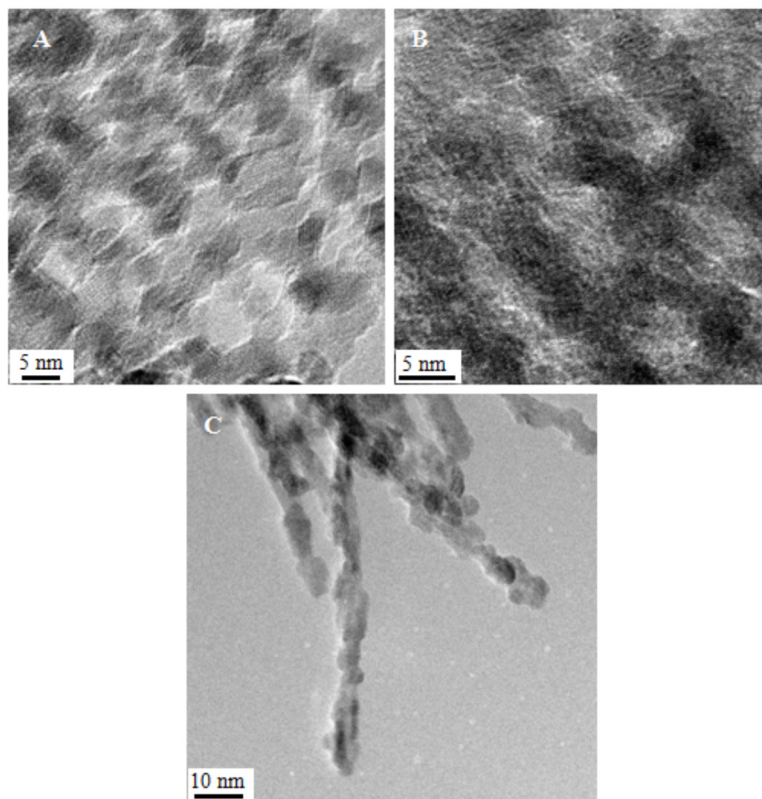
Figure S4.4. HRTEM images of (A) $CuFe_2O_4$ nanocast using KIT-6 template (B) $NiFe_2O_4$ nanocast prepared using KIT-6 as the template and (C) $NiFe_2O_4$ nanowires from SBA-15 (the images were obtained using Philips F20 Tecnai instrument, 160 kV).
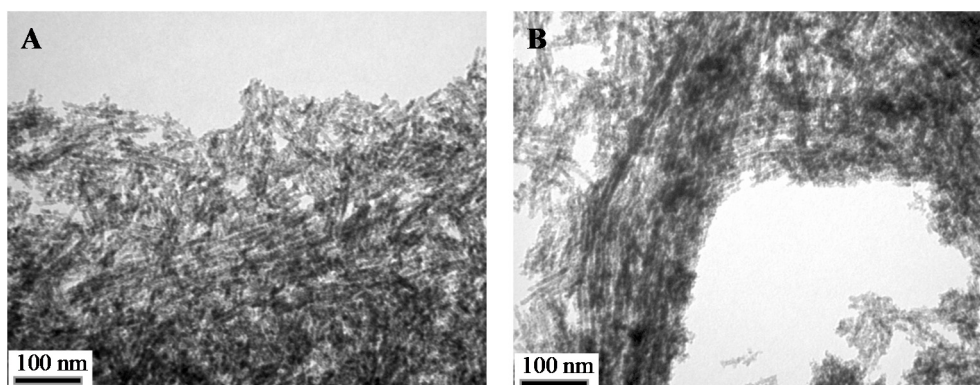
Figure S4.5. TEM images of Cu(20)/CeO_2 prepared using SBA-15 as the template with different loadings of nitrate precursor/silica: A) 1.5 g/g silica, B) 2 g/g silica.
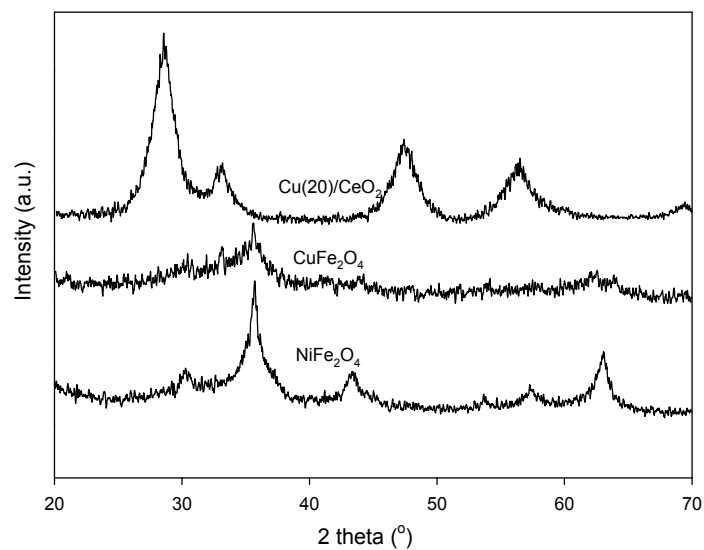
Figure S4.6. Wide angle powder XRD patterns for the mixed metal oxides prepared in this work prepared using MCM-48 as the template (as indicated) (Bruker SMART APEXII X-ray diffractometer with a Cu K_α radiation).
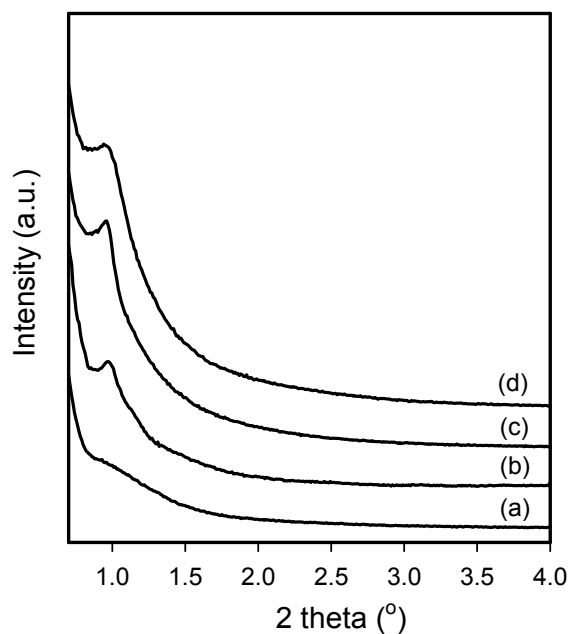
Figure S4.7. Low angle XRD patterns of nanocast mixed oxides prepared using SBA-15 as the template: (a) isolated nanowires $NiFe_2O_4$, (b) mesostructured $Cu(20)/CeO_2$, (c) mesostructured $CuFe_2O_4$, (d) nanowire bundles $NiFe_2O_4$ (Rigaku Multiplex, operated at 2 kW, using Cu K_α radiation).

76
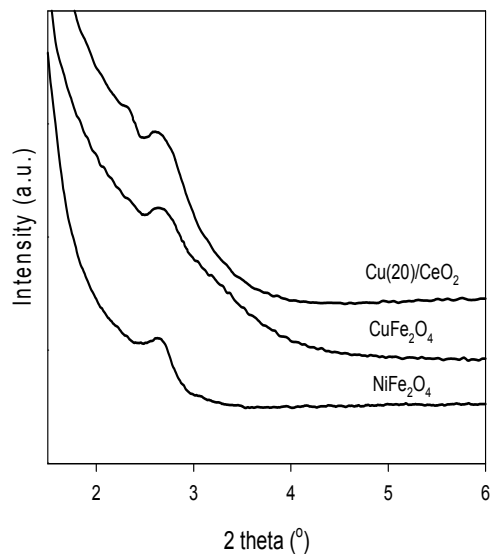
Figure S4.8. Low angle XRD patterns of nanocast mixed oxides prepared using MCM-48 nanospheres as the template (as indicated) (Bruker SMART APEXII X-ray diffractometer with a Cu K_α radiation).
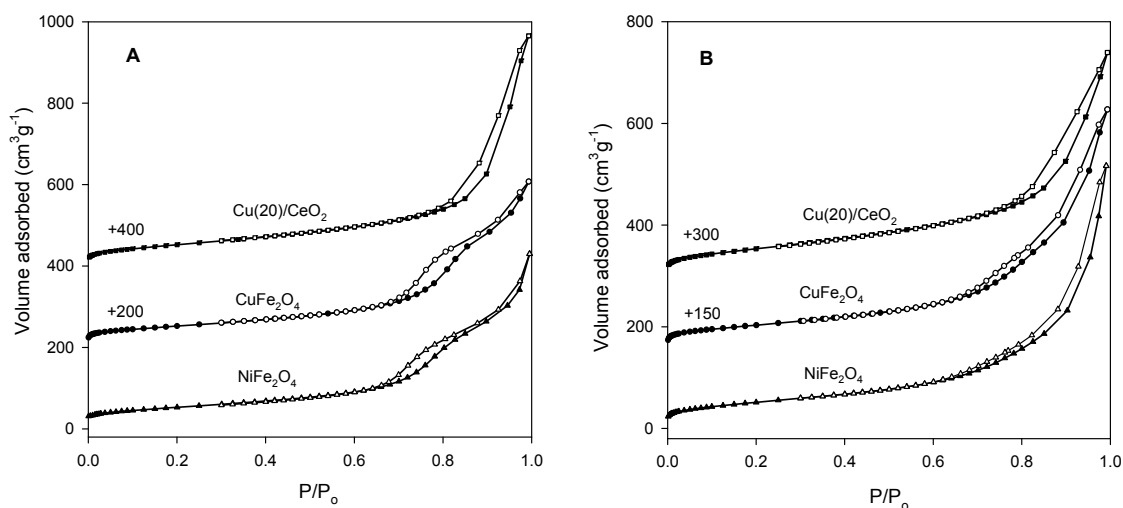
Figure S4.9. N_2 adsorption-desorption isotherms measured at -196°C for the mixed metal oxides prepared using (A) KIT-6 silica as a template, and (B) SBA-15 as a template (as indicated) (ASAP 2010).
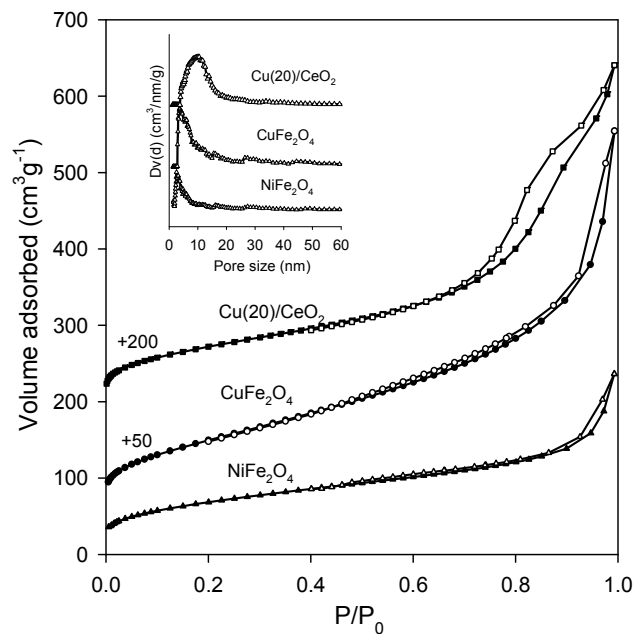
Figure S4.10. N_2 adsorption-desorption isotherms at -196°C and respective NLDFT pore size distributions (inset) deduced from the adsorption branch for the nanocast mixed metal oxides (as indicated).
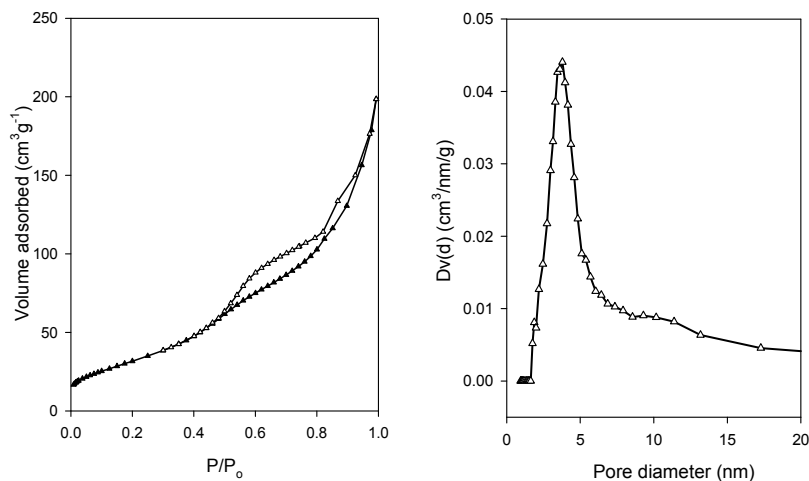
Figure S4.11. N_2 sorption isotherm and respective NLDFT pore size distribution (adsorption branch) of single oxide Co_3O_4 nanocast prepared using KIT-6 as the template.
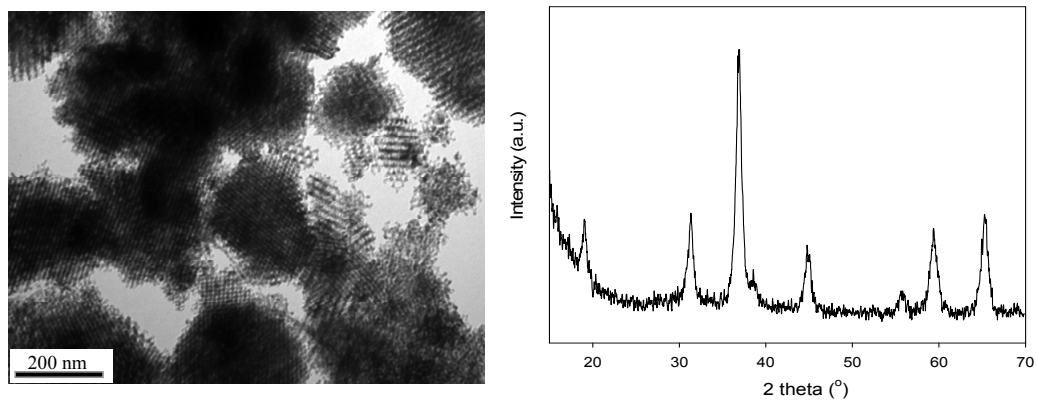
Figure S4.12. TEM image of Co_3O_4 prepared using KIT-6 as the template wide angle XRD pattern of Co_3O_4 using KIT-6 as the template.
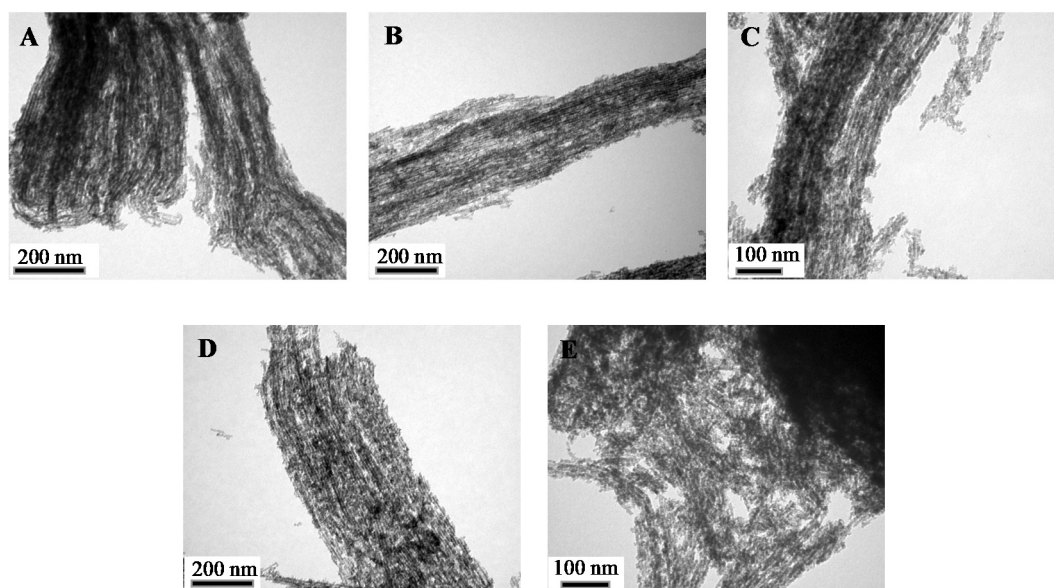
Figure S4.13. TEM images of $Cu(20)/CeO_2$ prepared using SBA-15 as the template in the presence of different solvents at varied reflux temperatures with fixed precursor loading of 2.5 g/1g silica: (A) n-hexane at 70°C, (B) cyclohexane at 70°C, (C) n-heptane at 70°C, (D) cyclohexane at 80°C, and (E) n-heptane at 100°C.
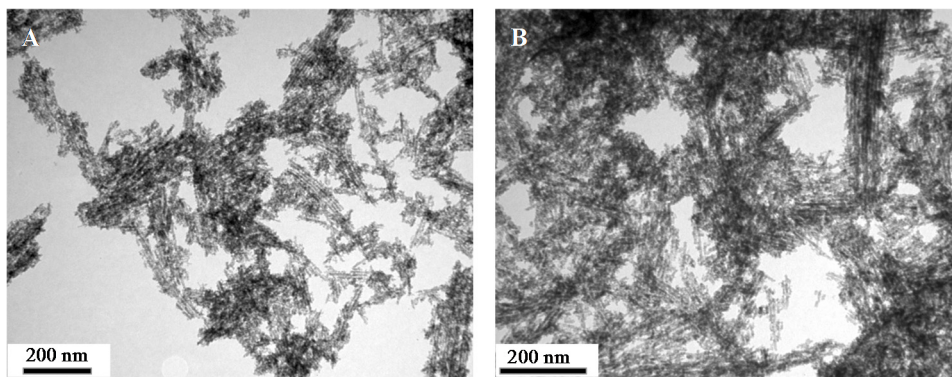
Figure S4.14. TEM images of A) Cu(20)/CeO$_2$ nanocast prepared using SBA-15 as the template without reflux process (the nitrate precursors were ground with silica and calcined at 500°C for 5 h). **B)** Cu(20)/CeO$_2$ prepared using SBA-15 as the template without reflux process (the nitrate precursors were ground with silica and preheated at 70°C before calcination at 500°C for 5 h).
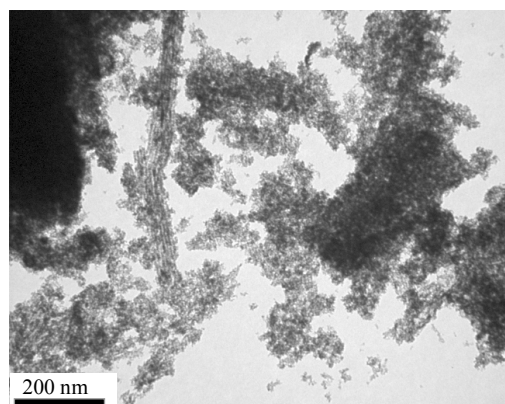
Figure S4.15. TEM image of Cu(20)/CeO$_2$ nanocast prepared using SBA-15 as the template via wet impregnation method using ethanol to dissolve the metal precursors.

Table S4.2. Physicochemical parameters of the different mesoporous mixed metal oxides derived from nitrogen physisorption measurements at -196°C

Samples	S_{BET} [a] (m^2g^{-1})	V_t [b] (cm^3g^{-1})	d_{NLDFT} [c] (nm)
Cu(20)/CeO$_2$-SBA-15	199	0.63	11.6
NiFe$_2$O$_4$-SBA-15	187	0.73	7.0
CuFe$_2$O$_4$-SBA-15	191	0.69	8.1
Cu(20)/CeO$_2$-KIT-6	195	0.71	16.0
NiFe$_2$O$_4$-KIT-6	191	0.58	8.1
CuFe$_2$O$_4$-KIT-6	188	0.58	9.1
Cu(20)/CeO$_2$-MCM-48	219	0.57	9.4
NiFe$_2$O$_4$-MCM-48	250	0.32	2.6
CuFe$_2$O$_4$-MCM-48	296	0.52	3.6

Acknowledgement

Chapter 5:

Tailored Mesostructured Copper/Ceria Catalysts with Enhanced Performance for Preferential Oxidation of CO at Low Temperature

Hoang Yen[1], Yongbeom Seo[3], Serge Kaliaguine[2], and Freddy Kleitz[1]

[1] Department of Chemistry and Centre de Recherche sur les Matériaux Avancés (CERMA), Université Laval, Quebec, G1V 0A6 (Canada)

[2] Department of Chemical Engineering, Université Laval, Quebec G1V 0A6 (Canada)

[3] Department of Chemistry, Graduate School of Nanoscience and Technology (WCU), KAIST, Daejeon (Republic of Korea)

Résumé

Dans ce chapitre, la performance des catalyseurs Cu/CeO$_2$ et CuM/CeO$_2$, préparés par nanocasting, est reportée dans le cas du procédé CO-PROX. Dans cette étude, des catalyseurs mésoporeux, de composition variable, ont été synthétisés en utilisant un procédé amélioré à partir d'une matrice rigide, selon une méthode initialement développée par l'auteur. La taille des pores, la surface spécifique et la structure des pores ont été ajustés en changeant le type de silice mésoporeuse utilisé comme matrice rigide (par exemple, des silices KIT-6 mûries à des températures différentes, SBA-15 et des nanosphères de MCM-48). Les oxydes métalliques ainsi synthétisés possèdent une surface spécifique élevée (jusqu'à 200 m^2 g^{-1}) et une taille de pores allant de 3 nm à 12 nm. La performance catalytique de ces matériaux est parmi les meilleures rapportée jusqu'à présent pour des catalyseurs à base de cuivre/oxyde de cérium pour la conversion du CO et la sélectivité du CO$_2$ à basse température. L'influence de la nature de la mésostructure et de la composition sur la réductibilité et les propriétés catalytiques est également démontrée.

Abstract

In this chapter, we report the catalytic performance in CO-PROX of Cu/CeO_2 and CuM/CeO_2 catalysts prepared by the nanocasting method. In this study, mesoporous catalysts with various compositions were synthesized using an improved hard templating method that we have developed in Chapter 4. The pore size, specific surface area, and pore structure were tailored by changing the type of mesoporous silica used as solid template (e.g., KIT-6 aged at different temperatures, SBA-15, and MCM-48 nanospheres). The resulting metal oxide materials possess a high surface area (up to 200 $m^2\,g^{-1}$) and a pore size ranging from 3 nm to 12 nm. The catalytic performance of these materials is among the best reported thus far for copper/ceria-based catalysts with respect to the CO conversion and CO_2 selectivity at low temperature. The effect of their mesostructure and composition on the reducibility and catalytic properties are also substantiated.

5.1. Introduction

Hydrogen as the most efficient and cleanest energy source for fuel cell power is produced mainly by reformation of hydrocarbons, followed by the water gas shift reaction. The CO (0.5–2 %) present in the hydrogen stream must be selectively removed because CO is highly poisonous to the electrocatalyst in proton-exchange membrane fuel cells (PEMFCs). Preferential oxidation (PROX) of CO in excess H_2 is therefore a key reaction for the practical use of H_2 in PEMFCs.[1,6,40,238-244]

Among the catalysts reported to be active for PROX, copper/ceria-based catalysts have been considered as promising candidates because of their low cost and high selectivity compared to catalysts based on gold or platinum. However, they usually only show noticeable activities above 100 °C, while the operating temperature of PEMFCs is around 80 °C.[6,238,239,245,246] Furthermore, the catalytic properties depend strongly on the preparation method and the CuO/CeO_2 interfacial area. [6,51,238,239,245,246] Despite numerous studies about PROX catalysts, little is known concerning the influence of pore size and pore structure on the catalytic performance.[239] Transition-metal oxides exhibiting mesoporous structures, for example, Co_3O_4 and CuO/Fe_2O_3, are active for CO oxidation at low temperature and show higher activity than the corresponding bulk materials.[238,240,241,244] The high activity of mesoporous metal oxides was correlated to their ordered mesostructure and high surface area. [238,240,241,244] Hard templating is a method known to enable the synthesis of materials that possess a highly defined pore architecture and a very high surface area, thus leading to unique physicochemical properties.[77,219,221,224,247-249] However, studies of surface redox reactivity and the confinement of reactions near to the surface owing to the dimension of the pores have been limited to a few compositions of catalysts for CO oxidation.[240,241,244]

Herein, we report the catalytic performance in CO-PROX of Cu/CeO_2 and CuM/CeO_2 (M = Fe, Cu) catalysts prepared by the nanocasting method.[250] In this study, mesoporous catalysts with various compositions were synthesized using an improved hard templating method that we have developed in the previous chapter. The pore size, specific surface area, and pore structure were tailored by changing the type of mesoporous silica used as solid template (e.g., KIT-6 aged at different temperatures, SBA-15, and MCM-48 nanospheres). The resulting metal oxide materials possess a high surface area (up to 200

$m^2 g^{-1}$) and a pore size ranging from 3 nm to 12 nm. The catalytic performance of these materials is among the best reported thus far for copper/ceria-based catalysts with respect to the CO conversion and CO_2 selectivity at low temperature. The effect of their mesostructure and composition on the reducibility and catalytic properties are also substantiated.

5.2. Results and discussion

5.2.1. Structural properties of nanostructured Cu(Fe,Co)/CeO₂ materials

Mesoporous silica templates with different pore structures (KIT-6, SBA-15, and MCM-48) were synthesized according to the literature and details of synthesis was described in the Chapter 4.[228-230] The pore size of the KIT-6 was varied by changing the aging temperature (40, 100, and 130ºC).[228,229] The nanocast catalysts were prepared by one-step-impregnation hard templating (see SI).
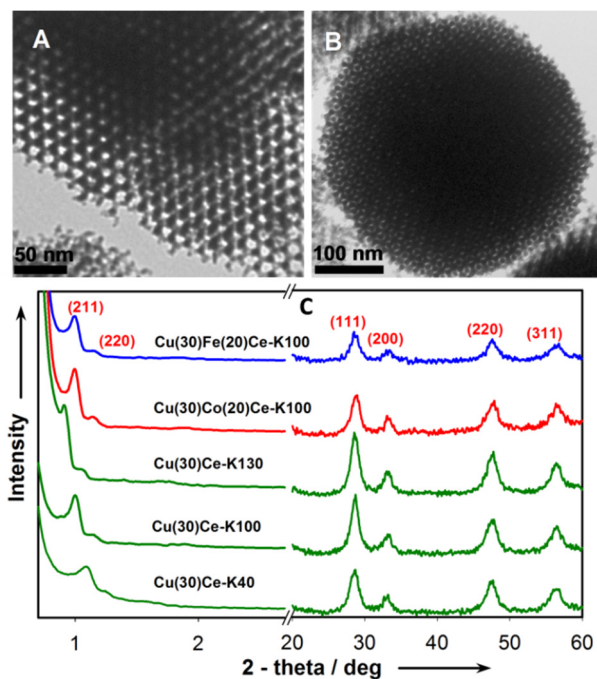
Figure 5.1. TEM images of A) Cu(30)Ce-K40, B) Cu(30)Fe(20)Ce-K100, and C) Powder XRD patterns of the samples templated from KIT-6.

The samples prepared from KIT-6 were labeled as Cu(x)CeM(y)-K-T, with T representing the aging temperature of KIT-6, x (x=10–30) and y (y=20) are nominal molar percentages

of Cu or M to Ce (M=Co or Fe), respectively. The samples using SBA-15 and MCM-48 hard templates were denoted as Cu(x)Ce-SBA and Cu(x)Ce-MCM, respectively.

Representative TEM images of the nanocast materials replicated from KIT-6 and SBA-15 templates confirm the long-range periodic order of the mesopores (Figure 5.1 A and B, and Figure S5.1 in SI). The TEM image of Cu/CeO$_2$ replicated from MCM-48 spheres clearly show the mesoporous spherical particle morphology. Mesoporosity was further confirmed by N$_2$ adsorption–desorption measurements (Figure S5.2). All of the samples casted from SBA-15, as well as from KIT-6 aged at 100 and 130ºC, showed type IV isotherms with a capillary condensation step above P/P$_0$=0.4, which are rather typical for mesoporous metal oxide nanocasts.[240,241,244,248]

Narrow pore size distributions were observed for all the samples except for Cu/CeO$_2$ produced from KIT-6-40. Pore-size analysis, obtained from the adsorption branch by NLDFT methods, indicated mesopores of approximately 5 nm for the products prepared from SBA-15, KIT-6-100, and KIT-6-130; the sample replicated from MCM-48 showed a smaller pore size of 2.6 nm. On the other hand, Cu(30)Ce-K40 exhibited additional pore-size distributions at about 12 nm and 16 nm, which is rather similar to what is observed when metal oxides could grow randomly within one set of the pore system of the bicontinuous structure, possibly owing to low interconnectivity between the two subnetworks of mesopore channels in the parent KIT-6 silica aged at low temperature.[224,244,247-249] Textural parameters of the mesoporous metal oxide samples are given in Table S5.1. Specific BET surface area, pore size, and pore volume of the nanocast Cu(30)Ce-K samples all decrease with higher aging temperature of the KIT-6 silica template. The samples prepared from cubic (*Ia3d*) KIT-6-100 and 2D hexagonal (*p6mm*) SBA-15 have the same pore size ($\approx$5 nm), specific surface area ($\approx$150 m^2 g^{-1}), and pore volume ($\approx$0.3 cm^3 g^{-1}). In contrast, Cu(30)Ce-K40 and Cu(30)Ce-MCM have a noticeably higher surface area ($\approx$200 m^2 g^{-1}), however the former has larger pore size and higher pore volume. Note that variation in copper content and additional incorporation of Co or Fe dopants have a minor effect on surface area and pore volume of the nanocast products. However, such differences in composition also have a significant impact on the reducibility and catalytic properties for CO-PROX (see below).

The excellent mesostructure order of the mesoporous metal oxides was also demonstrated by low-angle XRD patterns (Figure 5.1 C and Figure S5.3). All the patterns exhibit a main strong peak at low 2θ value, which could be indexed to the (211) and (100) reflections of the *Ia3d* and *p6mm* symmetries, respectively. The d values calculated from the (211) reflection of the cubic mesophase are 8.11, 8.84, and 9.71 nm, corresponding to unit-cell parameters (a_o) of 19.9, 21.7, and 23.8 nm for the mesoporous Cu(30)Ce samples derived from KIT-6 aged at 40, 100, and 130°C, respectively. The crystalline nature of the walls of the mesoporous materials was confirmed by wide-angle PXRD analysis (Figure 5.1 C and Figure S5.4), which reveals peaks corresponding to the pure face-centered-cubic (fcc) structure of CeO_2. The absence of other oxide phases of copper, cobalt, or iron suggests that these metal species are highly dispersed or incorporated in the ceria lattice.

5.2.2. Elemental analyses of nanostructured Cu(Fe,Co)/CeO$_2$ materials

The quantification of bulk and surface composition was carried out by AAS and XPS (Table S5.2). The remaining Si content determined by AAS is about 3.5 wt % in all samples. It is likely that ceria-bound Si species could not be totally removed in the presence of Si-O-Ce bonds (isolated SiO_2 is readily dissolved with NaOH), which is consistent with other reports on the preparation of CeO_2 using silica template.[251] Surface Cu/Ce ratios in the samples were 2.1–2.8 times higher than the respective Cu/Ce ratios in the bulk. This result confirms the surface enrichment with Cu and its high dispersion, in agreement with the elemental EDX mapping (Figure S5.5) and XRD results. From the XPS spectra (Figure S5.6), it is apparent that most Cu present in these samples is in +1 oxidation state, owing to the presence of low Cu $2p_{3/2}$ binding energy (932 eV) and the absence of shake-up peaks that are characteristics of Cu^{2+} at 939–944 eV.[51,246] Cerium species in all of the samples seem to be mostly in a +4 oxidation state. These observations are indicative of a redox equilibrium ($Cu^{1+}+Ce^{4+} \rightarrow Cu^{2+}+Ce^{3+}$), which has been claimed to be the source of a synergetic effect on catalyst reducibility.[51,245,246] These results prove that the copper species are well dispersed and in close contact with ceria.

5.2.3. Temperature programmed reduction studies

Temperature-programmed reduction by H_2 (H_2-TPR) of pure CeO_2 and metal-doped CeO_2 samples were performed to investigate reducibility characteristics of the catalysts (Figure 5.2). Two broad peaks appear at about 582 and 781°C for pure CeO_2, belonging to the reduction of surface and bulk ceria, respectively.[252] Bulk CuO shows a single reduction peak at 320°C. For Cu(x)Ce-K100 materials, hydrogen consumption can roughly be divided in two reductive peaks (denoted as α and β), which can be attributed to the reduction of well-dispersed surface copper species and copper in the ceria lattice, respectively, at noticeably lower temperature compared to the bulk oxide.[51,245,246,252,253] With an increase of the Cu content from 10 to 30 %, the temperature of the α peak decreases slightly and the associated H_2 consumption increases from 0.21 to 0.5mmol per gram of catalyst, reflecting higher amount of the most reducible Cu species on the surface. The β peak position drops strongly from 321 to 223°C, and the total H_2 consumption below 400°C increases from 0.78 to 1.65 mmol g^{-1} with increasing Cu content.
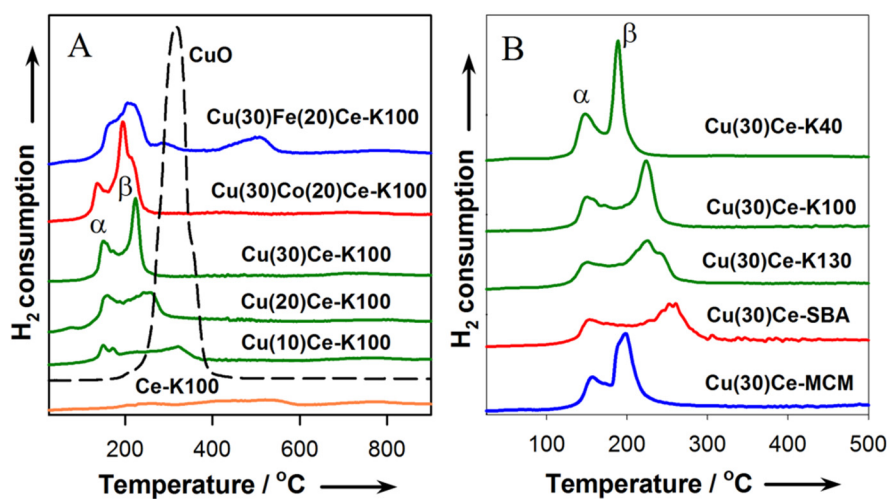
Figure 5.2. H_2-TPR profiles of the compositions replicated from A) KIT-6-100 and B) Cu(30)Ce from different mesoporous silica templates.

Note that the total H_2 consumption always surpasses the amount needed to totally reduce $Cu^{+/2+}$ species into Cu^0, which implies that some of Ce^{4+} ions are also reduced at lower temperature along with reduction of $Cu^{+/2+}$. Indeed, the H_2-TPR results demonstrate that there is a strong interaction between copper and cerium species. Doping of Co or Fe into the copper/ceria structure leads to higher H_2 consumption (Table S5.3), and an

additional peak appears at 489°C in the case of the Fe incorporation. Moreover, Figure 5.2 B shows the H_2-TPR profiles of the Cu(30)Ce materials nanocast from different mesoporous silica templates. These samples have similar content and segregation of Cu species. The Cu(30)Ce-MCM has the smallest pore size (≈2.6 nm), but higher H_2 uptake for the α peak compared to those of the Cu(30)Ce-K130 and Cu(30)Ce-SBA samples, which have a larger pore size (≈4.9 nm), probably because of the higher surface area of the Cu(30)Ce-MCM sample. For Cu(30)Ce-K samples, the total H_2 consumption below 400°C and the temperatures of the α peaks are the same, while the β peak shifts to lower temperature with decreased aging temperature of the KIT-6 templates. Notably, the H_2 uptake at the α peaks is 0.36, 0.52, and 0.94 for the samples prepared from KIT-6 templates aged at 130, 100, and 40°C, respectively, thus suggesting that the catalysts become more reducible with lower aging temperature of the parent silica template. Thus, these results evidence that both the composition and textural parameters of the catalysts have pronounced effects on their reducibilities. In addition, contributions of other effects, such as differences in Cu dispersion in CeO_2 originating from variation in silanol densities in the silica hard templates, which could play a role in the process of nanocasting (templates aged at varying temperatures), cannot be excluded.

5.2.4. Raman spectroscopy analyses

Oxygen vacancies are believed to play an important role in CO oxidation and can be considered as an indicator for promotion of the reaction.[51,246] Direct evidence of oxygen vacancies and defects can be provided by Raman spectroscopy, as they cause changes in the vibrational structure of the ceria lattice. As shown in Figure 5.3 and Figure S5.7, for pure CeO_2, a broad band with high intensity at 462 cm^{-1} is assigned to the F2$_g$ vibration mode of the CeO_2 lattice. The bands at 580 and 1160 cm^{-1} can be ascribed to the presence of oxygen vacancies and defects in the CeO_2 lattice.[7] The Raman spectra of copper/ceria samples exhibit an increase in intensity of the band at 1160 cm^{-1}, while the F2$_g$ vibration band shifts from 462 to 446 cm^{-1} and becomes broader and partially overlaps with the band at 580 cm^{-1}. The reason for these features could be the presence of oxygen vacancies, which are related to structural defects generated by incorporation of heterovalent atoms.[201,203-205] These observations made by Raman spectroscopy agree well with the above

conclusions concerning reducibility and correlation with the textural characteristic of the catalysts. The increase in copper content, surface area, and pore size leads to higher number of oxygen vacancies and increased reducibility. Here, oxides with 3D cubic pore structure seem to exhibit more oxygen vacancies and higher reducibility than the analog with 2D hexagonal pore structure. This result could tentatively be correlated to the continuous pore structure of the cubic mesophase possibly associated to subtle variations in wall thickness of the different replicas.
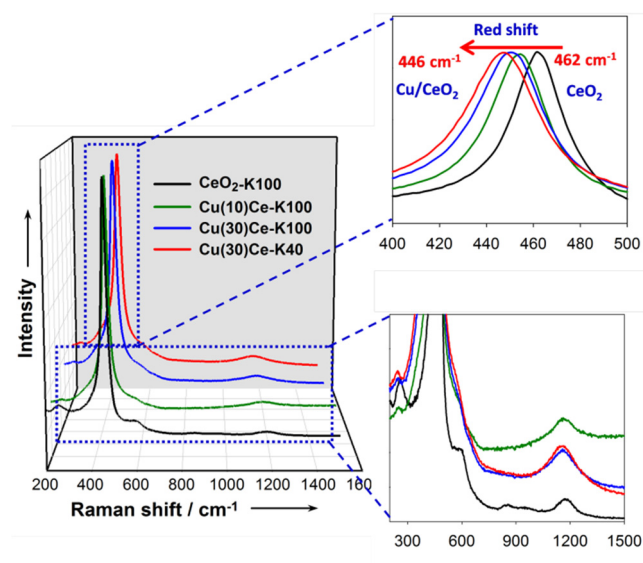
Figure 5.3. Raman spectra of the nanocast mixed oxide samples with various compositions and structures.

5.2.5. Catalytic performance of Cu(Fe,Co)/CeO$_2$ catalysts in CO-PROX process

The corresponding activity and selectivity for CO-PROX of all the samples, plotted as function of temperature, are given in Figure 5.4 and Figure S5.8. The light-off temperature of CO (T50) decreases in the following order for copper/ceria catalysts: Cu(10)Ce-K100>Cu(20)Ce-K100>Cu(30)Ce-K130>Cu(30)Ce-SBA>Cu(30)Ce-MCM>Cu(30)Ce-K100>Cu(30)Ce-K40, in accordance with the evolutions in oxygen vacancies and reducibility. Especially, a complete CO conversion with 100 % selectivity was achieved at around 40ºC in the case of Cu(30)Ce-K40, which is thus among the most active copper/ceria catalysts reported to date. Considering the low temperature, this material might also be exploited for practical application in gas sensors or breathing-protection

masks. Furthermore, the incorporation of 20 % Fe extends the full CO conversion (80–160ºC) and improves selectivity to CO_2, while Co incorporation does not provide substantial improvement. Further studies will be necessary to clarify the origin of the impact of the Fe and Co doping. Note that the stability of the catalyst was verified for the example of Cu(30)Ce-K100, and only a slight deterioration of the catalytic performance was found after three cycles.
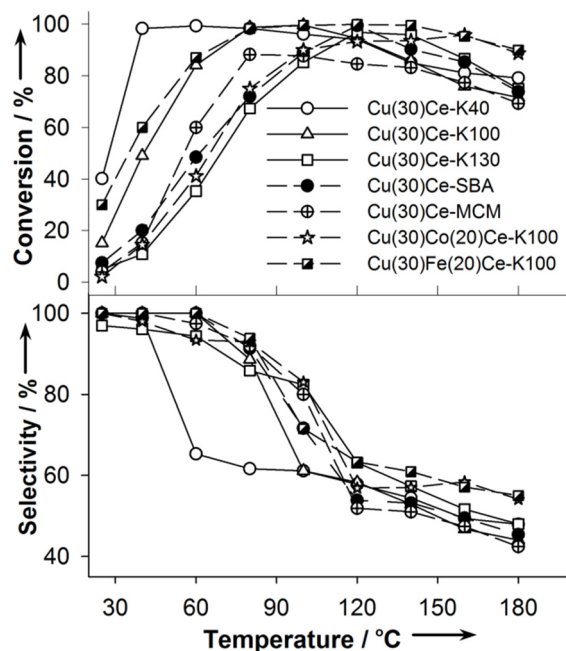
Figure 5.4. Conversion and selectivity as a function of temperature for CO-PROX over the nanocast catalysts (1.64 % CO, 1.62 % O_2, 90.25 % H_2, balance He, space velocity: 37 l h^{-1} g^{-1}).

5.3. Conclusions

In summary, we have shown that highly active and selective mesoporous copper/ceria catalysts with tailored compositions and textural parameters can be obtained through nanocasting using mesoporous silica phases as hard templates. The products are promising materials for application as CO-PROX catalysts or as gas sensors. In addition to the role of composition and specific surface area, the reducibility and catalytic performance are also influenced by structural parameters such as pore size and pore structure. This study demonstrates that a fine control over nanoscale structural features offers new perspectives for catalyst design. In the current chapter, we have developed efficient catalysts for CO-PROX in order to purify hydrogen fuel. Concerning the critical issue of hydrogen storage,

the next two chapters will focus on the study of the catalytic properties of bimetallic CuNi catalysts for hydrogen generation from ammonia-borane and hydrous hydrazine.

5.4. Experimental section

5.4.1. Synthesis of nanocast mixed metal oxides

For the preparation of the nanocast metal oxides, preground nitrate salts (2.75 g) in desired proportions ($Cu(NO_3)_2 \cdot 3\,H_2O$, $Ce(NO_3)_3 \cdot 6\,H_2O$, $Co(NO_3)_2 \cdot 6\,H_2O$, $Fe(NO_3)_3 \cdot 9\,H_2O$) were mixed and ground with the silica template (1g, pretreated in vacuum at 150°C for 2 h) in an agate mortar in the presence of n-hexane (10 ml). Metal precursors (1.5 g) were used in the case of KIT-6 aged at 40°C as the template. The resulting homogeneous mixture was subsequently dispersed in n-hexane (30 ml) and heated to reflux (80°C) for 20 h. After filtration, the samples were dried at 70°C for 24 h, and calcined under air at 500°C for 5h. The silica template was then removed by treatment with NaOH (1-2M) solution at room temperature. Finally, the resulting Cu/CeO_2 or CuM/CeO_2 powders were washed with water and ethanol, and then dried at 70°C.

5.4.2. Catalyst Characterization

The chemical composition of the samples was analyzed by atomic absorption (AAS) on a M1100B Perkin-Elmer atomic absorption spectrophotometer. The Raman spectra were recorded at 22.0 ± 0.5°C using a LABRAM 800HR Raman spectrometer (Horiba Jobin Yvon,Villeneuve d'Ascq, France) coupled to an Olympus BX 30 fixed stage microscope. The excitation light source was the 514.5 nm line of an Ar^+ laser (Coherent, INNOVA 70C Series Ion Laser, Santa Clara, CA). The laser beam was focused using a 100× objective, generating intensity at the sample of approximately 5 mW. The confocal hole and the entrance slit of the monochromator were fixed at 600 and 200 μm, respectively. Data were collected by a one-inch open electrode Peltier-cooled CCD detector (1024×256 pixels). Temperature-programmed reduction experiments were performed on RMX-100 instrument. Each sample (20mg) was pretreated at 500°C for 1h at ramping rate of 10°C/min under 20% O_2 balanced with He (10 ml/min) and TPR was then performed under H_2 (5% balanced in Ar) at ramping rate of 5°C/min. Other characterization techniques (e.g. TEM, XRD, N_2 physical adsorption) were performed as described in Chapter 4.

5.5. Supporting information
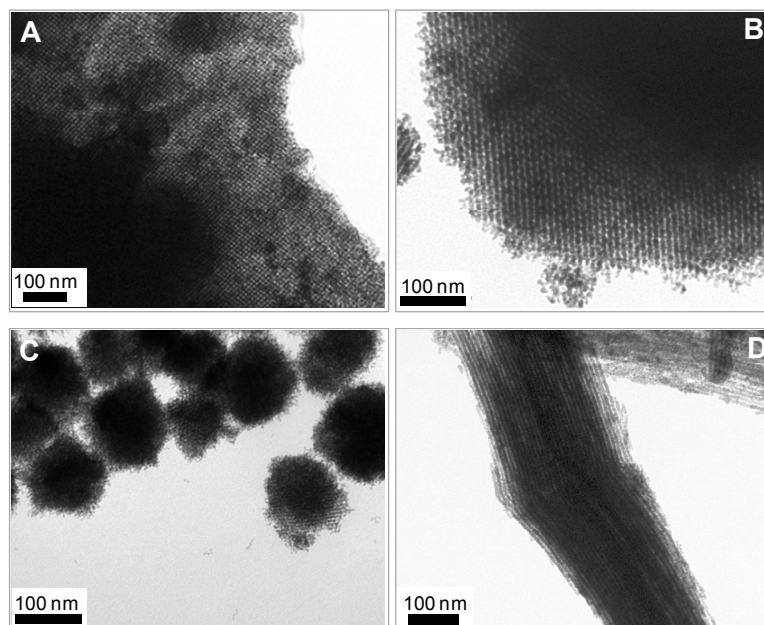
Figure S5.1. Representative TEM images of the nanocast mixed oxides prepared from different mesoporous silica templates: (A) Cu(30)Ce-K100, (B) Cu(30)Co(20)Ce-K100, (C) Cu(30)Ce-MCM and (D) Cu(30)Ce-SBA (JEOL JEM 1230 operated at 120 kV).

Table S5.1. Physicochemical parameters of the different mesoporous mixed metal oxides derived from nitrogen physisorption measurements at -196°C.

Samples	S_{BET} [a]	V_t [b]	d_{NLDFT} [c]
	(m^2g^{-1})	(cm^3g^{-1})	(nm)
Cu(10)Ce-K100	151	0.39	4.9
Cu(20)Ce-K100	139	0.30	4.9
Cu(30)Ce-K100	146	0.30	4.9
Cu(30)Ce-K40	197	0.90	7/12
Cu(30)Ce-K130	126	0.21	4.9
Cu(30)Ce-SBA	154	0.29	4.9
Cu(30)Ce-MCM	200	0.20	2.6
Cu(30)Fe(20)Ce-K100	153	0.26	4.9
Cu(30)Co(20)Ce-K100	162	0.24	4.9

[a] S_{BET}, apparent BET specific surface area deduced from the isotherm analysis in the relative pressure range from 0.05 to 0.20; [b] V_t, total pore volume at relative pressure 0.95; [c] d_{NLDFT}, pore diameter calculated from the adsorption branch (NLDFT kernel of metastable adsorption isotherms).
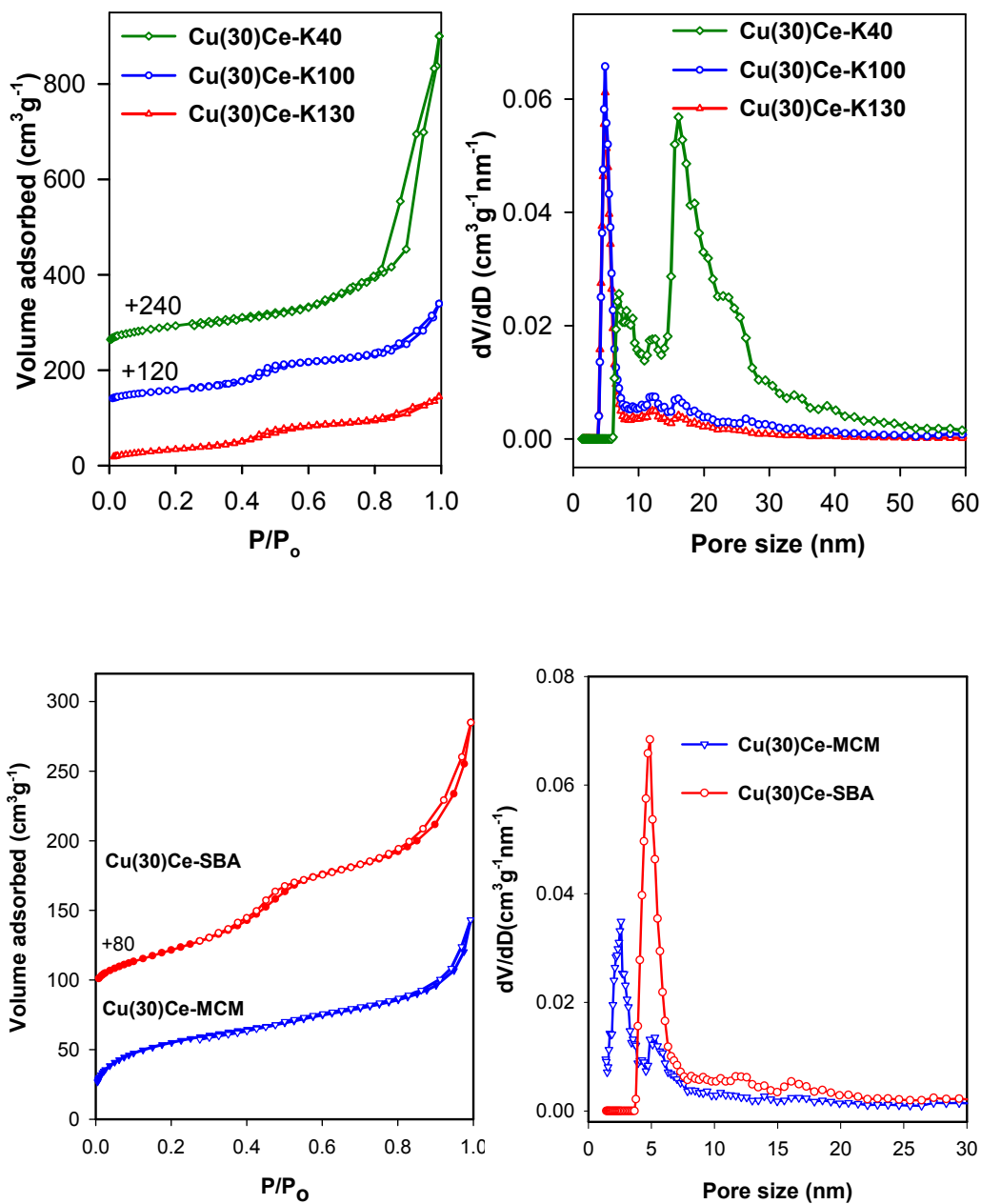
Figure S5.2. N_2 adsorption-desorption isotherms at -196°C (left) and respective NLDFT pore size distributions (right) deduced from the adsorption branch for the nanocast mixed metal oxides (as indicated) (ASAP 2010).
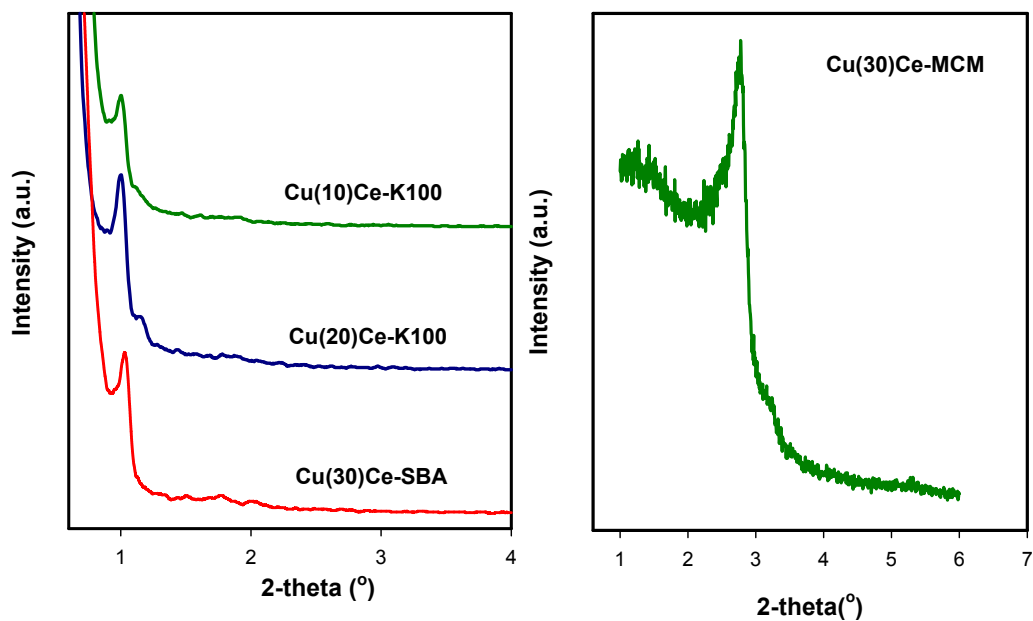
Figure S5.3. Low-angle XRD patterns for the mixed metal oxides prepared in this work using different mesoporous silicas as the templates (as indicated) (Bruker SMART APEXII X-ray diffractometer with a Cu K_α radiation).
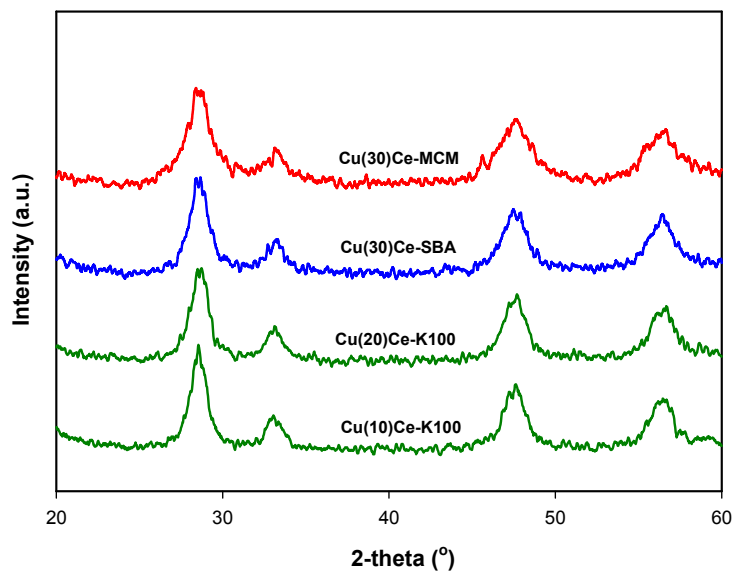
Figure S5.4 Wide-angle powder XRD patterns of nanocast mixed metal oxides prepared using different mesoporous silicas as templates (as indicated) (Bruker SMART APEXII X-ray diffractometer with a Cu K_α radiation).
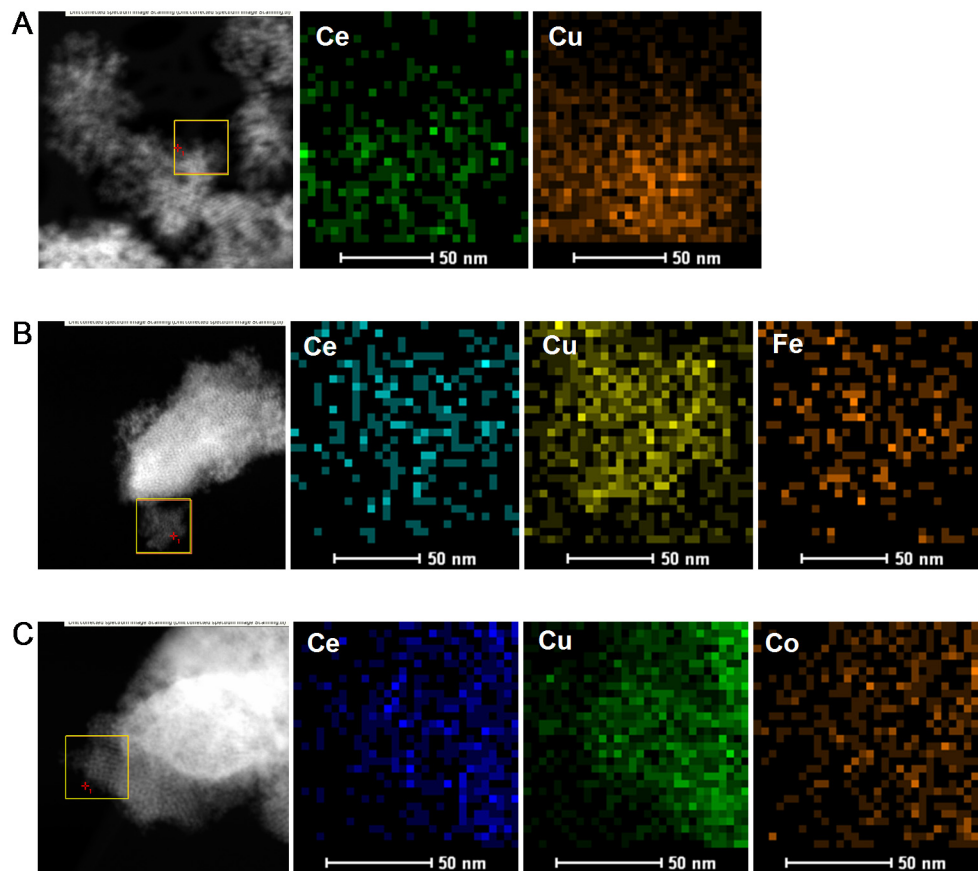
Figure S5.5. EDX mapping of the samples: (A) Cu(30)Ce-K100, (B) Cu(30)Fe(20)Ce-K100, (C) Cu(30)Co(20)Ce-K100.

Table S5.2. Nominal and actual molar ratio of Cu/Ce of the prepared composite oxides

Samples	Cu/Ce nominal ratio	Cu/Ce actual ratio in the bulk	Cu/Ce surface ratio
Cu(10)Ce-K100	0.10	0.11	0.28
Cu(20)Ce-K00	0.20	0.19	0.53
Cu(30)Ce-K100	0.30	0.30	0.63
Cu(30)Ce-K40	0.30	0.28	0.63
Cu(30)Ce-K130	0.30	0.31	0.69
Cu(30)Ce-SBA	0.30	0.29	0.65
Cu(30)Ce-MCM	0.30	0.27	0.61
Cu(30)Fe(20)Ce-K100	0.30	0.29	0.70
Cu(30)Co(20)Ce-K100	0.30	0.30	0.82
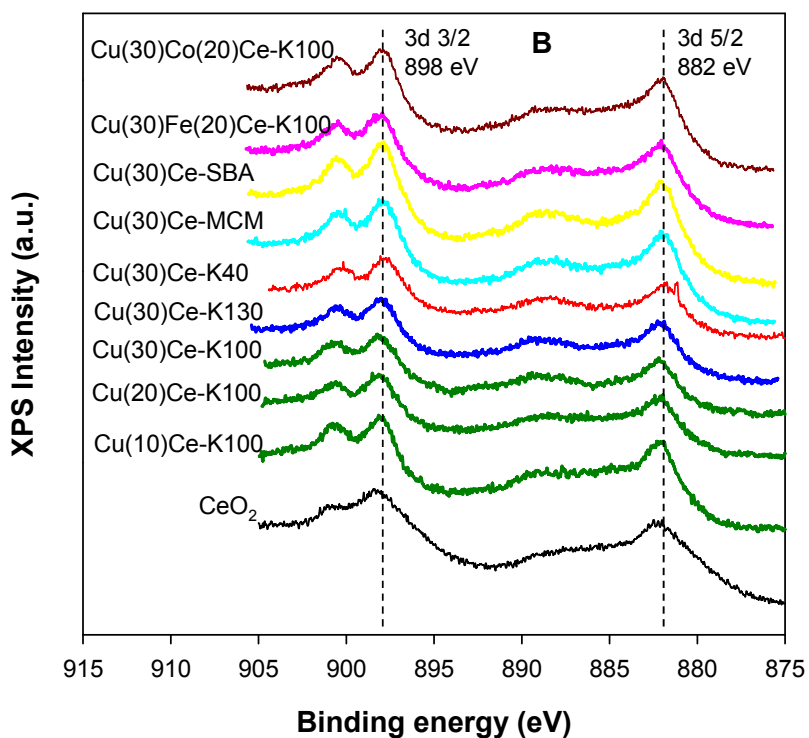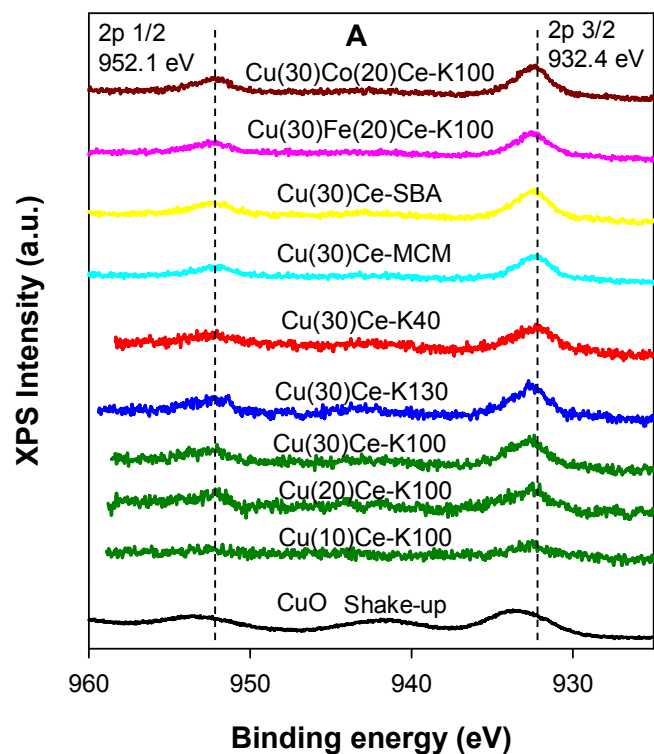
Figure S5.6. Cu2p (A) and Ce3d (B) XPS spectra of the prepared catalysts (the spectra are normalized by their peak intensity and energy corrected for adventitious carbon at 284.6 eV).

Table S5.3. H_2 consumption of prepared nanocast mixed oxides

Sample	H_2 consumption of the peak α (mmol/g)	Total H_2 consumption below 400ºC (mmol/g)
Cu(10)Ce-K100	0.21	0.99
Cu(20)Ce-K100	0.27	1.62
Cu(30)Ce-K100	0.52	2.15
Cu(30)Ce-K40	0.94	2.17
Cu(30)Ce-K130	0.36	2.16
Cu(30)Ce-SBA	0.35	2.08
Cu(30)Ce-MCM	0.50	1.77
Cu(30)Co(20)Ce-K100	0.59	2.42
Cu(30)Fe(20)Ce-K100	0.43	2.24
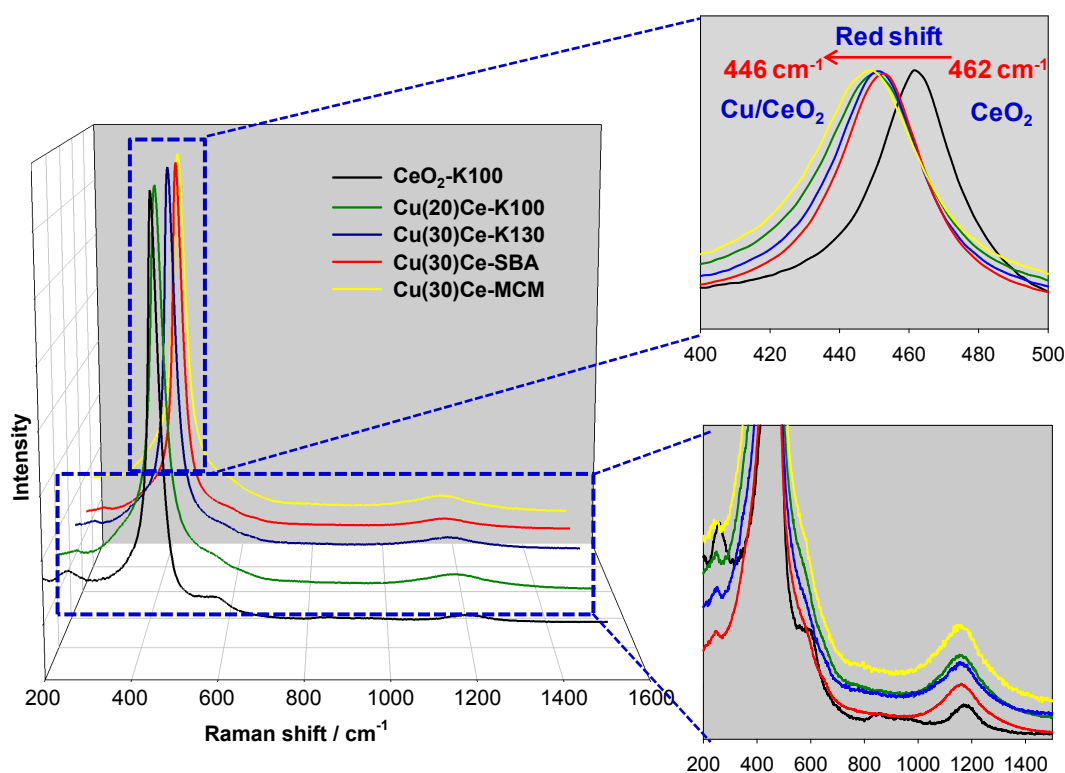
Figurre S5.7. Raman spectra of the nanocast metal oxides samples with various compositions and structures (as indicated).
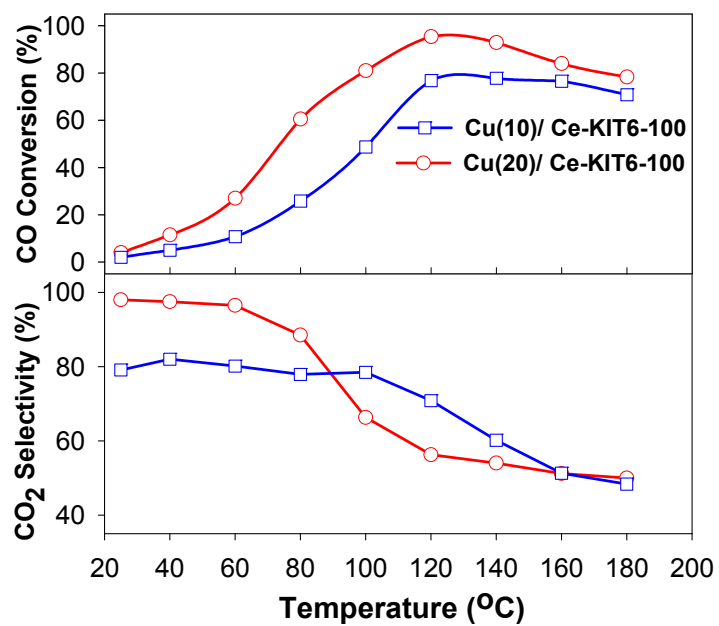
Figure S5.8. Conversion and selectivity as function of temperature over the nanocast samples Cu(10)Ce-K100 and Cu(20)Ce-K100.

Chapter 6:

High-performance solid catalysts for H$_2$ generation from ammonia borane: progress through synergetic Cu–Ni interaction

Hoang Yen and Freddy Kleitz

Department of Chemistry, Centre de Recherche sur les Matériaux Avancés (CERMA), Université Laval, Quebec, G1V 0A6, QC

Résumé

Les matériaux pour le stockage d'hydrogène, en particulier les composés B-N comme le borazane (ammoniaborane, AB), avec une capacité de stockage potentielle de 19,6 % massique de H_2 et 0,145 kg_{H2} l^{-1} ont été considérés comme des solutions possibles pour aborder les problèmes de stockage de H_2. Dans ce travail, des performances catalytiques extrêmement élevées sont reportées, avec des catalyseurs CuO-NiO facilement préparés, pour l'évolution de H_2 à partir du borazane en solution aqueuse. Ces catalyseurs à base de métaux non nobles peuvent être synthétisés soit par le simple traitement thermique d'un mélange des précurseurs métalliques, soit par le biais d'une méthode améliorée de nanocasting. Ce travail démontre clairement que les précurseurs métalliques, leur composition et les conditions de traitement thermique ont une influence importante sur l'interaction synergique existant entre les espèces Cu et NiO, ce qui est déterminant dans l'accélération de l'évolution d'hydrogène partir de AB. Par conséquent, cette découverte met en évidence que des combinaisons de métaux non nobles peuvent fournir des approches viables pour le développement de nouveaux catalyseurs utiles.

Abstract

Chemical hydrogen storage materials, in particular B–N compounds such as ammonia-borane (AB) with a potential storage capacity of 19.6 wt% H_2 and 0.145 kg_{H2} l^{-1}, have been regarded as potential solutions for addressing H_2 storage issues. In this work, we report the exceedingly high catalytic performance of easily prepared bi-component CuO–NiO catalysts for the H_2 evolution from ammonia-borane in aqueous solution. These non-noble metal catalysts could be synthesized either by simple thermal treatment of a physical mixture of the metal precursors or through an improved hard templating method. This work clearly shows that metal precursors, composition, and heat treatment conditions have a profound influence on the synergetic interaction existing between Cu species and NiO, which is decisive in accelerating the hydrogen evolution of AB. Therefore, the present finding demonstrates that combinations of non-noble metals can provide viable approaches for the development of practical catalysts.

6.1. Introduction

Hydrogen is considered to be the best alternative to hydrocarbon fuels due to its high energy content and environmentally benign nature. However, safe storage of H_2 for controlled delivery is still a major hurdle for its widespread usage.[7,8,254] Ammonia borane (H_3N-BH_3, AB) is a particularly appealing molecule for chemical hydrogen storage applications owing to its high gravimetric capacity of H_2 (theoretical 19.6 wt%), good stability and solubility in relatively polar coordinating solvents under ambient conditions. Catalytic hydrolysis, which can in theory produce 3 mol of H_2 per mol of AB (as shown in eq (6.1)), is an effective approach for the release of H_2 stored in AB.[10-12,255]

$$H_3NBH_3 + 2H_2O \rightarrow NH_4^+ + BO_2^- + 3H_2 \qquad (6.1)$$
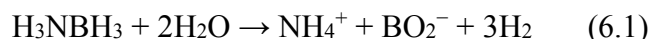
Thus, finding cost effective and highly efficient catalysts for this reaction is of extreme significance to make the AB complex a practical H_2 storage medium.[9,12,254] Although rapid hydrogen generation has been achieved using noble metal catalysts (such as Pt, Ru, and Rh), there is a high demand for cheaper and abundant non-noble transition metal catalysts exhibiting high activity.[32,36,256,257] However, a problem of the non-noble transition metals is the instability of their low valence states,[258-261] which are the required active states for hydrolysis of AB. Therefore, reductive pre-treatment, storage under an inert atmosphere and/or use of protective agents are nearly unavoidable before application to attain an effective catalyst.[43,46,47,258] Nevertheless, among transition metal oxides, copper oxides were reported to be catalysts operating in AB hydrolysis without the need for a reductive pre-treatment. However, Cu containing catalysts are found to be modestly active and the agglomeration of Cu metal species, which are formed under reductive reaction conditions, decreases drastically the catalytic activity.[259-265] Therefore, facile preparation of highly active Cu-based catalysts is of great practical and scientific interest. Furthermore, it is well-documented that the performance of a solid catalyst is strongly correlated with its surface properties and cooperative synergetic effects between Cu species and an oxide support can possibly endow mixed hybrid (Cu/oxide) catalysts with enhanced catalytic activity and selectivity.[266,267]

Herein, we report the superior catalytic performance in AB hydrolysis of bi-component CuO–NiO catalysts which could be prepared either by simple thermal treatment

113

of a physical mixture of the metal precursors or through an improved hard templating method.[250] We show that metal precursors, composition, and heat treatment conditions have a profound influence on the synergetic interaction existing between Cu species and NiO, which is decisive in accelerating the hydrogen evolution of AB. Hydrolysis completion could be achieved in 2 min in the case of the optimal catalyst $Cu_{0.5}Ni_{0.5}$ obtained by nanocasting, with an initial turnover frequency (TOF) value of 3600 h^{-1} under ambient conditions, which is the highest value reported thus far among all of the non-noble metal-based catalysts for this reaction. Moreover, kinetics of hydrolysis and reducibility of the prepared catalysts were also substantiated.

6.2. Experimental section

6.2.1 Synthesis of CuO–NiO catalysts

Briefly, for the preparation of the nanocast metal oxides, 3 g of pre-ground nitrate salts in desired proportion ($Cu(NO_3)_2 \cdot 3H_2O$, $Ni(NO_3)_3 \cdot 6H_2O$) was mixed and ground with 1 g of a mesoporous silica KIT-6 template[228,229] (pre-treated under vacuum at 150ºC for 2 h) in an agate mortar in the presence of 10 ml of cyclohexane. The resulting homogeneous mixture was subsequently dispersed in 30 ml of cyclohexane and refluxed at 85ºC for 20 h. After filtration, the samples were dried at 45ºC for 24 h, and calcined under air at 400ºC (heating rate of 1ºC min^{-1}) for 5 h. The silica template was then removed by treatment with 0.7 M NaOH at room temperature 3 times for 24 h. Finally, the resulting CuO–NiO mixed oxide powders were washed with water and ethanol, and then dried at 70ºC. For the preparation of thermally decomposed materials, 3 g of nitrate or chloride metal precursors in desired proportions were ground in an agate mortar and then the mixture was thermally decomposed in a muffle furnace at targeted temperature in air for 5 h with a ramping rate of 1ºC min^{-1}. The samples prepared from nitrate precursors were labelled as Cu_xNi_y-T, with T representing the heat treatment temperature, x and y are the nominal molar percentages of Cu and Ni, respectively. The sample prepared via nanocasting was designated as Cu_xNi_y-T-NC. The $Cu_{0.5}Ni_{0.5}$-400-IM sample was prepared by incipient wetting of an aqueous solution of copper nitrate on preformed NiO-400 followed by thermal decomposition at 400ºC.

114

6.2.2 Catalyst characterization

Structure analyses (XRD and TEM)

TEM images and XRD patterns were obtained as described in the Chapter 4.

Elemental and surface analyses (AAS and XPS)

The chemical composition of the samples was analyzed by atomic absorption (AAS) on a M1100B Perkin-Elmer atomic absorption spectrophotometer. Samples for AAS measurements were prepared by dissolving catalysts (10 mg) in aqueous HCl solution (50 ml, 10 wt%) at 363 K and then diluting in DI water. Cu standards of 2 ppm and 4 ppm and Ni standards of 1 ppm and 2 ppm were used. Weight percentages were obtained from concentration measurements (wavelengths of 324.8 nm and 232 nm for Cu and Ni, respectively) and atomic percentages were calculated using the stoichiometry. The XPS measurements were carried out on an AXIS-ULTRA instrument by KRATOS (UK). The X-ray source is a monochromatic Al source operating at 300 watts. Survey scans were recorded with a pass energy of 160 eV and a step size of 1 eV. High energy resolution spectra were used for chemical analysis. They were recorded at 20 eV or 40 eV pass energy and a step size of 0.05 eV or 0.1 eV, depending on the amount of each element. Calculation of the apparent relative atomic concentrations was performed with the CasaXPS software, using relative sensitivity factors for Cu $2p_{3/2}$ and Ni $2p_{3/2}$.

Specific surface area determination

N_2 adsorption–desorption isotherms of the samples were measured at $-196^{\circ}C$ using a Quantachrome Autosorb-1MP instrument. Prior to measurement, the samples were outgassed at $150^{\circ}C$ for 7 h under turbomolecular pump vacuum. The Brunauer–Emmett–Teller (BET) equation was used to calculate the specific surface area, S_{BET}, from adsorption data obtained at P/P_0 between 0.05 and 0.2.

Temperature-programmed reduction (H_2-TPR)

TPR experiments were performed on an RMX-100 instrument. In a typical test, a 10 mg of catalyst was loaded in the middle of a quartz tubular reactor, with quartz wool supports on both sides. The catalyst was cleaned in helium flow and TPR was then performed under H_2 (5% balanced in Ar) with a flow rate of 10 ml min^{-1} and a ramping rate of $5^{\circ}C$ min^{-1}.

6.3. Results and discussion

6.3.1. Structural characterization of bicomponent CuNi catalysts

All the samples prepared by simple thermal decomposition of the nitrate salts at different temperatures show polyhedral shape and the particle size distribution ranged from 50 to 200 nm, as shown in Figure 6.1a and S6.1, (SI).
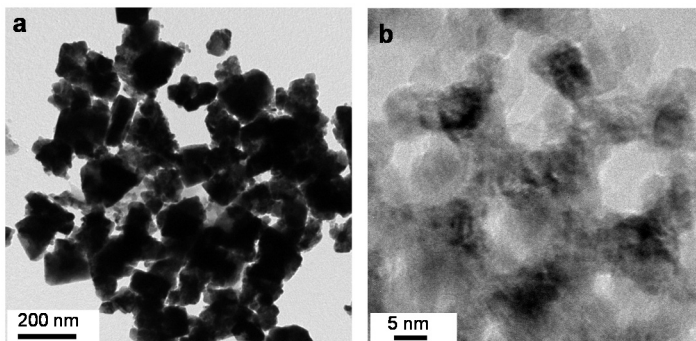
Figure 6.1. TEM images of (a) $Cu_{0.5}Ni_{0.5}$-400 and (b) $Cu_{0.5}Ni_{0.5}$-400-NC samples.

The mesoporous structure of the nanocast $Cu_{0.5}Ni_{0.5}$-400-NC replicated from mesoporous KIT-6 silica was confirmed by TEM observations (Figure 6.1b and S6.1, SI). Figure 6.2 and S6.2, SI show the powder X-ray diffraction (XRD) patterns of both the thermal and the nanocast products for various compositions obtained within the range of 400–600°C. The diffractograms of $Cu_{0.1}Ni_{0.9}$-400 and $Cu_{0.25}Ni_{0.75}$-400 consist mainly of peaks associated with the NiO cubic rock-salt phase, indicating that CuO is soluble in NiO and forms a cubic rock-salt solid solution, with a general formula corresponding to Cu_xNi_yO. At the Cu:Ni ratio = 0.5:0.5, NiO and/or Cu_xNi_yO appear as the main phase and a fraction of CuO is observed as a segregated phase. At copper-rich composition, i.e. $Cu_{0.75}Ni_{0.25}$, monoclinic CuO exists as the major phase beside the cubic structure of NiO as a minor phase. We observed that the maximum copper concentration that could be obtained for the solid solution is $Cu_{0.25}Ni_{0.75}$ with negligible phase segregation. Note that, this range associated with the formation of the solid solution is compatible with previously reported data.[268-270] However, in our case, a slight shift of the position of the (111) reflection to lower 2-theta was observed, this deviation being the highest in the case of $Cu_{0.5}Ni_{0.5}$. In addition, when comparing the diffraction peaks corresponding to the (111) and (200) planes of the single NiO and the mixed CuO–NiO oxide samples, it is observed that both the (200)

116

peak broadening and the relative I(111)/I(200) integrated intensity ratio are greater in the binary oxides than in the single NiO oxide, and these differences are the most pronounced for $Cu_{0.5}Ni_{0.5}$ calcined at 400ºC. This finding may be resulting from the substitution of some Ni^{2+} (0.69 Å) by Cu^{2+} having slightly larger radius (0.73 Å) and distortion of the cubic rock-salt matrix upon formation of new phases, Cu_xNi_yO (e.g., $Cu_xNi_{1-x}O$, $NiCuO_2$, Ni_2CuO_3).
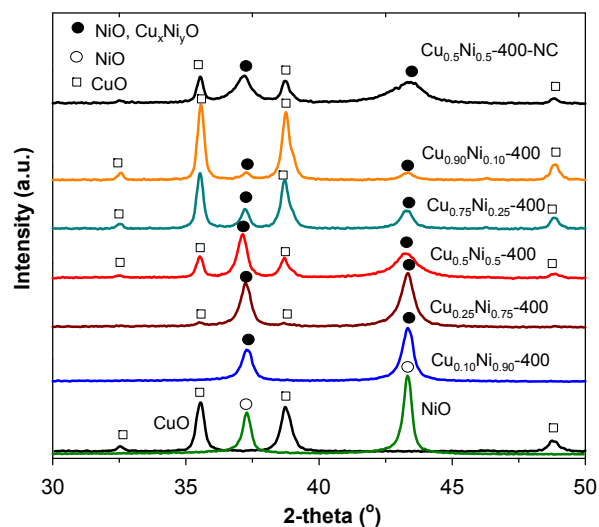
Figure 6.2. Wide-angle powder XRD patterns of the single and mixed oxide samples of various compositions, as indicated.

Here, the driving force of this structural distortion can arise from the accommodation of the Jahn–Teller distortion of the Cu^{2+} site symmetry, from octahedral to semi-square planar, and a distortion of the Ni^{2+} site from its ideal octahedral coordination; this distorted structure would induce local strain around the Cu-rich planes.[269] The shift of the Bragg peaks reflects a significant change in the lattice parameters and inter-atomic distances. This is known to potentially have a significant impact on the electronic structure, and affect the adsorptive and catalytic properties of a material.[69,195,271]

The position of the (111) plane and relative peak intensities are almost unchanged for $Cu_{0.5}Ni_{0.5}$ heated at 400 and 500ºC. However, the sample calcined at 600ºC shows less pronounced deviations in the XRD reflections compared to NiO, which is consistent with an enhanced segregation between CuO and NiO phases occurring at higher annealing temperatures. For the samples obtained by thermal treatment of the salts at 400 or 500ºC,

the crystallite size associated with the CuO phase and that of NiO and/or Cu_xNi_yO solid solution are found to be around 40 and 24 nm, respectively, as estimated using the Scherrer equation. The NiO crystallite size is only slightly increasing up to 30 nm when calcined at 600°C. The less intense and broader diffraction peaks in the XRD pattern of the nanocast product indicate that this sample consists of smaller crystallites due to limited crystal growth in the confined space of the silica nanopores.[248,250,267]

The textural parameters of all the oxide samples under study are given in Table S6.1, SI. The samples obtained by thermal treatment of nitrate metal salts show low specific BET surface area (~10 m^2 g^{-1}), whereas the nanocast sample has noticeably higher surface area (~73 m^2 g^{-1}). Variations in composition and thermal decomposition temperature have minor effects on the BET specific surface area of the products.

6.3.2. Composition and temperature programmed reduction analyses

Quantification of bulk and surface composition was carried out by atomic absorption spectroscopy (AAS) and X-ray photoelectron spectroscopy (XPS), respectively (Table S6.2). Surface Ni enrichment is observed for all the binary CuO–NiO samples, irrespective of the mixture composition or synthesis conditions. From the XPS spectra (Figure S6.3a, SI), it is apparent that most Cu present in the samples is in +2 oxidation state owing to the occurrence of high Cu $2p_{3/2}$ binding energy (933.5 eV) and the presence of strong shake-up peaks characteristic of Cu^{2+} at 939–944 eV.[195,260,261,265] However, it could be possible that some of the Cu in the mixed oxide catalysts is in +1 oxidation state, as both $2p_{3/2}$ and $2p_{1/2}$ peaks are slightly broadened towards lower binding energies. The Ni 2p spectra (Figure S6.3b, SI) of the catalysts displayed two peaks. A lower binding energy peak at 853.3 eV is attributed to Ni^{2+} in NiO and the higher binding energy peak at 855.5 eV is assigned to surface hydroxyl groups (e.g., Ni–OH) most likely originating from interactions between the oxide surface and ambient water vapor,[272,273] and, in the case of the nanocast, such hydroxyl groups could also be formed during template removal followed by washing. Investigation of the reducibility of the mixed CuO–NiO oxides can provide evidence of the intimate interactions between the metals in these hybrids, which is critical for the catalytic properties. To do so, H_2 temperature-programmed reduction (H_2-TPR) of single and binary $Cu_{0.5}Ni_{0.5}$ oxides was performed (Figure 6.3 and S6.4, SI). In these experiments, the onset

118

temperature of the reduction process, T_{onset}, can be taken as an indicator that reflects the most reducible metal species present in the catalyst. The TPR profiles of bulk CuO and NiO show T_{onset} at 250 and 270°C, with the prominent reduction peaks centred at 300 and 350°C, for the two oxides, respectively. This suggests that CuO is more readily reduced than NiO. The lower T_{onset} for mixed $Cu_{0.5}Ni_{0.5}$ oxides compared to that of single CuO and NiO oxides corroborates the presence of an intimate interaction between the metals, thus enhancing the reducibility of both Cu and Ni species. Moreover, the temperatures of the onset and completion of the reduction process are approximately 25°C and 85°C lower for the $Cu_{0.5}Ni_{0.5}$-400-NC nanocast sample compared to $Cu_{0.5}Ni_{0.5}$-400, which we attribute essentially to the high surface area and nanocrystalline nature of the former. With an increase of the annealing temperature from 400 to 600°C, both the T_{onset} and the maximum temperature for reduction increase (Figure S6.4), indicative of a lower reducibility of the metal species most likely due to the higher degree of crystallinity and segregation of oxide phases, as also evidenced by XRD.
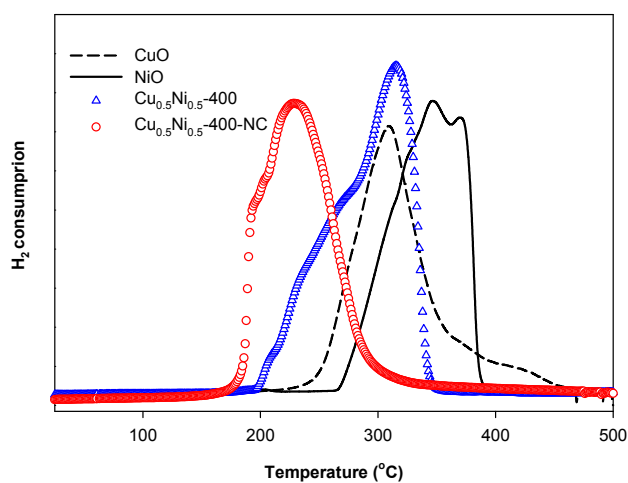
Figure 6.3 H_2-TPR profiles of CuO, NiO and $Cu_{0.5}Ni_{0.5}$ samples.

The above XRD and H_2-TPR results demonstrate that there is a strong synergistic interaction between copper and nickel species existing in the Ni_xCu_yO solid solution which facilitates reduction of both copper and nickel and can therefore have a beneficial influence on the catalytic H_2 evolution from ammonia borane (vide infra).

6.3.3. Catalytic properties in hydrogen evolution from ammonia-borane

6.3.3.1. Effects of composition and structure

The catalytic performance of the catalysts toward hydrolytic dehydrogenation of the AB complex was evaluated on the basis of the amount of H_2 gas released, which is measured volumetrically during reaction using a typical water-filled scaled burette system. The as-synthesized catalysts were tested without any reductive pre-treatment. Figure 6.4 and S6.5 (SI) show plots of H_2 generated against time during catalytic hydrolysis of AB at 25°C over catalysts of different compositions. It can be seen that CuO exhibits some noticeable activity in this reaction, while NiO exhibits almost no catalytic activity towards the hydrolysis of AB within 100 min. Interestingly, the hydrogen release in the presence of binary CuO–NiO oxides is significantly accelerated. Such an improvement of the catalytic activity of binary CuO–NiO oxides in comparison to the individual counterparts corroborates a cooperative/synergetic effect[25] between the Cu and Ni species.
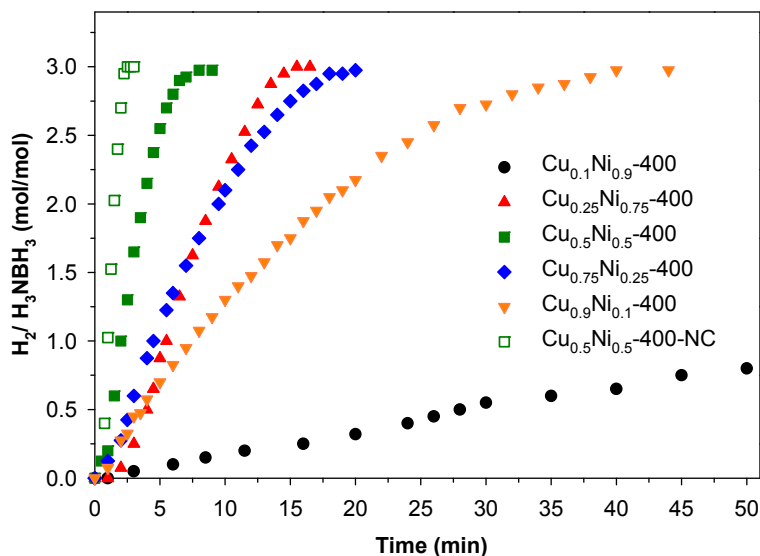
Figure 6.4. Plots of time vs. volume of H_2 generated from the hydrolysis of AB catalyzed by binary CuO–NiO oxides with different compositions. (H_3NBH_3 = 1.48 mmol, catalyst = 10 mg, H_2O = 10 ml, T = 25°C).

Sample $Cu_{0.5}Ni_{0.5}$-400 is the most active catalyst for AB hydrolysis with a completion time of 7 min, whereas it takes almost three to six times as long for either the copper-rich ($Cu_{0.75}Ni_{0.25}$-400, $Cu_{0.9}Ni_{0.1}$-400) or the nickel-rich ($Cu_{0.25}Ni_{0.75}$-400, $Cu_{0.1}Ni_{0.9}$-400) compositions. In an attempt to correlate catalytic activity, composition and structure

parameters, the d-spacing value of the (111) reflection and the hydrogen generation rate were plotted as functions of catalyst composition, as depicted in Figure S6.6. This graph shows a volcano hill-type behavior, indicating a maximum in the normalized production rate and lattice expansion for the sample with a composition of $Cu_{0.5}Ni_{0.5}$. The catalytic activity of $Cu_{0.5}Ni_{0.5}$-500 is almost identical to that of $Cu_{0.5}Ni_{0.5}$-400, however the sample annealed at higher temperature, $Cu_{0.5}Ni_{0.5}$-600, exhibits a dramatically reduced activity with only 75% of the stoichiometric amount of H_2 evolved within 40 min (Figure S6.7). Such a sharp drop in the catalytic activity observed over $Cu_{0.5}Ni_{0.5}$-600 may be due to the degradation of the solid solution phase upon heating at 600ºC, ultimately yielding segregated copper oxide and nickel oxide phases, as judged from the XRD results.

Since $Cu_{0.5}Ni_{0.5}$-400 exhibits the highest hydrolysis activity among all the hybrid systems prepared, the nanocasting method was implemented to synthesize this composition with high specific surface area (sample $Cu_{0.5}Ni_{0.5}$-400-NC). Impressively, with such high surface area (73 $m^2\ g^{-1}$) and the optimum $Cu_{0.5}Ni_{0.5}$-400-NC composition, the hydrolysis of AB is completed within only 2 min. The TOF value achieved is 3600 h^{-1} (mol of H_2 per mol of Cu per hour) for $Cu_{0.5}Ni_{0.5}$-400-NC, while it is 1080 h^{-1} for $Cu_{0.5}Ni_{0.5}$-400. This value is among the highest values reported thus far in the hydrolysis of AB using Cu-based catalysts, as well as other non-noble metal-based systems (see Table S6.3).[43,46,47,258-264] Furthermore, an induction time as short as 30 s was observed for both materials obtained by thermal decomposition ($Cu_{0.5}Ni_{0.5}$-400) and nanocasting ($Cu_{0.5}Ni_{0.5}$-400-NC) in the first catalytic cycle at a reaction temperature of 25ºC, which is much faster than the best copper-based catalyst ever reported,[259-262,264] thus reflecting fast activation of the catalyst. In AB hydrolysis, the formation of an activated complex is usually postulated through the interaction of an AB molecule with the surface of the solid catalyst, which then dissociates upon attack of a water molecule, releasing hydrogen.[257] In our case, we may speculate that the greater activity of the $Cu_{0.5}Ni_{0.5}$ systems could originate from the presence of copper surface sites in the copper–nickel solid solution which favor formation of the activated complex with AB more readily than other Cu species reported previously. Considering the poor catalytic performance of individual components, where NiO is inactive and CuO exhibits low activity towards catalytic hydrolysis of AB, a synergetic interaction between copper and nickel in solid solution seems to be the key towards a significant enhancement

of catalytic activity for AB hydrolysis. It is thus plausible that occurrence of intermetallic electronic interactions in the distorted cubic rock-salt structure of the copper–nickel solid solution induces modification of the catalyst surface, and consequently, significantly tunes the reducibility of the catalyst as well as the interaction between the catalyst surface and AB, accounting for the high activity of copper–nickel catalysts.

6.3.3.2. Effects of precursor and synthesis conditions

For comparison purpose, a catalyst was also prepared by post-impregnation of Cu nitrate (precursor to CuO) on pre-formed NiO followed by thermal decomposition of the nitrate at 400ºC (material designated as $Cu_{0.5}Ni_{0.5}$-400-IM). The XRD pattern (Figure S6.8) of this $Cu_{0.5}Ni_{0.5}$-400-IM sample exhibits separated major phases of CuO and NiO oxides, suggesting that post-impregnation is less effective to yield a CuNi solid solution. The TPR profile of $Cu_{0.5}Ni_{0.5}$-400-IM (Figure S6.4) displays two clearly separated steps corresponding to the reduction of CuO and NiO respectively. This is in line with lower interactions between the metals in this preparation. Consequently, this post-impregnated $Cu_{0.5}Ni_{0.5}$-400-IM, consisting of almost separated oxide phases, shows much lower activity than the one-pot $Cu_{0.5}Ni_{0.5}$-400 preparation, as it required 40 min to reach 70% of the theoretical maximum amount of H_2 (see Figure S6.9, SI). In addition, another catalyst prepared this time using copper chloride instead of copper nitrate as the precursor under otherwise same synthesis conditions, also showing evidence of more separated oxide phases, similarly presents much lower activity (Figure S6.10a, b, SI). These complementary results support the necessity of the presence of a distorted cubic solid solution Cu_xNi_yO to achieve high catalytic reactivity. Evidently, synthesis conditions, composition, as well as nature of precursors have pronounced effects on the interaction between copper and nickel species in the catalysts, which is strongly correlated with their reducibility and, hence, their catalytic activity.

6.3.3.3. Phase analyses of used catalysts

The phase and surface composition of the CuO–NiO hybrids after AB hydrolysis were examined by XRD and XPS. The XRD patterns (Figure S6.11, SI) of the spent catalysts reveal the presence of two major phases of NiO and Cu, and traces of Cu_2O, in line with the reduction of copper cations during the reaction. In the XPS spectra of the used catalysts

122

(Figure 6.5 and S6.12, SI), intense signals of Cu 2p are observed at low binding energies of around 932 and 952 eV with much lower intensities of the satellite peaks. These characteristics have typically been documented for reduced copper species of Cu(I) and Cu(0).[195,260,261,265] The Ni $2p_{3/2}$ peak of the used catalysts appears at a higher binding energy of 855.8 eV, characteristic of the Ni–OH bond, and may thus be attributed to higher concentrations of –OH species on the surface of the catalyst after a prolonged period in an aqueous reaction medium. The increase of surface hydroxyl species was also confirmed by a shift of the O 1s peak from ~529 eV for the fresh catalyst to a higher binding energy of ~531 eV for the used catalyst. Strong satellite peaks at 860.9 and 880.2 eV are also observed, indicative of the presence of Ni(II).[272,273] Note that copper at low valance states was found to be active phases for AB hydrolysis.[258-262,264] In our case also, copper cations in the CuO–NiO material were reduced to form Cu(I) or Cu(0), which then act as active sites for AB hydrolysis. In contrast, NiO is considered almost inactive and acts as a support stabilizing and participating in the reduction process of copper via formation of the copper–nickel solid solution.
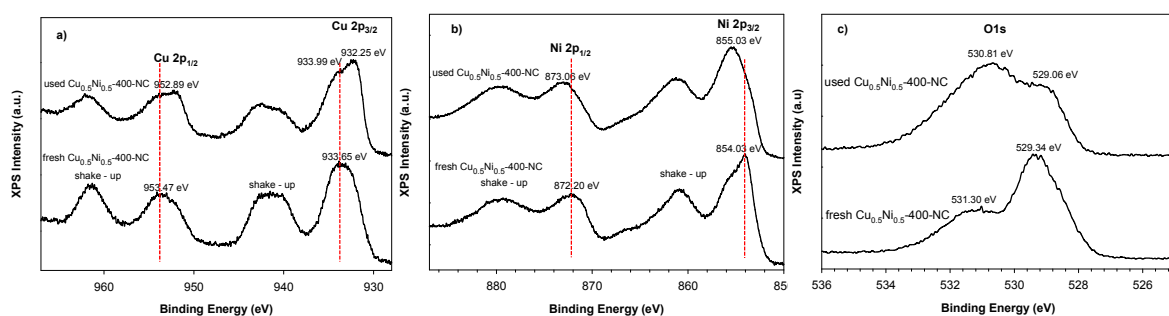
Figure 6.5. (a–c) XPS spectra of the fresh and used nanocast catalysts (the spectra are normalized by their peak intensity and energy corrected for adventitious carbon at 284.6 eV).

6.3.3.4. Kinetic studies

Finally, AB hydrolysis kinetics were evaluated over the Cu$_{0.5}$Ni$_{0.5}$-400-NC and Cu$_{0.5}$Ni$_{0.5}$-400 catalysts by varying substrate and catalyst concentrations, and temperature (Figure 6.6, S6.13 and S6.14, SI). Hydrolysis catalyzed by binary CuO–NiO hybrids was found to follow a first order with respect to the catalyst concentration (the line slope is of 1.03) and it is essentially independent of the AB concentration with a line slope of 0.1. From these data, the apparent activation energies for hydrolytic dehydrogenation were estimated to be

39 and 42 kJ mol^{-1} for Cu$_{0.5}$Ni$_{0.5}$-400-NC and Cu$_{0.5}$Ni$_{0.5}$-400, respectively, which are the lowest reported thus far for the hydrolysis of AB using copper-based catalysts, and compare well to the values reported for other catalytic systems.[32,43,47,262,264] The similar apparent activation energy over Cu$_{0.5}$Ni$_{0.5}$-400-NC and Cu$_{0.5}$Ni$_{0.5}$-400 implies that the higher reaction rate of the former resulted essentially from its greater population of active sites. In addition, note that, ammonia, an undesirable byproduct, was not detected in the gas generated during the reaction.
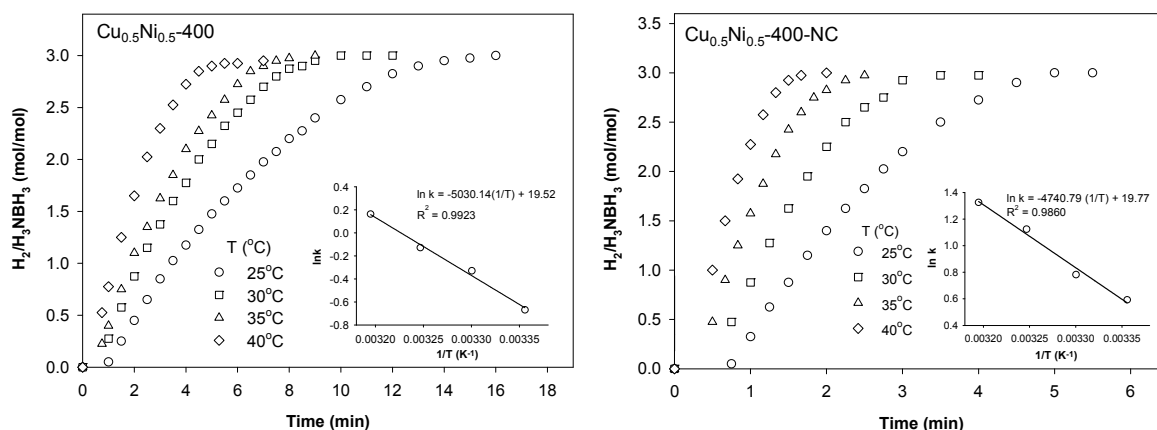
Figure 6.6. Plots of the volume of generated H$_2$vs. time over Cu$_{0.5}$Ni$_{0.5}$-400 and Cu$_{0.5}$Ni$_{0.5}$-400-NC catalysts at different temperatures ([Cu] = 3.2 mM, [AB] = 1.48 mM). (Inset: Arrhenius plot).

A reusability test shows that the Cu$_{0.5}$Ni$_{0.5}$ catalysts still exhibit high activity after 6 cycles of reaction (Figure S6.15, SI). The small activity loss may be due to an increase in the concentration of metaborate and, consequently, the viscosity of the solution during the AB hydrolysis.

6.4. Conclusions

In summary, we have presented the facile synthesis of high-performance and low-cost catalysts for hydrogen evolution from AB hydrolysis under ambient conditions. The catalysts consist of binary copper–nickel oxides where synergetic interactions are revealed under the form of a solid solution (Cu$_x$Ni$_y$O). The resultant Cu$_{0.5}$Ni$_{0.5}$ hybrid exhibits the highest catalytic activity among all of Cu-based catalysts for AB hydrolysis, with satisfying stability probed over 6 cycles. Although further improvement of the stability of the high surface area equivalent is needed, the present finding demonstrates that combinations of

non-noble metals can provide viable solutions for the development of practical catalysts, first for H_2 generation from AB hydrolysis, but possibly also for other reactions. In an effort to improve the stability of the catalysts and further study the catalytic performance of these bimetallic CuNi systems for hydrogen storage application, series of mixed metal CuNi catalysts supported either on mesoporous carbon or silica nanospheres have been investigated in AB hydrolysis and selective decomposition of hydrous hydrazine. The results will be presented in the next chapter.

6.5. Supporting information
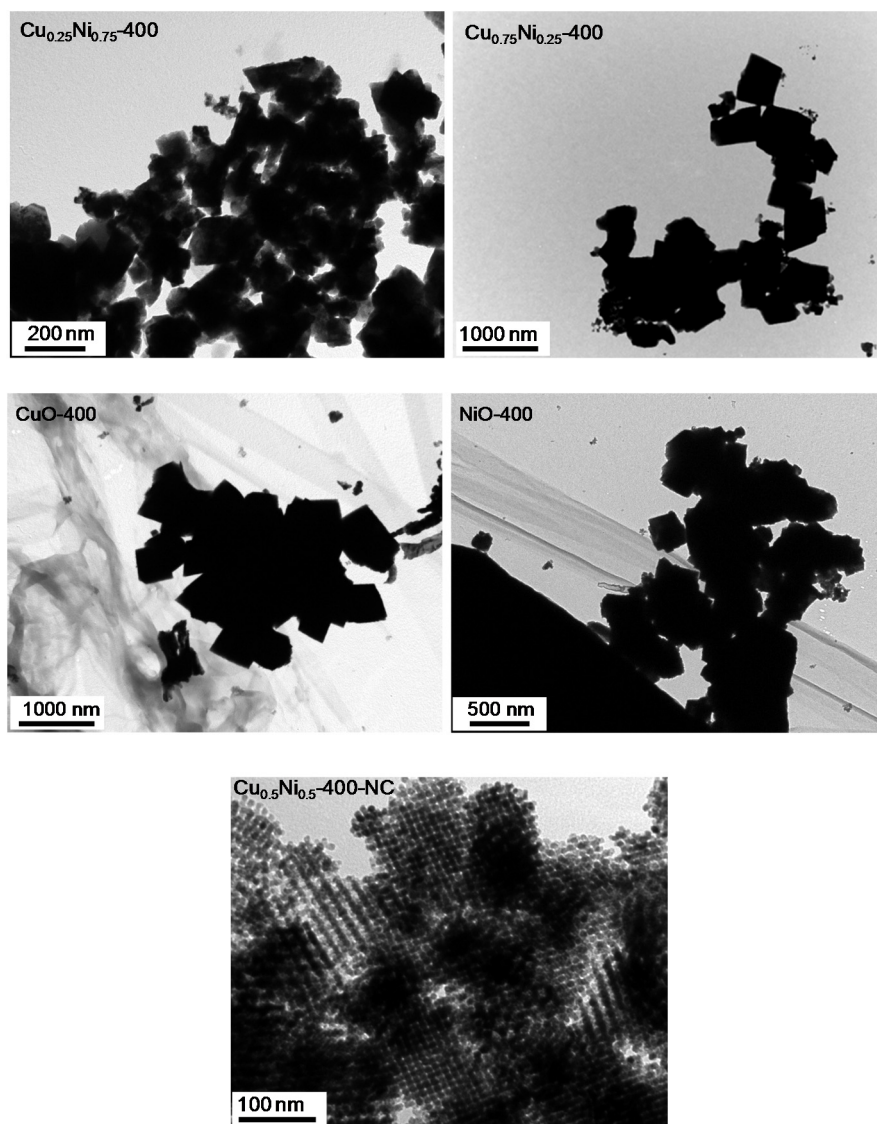
Figure S6.1. Representative TEM images of the samples of different compositions (as indicated) prepared by thermal decomposition of metal nitrate precursors and the nanocasting approach.
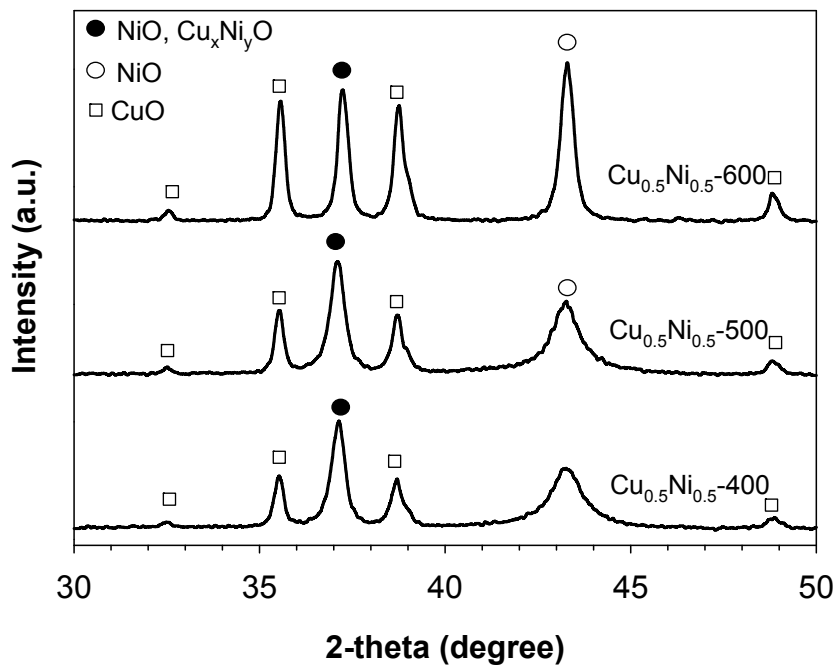
Figure S6.2. Wide-angle powder XRD patterns of mixed metal oxides prepared at different temperatures (as indicated) (Bruker SMART APEXII X-ray diffractometer with a Cu K_α radiation).
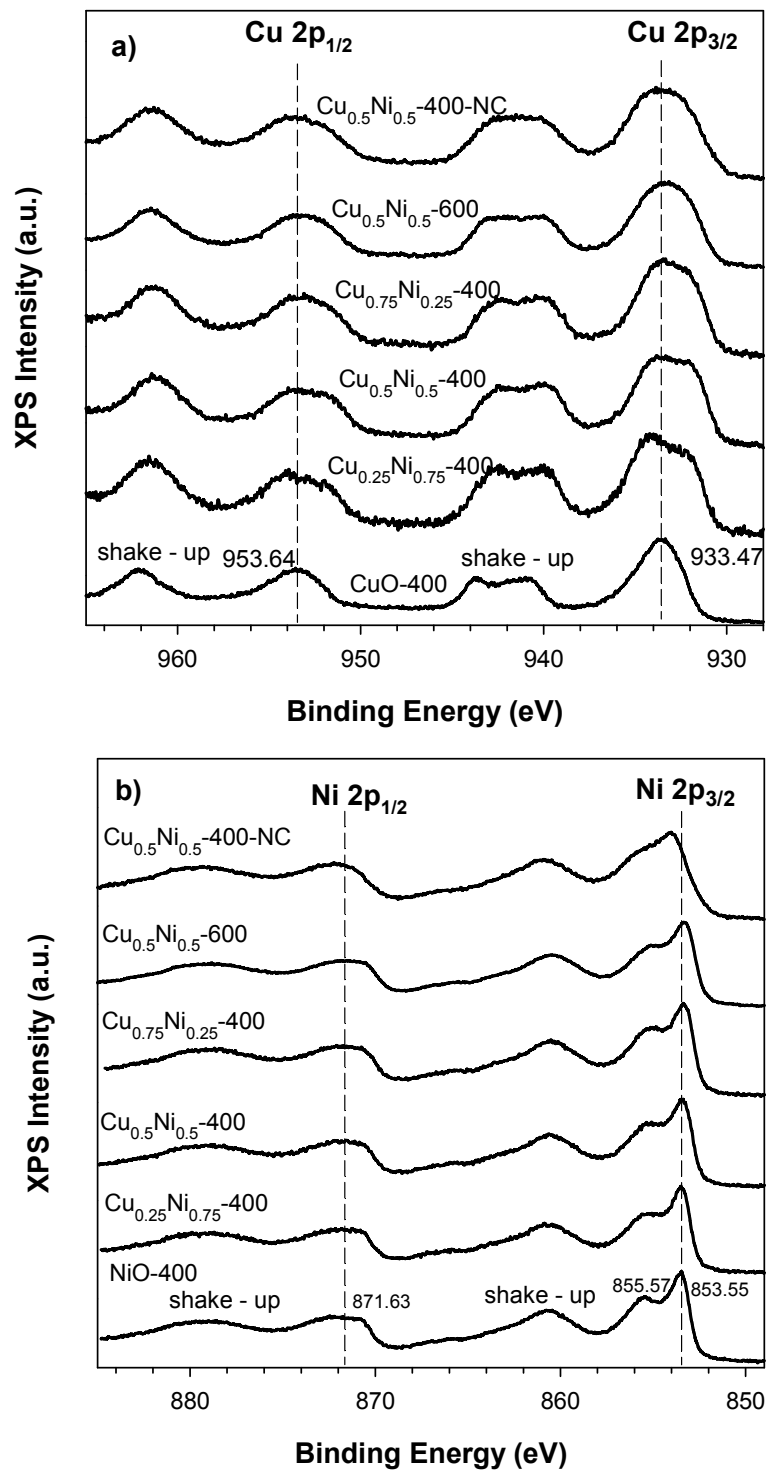
Figure S6.3. (a-b) XPS spectra of the prepared catalysts (the spectra are normalized by their peak intensity and energy corrected for adventitious carbon at 284.6 eV).
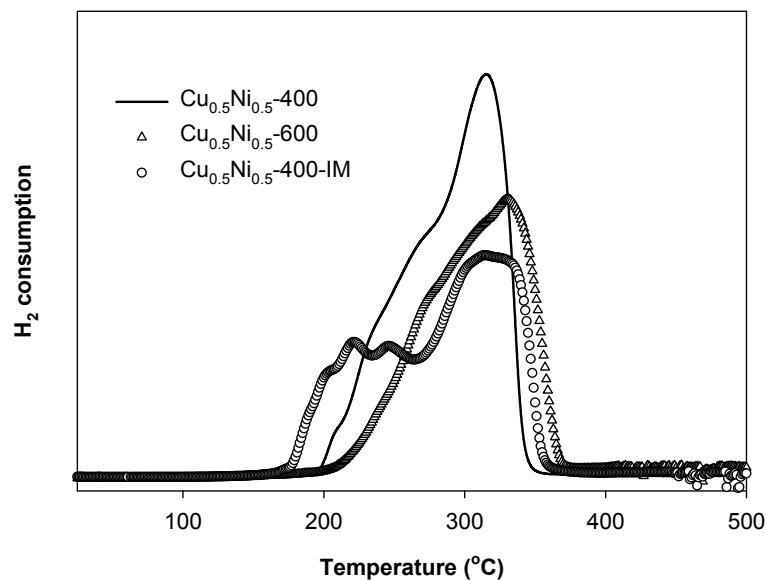
Figure S6.4 H_2-TPR profiles of the samples prepared by one-step thermal treatment at 400 and $600^{\circ}C$ and by post impregnation of copper nitrate on pre-formed NiO (as indicated).
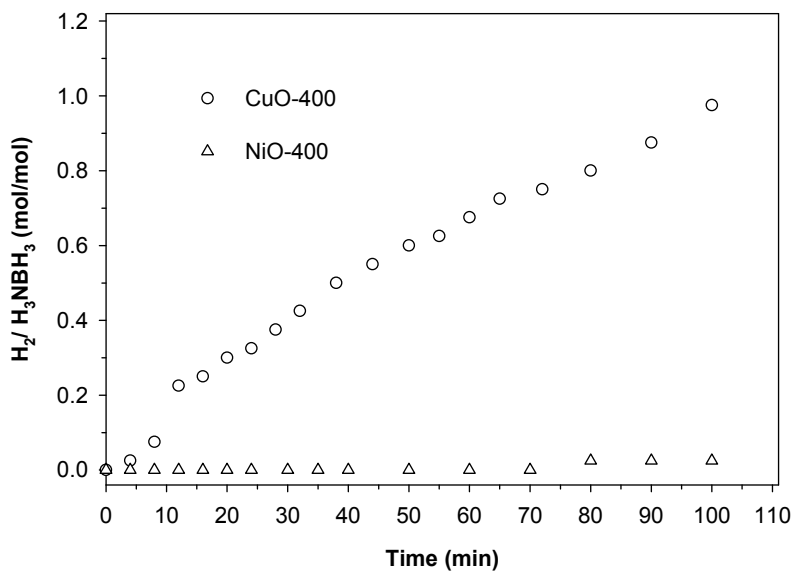
Figure S6.5. Time versus volume of hydrogen generated from the hydrolysis of AB catalyzed by single oxides CuO and NiO (H_3NBH_3 = 1.48 mmol, catalyst = 10 mg, H_2O = 10 ml, T = $25^{\circ}C$).
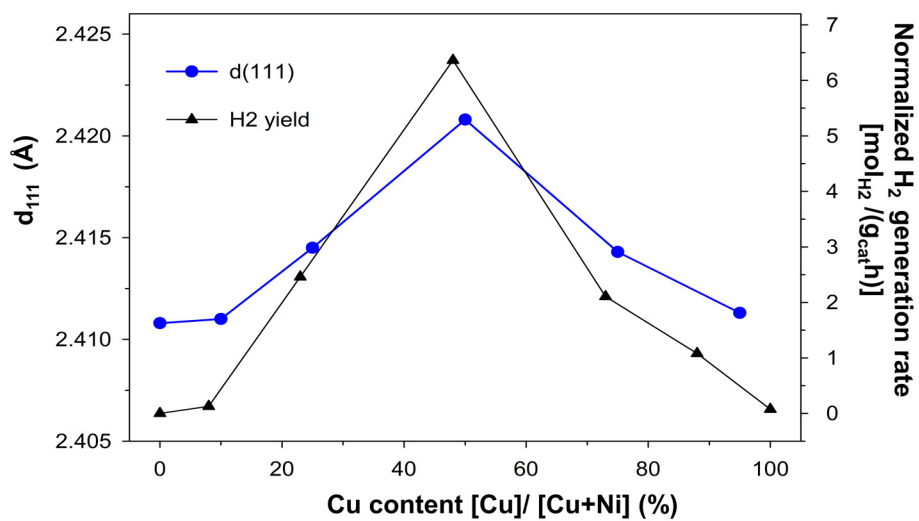
Figure S6.6. Lattice spacing d corresponding to (111) planes and reaction rates at half conversion as functions of composition.
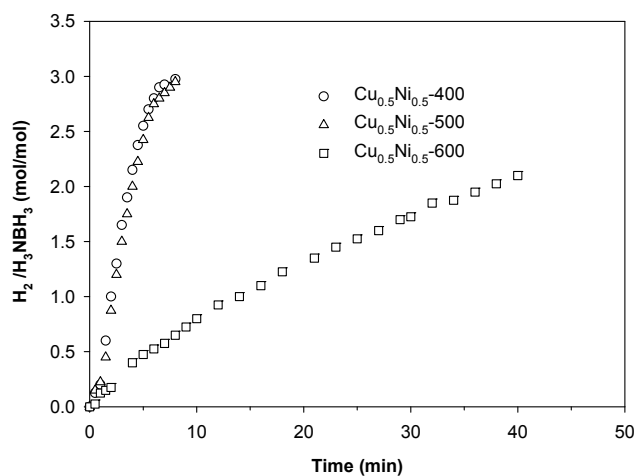
Figure S6.7. Time versus volume of hydrogen generated from the hydrolysis of AB catalyzed by binary CuO-NiO oxides prepared at different thermal treatment temperatures (H_3NBH_3 = 1.48 mmol, catalyst = 10 mg, H_2O = 10 ml, T = 25°C).

130
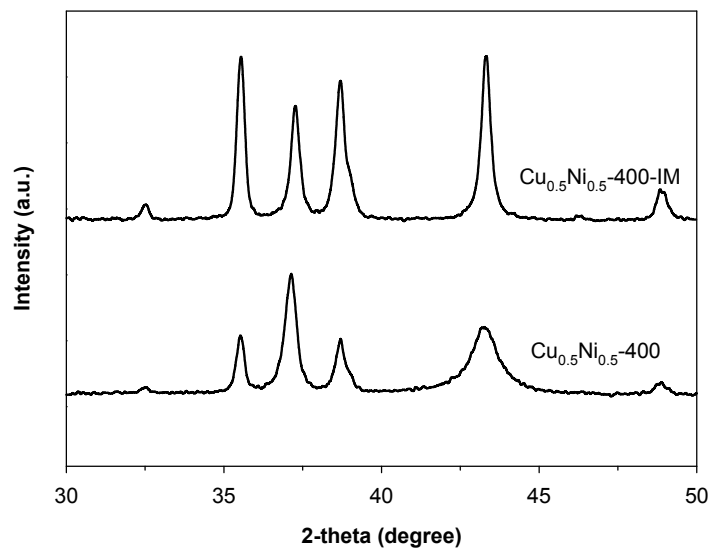
Figure S6.8. XRD patterns of the samples obtained by one-step thermal treatment and post-impregnation (as indicated).
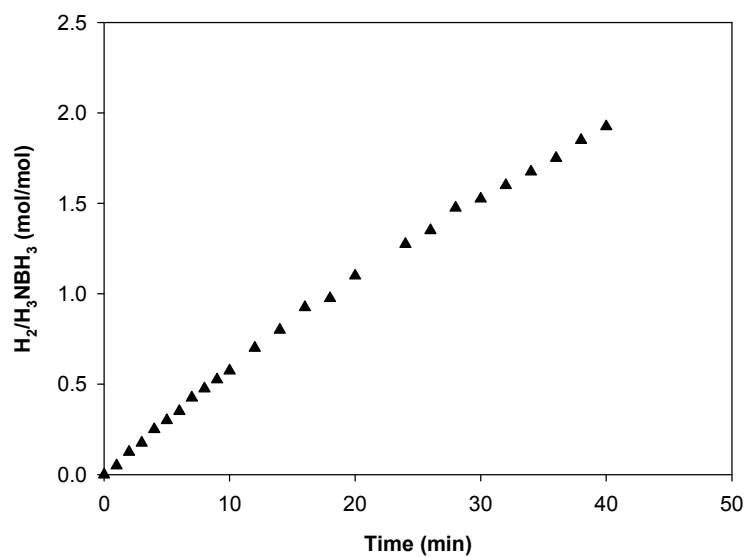
Figure S6.9. Time versus volume of hydrogen generated from the hydrolysis of AB catalyzed by $Cu_{0.5}Ni_{0.5}$-400-IM sample (H_3NBH_3 = 1.48 mmol, catalyst = 10 mg, H_2O = 10 ml, T = 25°C).
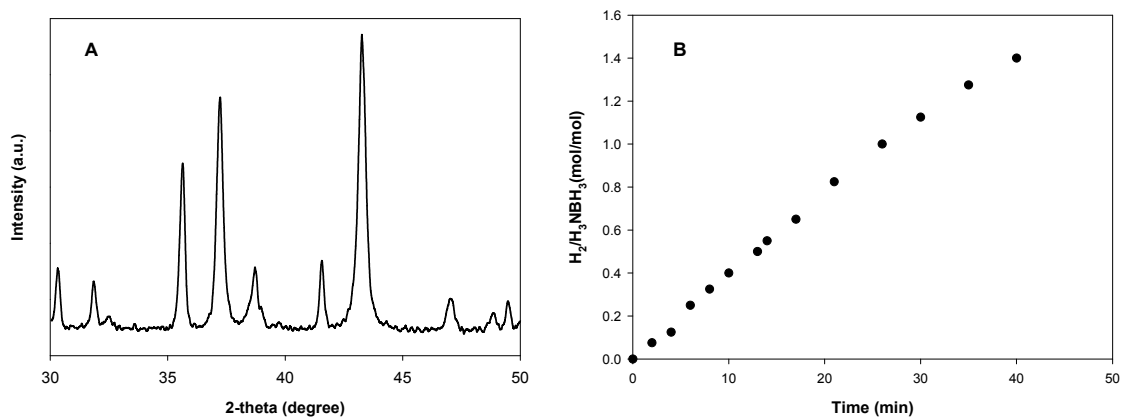
Figure S6.10. (A) XRD pattern and (B) Time versus volume of hydrogen generated from hydrolysis of AB catalyzed by binary CuO-NiO oxides sample prepared using copper chloride precursor (H_3NBH_3 = 1.48 mmol, catalyst = 10 mg, H_2O = 10 ml, T = 25°C).
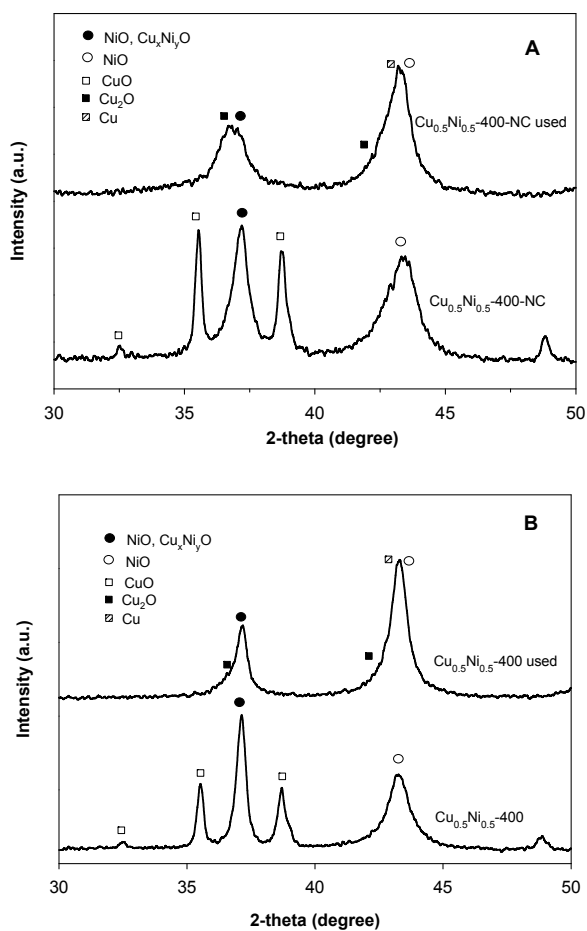
Figure S6.11. Wide angle XRD patterns of the fresh and spent catalysts: (A) nanocast material, (B) material by thermal decomposition of nitrate salts.
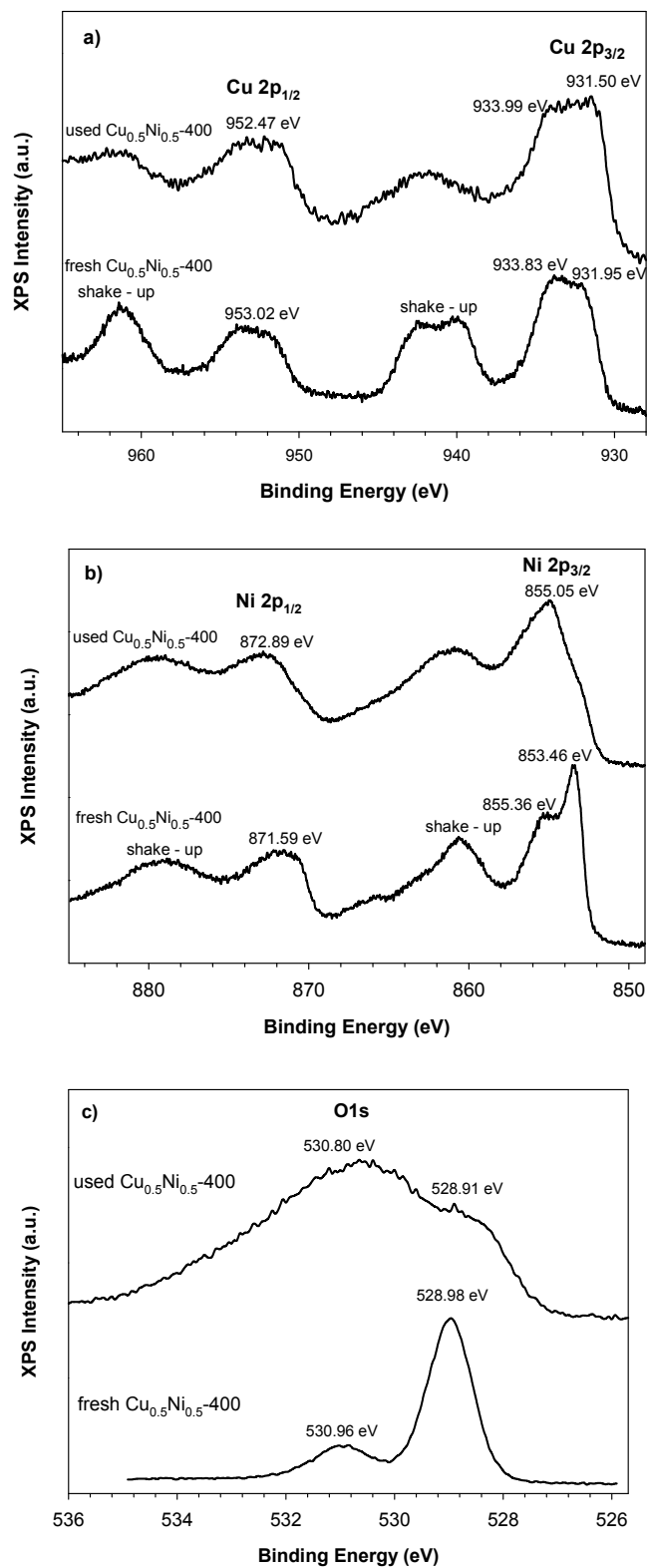
Figure S6.12a-c XPS spectra of the fresh and used catalysts prepared via thermal decomposition (the spectra are normalized by their peak intensity and energy corrected for adventitious carbon at 284.6 eV).
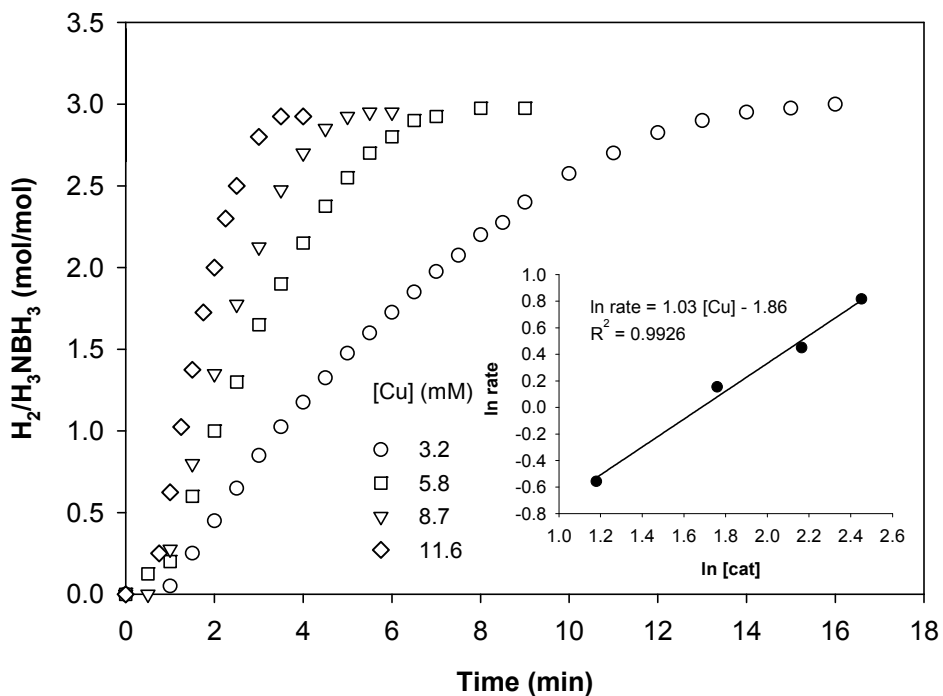
Figure S6.13. Plot of time versus volume of hydrogen generated using $Cu_{0.5}Ni_{0.5}$-400 at different catalyst concentrations ([AB] = 1.48 mmol, T = 25°C). (Inset: ln [Cu] *vs* ln rate plot).
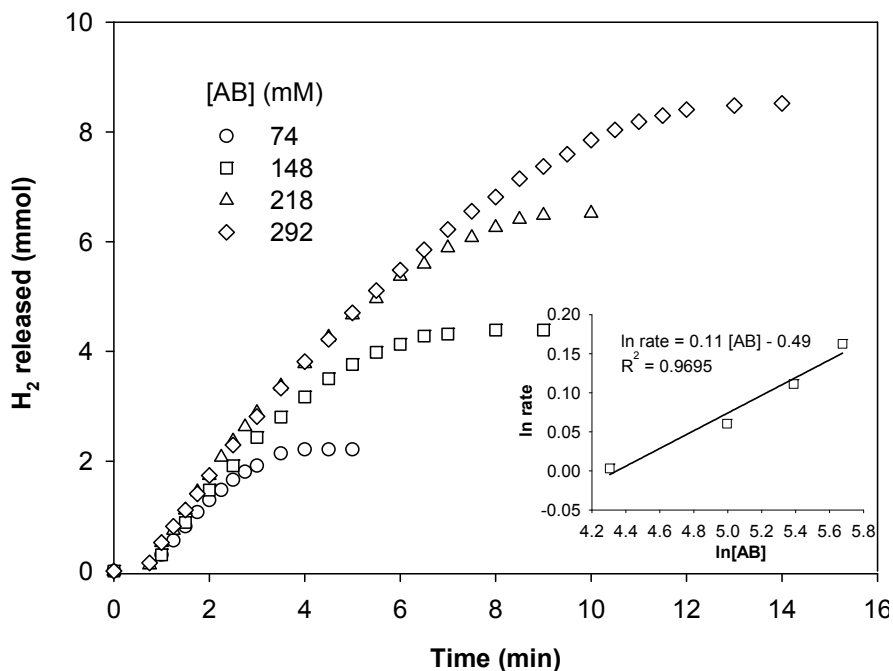
Figure S6.14. The plot of time versus volume of hydrogen generated from the hydrolysis of AB catalyzed by $Cu_{0.5}Ni_{0.5}$-400 at different AB concentrations ([Cu] = 5.8 mmol, T = 25°C). (Inset: ln[AB] *vs* ln rate plot).

134
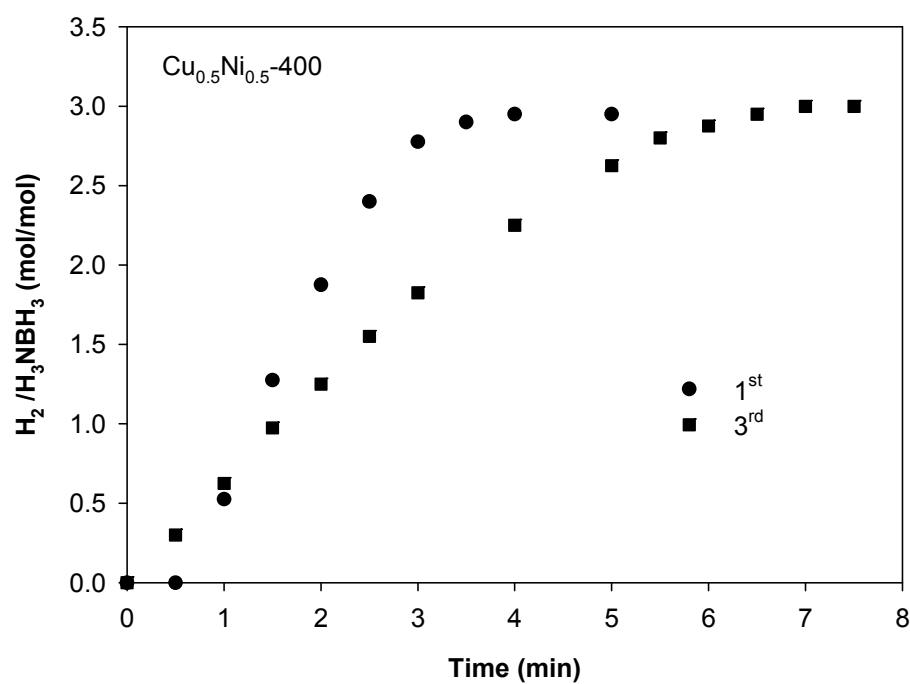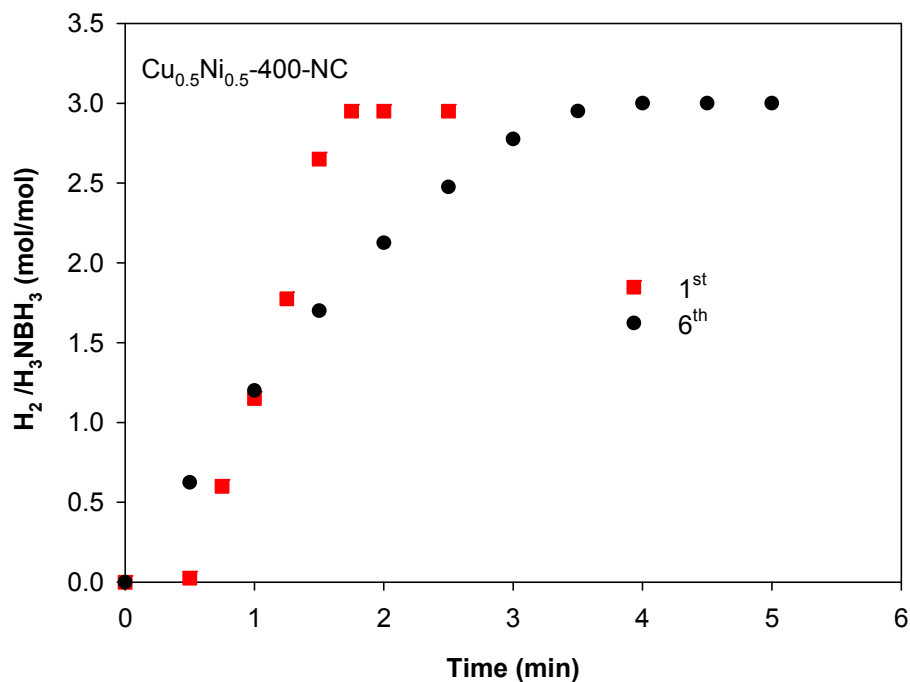
Figure S6.15. Time versus volume of hydrogen generated from the hydrolysis of AB catalyzed by $Cu_{0.5}Ni_{0.5}$-400-NC and $Cu_{0.5}Ni_{0.5}$-400 over several cycles for reusability test. ([Cu] = 11.6 mmol, [AB] = 1.48 mmol, T = 25°C).

Table S6.1. Textural and structural parameters of the prepared samples derived from nitrogen physisorption measurements at -196°C and X-ray diffraction

Samples	S_{BET} [a] (m^2g^{-1})	d spacing of NiO (111) plane[b]
$Cu_{0.1}Ni_{0.9}$-400	12	2.4119
$Cu_{0.25}Ni_{0.75}$-400	11	2.4145
$Cu_{0.5}Ni_{0.5}$-400	10	2.4208
$Cu_{0.75}Ni_{0.25}$-400	3	2.4143
$Cu_{0.9}Ni_{0.1}$-400	3	2.4113
$Cu_{0.5}Ni_{0.5}$-500	8	2.4233
$Cu_{0.5}Ni_{0.5}$-600	7	2.4145
$Cu_{0.5}Ni_{0.5}$-400-IM	12	2.4120
$Cu_{0.5}Ni_{0.5}$-400-NC	73	2.4162
CuO-400	3	-
NiO-400	28	2.4108

[a] S_{BET}, apparent BET specific surface area deduced from the adsorption isotherm analysis in the relative pressure range from 0.05 to 0.20; [b]Obtained from XRD

Table S6.2. Nominal and actual molar ratio of Cu/Ni of the prepared composite oxides

Samples	Cu/Ni nominal ratio	Cu/Ni actual ratio in the bulk	Cu/Ni surface ratio
$Cu_{0.25}Ni_{0.75}$-400	0.33	0.30	0.21
$Cu_{0.5}Ni_{0.5}$-400	1.00	0.89	0.23
$Cu_{0.75}Ni_{0.25}$-400	3.00	2.56	0.21
$Cu_{0.5}Ni_{0.5}$-400-NC*	1.00	0.85	0.55
$Cu_{0.5}Ni_{0.5}$-600	1.00	0.87	0.57

*The Si content determined by XPS is about 2.78 at% in the nanocast $Cu_{0.5}Ni_{0.5}$-400-NC sample.

Table S6.3. Activity performances of various transition-metal-based catalysts for ammonia-borane hydrolysis

Catalyst	TOF (mol$_{H2}$(mol$_{metal}$)$^{-1}$h^{-1})	Reaction completion time at 25°C (min)	Reference
Pt/ C	4998	1.5	274
Au@Co core-shell NPs	816	10	275
AuNi@MIL-101	3972	2.5	36
Fe NPs	280	7	276
Ni NPs	528	7	277
Ni/ C	1842	6	43
Ni/ Al$_2$O$_3$	135	50	278
Cu/ zeolite	47	120	279
Cu NPs@SiO$_2$-CuFe$_2$O$_4$	2400	50	262
Bulky Cu/ NiO	1080	8	This work
Mesoporous Cu/ NiO	3600	2	This work

Acknowledgements

Chapter 7:

On the role of Metal-Support Interactions, Particle size, and Metal-Metal Synergy in CuNi Nanocatalysts for H$_2$ Generation

Hoang Yen[a], Yongbeom Seo[b], Serge Kaliaguine[c] and Freddy Kleitz[a]

[a]Department of Chemistry and Centre de Recherche sur les Matériaux Avancés (CERMA), Université Laval, Quebec GIV 0A6, Canada.

[b]Center for Functional Nanomaterials, Department of Chemistry and Graduate School of Nanoscience & Technology (WCU), KAIST, Daejeon, Korea

[c]Department of Chemical Engineering, Université Laval, Canada

Résumé

Des nanocatalyseurs bimétalliques performants à base de métaux non nobles sont très recherchés pour le développement de nouveaux matériaux pour le stockage d'énergie. Dans ce travail, une méthode simple pour la synthèse de catalyseurs de Cu-Ni dispersés sur des nanosphères de carbone ou de silice mésoporeuse est décrite à partir de précurseurs de nitrates métalliques peu coûteux. Les nanocatalyseurs mésoporeux de $Cu_{0.5}Ni_{0.5}$ supportés sur du carbone mésoporeux présentent une excellente performance catalytique pour l'hydrolyse du borazane (AB) et la décomposition de l'hydrazine aqueuse avec une sélectivité en hydrogène de 100%, en solution aqueuse alcaline à 60°C. La composition chimique et la taille des particules métalliques, ayant une influence majeure sur les propriétés catalytiques des matériaux bimétalliques CuNi supportés, peuvent être facilement contrôlées en réglant la charge de métal et le rapport de précurseurs métalliques. Une fréquence de cycle catalytique (TOF) extrêmement élevée de 3288 ($mol_{H2}mol_{metal}^{-1}h^{-1}$) a été obtenue et la réaction de déshydrogénation de AB est complète en 1 min dans le cas d'un catalyseur développé par contrôle précis de la taille des particules du métal, de la composition, et des propriétés du support.

Abstract

Efficient bimetallic nanocatalysts based on non-noble metals are highly desired for the development of new energy storage materials. In this work, we report a simple method for the synthesis of highly dispersed CuNi catalysts supported on mesoporous carbon or silica nanospheres using low cost metal nitrate precursors. The mesoporous carbon-supported $Cu_{0.5}Ni_{0.5}$ nanocatalysts exhibit excellent catalytic performance for the hydrolysis of ammonia borane and decomposition of hydrous hydrazine with 100% hydrogen selectivity in aqueous alkaline solution at 60ºC. The chemical composition and size of the metal particles, which have a significant influence on the catalytic properties of the bimetallic CuNi supported materials, can be readily controlled by adjusting the metal loading and ratio of metal precursors. An exceedingly high turnover frequency of 3288 ($mol_{H2}mol_{metal}^{-1}h^{-1}$) and complete reaction within 1 min in dehydrogenation of ammonia-borane were achieved over a tailored-made catalyst obtained through precise monitoring of metal particle size, composition and support properties.

7.1 Introduction

Bimetallic nanomaterials have attracted extensive theoretical and practical interest.[22,89,91,280-282] Catalytic properties of bimetallic nanomaterials often differ significantly from the constituent elements because of the modification of the surface geometric and electronic structures.[59,96,98,282-284] In addition to intrinsic changes in the bimetallic nanocatalysts brought about by composition and geometric features (e.g., particle size and shape), an electronic perturbation of the catalytic sites due to electronic metal-support interactions also has a strong influence on the inherent reactivity.[16,103-110,285-288] Therefore, the use of supported bimetallic nanomaterials is an interesting and important strategy for developing new catalysts with enhanced activity and selectivity. Because catalysis occurs on the surface, there are economic and fundamental incentives to produce catalysts in the form of highly dispersed supported metal nanoparticles. This could be achieved through the choice of a suitable support, the selection of proper metal precursors and the preparation method.[102,289-291]

On the other hand, the safe and efficient storage of hydrogen is recognized as one of the major technological barriers preventing the widespread hydrogen on-board application.[7,8,254] Catalyst-assisted hydrogen generation by decomposition of hydrogen storage molecules is one of the most studied and desired approaches towards a hydrogen-powered society.[9,12,292] Among the potential candidates for effective chemical hydrogen storage, ammonia borane (AB; NH_3BH_3) and hydrous hydrazine ($N_2H_4.H_2O$) with high hydrogen contents have been shown to be promising hydrogen carriers for storage and transportation.[256-265,274-279,293-298] Binary metallic nanocatalysts based on the combination of noble and non-noble metals have been widely investigated for hydrogen release from both AB and hydrazine.[32-36,41,42,256,275] Although noble metal-based catalysts have been shown to be effective in these reactions, the high cost hinders their widespread application, so that there is considerable current efforts devoted to explore efficient alternatives based on non-noble metals.[41,261,293,294] For example, bimetallic Ni-Fe, Cu-Co, Ni-Co nanoparticles were reported to be active catalysts for these reactions.[41,259,261,265,293] Nevertheless, the use of colloidal nanoparticles will raise problems of handling, stability and separation. Therefore, in the perspective of practical applications, supported metallic catalysts are preferred to avoid such problems.

Bimetallic CuNi nanocatalysts are of interest in heterogeneous catalysis for several important reactions such as methanol synthesis, water-gas shift, and steam reforming.[299-304] However, to the best of our knowledge, exploration of supported CuNi nanocatalysts in hydrogen generation from AB and hydrazine in solution has not been investigated. Herein, highly active, selective and robust catalysts composed of CuNi particles supported on mesoporous carbon or silica nanospheres for hydrogen generation both from AB hydrolysis and hydrous hydrazine decomposition have now been revealed. The selected supports with mesoporous structure and spherical morphology at the nano-scale could provide high surface area for high dispersion of the catalyst nanoparticles, as well as efficient transport of the reaction agents. Among the supported CuNi catalysts tested for AB hydrolysis reaction, mesoporous carbon supported $Cu_{0.5}Ni_{0.5}$ catalyst exhibits the highest catalytic activity with a TOF up to 3288 ($mol_{H2}mol_{metal}^{-1}min^{-1}$). Interestingly, supported $Cu_{0.5}Ni_{0.5}$ nanocatalyts show 100% conversion of $N_2H_4.H_2O$ with 100% to H_2 selectivity at 60°C. To gain more insight into this catalytic system, the influences of support structure, compositions, as well as the size of the metal particles, on the resulting catalyst reactivity were also substantiated.

7.2 Results and discussion

7.2.1 Texture, crystalline phases and surface properties

Evenly distributed CuNi nanoparticles supported on mesoporous carbon nanospheres (MCNS) with varying compositions and metal loading of 20 wt% were prepared using inexpensive nitrate metal precursors by simple incipient wetness method (see SI). Transmission electron microscopy (TEM) and scanning TEM high angle annular dark field (HAADF-STEM) images (Figure 7.1a,b and S7.1) clearly reveal spherical mesoporous carbon particles (around 400-500 nm in size) with well-dispersed metal nanoparticles. From the TEM observations, the average particle size for the supported Ni and CuNi nanoparticles was mainly ranging from 5 to 10 nm, while a slightly larger particle size (13 nm) was observed for the supported Cu nanoparticles. It can be observed that the combination of Cu and Ni has a positive promoting effect on metal dispersion. The elemental analysis by energy dispersive spectroscopy (EDS) phase mappings (Figure 7.1c) demonstrates the uniform dispersion of Cu/Ni elements over the support. The

compositional line profiles of Cu and Ni along the line that is indicated in the HAADF-STEM images (Figure 7.1d and S7.1b,e) of CuNi/ MCNS of different Cu/Ni ratios suggest that Cu and Ni are distributed essentially in solid solution. This feature agrees well with XRD results and the signal intensities are consistent with the nominal compositions.
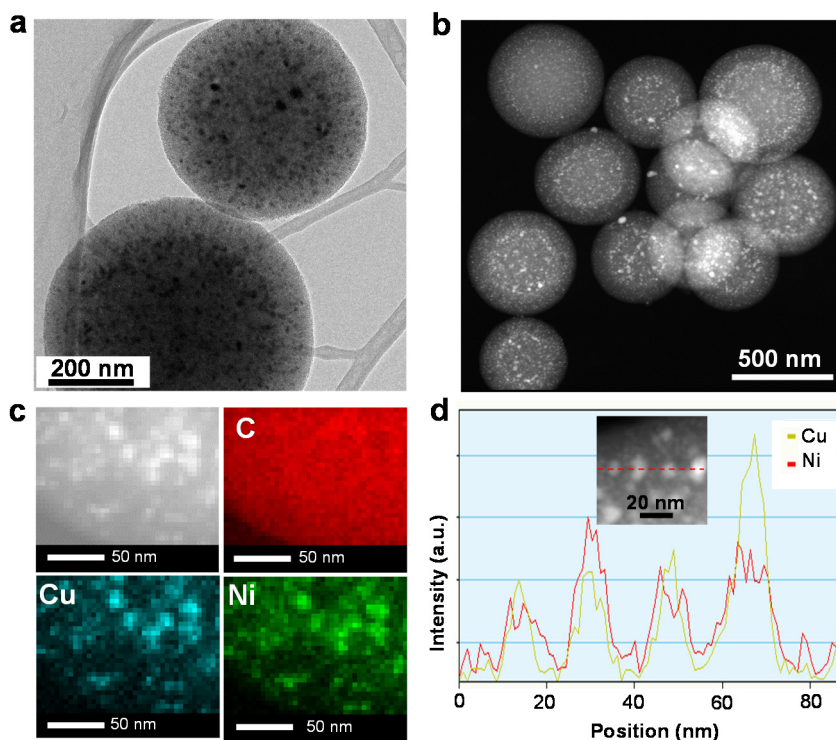
Figure 7.1. (a) TEM image, (b) Scanning TEM high angle annu-lar dark field (STEM-HAADF) image and (c) the corresponding energy dispersive spectroscopy (EDS) phase mapping with (d) line-scanning profiles across the metal particles as indicated in the inset of $Cu_{0.5}Ni_{0.5}$/MCNS catalyst.

Porosity of the prepared catalysts was confirmed by N_2 adsorption–desorption measurements. All of the samples show type IV isotherms characteristic of mesostructured materials with narrow pore size distributions centered around 3nm (Figure S7.2). Textural parameters of the prepared catalysts are given in Table S7.1. Specific BET surface area, pore size, and pore volume of the CuNi/ MCNS are quite comparable. Powder X-ray diffraction patterns (Figure 7.2) for CuNi/MCNS of different compositions are typical for fcc structures and the peaks can be assigned to (111) and (200) planes. In the case of Cu/MCNS, one minor characteristic peak of Cu_2O at 36.4º is observed. The broad and

147

asymmetric peaks at 2θ=42-46º and 48-52º of the XRD patterns of bimetallic CuNi/ MCNS can be resolved into two peaks corresponding to a Cu phase and a CuNi alloy phase.
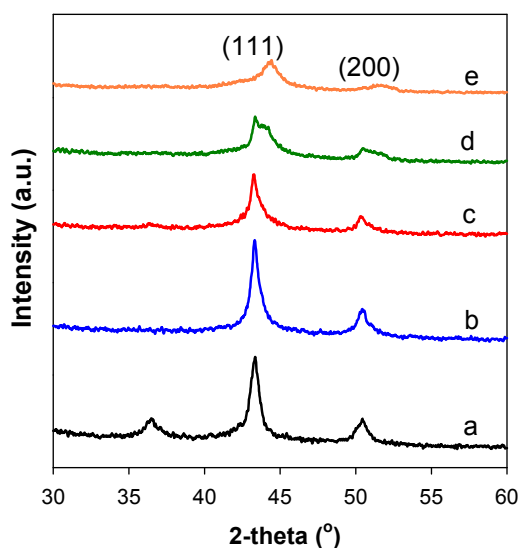
Figure 7.2. XRD patterns of catalysts with various compositions: (a) Cu/MCNS, (b) $Cu_{0.75}Ni_{0.25}$/MCNS, (c) $Cu_{0.5}Ni_{0.5}$/MCNS, (d) $Cu_{0.25}Ni_{0.75}$/MCNS, (e) Ni/MCNS.

The chemical states of active metals in the near-surface region were obtained from XPS analyses. The XPS spectra of Cu 2p exhibit the peaks mainly associated with metallic Cu^0 and Cu^+ with binding energy of Cu $2p_{3/2}$ and Cu $2p_{1/2}$ at 932.3 eV and 952.2 eV, respectively (Figure 7.3).
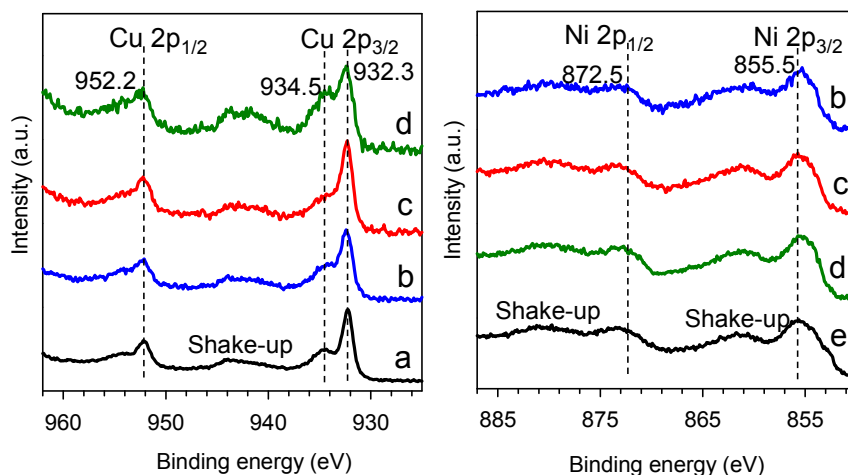
Figure 7.3. XPS spectra of catalysts with various compositions: (a) Cu/MCNS, (b) $Cu_{0.75}Ni_{0.25}$/MCNS, (c) $Cu_{0.5}Ni_{0.5}$/MCNS, (d) $Cu_{0.25}Ni_{0.75}$/MCNS, (e) Ni/MCNS.

148

In addition, the minor peaks located at 934.5 eV and low intensity satellites at 940-945 eV can be attributed to Cu^{2+}.[259,261,272,302] The presence of Cu^{2+} in the catalysts suggests a thin oxidized layer formed during exposure of the samples to air. Meanwhile, the XPS spectra of Ni 2p contain main peaks attributable to Ni^{2+} with the binding energy of Ni $2p_{3/2}$ and Ni $2p_{1/2}$ at 855.5 and 872.5 eV, respectively (Figure 7.3).[272,302] The dominant of Ni^{2+} state in the XPS profiles indicates Ni is more susceptible to be oxidized than Cu.

7.2.2 Catalytic performance in ammonia-borane hydrolysis and decomposition of hydrazine

7.2.2.1 Influences of composition

Recently, catalytic hydrolysis of AB ($H_3NBH_3 + 2H_2O \rightarrow NH_4^+ + BO_2^- + 3H_2$) and decomposition of hydrazine have received considerable research interest as potential approaches towards hydrogen energy-based systems.[9,12,292] Moreover, these processes have been used widely as adequate model reactions to study the catalytic properties of novel catalysts. [256-265,274-279,293-298] The prepared CuNi supported nanocatalysts were first tested for the catalytic hydrolysis of AB to generate H_2 at 25-40°C.
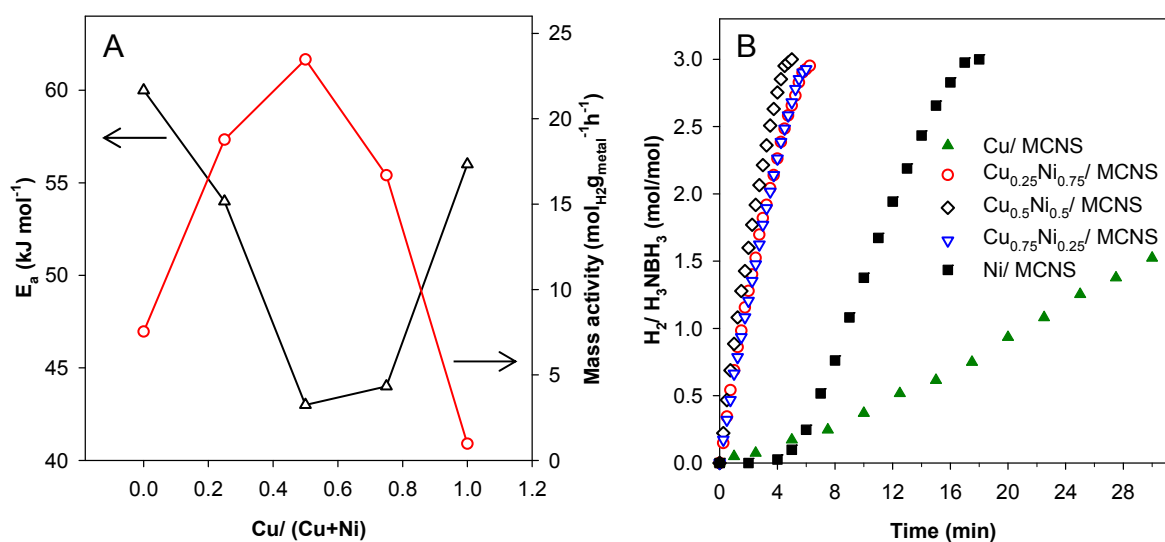
Figure 7.4. (A) Mass activity at 25°C and apparent activation energy as a function of Cu molar fraction. (B) Plots of time vs. volume of H_2 generated from the hydrolysis of AB catalyzed by binary CuNi/MCNS with different compositions. (H_3NBH_3 = 1.48 mmol, Metal/[AB] = 0.036, H_2O = 10 ml, T = 25°C).

Figure 7.4A shows the plots of mass activity and apparent activation energy for AB hydrolysis catalyzed by Cu-Ni/MCNS nanocatalysts as a function of the composition. It can be observed that the activity of the catalysts strongly depends on the Cu-Ni composition. Obviously, the H_2 generation rates of all bimetallic CuNi catalysts are greatly enhanced compared to the corresponding monometallic counterparts. Among the tested CuNi/MCNS catalysts, $Cu_{0.5}Ni_{0.5}$ shows the highest mass activity of 23.5 $mol_{H2}g_{metal}^{-1}h^{-1}$, and the dehydrogenation reaction of AB is complete within 5 min at 25°C (Figure 7.4B). An induction period from 0.5 to 4 min was observed for the monometallic Cu and Ni supported catalysts, whereas gas evolution was observed to occur immediately when the catalyst was in contact with AB in the case of the bimetallic CuNi nanohybrids (Figure 7.4B). It has been documented that, an induction period was often observed with fresh Cu- and Ni-based catalysts.[43,47,257,259,261] In AB hydrolysis, it is believed that the formation of an intermediate species during the induction time is essential to initiate the reaction. The formation of an activated complex is usually postulated through the interaction of an AB molecule with the surface of the solid catalyst, which then dissociates upon attack of a water molecule, releasing hydrogen.[257] Thus, the interaction between Cu and Ni here must facilitate the formation of the required activated intermediate species. The apparent activation energies for $Cu_{0.25}Ni_{0.75}$, $Cu_{0.5}Ni_{0.5}$, and $Cu_{0.75}Ni_{0.25}$/MCNS were determined to be approximately 54, 43, and 44 kJ mol^{-1}, respectively, whereas, the monometallic Cu/MCNS and Ni/MCNS catalysts show higher activation energies, i.e., 56 kJ mol^{-1} for Cu/MCNS and 60 kJ mol^{-1} for Ni/MCNS. These results clearly indicate a catalytic synergistic effect in the hydrolysis of AB over bimetallic CuNi nanocatalysts, which is in agreement with our previous observations for non-supported nanocast catalysts.[294]

The prepared bimetallic CuNi/MCNS catalysts were further examined in the catalytic decomposition of hydrazine. The hydrogen of hydrazine could be released by complete and desired decomposition through the pathway 1 or incomplete and undesired decomposition to ammonia by pathway 2: [292]

$H_2NNH_2 \rightarrow N_2 + 2H_2$ (pathway 1)

$3H_2NNH_2 \rightarrow 4NH_3 + N_2$ (pathway 2)
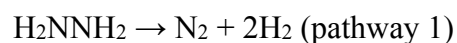
Pathway 2 not only decreases the yield of H_2 but also produces ammonia as a by-product, which would poison the catalysts of hydrogen-fueled cells. In our case, the prepared

150

bimetallic CuNi/MCNS catalysts exhibit high catalytic activity in $N_2H_4.H_2O$ decomposition for hydrogen generation in the presence of NaOH at 60°C (Figure 7.5). Interestingly, all the bimetallic CuNi/MCNS catalysts showed 100% selectivity to H_2 via pathway 1 and the reaction was complete within 50 min in the case of $Cu_{0.5}Ni_{0.5}$/MCNS, whereas Cu/MCNS exhibits much lower activity and selectivity (50.5%). However, in this case, Ni/MCNS displays higher activity compared to $Cu_{0.75}Ni_{0.25}$/ MCNS and Cu/MCNS.
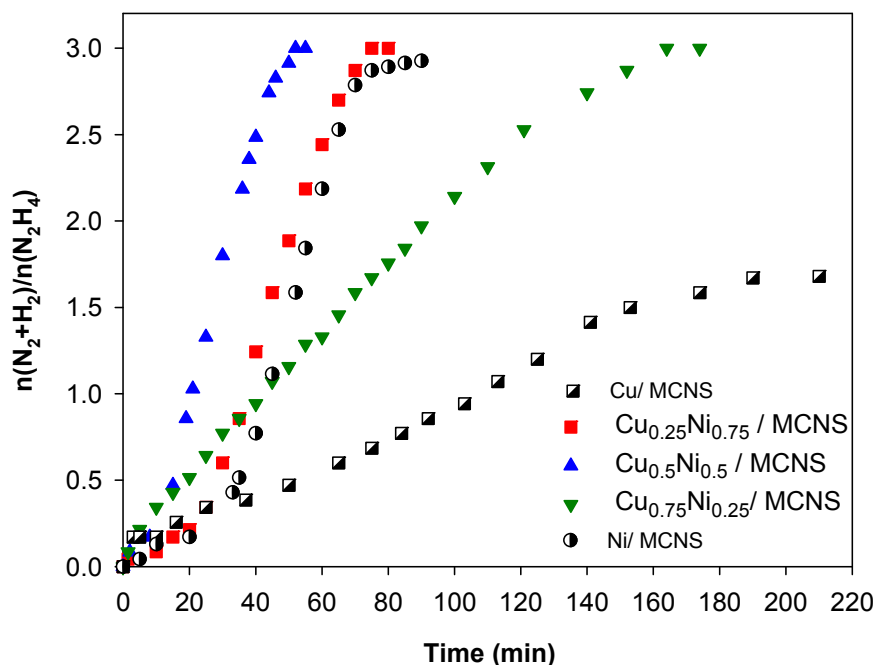
Figure 7.5. Time course plots of the hydrogen evolution by decomposition of hydrous hydrazine in NaOH (0.5M) at 60°C (Metal/H_2NNH_2 = 0.28).

The hydrogen generation rate per unit mole of active metal over $Cu_{0.5}Ni_{0.5}$/MCNS is about 21.8 h^{-1}, which is even comparable to NiPt alloy nanoparticles.[35] It is worth noting that, CuNi nanoparticles were reported to show poor activity and selectivity to H_2 (15%) at 70°C in similar reaction conditions.[41] The improved activity and selectivity of the supported bimetallic CuNi nanocatalysts in the present work may result from a different preparation method and the type of metal precursors used, which are factors that may strongly affect the structure and properties of the catalysts. In general, surfactants and organic solvents which are frequently used in preparations of nanoparticles may remain on the catalyst surface and thus interfere in the catalytic reaction.[32,85] We have proven previously that the choice of metal precursors has great impact on the catalyst performance in AB hydrolysis.[294] In the

present case, the variation trend of activity for CuNi/MCNS catalysts with different Cu/Ni ratios was found to be similar for both AB hydrolysis and hydrazine decomposition reactions. This catalytic enhancement in both reactions and the activation energy dependence on the catalyst composition which we observed might arise from modifications of the surface electronic structure in the bimetallic nanohybrids.[59,105,110] The electronic effect on the binding strength of intermediates is due to the change in the electronic structure of a catalyst. For transition metals, the way their d-states interact with the adsorbate largely determines the binding strength. The rule is that the lower in energy the d-states are relative to the highest occupied state - the Fermi energy - of the metal, the weaker the interaction with adsorbate states due to the occupancy of anti-bonding states. The effect of alloying can also be understood in terms of d band shifts. The calculated d-band centers of Cu and Ni are of -2.67 eV and -1.29 eV, respectively.[59] The d-band center position of CuNi alloy was proven to shift upward from Cu to Ni, suggesting the binding strength to CuNi bimetallic surface would lie in between Cu and Ni. Thus, the interaction between CuNi bimetallic surface and reacting species would neither be too weak nor too strong as in the cases of Cu and Ni individuals. According to Sabatier's principle, this would explain the enhanced activity of CuNi bimetallic catalysts. [59,280,299] It was proven theoretically and experimentally that the electronic structure of a bimetallic CuNi surface can be engineered by controlling compositions, which substantially impacts the adsorbate binding energy, and consequently, impact the activity and selectivity of the catalysts. [299-304]

7.2.2.2 Effects of support and metal particle size

In addition to composition, electronic metal-support interactions and particle size of the active components usually have a significant impact on the catalyst reactivity. Support effect and size-dependent catalytic activity of metal nanoparticles in heterogeneous catalysis are well-documented for many catalytic systems in various reactions.[16,56,82,103-110, 285-288] It would be both of fundamental and practical interest to clarify the influence of support and particle size for the supported CuNi nanocatalysts. To do so, mesoporous silica MCM-48 and mesoporous carbon CMK-1 nanospheres were also deployed as supports,[230,305,306] and metal particle sizes in a range of 6.7 to 18 nm were obtained by varying the metal loading (5-20 wt%). Since supported $Cu_{0.5}Ni_{0.5}$ nanocomposite has

highest activity among the tested catalysts, this composition was therefore applied to other supports. The ordered mesoporous structures of MCM-48 and CMK-1 nanospheres were first confirmed by small angle X-ray diffraction (Figures S7.3) with the reflections appearing at low 2θ angles from 1-6° characteristic of Ia3d structure of MCM-48 and lower symmetry $I4_132$ of the nanocast mesostructure of CMK-1. [230,305,306] Figure 7.6 shows typical TEM images and element mapping of $Cu_{0.5}Ni_{0.5}$/MCM-48 and $Cu_{0.5}Ni_{0.5}$/CMK-1 with various metal particle sizes. The ordered mesostructure of MCM-48 and CMK-1 supports are also clearly observed from the TEM images.
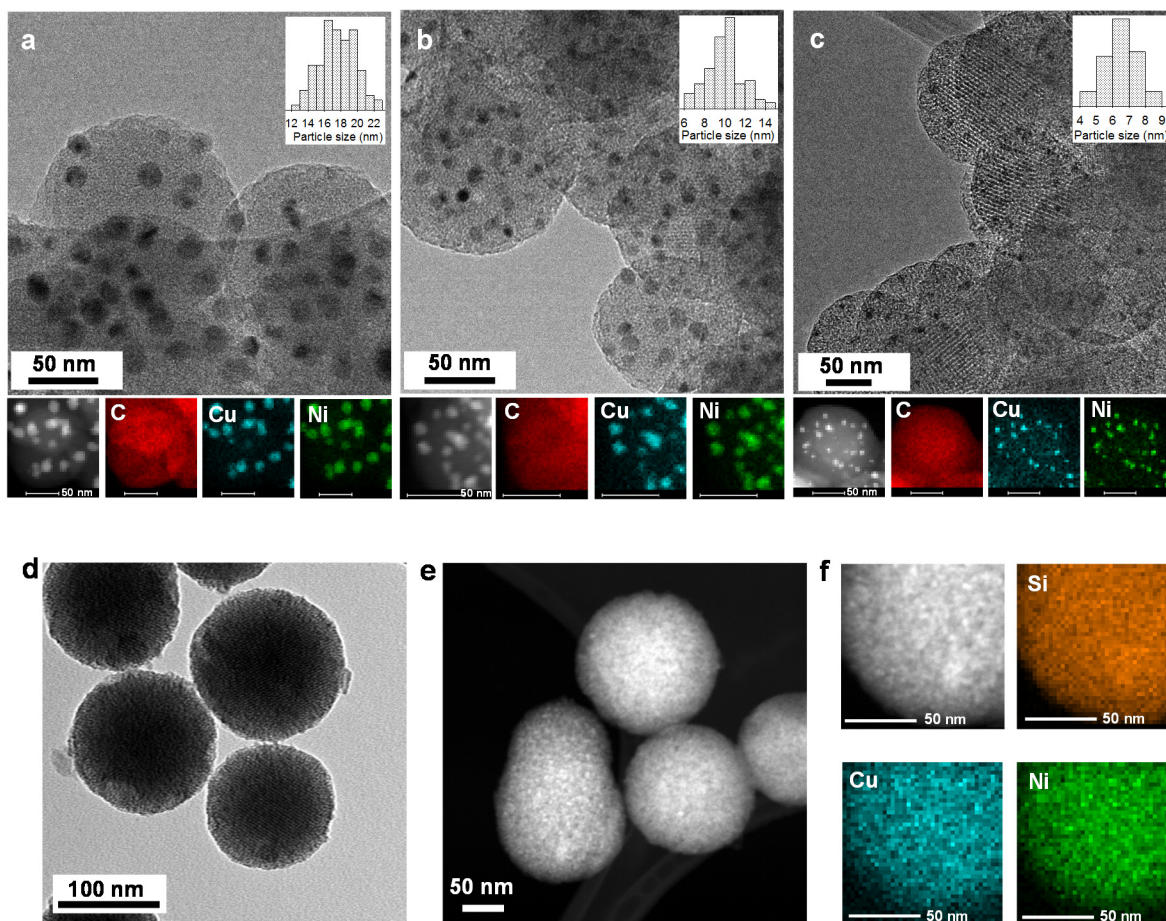
Figure 7.6. (a,b,c) HRTEM and STEM-HAADF images and corresponding EDS element mapping of $Cu_{0.5}Ni_{0.5}$/CMK-1 of different metal particle sizes (insets are metal particle size distributions). (d,e,f) TEM, STEM-HAADF images and EDS element mapping of $Cu_{0.5}Ni_{0.5}$/ MCM-48.

The metal particles are well dispersed with volume-averaged particle size of 6.7, 10.6 and 18 nm for $Cu_{0.5}Ni_{0.5}$/CMK-1. For $Cu_{0.5}Ni_{0.5}$/MCM-48, it can be observed that the metal particles are highly dispersed in silica matrix. Element mapping of Cu and Ni confirms the

uniform distribution of Cu and Ni for all the samples. The XRD pattern of $Cu_{0.5}Ni_{0.5}$/MCM-48 (Figure S7.4) shows no visible peaks in the range of 2θ=30-60°, suggesting the metal particles immobilized on MCM-48 nanospheres present an amorphous nature and/or are too small to be detected by XRD, in agreement with TEM observation. The visible diffraction peaks of $Cu_{0.5}Ni_{0.5}$/CMK-1 belong to the (111) and (200) planes in fcc structure of Cu and CuNi alloy phases (Figure S7.4). The porosity parameters obtained from nitrogen physisorption analyses (Figure S7.5, 7.6) of the prepared catalysts are presented in Table S7.1. All of the mesoporous supports (MCNS, CMK-1, MCM-48) possess high specific surface area (1500-1600 m^2/g) and narrow pore size distribution in the range of 3-3.4 nm. The chemical states of Cu and Ni obtained from XPS study for $Cu_{0.5}Ni_{0.5}$/CMK-1 are similar for the $Cu_{0.5}Ni_{0.5}$/MCNS catalyst, meaning Cu, Cu^+ and Ni^{2+} coexist as main states on the surface of the catalysts. The binding energies of Cu 2p appear primarily at 932.4 eV and 952.5 eV characteristic of Cu and Cu^+ (Figure S7.7), with a shoulder at 934.5 eV and low intensity of shake-up peak indicating the presence of Cu^{2+}. The Cu $2p_{3/2}$ and Cu $2p_{1/2}$ peaks of $Cu_{0.5}Ni_{0.5}$/MCM-48 shift slightly to higher binding energy at 932.7 and 952.5 eV compared to Cu 2p of $Cu_{0.5}Ni_{0.5}$ supported on carbon materials, indicating a larger portion of Cu^+ in the silica supported catalyst. In addition, the shake-up peak characteristic of Cu^{2+} with low intensity can be observed. These results indicate that Cu species supported on MCM-48 are primarily in the valence state of Cu^+ and partly in the states of Cu and Cu^{2+}.

The activity of $Cu_{0.5}Ni_{0.5}$ supported on different mesoporous materials with metal loading of 20 wt% were tested in AB hydrolysis. The activities of carbon supported $Cu_{0.5}Ni_{0.5}$/CMK-1 and $Cu_{0.5}Ni_{0.5}$/MCNS catalysts are com-parable (reaction completed within 2 min) and are 3-fold higher than that of silica supported $Cu_{0.5}Ni_{0.5}$/MCM-48 catalyst (reaction completed in 7min) (Figure S7.7). Thus, one may suggest that, the observed differences in activity could be associated to optimum metal particle size, electronic-metal support interactions, facilitated mass transfer, or a combination of these characteristics. The apparent activation energy and effective reaction order can be used as simple diagnostic criteria for estimation of mass-transport limitations.[58]
If the mass transfer is the rate-controlling step, the apparent activation energy is in the range of less than 5-10 kJ mol^{-1} due to the weak dependence of effective diffusivity upon temperature. According to Fick's first law, the rate of diffusion (interphase and

intraparticle) is proportional to the concentration gradient, i.e., it is first order. In the case when interphase mass transfer limitations strongly dominate, a first-order of reaction is observed. In our reaction conditions, hydrolysis catalyzed by both carbon- and silica-supported CuNi catalysts was found to be essentially independent of the AB concentration with a line slope of 0.02 and 0.07 for the silica- and carbon-supported catalysts, respectively (Figure S7.8). In addition, the apparent activation energy was found in the range 43-60 kJ mol^{-1} for the catalysts with different Cu/Ni ratios. Note that, the particle size of the CMK-1 and MCM-48 supports are in the same range of about 150 nm, whereas the MCNS support has a larger particle size of about 400-500 nm, while the pore size of the catalysts are comparable. Thus, effect of mass transfer can be viewed as negligible in our reaction systems. Therefore, the substantially higher performance of the carbon-supported catalysts originates essentially from the intrinsic activity and/or the amount of the active phases.
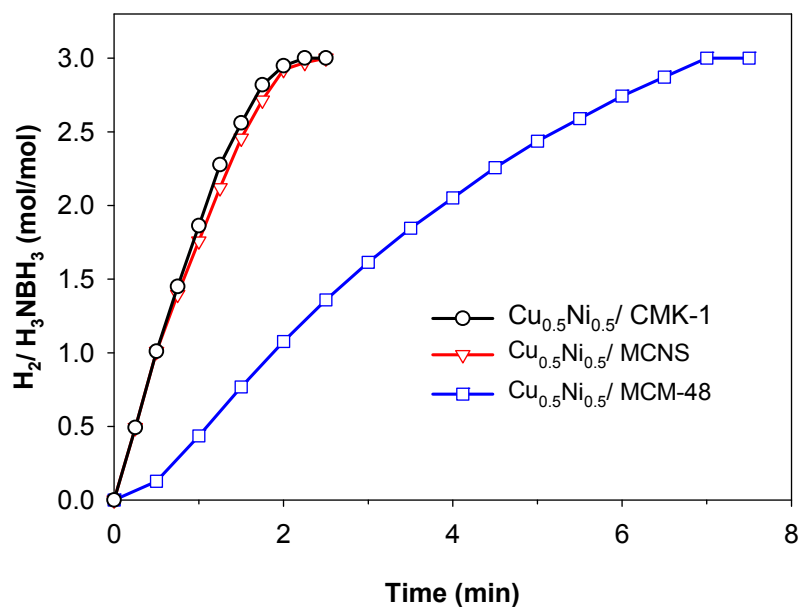
Figure 7.7. Plots of time vs. volume of H_2 generated from the hydrolysis of AB catalyzed by different supported $Cu_{0.5}Ni_{0.5}$ catalysts. (H_3NBH_3 = 1.48 mmol, Metal/[AB] = 0.072, H_2O = 10 ml, T = 25°C).

Interestingly, it is observed that the mean sizes of metal particles of the three catalysts are different and decrease, in order of $Cu_{0.5}Ni_{0.5}$/CMK-1 > $Cu_{0.5}Ni_{0.5}$/MCNS > $Cu_{0.5}Ni_{0.5}$/MCM-48, which means that the activity of the catalysts seems to decrease as the

155

metal particle size decreases. In order to study the size dependence of catalytic activity, three catalysts with metal average particle sizes of 6.7, 10.6 and18 nm were obtained by using the metal loading of 5, 10 and 20 wt%, respectively, on the same support - CMK-1. The CMK-1 was chosen as support to examine the particle size effect owing to fact that the metals supported on CMK-1 carbon exhibit a narrower particle size distribution, and, practically, the dispersion of metal particles is also more readily visible on CMK-1. The mass activity in the catalytic AB hydrolysis increases with the decreasing metal particle sizes of the catalysts (Figure 7.8).
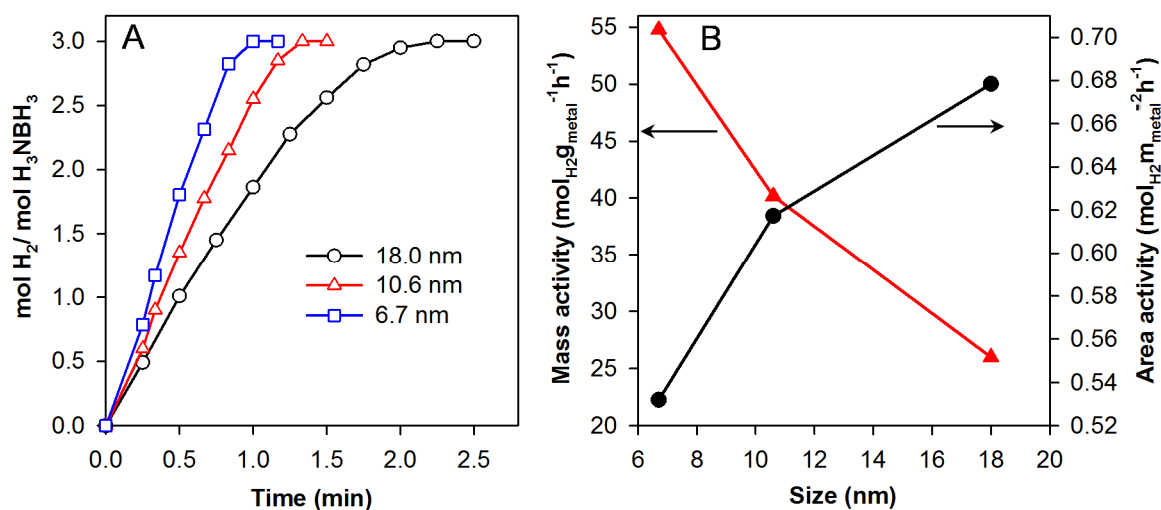
Figure 7.8. (A) Time course of hydrogen evolution from AB hydrolysis over $Cu_{0.5}Ni_{0.5}$/CMK-1 with different metal particle sizes. (B) Mass activity and area activity as a function of metal particle size in AB hydrolysis reaction catalyzed by $Cu_{0.5}Ni_{0.5}$/CMK-1 catalysts. (T = 25°C, Metal/AB = 0.072).

Remarkably, the $Cu_{0.5}Ni_{0.5}$/CMK-1 with metal particle size of 6.7 nm shows an extremely high activity, over which the hydrolysis is completed within 1 min and TOF value as high as 3288 ($mol_{H2}mol_{metal}^{-1}h^{-1}$), which is superior to any other non-noble based catalysts reported thus far and comparable to noble metal-based catalysts,[36,43,275-279,297,298] and the reusability tests reveal that the catalyst is still highly active after 6 subsequent runs of AB hydrolysis (Figure S7.9). The activity normalized to theoretical surface area of the metal particles, assuming spherical nanoparticles with all the surface being catalytically available, however decreases as the metal particle size decreases, indicating that larger particles are more active than small ones in catalytic hydrolysis of AB under the studied conditions. To

clarify this, one may consider different distribution of Cu and Ni species in the different catalytic systems under study. Indeed, the surface Ni/Cu ratio obtained from XPS analyses (Ni/Cu=1.08/1) (Table S7.2) was found to be close to the value in the bulk determined from ICP analyses for $Cu_{0.5}Ni_{0.5}$/CMK-1 with metal particle size of 18 nm. However, the catalysts show an enrichment in Ni at their surface as the metal particle size decreases, i.e., the surface Ni/Cu ratios are 1.28 and 2.36 for $Cu_{0.5}Ni_{0.5}$/CMK-1 with particle sizes of 10.6 and 6.7 nm, respectively. These results suggest that the coexistence of Cu and Ni on the catalyst surface is essential to activate AB. Furthermore, we observed that $Cu_{0.5}Ni_{0.5}$/MCNS having higher metal dispersion with average particle size of 7.7 nm exhibits slightly lower reaction rate compared to $Cu_{0.5}Ni_{0.5}$/CMK-1, with mean metal particle size of 18 nm. This behavior could be explained by the fact that $Cu_{0.5}Ni_{0.5}$/MCNS is also richer in Ni on surface demonstrating a Ni/Cu ratio of 2.86. Therefore, the positive effect originating from increasing surface metal area due to smaller particle size can be balanced by a negative effect brought by changes in the surface composition (i.e., enrichment in Ni). Interestingly, although the surface the Ni/Cu ratio of $Cu_{0.5}Ni_{0.5}$/MCM-48 is of 1.08, this catalyst shows much lower activity compared to carbon- supported catalysts. Here, such a sharp decline in catalytic activity for $Cu_{0.5}Ni_{0.5}$/MCM-48 may be due to stronger metal-silica interactions that could weaken the Cu-Ni interaction. To examine the metal-support interaction, H_2-temperature programmed reduction (H_2-TPR) of the silica-supported catalysts was performed (Figure 7.9). For comparison, TPR analyses of single metal silica-supported materials, i.e., Cu/MCM-48 and Ni/MCM48, were also carried out. The resulting TPR profile of Cu/MCM-48 shows a single reduction peak at 201ºC which can be attributed to the reduction of finely dispersed surface copper oxide species into copper. Meanwhile, a broad peak appears at 420ºC for Ni/MCM-48, corresponding to the reduction of nickel species in interaction with the silica support.[302,307] Note that, the reduction of single bulk NiO occurs at 350ºC, suggesting that the strong Ni-silica interaction makes the nickel species more difficult to reduce. For the $Cu_{0.5}Ni_{0.5}$/ MCM-48 catalyst, a reduction peak at 204ºC and a broad peak at around 400ºC can be assigned to the reduction of finely dispersed copper oxide species and nickel species closely interacting with the silica support, respectively. Thus, the presence of strong interaction between nickel and silica

could clearly impede the needed copper-nickel interaction which plays a vital role in enhancing the catalyst reactivity.
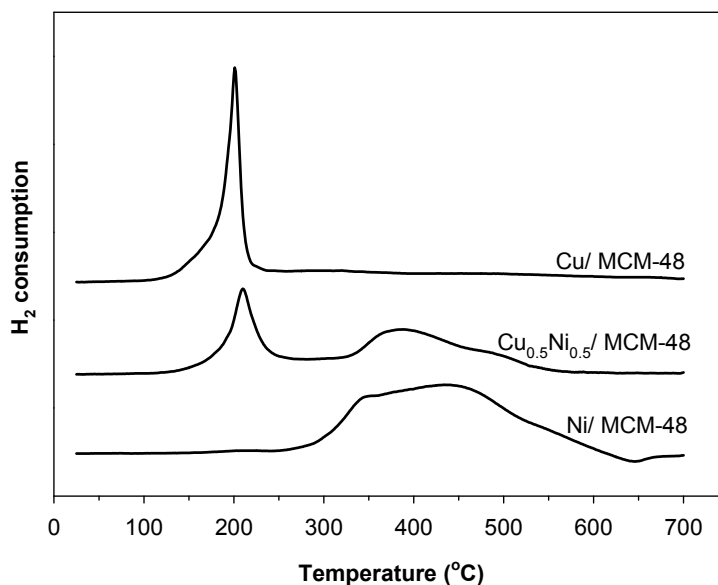
Figure 7.9. H_2-TPR profiles of silica supported catalysts Cu/ MCM-48, $Cu_{0.5}Ni_{0.5}$/MCM-48 and Ni/ MCM-48 (as indicated)

7.3. Conclusions

In conclusion, we have presented the development highly efficient nonprecious bimetallic supported CuNi catalysts using a simple incipient wetness with low-cost nitrate metal precursors. The above results reveal that composition, size of metal particle, and nature of support play critical roles in the activity and stability of the catalysts. The mesoporous carbon spheres-supported bimetallic Cu-Ni catalysts exhibit excellent performance in the catalytic hydrolysis of AB and catalytic decomposition of hydrous hydrazine with 100% H_2 selectivity. The metal particle sizes of the metal species can be controlled in the range from 6.7 to 18 nm with narrow size distribution on mesoporous carbon CMK-1 support simply by varying the metal loadings (5-20 wt%). The mass activity of the $Cu_{0.5}Ni_{0.5}$/CMK-1 catalyst was found to increase with decreasing metal particle size, however, the activity normalized to metal surface area declines slightly as the particle size decreases. Such observed size-dependence activity could be explained by modifications in surface composition as the particle size decreases. The $Cu_{0.5}Ni_{0.5}$/CMK-1 possessing average metal

158

particle size of 6.7 nm exhibits noticeably superior activity for dehydrogenation of AB with TOF as high as 3288 ($mol_{H2}mol_{metal}^{-1}h^{-1}$) under ambient conditions, making it one of the best non-noble catalysts and even comparable to noble metal based catalysts. The $Cu_{0.5}Ni_{0.5}$ supported on mesoporous MCM-48 silica nanospheres exhibits much lower activity for AB hydrolysis reaction compared to carbon-supported counterparts mainly due to the strong nickel-silica interaction that could hinder the required Cu-Ni synergistic interaction. The observed high performance of the bimetallic CuNi supported nanocatalysts makes it possible to propose that the alloying of Cu and Ni leads to modification of the catalyst surface through the intermetallic electronic interactions, consequently improving substantially the reactivity of the metals.

Given that two these reactions are emerging as the most promising approaches for chemical storage of hydrogen towards a hydrogen economy, the development of efficient and cost-effective catalysts, as well as knowledge about reactivity and selectivity of these reactions on nanocatalysts are of utmost importance. The present finding demonstrated that the optimum catalyst could be achieved through a combination of bimetallic effect along with tuning metal particle size and a proper choice of support.

7.4. Experimental section

7.4.1 Synthesis of mesoporous carbon nanospheres MCNSs

The MCNSs with diameter of around 500nm were synthesized according to modified Sheng Dai's approach.[308] Typically, a mixture consists of cetyltrimethylammonium chloride (CTAC) solution (12.48 g, 25 wt% in water), absolute ethanol (96ml), ammonia hydroxide solution (1.2 ml, 29 wt%), and deionized water (228ml) was stirred at 30°C for 1 h. Subsequently, resorcinol (2.4 g) was added and the resulting mixture was additionally stirred for 1 h. Then formadehyde solution (3.36 ml) and tetraethyl orthosilicate (TEOS, 4.32 ml) were added to above mixture and stirred for 24 h at 30°C. The brown solid product was recovered by centrifugation, washed with water and dried at 80°C overnight. For carbonization and template removal, the solid product was heated in a tubular furnace to 600°C (2 h, heating rate 1°C/min) and then 800°C (5 h, 5°C/min) under N_2 flow. The MSNSs were obtained by silica dissolution using HF 5wt%.

7.4.2. Synthesis of mesoporous carbon CMK-1

Mesoporous carbon prepared via nanocasting method using mesoporous silica MCM-48 is denoted as CMK-1. Synthesis of CMK-1 templated by MCM-48 involved impregnation with furfuryl alcohol in the presence of p-Toluene sulphonic acid (PTSA) as catalyst for carbonization, followed by carbonization at 900°C and removal of silica template via dissolution in HF solution. Briefly, 1 g of MCM-48 nanospheres was impregnated with 1 ml of furfuryl alcohol and 6μl of PTSA solution (0.05g of PTSA in 1 ml acetone). The impregnated sample was then pyrolysed at 350°C in inert atmosphere. The impregnation was repeated 2 times with the amount of precursor solution was of 0.7 ml for the second one. The composite material was carbonized at 900°C for 2 h in inert atmosphere. Finally, the silica framework was removed by dissolution in HF solution (5 wt. %).

7.4.3. Synthesis of supported metal catalyst

Cu, Ni catalysts were prepared via incipient wetness impregnation using metal nitrate precursors ($Cu(NO_3)_2.3H_2O$, $Ni(NO_3)_2.6H_2O$). Typically, for carbon supported catalyst, 1g of degassed support material was impregnated with 0.8ml of the solution (water and ethanol mixture in volume ratio of 1/1) containing the desired amount of metal precursors to achieve intended metal loadings of 5, 10 and 20 wt%. In the case of silica supported catalyst, water was used as solvent and citric acid (with molar ratio of citric acid/ metal = 1/1) was used as chelating agent to obtain uniform dispersion of metal species at high metal loading of 20 wt%. The impregnated catalyst precursors were dried overnight at 30°C in dynamic vacuum. Next, the catalyst precursors were subjected to heat treatment at 400°C for 5 h in N_2 flow to obtain the final products.

7.4.4 Catalyst characterization

High resolution TEM and Scanning TEM high angle annular dark field (STEM-HAADF) images were performed on Philips F20 Tecnai instrument operated at 300 kV. The chemical compositions of the samples were analyzed by Inductively Coupled Plasma Optical Emission Spectroscopy (ICP-OES) on a Perkin-Elmer Optima 4300DV spectrometer. TPR experiments were performed on an RMX-100 instrument. In a typical test, a 15 mg of catalyst was loaded in the middle of a quartz tubular reactor, with quartz wool supports on both sides. The catalyst was cleaned in argon flow and TPR was then performed under H_2

(5% balanced in Ar) with a flow rate of 10 ml min^{-1} and a ramping rate of 5°C min^{-1}. Other characterization techniques (TEM, XRD, N$_2$ physical adsorption) were obtained as described in the Chapter 6. Catalytic tests were detailed in Chapter 3.

7.5. Supporting information
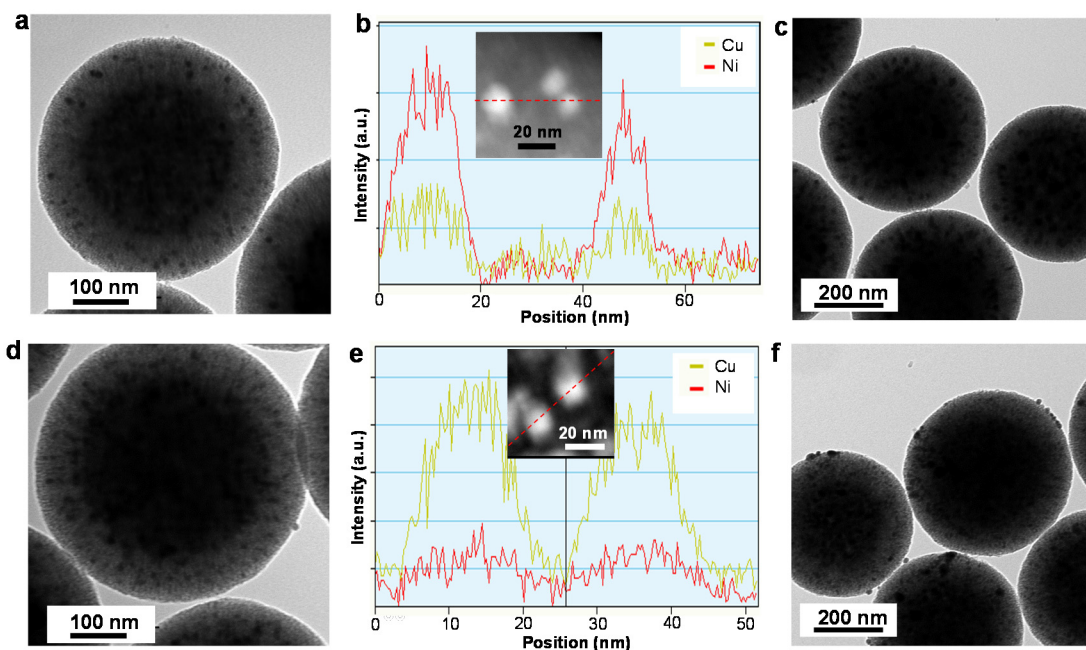
Figure S7.1. TEM images of (a) $Cu_{0.25}Ni_{0.75}$/ MCNS, (c) Cu/ MCNS, (d) $Cu_{0.75}Ni_{0.25}$/ MCNS, (f) Ni/MCNS and STEM-HAADF images and the corresponding line-scanning profiles across the metal particles as indicated of (b) $Cu_{0.25}Ni_{0.75}$/ MCNS and (e) $Cu_{0.75}Ni_{0.25}$/ MCNS catalysts.
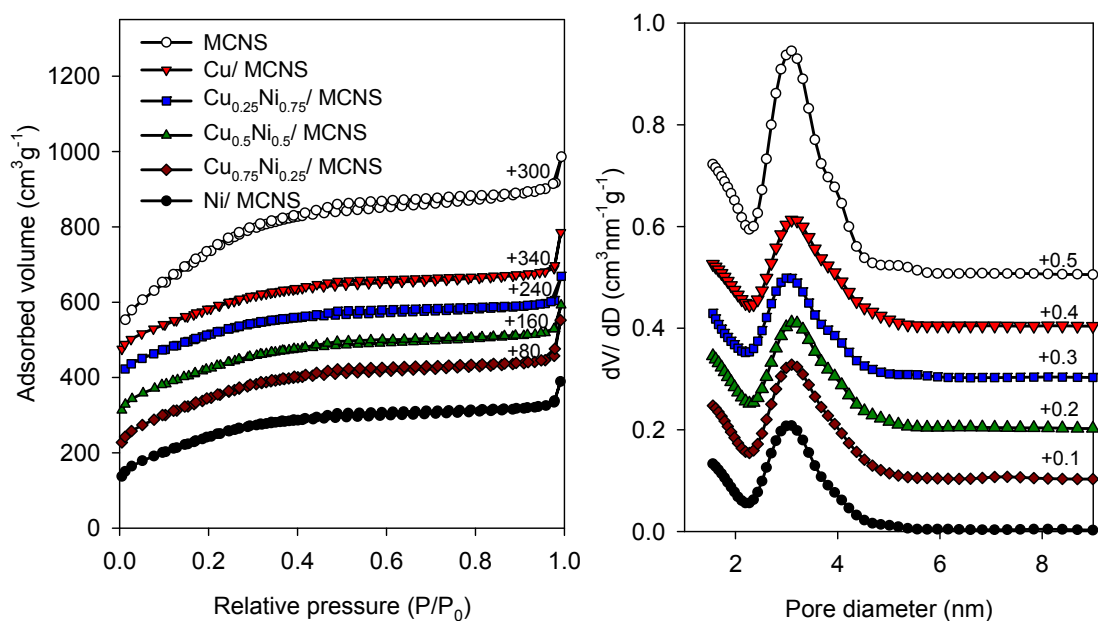
Figure S7.2. N_2 adsorption-desorption isotherms at $-196^{\circ}C$ (left) and respective QSDFT pore size distributions (right) deduced from the adsorption branch for the prepared catalysts (as indicated).
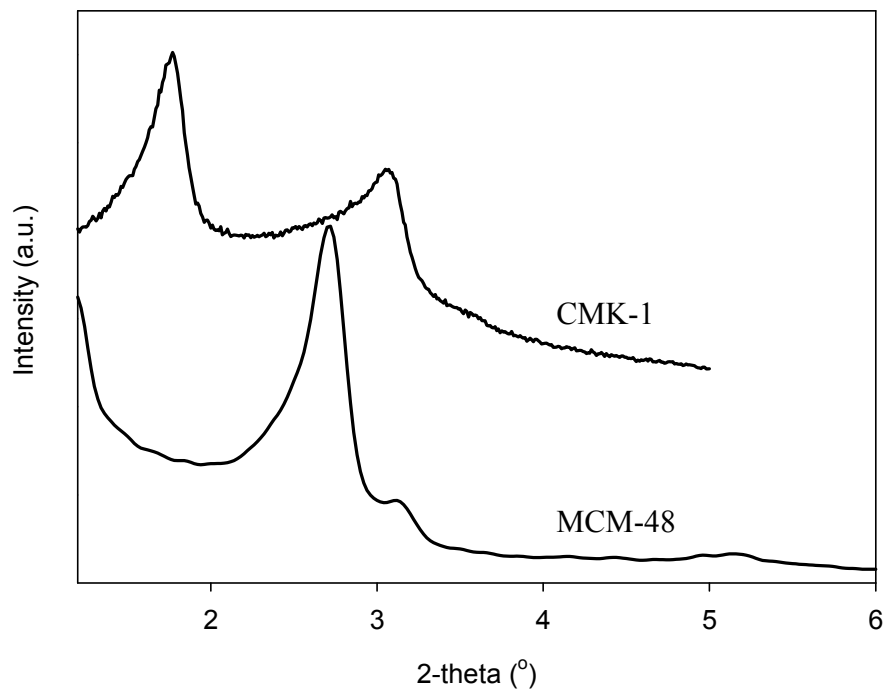
Figure S7.3. Small angle XRD patterns of ordered mesoporous carbon CMK-1 and silica MCM-48.
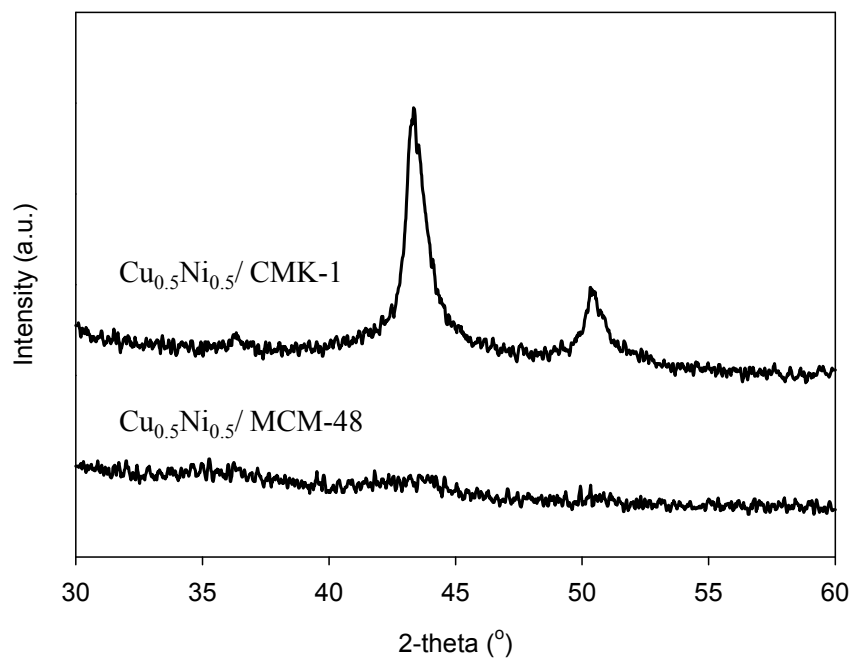
Figure S7.4. XRD patterns of $Cu_{05}Ni_{0.5}$/CMK-1 and $Cu_{05}Ni_{0.5}$/MCM-48.

163
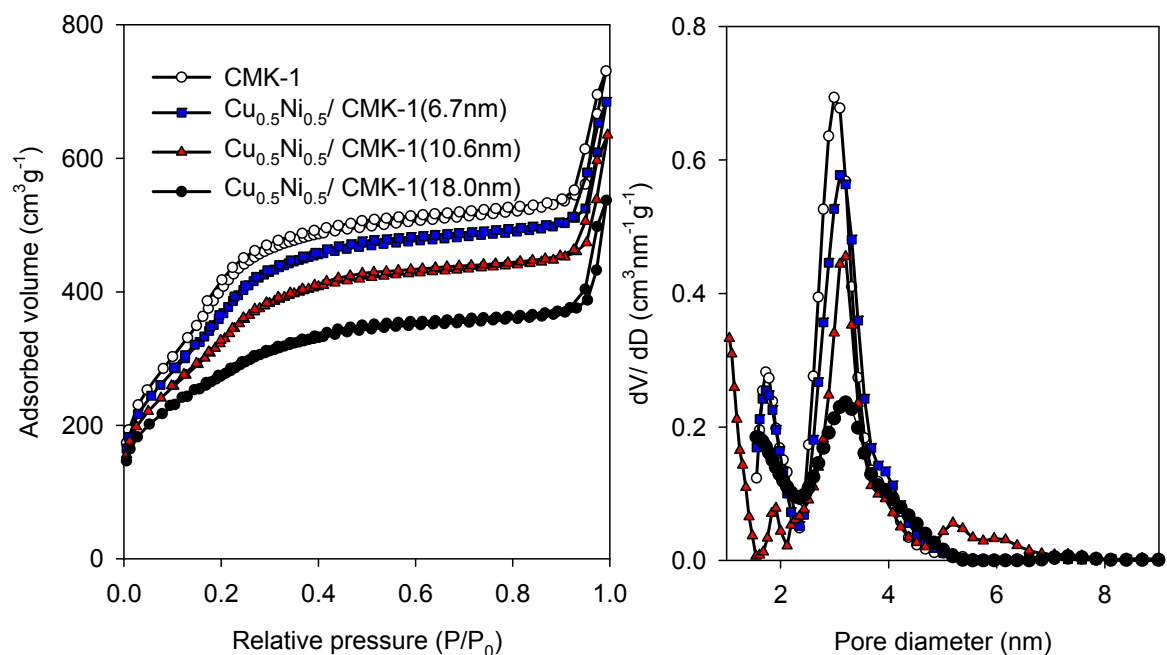
Figure S7.5 N_2 adsorption-desorption isotherms at -196°C (left) and respective QSDFT pore size distributions (right) deduced from the adsorption branch for the prepared catalysts (as indicated).
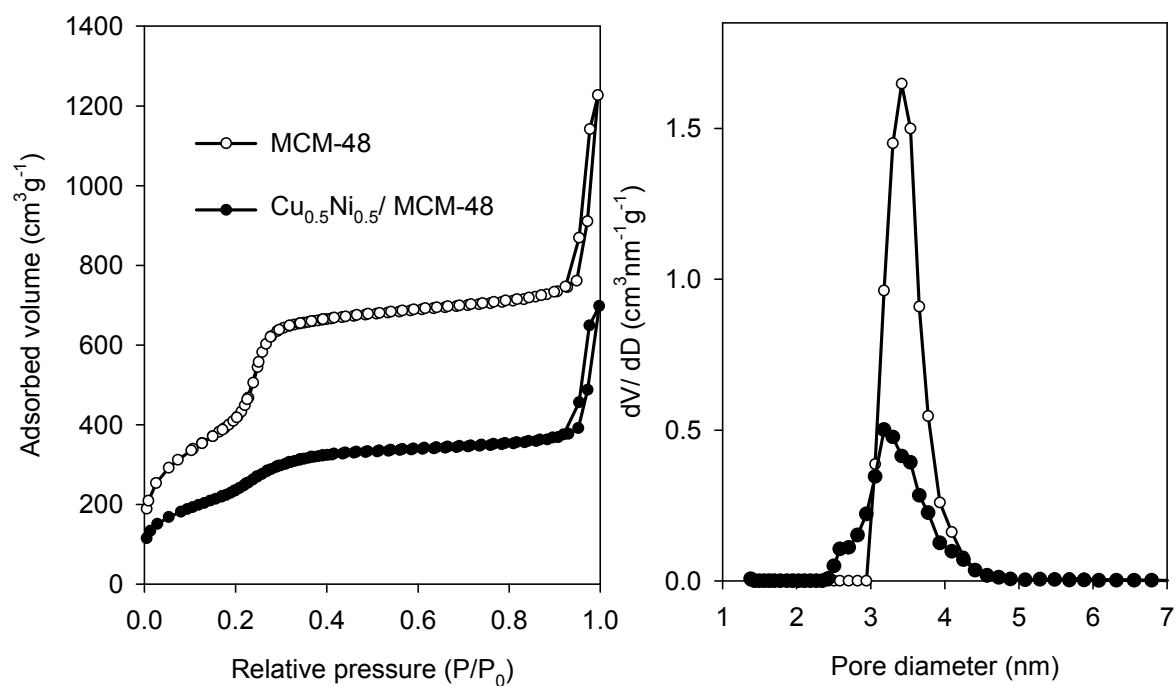
Figure S7.6. N_2 adsorption-desorption isotherms at -196°C (left) and respective NLDFT pore size distributions (right) deduced from the adsorption branch for the prepared catalysts (as indicated).

164
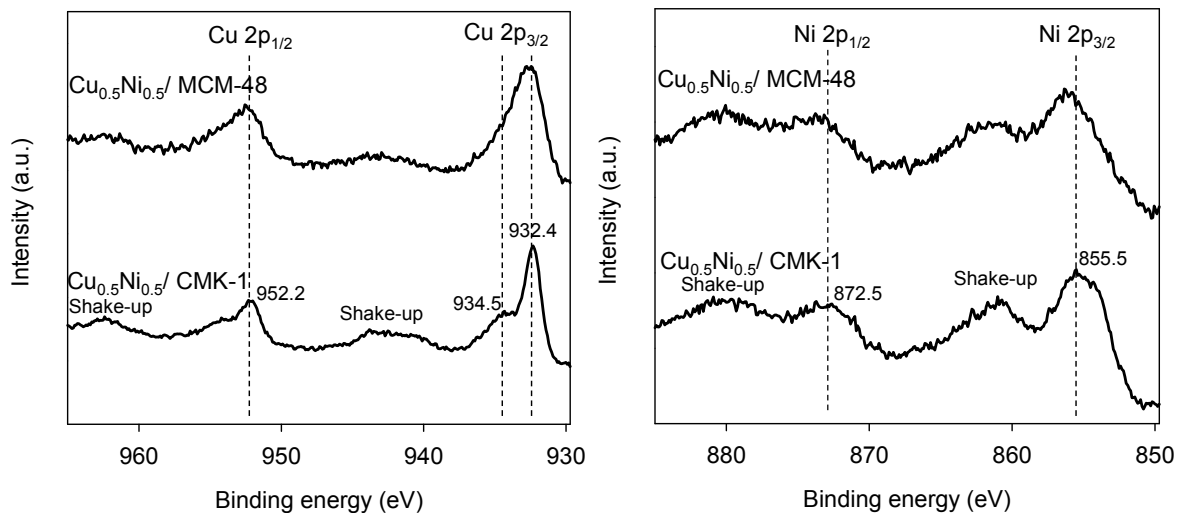
Figure S7.7. Cu 2p and Ni 2p XPS spectra of bimetallic CuNi supported on ordered mesoporous silica MCM-48 and carbon CMK-1.
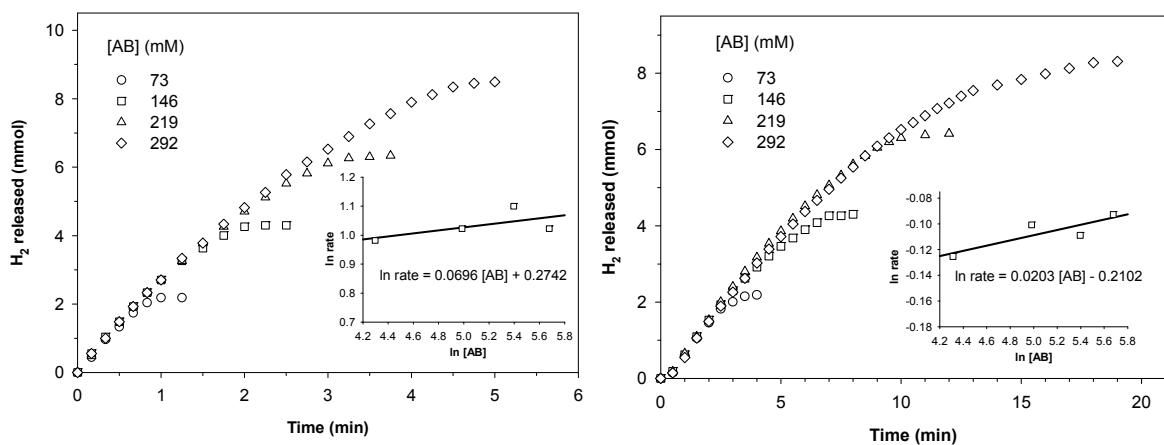
Figure S7.8. The plot of time versus volume of hydrogen generated from the hydrolysis of AB catalyzed by $Cu_{0.5}Ni_{0.5}$/ MCNS (left) and $Cu_{0.5}Ni_{0.5}$/ MCM-48 at different AB concentrations (Metal = 0.10 mmol, T = 25°C). (Inset: ln [AB] vs ln rate plot).
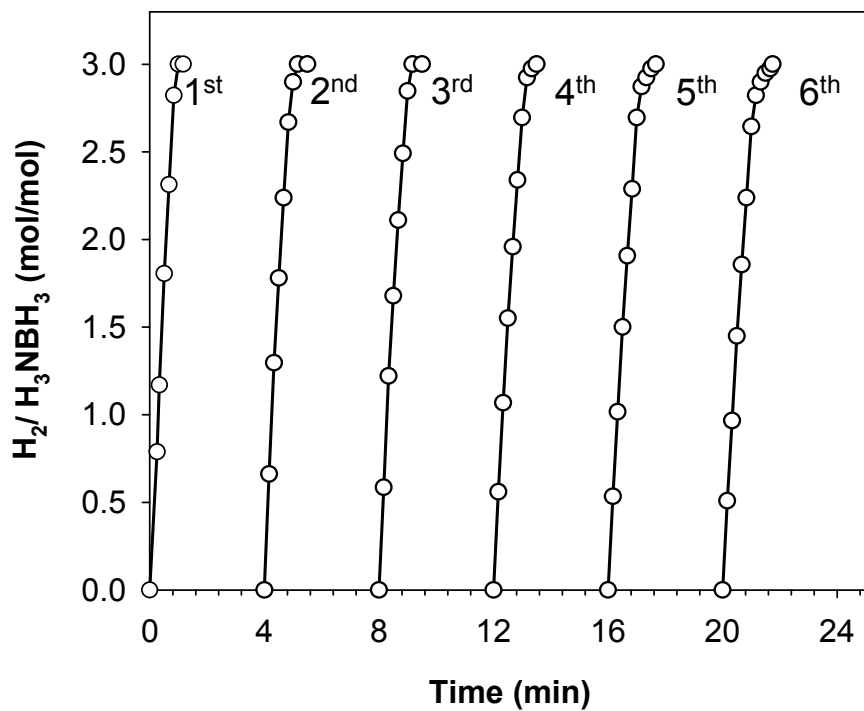
Figure S7.9. Plots of time vs. volume of H_2 generated from the hydrolysis of AB catalyzed by $Cu_{0.5}Ni_{0.5}/$ CMK-1(6.7 nm) from 1st to 6th cycle. An equivalent of AB in 2 ml H_2O was added to the reaction solution every 4 min.

Table S7.1. Textural parameters of the different mesoporous mixed metal oxides derived from nitrogen physisorption measurements at -196°C.

Sample	S_{BET} [a]	V_t [b]	d [c]
MCNS	1593	0.93	3.1
CMK-1	1535	0.86	3.0
MCM-48	1532	1.2	3.4
Cu/ MCNS	875	0.53	3.0
$Cu_{0.25}Ni_{0.75}$/ MCNS	979	0.55	3.0
$Cu_{0.5}Ni_{0.5}$/ MCNS	945	0.56	3.0
$Cu_{0.75}Ni_{0.25}$/ MCNS	958	0.57	3.0
Ni/ MCNS	877	0.50	3.0
$Cu_{0.5}Ni_{0.5}$/ CMK-1 (6.7 nm)	1385	0.81	3.0
$Cu_{0.5}Ni_{0.5}$/ CMK-1 (10.6 nm)	1213	0.73	3.0
$Cu_{0.5}Ni_{0.5}$/ CMK-1 (18 nm)	997	0.56	3.0
$Cu_{0.5}Ni_{0.5}$/ MCM-48	859	0.61	3.2

[a] S_{BET}, apparent BET specific surface area deduced from the isotherm analysis in the relative pressure range from 0.05 to 0.20; [b] V_t, total pore volume at relative pressure 0.95; [c] d, pore diameter calculated from the adsorption branch (QSDFT kernel of metastable adsorption isotherms for carbon materials and NLDFT for silica materials).[192,193]

Table S7.2 Elemental analyses of the prepared supported catalysts

Sample	Actual Metal loading (wt. %)	Ni/Cu ratio in the bulk	Ni/Cu surface ratio
Cu/ MCNS	19.8	-	-
Ni/ MCNS	18.8	-	-
$Cu_{0.25}Ni_{0.75}$/ MCNS	19.0	3.06	-
$Cu_{0.75}Ni_{0.25}$/ MCNS	19.3	0.33	-
$Cu_{0.5}Ni_{0.5}$/ MCNS	19.1	1.00	2.86
$Cu_{0.5}Ni_{0.5}$/ CMK-1 (18.0 nm)	18.9	0.98	1.08
$Cu_{0.5}Ni_{0.5}$/ CMK-1 (10.6 nm)	9.4	0.99	1.28
$Cu_{0.5}Ni_{0.5}$/ CMK-1 (6.7 nm)	4.7	1.00	2.36
$Cu_{0.5}Ni_{0.5}$/ MCM-48	18.7	0.96	1.08

Chapter 8:

Conclusions and future work

8.1 Conclusions

In this thesis, we have proposed a series of new, efficient and simple procedures to synthesize various nanostructured porous mixed metal oxides and some supported analogs. A wide variety of experimental studies have been performed to investigate composition, structure, porosity, and catalytic properties of the different metal or metal oxide catalyst systems, with a special emphasis on catalytic processes related to the production of hydrogen fuel.

First, we have developed a facile synthesis route for the preparation of crystalline nanostructured porous mixed metal oxides (e.g., Cu-CeO$_2$, NiFe$_2$O$_4$, CuFe$_2$O$_4$), based on the nanocasting method using various ordered mesoporous silica materials as hard templates. The preparation method, which uses molten nitrate salts in the presence of an organic solvent (e.g., n-hexane or cyclohexane) under refluxing conditions, is well-suited for a large variety of non-siliceous compositions, especially high-surface-area mixed metal oxides, which are difficult to prepare otherwise.

Next, we have shown that the above one-step impregnation method can be implemented to synthesize mesoporous copper/ceria catalysts that are highly active and selective for the selective oxidation of CO to CO$_2$ in the presence of hydrogen (i.e., the PROX process). The nanocasting technique enabled the synthesis of catalysts with precisely tuned compositions and textural parameters. The thus-obtained products are promising materials for application as CO-PROX catalysts or as gas sensors. In addition to the role of composition, this work also illustrates that the reducibility and catalytic performance of the materials are greatly influenced by the nature of the nanoporous structure (i.e., porosity and mesostructure). This study demonstrates that a fine control over nanoscale structural features offers new perspectives for catalyst design.

Concerning catalysts for hydrogen generation from hydrogen chemical storage compounds, we have presented a quite simple synthesis of high-performance and low-cost catalysts particularly efficient for the hydrogen evolution from ammonia borane (AB) hydrolysis under ambient conditions. The catalysts consist of binary copper–nickel oxides, in which synergetic interactions are revealed under the form of a solid solution (Cu$_x$Ni$_y$O).

The resultant $Cu_{0.5}Ni_{0.5}$ hybrid exhibits the highest catalytic activity among all of Cu-based catalysts for AB hydrolysis, with satisfying stability, as probed over 6 cycles. Although further improvement in the stability of the high-surface-area equivalent is needed, the present finding demonstrates that combinations of non-noble metals can provide viable solutions for the development of practical catalysts, first for H_2 generation from AB hydrolysis, but possibly also for other reactions.

Following this work, catalysts consisting of bimetallic CuNi supported on mesoporous carbon spheres were shown to exhibit excellent catalytic performance both in catalytic hydrolysis of AB and decomposition of hydrous hydrazine with 100% hydrogen selectivity. The $Cu_{0.5}Ni_{0.5}$/CMK-1 material possessing average metal particle size of 7 nm demonstrates superior activity for dehydrogenation of AB with TOF as high as 3288 ($mol_{H2}mol_{metal}^{-1}h^{-1}$) under ambient conditions, making it one of the best non-noble catalyst and even comparable to noble metal-containing catalysts. The present finding demonstrated that the optimum catalyst could be achieved through a combination of bimetallic effects along with adequate tailoring of metal particle size and proper choice of support. Given that two these reactions are emerging as some of the most promising approaches for chemical storage of H_2 in the perspective of a hydrogen economy, the development of such efficient and cost-effective catalysts is of great significance Furthermore, this study contributes new fundamental insights into reactivity and selectivity for these reactions over nanocatalysts, which may prove to be also useful more generally for other nanostructured systems.

8.2 Recommendations for future work

There is no doubt catalysis will play a central role in the transition from a petroleum-based economy to a future economy based on renewable fuels and sustainable chemicals. This thesis has covered different aspects associated with synthesis, characterization and reaction studies of families of nanoporous materials, which were designed primarily for the catalytic production and purification of hydrogen for fuel cells. Nevertheless, there are several other important areas that might be a natural extension of the research presented in this thesis. The first one is related more generally to the synthesis of high-surface-area metal oxides. Besides the mixed metal oxides reported in our publications, other nanostructured materials (such as $MnCo_2O_4$, $CoMn_2O_4$, $NiCo_2O_4$) can be developed based on our improved

nanocasting method. These nanoporous mixed metal oxide materials have great potential in the field of electrochemistry (e.g., electrocatalysts, electrode materials for batteries, etc.) and research regarding the electrochemical properties of some of these compositions is ongoing in collaboration with the team of Dr. Claudio Gerbaldi, Polytechnic School of Turin, Italy. We have explored the catalytic performance of nanocast materials of different compositions and structures in the PROX reaction. The viability of the production of metal oxides using the nanocasting method may be questionable for large-scale practical application. However, the $Cu-CeO_2$ catalysts prepared using KIT-6 as the template are still quite promising to be deployed in CO gas sensor devices. Here, it remains interesting to further pinpoint the detailed reasons for the differences in the activities observed experimentally over the various catalysts studied, especially when Fe or Co cations are inserted in the catalysts or for different mesostructures (2-D hexagonal vs 3-D cubic for instance). In this thesis, the combination of Cu and Ni was proven to lead to highly efficient systems for the catalytic hydrogen generation from AB and hydrazine. The supported bimetallic CuNi catalysts prepared by a simple incipient wetness method using inexpensive nitrate metal salts have great potential for practical applications. However, remaining issues concerning the chemical storage media (e.g., cost-effective production and recycling of AB and hydrazine) have also to be solved. The causes of the enhanced reactivity of bi-component CuNi compared to the individual constituents and the effect of support, as well as metal particle size, still are open questions and more fundamental mechanistic studies may provide additional understading. Finally, there is no reason why such catalysts (e.g., CuNi or other combinations of non-noble metals self-supported or supported on mesoporous colloidal particles) or the methods developed to synthesize these catalysts, could not be adapted for other important reactions for energy applications such as hydrogenolysis of sugar alcohols to valuable platform chemicals. In addition to the research presented in this thesis, we have developed several other CuZn-based nanoporous catalysts for the conversion of biomass derived compounds. Characterization and investigation of the reactivity of these materials is currently underway.

References

(1)   Farrauto, R.; Hwang, S.; Shore, L.; Ruettinger, W.; Lampert, J.; Giroux, T.; Liu, Y.; Ilinich, O.: New material needs for hydrocarbon fuel processing: Generating hydrogen for the PEM fuel cell. *Ann. Rev. Mater. Res.* **2003**, *33*, 1-27.

(2)   Holladay, J. D.; Hu, J.; King, D. L.; Wang, Y.: An overview of hydrogen production technologies. *Catal. Today* **2009**, *139*, 244-260.

(3)   Tanksale, A.; Beltramini, J. N.; Lu, G. M.: A review of catalytic hydrogen production processes from biomass. *Renew. Sust.Energ. Rev.* **2010**, *14*, 166-182.

(4)   Han, Z.; Eisenberg, R.: Fuel from Water: The photochemical generation of hydrogen from water. *Acc. Chem. Res.* **2014**, *47*, 2537-2544.

(5)   Farrauto, R. J.: Introduction to solid polymer membrane fuel cells and reforming natural gas for production of hydrogen. *Appl. Catal. B* **2005**, *56*, 3-7.

(6)   Park, E. D.; Lee, D.; Lee, H. C.: Recent progress in selective CO removal in a H_2-rich stream. *Catal. Today* **2009**, *139*, 280-290.

(7)   Schlapbach, L.; Zuttel, A.: Hydrogen-storage materials for mobile applications. *Nature* **2001**, *414*, 353-358.

(8)   Yang, J.; Sudik, A.; Wolverton, C.; Siegel, D. J.: High capacity hydrogen storage materials: attributes for automotive applications and techniques for materials discovery. *Chem. Soc. Rev.* **2010**, *39*, 656-675.

(9)   Yadav, M.; Xu, Q.: Liquid-phase chemical hydrogen storage materials. *Energ. Environ. Sci.* **2012**, *5*, 9698-9725.

(10)   Hamilton, C. W.; Baker, R. T.; Staubitz, A.; Manners, I.: B-N compounds for chemical hydrogen storage. *Chem. Soc. Rev.* **2009**, *38*, 279-293.

(11)   Staubitz, A.; Robertson, A. P. M.; Manners, I.: Ammonia-borane and related compounds as dihydrogen sources. *Chem. Rev.* **2010**, *110*, 4079-4124.

(12)   Sanyal, U.; Demirci, U. B.; Jagirdar, B. R.; Miele, P.: Hydrolysis of ammonia borane as a hydrogen source: Fundamental issues and potential solutions towards implementation. *ChemSuschem* **2011**, *4*, 1731-1739.

(13)   Somorjai, G. A.; Park, J. Y.: Molecular factors of catalytic selectivity. *Angew. Chem. Inter. Ed.* **2008**, *47*, 9212-9228.

(14)   Uzio, D.; Berhault, G.: Factors governing the catalytic reactivity of metallic nanoparticles. *Catal. Rev,* **2010**, *52*, 106-131.

(15)   Norskov, J. K.; Bligaard, T.; Hvolbaek, B.; Abild-Pedersen, F.; Chorkendorff, I.; Christensen, C. H.: The nature of the active site in heterogeneous metal catalysis. *Chem. Soc. Rev.* **2008**, *37*, 2163-2171.

(16)   Campbell, C. T.: Catalyst-support interactions electronic perturbations. *Nat. Chem.* **2012**, *4*, 597-598.

(17)   Hayden, B. E.: Particle size and support effects in electrocatalysis. *Acc. Chem. Res.* **2013**, *46*, 1858-1866.

(18)   Surnev, S.; Fortunelli, A.; Netzer, F. P.: Structure-property relationship and chemical aspects of oxide-metal hybrid nanostructures. *Chem. Rev.* **2013**, *113*, 4314-4372.

(19)   Wu, J.; Li, P.; Pan, Y.-T.; Warren, S.; Yin, X.; Yang, H.: Surface lattice-engineered bimetallic nanoparticles and their catalytic properties. *Chem. Soc. Rev.* **2012**, *41*, 8066-8074.

(20)   Li, Y.; Somorjai, G. A.: Nanoscale advances in catalysis and energy applications. *Nano Lett.* **2010**, *10*, 2289-2295.

(21)   Bell, A. T.: The impact of nanoscience on heterogeneous catalysis. *Science* **2003**, *299*, 1688-1691.

(22)   Huber, G. W.; Shabaker, J. W.; Dumesic, J. A.: Raney Ni-Sn catalyst for H_2 production from biomass-derived hydrocarbons. *Science* **2003**, *300*, 2075-2077.

(23)   Valden, M.; Lai, X.; Goodman, D. W.: Onset of catalytic activity of gold clusters on titania with the appearance of nonmetallic properties. *Science* **1998**, *281*, 1647-1650.

(24)   Studt, F.; Sharafutdinov, I.; Abild-Pedersen, F.; Elkjaer, C. F.; Hummelshoj, J. S.; Dahl, S.; Chorkendorff, I.; Norskov, J. K.: Discovery of a Ni-Ga catalyst for carbon dioxide reduction to methanol. *Nat. Chem.* **2014**, *6*, 320-324.

(25)   Zaera, F.: Nanostructured materials for applications in heterogeneous catalysis. *Chem. Soc.Rev.* **2013**, *42*, 2746-2762.

(26)   Zhou, Z.-Y.; Tian, N.; Li, J.-T.; Broadwell, I.; Sun, S.-G.: Nanomaterials of high surface energy with exceptional properties in catalysis and energy storage. *Chem. Soc. Review.* **2011**, *40*, 4167-4185.

(27)   Somorjai, G. A.; Frei, H.; Park, J. Y.: Advancing the frontiers in nanocatalysis, biointerfaces, and renewable energy conversion by innovations of surface techniques. *J. Am. Chem. Soc.* **2009**, *131*, 16589-16605.

(28)   Spivey, J. J.: Catalysis in the development of clean energy technologies. *Catal. Today* **2005**, *100*, 171-180.

(29)   Tran, N. H.; Kannangara, G. S. K.: Conversion of glycerol to hydrogen rich gas. *Chem. Soc. Rev.* **2013**, *42*, 9454-9479.

(30)   Liu, K.; Wang, A.; Zhang, T.: Recent advances in preferential oxidation of CO reaction over platinum group metal catalysts. *ACS Catal.* **2012**, *2*, 1165-1178.

(31)   Lima Fonseca, J. d. S.; Ferreira, H. S.; Bion, N.; Pirault-Roy, L.; Rangel, M. d. C.; Duprez, D.; Epron, F.: Cooperative effect between copper and gold on ceria for CO-PROX reaction. *Catal.Today* **2012**, *180*, 34-41.

(32)   Sun, D.; Mazumder, V.; Metin, O.; Sun, S.: Catalytic hydrolysis of ammonia borane via cobalt palladium nanoparticles. *ACS Nano* **2011**, *5*, 6458-6464.

(33)   Yang, X.; Cheng, F.; Liang, J.; Tao, Z.; Chen, J.: Pt_xNi_{1-x} nanoparticles as catalysts for hydrogen generation from hydrolysis of ammonia borane. *Inter. J. Hydrogen Energy* **2009**, *34*, 8785-8791.

(34)   Chen, W.; Ji, J.; Feng, X.; Duan, X.; Qian, G.; Li, P.; Zhou, X.; Chen, D.; Yuan, W.: Mechanistic insight into size-dependent activity and durability in Pt/CNT catalyzed hydrolytic dehydrogenation of ammonia borane. *J. Am. Chem. Soc.* **2014**, *136*, 16736-16739.

(35)   Singh, S. K.; Xu, Q. A.: Bimetallic Ni-Pt nanocatalysts for selective decomposition of hydrazine in aqueous solution to hydrogen at room temperature for chemical hydrogen storage. *Inorg. Chem.* **2010**, *49*, 6148-6152.

(36)   Zhu, Q.-L.; Li, J.; Xu, Q.: Immobilizing metal nanoparticles to metal-organic frameworks with size and location control for optimizing catalytic performance. *J. Am. Chem. Soc.* **2013**, *135*, 10210-10213.

(37)   Kipnis, M.: Gold in CO oxidation and PROX: The role of reaction exothermicity and nanometer-scale particle size. *Appl. Catal. B.* **2014**, *152*, 38-45.

(38) Chen, L.; Ma, D.; Zhang, Z.; Guo, Y.; Ye, D.; Huang, B.: Synergistic effect of a carbon black supported PtAg non-alloy bimetal nanocatalyst for CO preferential oxidation in excess hydrogen. *ChemCatchem* **2012**, *4*, 1960-1967.

(39) Xu, H.; Fu, Q.; Yao, Y.; Bao, X.: Highly active Pt-Fe bicomponent catalysts for CO oxidation in the presence and absence of H-2. *Energ. Environ. Sci.* **2012**, *5*, 6313-6320.

(40) Alayoglu, S.; Nilekar, A. U.; Mavrikakis, M.; Eichhorn, B.: Ru-Pt core-shell nanoparticles for preferential oxidation of carbon monoxide in hydrogen. *Nat. Mater.* **2008**, *7*, 333-338.

(41) Singh, S. K.; Singh, A. K.; Aranishi, K.; Xu, Q.: Noble-Metal-Free bimetallic nanoparticle-catalyzed selective hydrogen generation from hydrous hydrazine for chemical hydrogen storage. *J. Am. Chem. Soc.* **2011**, *133*, 19638-19641.

(42) Hu, J.; Chen, Z.; Li, M.; Zhou, X.; Lu, H.: Amine-Capped Co nanoparticles for highly efficient dehydrogenation of ammonia borane. *Acs Appl. Mater. Interfaces* **2014**, *6*, 13191-13200.

(43) Li, P.-Z.; Aijaz, A.; Xu, Q.: Highly dispersed surfactant-free nickel nanoparticles and their remarkable catalytic activity in the hydrolysis of ammonia borane for hydrogen generation. *Angew. Chem. Int. Ed.* **2012**, *51*, 6753-6756.

(44) Qiu, F. Y.; Wang, Y. J.; Wang, Y. P.; Li, L.; Liu, G.; Yan, C.; Jiao, L. F.; Yuan, H. T.: Dehydrogenation of ammonia borane catalyzed by in situ synthesized Fe-Co nano-alloy in aqueous solution. *Catal. Today* **2011**, *170*, 64-68.

(45) Meng, X. Y.; Yang, L.; Cao, N.; Du, C.; Hu, K.; Su, J.; Luo, W.; Cheng, G. Z.: Graphene-Supported Trimetallic Core-Shell Cu@CoNi Nanoparticles for Catalytic Hydrolysis of Amine Borane. *Chempluschem* **2014**, *79*, 325-332.

(46) Zhou, X.; Chen, Z.; Yan, D.; Lu, H.: Deposition of Fe-Ni nanoparticles on polyethyleneimine-decorated graphene oxide and application in catalytic dehydrogenation of ammonia borane. *J. Mater. Chem.* **2012**, *22*, 13506-13516.

(47) Metin, O.; Mazumder, V.; Ozkar, S.; Sun, S.: Monodisperse nickel nanoparticles and their catalysis in hydrolytic dehydrogenation of ammonia borane. *J. Am. Chem. Soc.* **2010**, *132*, 1468-+.

(48) Wang, J.; Li, Y.; Zhang, Y.: Precious-Metal-Free nanocatalysts for highly efficient hydrogen production from hydrous hydrazine. *Adv. Funct. Mater.* **2014**, *24*, 7073-7077.

(49) Wang, H. L.; Yan, J. M.; Li, S. J.; Zhang, X. W.; Jiang, Q.: Noble-metal-free NiFeMo nanocatalyst for hydrogen generation from the decomposition of hydrous hydrazine. *J. Mater. Chem. A* **2015**, *3*, 121-124.

(50) Zhang, J. J.; Kang, Q.; Yang, Z. Q.; Dai, H. B.; Zhuang, D. W.; Wang, P.: A cost-effective NiMoB-La(OH)$_3$ catalyst for hydrogen generation from decomposition of alkaline hydrous hydrazine solution. *J. Mater.Chem. A* **2013**, *1*, 11623-11628.

(51) Kydd, R.; Teoh, W. Y.; Wong, K.; Wang, Y.; Scott, J.; Zeng, Q.-H.; Yu, A.-B.; Zou, J.; Amal, R.: Flame-Synthesized Ceria-Supported Copper Dimers for Preferential Oxidation of CO. *Adv. Funct. Mater.* **2009**, *19*, 369-377.

(52) Arango-Diaz, A.; Moretti, E.; Talon, A.; Storaro, L.; Lenarda, M.; Nunez, P.; Marrero-Jerez, J.; Jimenez-Jimenez, J.; Jimenez-Lopez, A.; Rodriguez-Castellon, E.: Preferential CO oxidation (CO-PROX) catalyzed by CuO supported on nanocrystalline CeO$_2$ prepared by a freeze-drying method. *Appl. Catal. A* **2014**, *477*, 54-63.

(53) Liu, X.; Han, L.; Liu, W.; Yang, Y.: Synthesis of Co/Ni unitary- or binary-doped CeO$_2$ mesoporous nanospheres and their catalytic performance for CO oxidation. *Eur. J. Inorg. Chem.* **2014**, 5370-5377.

(54)   Gamarra, D.; Belver, C.; Fernandez-Garcia, M.; Martinez-Arias, A.: Selective CO oxidation in excess H_2 over copper-ceria catalysts: Identification of active entities/species. *J. Am. Chem. Soc.* **2007**, *129*, 12064.

(55)   Chorkendorff, I.; Niemantsverdriet, J. W.: *Concepts of Modern Catalysis and Kinetics*; Wiley, 2007.

(56)   Boudart, M.; Djega-Mariadassou, G.: *Kinetics of Heterogeneous Catalytic Reactions*; Princeton University Press, 2014.

(57)   Hagen, J.: *Industrial Catalysis: A Practical Approach*; Wiley, 2006.

(58)   Ertl, G.; Knözinger, H.; Schüth, F.; Weitkamp, J.: *Handbook of Heterogeneous Catalysis, Volume 1,* Wiley, 2008.

(59)   Nilsson, A.; Pettersson, L. G. M.; Norskov, J.: *Chemical Bonding at Surfaces and Interfaces*; Elsevier Science, 2011.

(60)   Hammer, B.; Norskov, J. K.: Theoretical surface science and catalysis - Calculations and concepts. In *Advances in Catalysis, Vol 45: Impact of Surface Science on Catalysis*; Gates, B. C., Knozinger, H., Eds., 2000; Vol. 45; pp 71-129.

(61)   Somorjai, G. A.: *Introduction to Surface Chemistry and Catalysis*; Wiley, 1994.

(62)   Zhang, Q.; Wang, H.: Facet-Dependent catalytic activities of Au nanoparticles enclosed by high-index facets. *Acs Catal.* **2014**, *4*, 4027-4033.

(63)   Zhou, K.; Li, Y.: Catalysis based on nanocrystals with well-defined facets. *Angew. Chem. Int. Ed.* **2012**, *51*, 602-613.

(64)   Liu, G.; Yu, J. C.; Lu, G. Q.; Cheng, H.-M.: Crystal facet engineering of semiconductor photocatalysts: motivations, advances and unique properties. *Chem.Commun.* **2011**, *47*, 6763-6783.

(65)   Zaera, F.: Shape-Controlled nanostructures in heterogeneous catalysis. *ChemSuschem* **2013**, *6*, 1797-1820.

(66)   Li, Y.; Liu, Q.; Shen, W.: Morphology-dependent nanocatalysis: metal particles. *Dalton Trans.* **2011**, *40,* 5811-5826.

(67)   Vojvodic, A.; Norskov, J. K.; Abild-Pedersen, F.: Electronic structure effects in transition metal surface chemistry. *Top. Catal.* **2014**, *57*, 25-32.

(68)   Pushkarev, V. V.; Zhu, Z.; An, K.; Hervier, A.; Somorjai, G. A.: Monodisperse metal nanoparticle catalysts: synthesis, characterizations, and molecular studies under reaction conditions. *Top. Catal.* **2012**, *55*, 1257-1275.

(69)   Che, M.; Vedrine, J. C.: *Characterization of Solid Materials and Heterogeneous Catalysts: From Structure to Surface Reactivity*; Wiley, 2012.

(70)   Yang, J.; Chen, X.; Yang, X.; Ying, J. Y.: Stabilization and compressive strain effect of AuCu core on Pt shell for oxygen reduction reaction. *Energ. Environ. Sci.* **2012**, *5*, 8976-8981.

(71)   Strasser, P.; Koh, S.; Anniyev, T.; Greeley, J.; More, K.; Yu, C.; Liu, Z.; Kaya, S.; Nordlund, D.; Ogasawara, H.; Toney, M. F.; Nilsson, A.: Lattice-strain control of the activity in dealloyed core-shell fuel cell catalysts. *Nat. Chem.* **2010**, *2*, 454-460.

(72)   Weaver, J. F.: Surface chemistry of late transition metal oxides. *Chem. Rev.* **2013**, *113*, 4164-4215.

(73)   Barteau, M. A.: Organic reactions at well-defined oxide surfaces. *Chem. Rev.* **1996**, *96*, 1413-1430.

(74)   Woodruff, D. P.: Quantitative structural studies of corundum and rocksalt oxide surfaces. *Chem. Rev.* **2013**, *113*, 3863-3886.

178

(75)   An, K.; Somorjai, G. A.: Size and shape control of metal nanoparticles for reaction selectivity in catalysis. *ChemCatchem* **2012**, *4*, 1512-1524.

(76)   Schauermann, S.; Nilius, N.; Shaikhutdinov, S.; Freund, H.-J.: Nanoparticles for heterogeneous catalysis: new mechanistic insights. *Acc. Chem. Res.* **2013**, *46*, 1673-1681.

(77)   Bruce, P. G.; Scrosati, B.; Tarascon, J.-M.: Nanomaterials for rechargeable lithium batteries. *Angew. Chem. Int. Ed.* **2008**, *47*, 2930-2946.

(78)   An, K.; Alayoglu, S.; Ewers, T.; Somorjai, G. A.: Colloid chemistry of nanocatalysts: A molecular view. *J. Colloid Interf. Sci.* **2012**, *373*, 1-13.

(79)   Jia, C.-J.; Schueth, F.: Colloidal metal nanoparticles as a component of designed catalyst. *Phys. Chem. Chem. Phys.* **2011**, *13*, 2457-2487.

(80)   Somorjai, G. A.; Tao, F.; Park, J. Y.: The nanoscience revolution: Merging of colloid science, catalysis and nanoelectronics. *Top. Catal.* **2008**, *47*, 1-14.

(81)   Tsung, C.-K.; Kuhn, J. N.; Huang, W.; Aliaga, C.; Hung, L.-I.; Somorjai, G. A.; Yang, P.: Sub-10 nm Platinum nanocrystals with size and shape control: Catalytic study for ethylene and pyrrole hydrogenation. *J. Am. Chem. Soc.* **2009**, *131*, 5816-5822.

(82)   Van Santen, R. A.: Complementary structure sensitive and insensitive catalytic relationships. *Acc. Chem. Res.* **2009**, *42*, 57-66.

(83)   Kleis, J.; Greeley, J.; Romero, N. A.; Morozov, V. A.; Falsig, H.; Larsen, A. H.; Lu, J.; Mortensen, J. J.; Dulak, M.; Thygesen, K. S.; Norskov, J. K.; Jacobsen, K. W.: Finite size effects in chemical bonding: from small clusters to solids. *Catal. Lett.* **2011**, *141*, 1067-1071.

(84)   Srivastava, S.; Thomas, J. P.; Rahman, M. A.; Abd-Ellah, M.; Mohapatra, M.; Pradhan, D.; Heinig, N. F.; Leung, K. T.: Size-Selected TiO_2 nanocluster catalysts for efficient photoelectrochemical water splitting. *ACS Nano* **2014**, *8*, 11891-11898.

(85)   Che, M.; Bennett, C. O.: The influence of particle-size on the catalytic properties of supported metals. *Adv. Catal.* **1989**, *36*, 55-172.

(86)   Reske, R.; Mistry, H.; Behafarid, F.; Cuenya, B. R.; Strasser, P.: Particle size effects in the catalytic electroreduction of CO_2 on Cu nanoparticles. *J. Am. Chem. Soc.* **2014**, *136*, 6978-6986.

(87)   Musselwhite, N.; Somorjai, G. A.: Investigations of structure sensitivity in heterogeneous catalysis: from single crystals to monodisperse nanoparticles. *Top. Catal.* **2013**, *56*, 1277-1283.

(88)   Bezemer, G. L.; Bitter, J. H.; Kuipers, H.; Oosterbeek, H.; Holewijn, J. E.; Xu, X. D.; Kapteijn, F.; van Dillen, A. J.; de Jong, K. P.: Cobalt particle size effects in the Fischer-Tropsch reaction studied with carbon nanofiber supported catalysts. *J. Am. Chem. Soc.* **2006**, *128*, 3956-3964.

(89)   Ferrando, R.; Jellinek, J.; Johnston, R. L.: Nanoalloys: From theory to applications of alloy clusters and nanoparticles. *Chem. Rev.* **2008**, *108*, 845-910.

(90)   Greeley, J.; Mavrikakis, M.: Alloy catalysts designed from first principles. *Nat. Mater.* **2004**, *3*, 810-815.

(91)   Alonso, D. M.; Wettstein, S. G.; Dumesic, J. A.: Bimetallic catalysts for upgrading of biomass to fuels and chemicals. *Chem. Soc. Rev.* **2012**, *41*, 8075-8098.

(92)   Kuld, S.; Conradsen, C.; Moses, P. G.; Chorkendorff, I.; Sehested, J.: Quantification of zinc atoms in a surface alloy on copper in an industrial-type methanol synthesis catalyst. *Angew. Chem. Int. Ed.* **2014**, *53*, 5941-5945.

(93)   Ou, L. H.: The origin of enhanced electrocatalytic activity of Pt-M (M = Fe, Co, Ni, Cu, and W) alloys in PEM fuel cell cathodes: A DFT computational study. *Comput. Theor. Chem.* **2014**, *1048*, 69-76.

(94)   Chia, M.; O'Neill, B. J.; Alamillo, R.; Dietrich, P. J.; Ribeiro, F. H.; Miller, J. T.; Dumesic, J. A.: Bimetallic RhRe/C catalysts for the production of biomass-derived chemicals. *J. Catal.* **2013**, *308*, 226-236.

(95)   Holewinski, A.; Idrobo, J.-C.; Linic, S.: High-performance Ag-Co alloy catalysts for electrochemical oxygen reduction. *Nat. Chem.* **2014**, *6*, 828-834.

(96)   Kim, D.; Resasco, J.; Yu, Y.; Asiri, A. M.; Yang, P.: Synergistic geometric and electronic effects for electrochemical reduction of carbon dioxide using gold-copper bimetallic nanoparticles. *Nat. Commun.* **2014**, *5*.

(97)   Chen, M. S.; Kumar, D.; Yi, C. W.; Goodman, D. W.: The promotional effect of gold in catalysis by palladium-gold. *Science* **2005**, *310*, 291-293.

(98)   Prieto, G.; Beijer, S.; Smith, M. L.; He, M.; Au, Y.; Wang, Z.; Bruce, D. A.; de Jong, K. P.; Spivey, J. J.; de Jongh, P. E.: Design and synthesis of copper-cobalt catalysts for the selective conversion of synthesis gas to ethanol and higher alcohols. *Angew. Chem.Int. Ed.* **2014**, *53*, 6397-6401.

(99)   He, L.; Huang, Y. Q.; Liu, X. Y.; Li, L.; Wang, A. Q.; Wang, X. D.; Mou, C. Y.; Zhang, T.: Structural and catalytic properties of supported Ni-Ir alloy catalysts for H_2 generation via hydrous hydrazine decomposition. *Appl. Catal. B* **2014**, *147*, 779-788.

(100)   Ouyang, R.; Liu, J.-X.; Li, W.-X.: Atomistic theory of ostwald ripening and disintegration of supported metal particles under reaction conditions. *J. Am. Chem. Soc.* **2013**, *135*, 1760-1771.

(101)   Hansen, T. W.; Delariva, A. T.; Challa, S. R.; Datye, A. K.: Sintering of catalytic nanoparticles: particle migration or ostwald ripening? *Acc. Chem. Res.* **2013**, *46*, 1720-1730.

(102)   Farmer, J. A.; Campbell, C. T.: Ceria Maintains Smaller Metal Catalyst Particles by Strong Metal-Support Bonding. *Science* **2010**, *329*, 933-936.

(103)   Campbell, C. T.: The energetics of supported metal nanoparticles: relationships to sintering rates and catalytic activity. *Acc. Chem. Res.* **2013**, *46*, 1712-1719.

(104)   Jenness, G. R.; Schmidt, J. R.: Unraveling the role of metal-support interactions in heterogeneous catalysis: oxygenate selectivity in Fischer-Tropsch synthesis. *Acs Catal.* **2013**, *3*, 2881-2890.

(105)   Acerbi, N.; Tsang, S. C. E.; Jones, G.; Golunski, S.; Collier, P.: Rationalization of interactions in precious metal/ceria catalysts using the d-band center model. *Angew. Chem. Int. Ed.* **2013**, *52*, 7737-7741.

(106)   Hu, P.; Huang, Z.; Amghouz, Z.; Makkee, M.; Xu, F.; Kapteijn, F.; Dikhtiarenko, A.; Chen, Y.; Gu, X.; Tang, X.: Electronic metal- support interactions in single- atom catalysts. *Angew. Chem. Int. Ed.* **2014**, *53*, 3418-3421.

(107)   Mudiyanselage, K.; Senanayake, S. D.; Feria, L.; Kundu, S.; Baber, A. E.; Graciani, J.; Vidal, A. B.; Agnoli, S.; Evans, J.; Chang, R.; Axnanda, S.; Liu, Z.; Sanz, J. F.; Liu, P.; Rodriguez, J. A.; Stacchiola, D. J.: Importance of the metal-oxide interface in catalysis: In situ studies of the Water-Gas Shift reaction by ambient-pressure X-ray photoelectron spectroscopy. *Angew. Chem. Int. Ed.* **2013**, *52*, 5101-5105.

(108)   Carrasco, J.; Barrio, L.; Liu, P.; Rodriguez, J. A.; Veronica Ganduglia-Pirovano, M.: Theoretical studies of the adsorption of CO and C on Ni(111) and Ni/CeO$_2$(111): Evidence of a strong metal-support interaction. *J. Phys. Chem. C* **2013**, *117*, 8241-8250.

(109) Yang, Z.; Xie, L.; Ma, D.; Wang, G.: Origin of the high activity of the ceria-supported copper catalyst for H_2O dissociation. *J. Phys. Chem. C* **2011**, *115*, 6730-6740.

(110) Bruix, A.; Rodriguez, J. A.; Ramirez, P. J.; Senanayake, S. D.; Evans, J.; Park, J. B.; Stacchiola, D.; Liu, P.; Hrbek, J.; Illas, F.: A new type of strong metal-support interaction and the production of H_2 through the transformation of water on $Pt/CeO_2(111)$ and $Pt/CeO_x/TiO_2(110)$ catalysts. *J. Am. Chem. Soc.* **2012**, *134*, 8968-8974.

(111) Chiesa, M.; Giamello, E.; Di Valentin, C.; Pacchioni, G.; Sojka, Z.; Van Doorslaer, S.: Nature of the chemical bond between metal atoms and oxide surfaces: New evidences from spin density studies of K atoms on alkaline earth oxides. *J. Am. Chem. Soc.* **2005**, *127*, 16935-16944.

(112) Graciani, J.; Mudiyanselage, K.; Xu, F.; Baber, A. E.; Evans, J.; Senanayake, S. D.; Stacchiola, D. J.; Liu, P.; Hrbek, J.; Fernandez Sanz, J.; Rodriguez, J. A.: Highly active copper-ceria and copper-ceria-titania catalysts for methanol synthesis from CO_2. *Science* **2014**, *345*, 546-550.

(113) Haruta, M.: Catalysis of gold nanoparticles deposited on metal oxides. *Cattech* **2002**, *6*, 102-115.

(114) Xu, C.; Du, Y.; Li, C.; Yang, J.; Yang, G.: Insight into effect of acid/base nature of supports on selectivity of glycerol oxidation over supported Au-Pt bimetallic catalysts. *Appl. Catal. B* **2015**, *164*, 334-343.

(115) Sarkar, B.; Pendem, C.; Konathala, L. N. S.; Tiwari, R.; Sasaki, T.; Bal, R.: Cu nanoclusters supported on nanocrystalline SiO_2-MnO_2: a bifunctional catalyst for the one-step conversion of glycerol to acrylic acid. *Chem.Commun.* **2014**, *50*, 9707-9710.

(116) Crisci, A. J.; Tucker, M. H.; Dumesic, J. A.; Scott, S. L.: Bifunctional solid catalysts for the selective conversion of fructose to 5-Hydroxymethylfurfural. *Top. Catal.* **2010**, *53*, 1185-1192.

(117) Lu, G. Q.; Zhao, X. S.; Wei, T. K.: *Nanoporous materials: science and engineering*; Imperial College Press, 2004; Vol. 4.

(118) Prieto, G.; Shakeri, M.; de Jong, K. P.; de Jongh, P. E.: Quantitative relationship between support porosity and the stability of pore-confined metal nanoparticles studied on $CuZnO/SiO_2$ methanol synthesis catalysts. *ACS Nano* **2014**, *8*, 2522-2531.

(119) Shakeri, M.; Gebbink, R. J. M. K.; de Jongh, P. E.; de Jong, K. P.: Tailoring the window sizes to control the local concentration and activity of (salen)co catalysts in plugged nanochannels of SBA-15 materials. *Angew. Chem. Int. Ed.* **2013**, *52*, 10854-10857.

(120) Dolores Gonzalez, M.; Salagre, P.; Linares, M.; Garcia, R.; Serrano, D.; Cesteros, Y.: Effect of hierarchical porosity and fluorination on the catalytic properties of zeolite beta for glycerol etherification. *Appl. Catal. A* **2014**, *473*, 75-82.

(121) Kim, N. I.; Cheon, J. Y.; Kim, J. H.; Seong, J.; Park, J. Y.; Joo, S. H.; Kwon, K.: Impact of framework structure of ordered mesoporous carbons on the performance of supported Pt catalysts for oxygen reduction reaction. *Carbon* **2014**, *72*, 354-364.

(122) Hindle, K. T.; Jackson, S. D.; Stirling, D.; Webb, G.: The hydrogenation of para-toluidine over rhodium/silica: The effect of metal particle size and support texture. *J. Catal.* **2006**, *241*, 417-425.

(123) Prieto, G.; Meeldijk, J. D.; de Jong, K. P.; de Jongh, P. E.: Interplay between pore size and nanoparticle spatial distribution: Consequences for the stability of $CuZn/SiO_2$ methanol synthesis catalysts. *J. Catal.* **2013**, *303*, 31-40.

(124) Ren, L.-H.; Zhang, H.-L.; Lu, A.-H.; Hao, Y.; Li, W.-C.: Porous silica as supports for controlled fabrication of Au/CeO$_2$/SiO$_2$ catalysts for CO oxidation: Influence of the silica nanostructures. *Microporous Mesoporous Mater.* **2012**, *158*, 7-12.

(125) Prieto, G.; Zecevic, J.; Friedrich, H.; de Jong, K. P.; de Jongh, P. E.: Towards stable catalysts by controlling collective properties of supported metal nanoparticles. *Nat. Mater.* **2013**, *12*, 34-39.

(126) Balcar, H.; Cejka, J.: Mesoporous molecular sieves as advanced supports for olefin metathesis catalysts. *Coord. Chem. Rev.* **2013**, *257*, 3107-3124.

(127) Tueysuez, H.; Schueth, F.: Ordered mesoporous materials as catalysts. In *Advances in Catalysis, Vol 55*; Gates, B. C., Jentoft, F. C., Eds., 2012; Vol. 55; pp 127-239.

(128) Luque, R.; Garcia Martinez, J.: Editorial: From mesoporous supports to mesoporous catalysts: Introducing functionality to mesoporous materials. *ChemCatchem* **2013**, *5*, 827-829.

(129) Kresge, C. T.; Roth, W. J.: The discovery of mesoporous molecular sieves from the twenty year perspective. *Chem. Soc. Rev.* **2013**, *42*, 3663-3670.

(130) Ren, Y.; Ma, Z.; Bruce, P. G.: Ordered mesoporous metal oxides: synthesis and applications. *Chem. Soc. Rev.* **2012**, *41*, 4909-4927.

(131) Ye, Y.; Jo, C.; Jeong, I.; Lee, J.: Functional mesoporous materials for energy applications: solar cells, fuel cells, and batteries. *Nanoscale* **2013**, *5*, 4584-4605.

(132) Wagner, T.; Haffer, S.; Weinberger, C.; Klaus, D.; Tiemann, M.: Mesoporous materials as gas sensors. *Chem. Soc. Rev.* **2013**, *42*, 4036-4053.

(133) Nair, M. M.; Yen, H.; Kleitz, F.: Nanocast mesoporous mixed metal oxides for catalytic applications. *CR Chim.* **2014**, *17*, 641-655.

(134) Soler-illia, G. J. D.; Sanchez, C.; Lebeau, B.; Patarin, J.: Chemical strategies to design textured materials: From microporous and mesoporous oxides to nanonetworks and hierarchical structures. *Chem. Rev.* **2002**, *102*, 4093-4138.

(135) Wan, Y.; Zhao, D.: On the controllable soft-templating approach to mesoporous silicates. *Chem. Rev.* **2007**, *107*, 2821-2860.

(136) Boettcher, S. W.; Fan, J.; Tsung, C. K.; Shi, Q. H.; Stucky, G. D.: Harnessing the sol-gel process for the assembly of non-silicate mesostructured oxide materials. *Acc. Chem. Res.* **2007**, *40*, 784-792.

(137) Wan, Y.; Shi, Y.; Zhao, D.: Designed synthesis of mesoporous solids via nonionic-surfactant-templating approach. *Chem. Commun.* **2007**, 897-926.

(138) Soler-Illia, G.; Crepaldi, E. L.; Grosso, D.; Sanchez, C.: Block copolymer-templated mesoporous oxides. *Curr. Opin. Colloid In.* **2003**, *8*, 109-126.

(139) Klabunde, K. J.; Richards, R. M.: *Nanoscale Materials in Chemistry*; Wiley, 2009.

(140) Beck, J. S.; Vartuli, J. C.; Roth, W. J.; Leonowicz, M. E.; Kresge, C. T.; Schmitt, K. D.; Chu, C. T. W.; Olson, D. H.; Sheppard, E. W.; McCullen, S. B.; Higgins, J. B.; Schlenker, J. L.: A new family of mesoporous molecular-sieves prepared with liquid-crystal templates. *J. Am. Chem. Soc.* **1992**, *114*, 10834-10843.

(141) Schmidt-Winkel, P.; Lukens, W. W.; Zhao, D. Y.; Yang, P. D.; Chmelka, B. F.; Stucky, G. D.: Mesocellular siliceous foams with uniformly sized cells and windows. *J. Am. Chem. Soc.* **1999**, *121*, 254-255.

(142) Kipkemboi, P.; Fogden, A.; Alfredsson, V.; Flodstrom, K.: Triblock copolymers as templates in mesoporous silica formation: Structural dependence on polymer chain length and synthesis temperature. *Langmuir* **2001**, *17*, 5398-5402.

182

(143)   Kim, T. W.; Ryoo, R.; Kruk, M.; Gierszal, K. P.; Jaroniec, M.; Kamiya, S.; Terasaki, O.: Tailoring the pore structure of SBA-16 silica molecular sieve through the use of copolymer blends and control of synthesis temperature and time. *J. Phys. Chem. B* **2004**, *108*, 11480-11489.

(144)   Choi, M.; Heo, W.; Kleitz, F.; Ryoo, R.: Facile synthesis of high quality mesoporous SBA-15 with enhanced control of the porous network connectivity and wall thickness. *Chem. Commun.* **2003**, 1340-1341.

(145)   Zhao, D. Y.; Huo, Q. S.; Feng, J. L.; Chmelka, B. F.; Stucky, G. D.: Nonionic triblock and star diblock copolymer and oligomeric surfactant syntheses of highly ordered, hydrothermally stable, mesoporous silica structures. *J. Am. Chem. Soc.* **1998**, *120*, 6024-6036.

(146)   Antonelli, D. M.; Ying, J. Y.: Synthesis of hexagonally packed mesoporous TiO_2 by a modified sol-gel method. *Angew. Chem. Int. Ed.* **1995**, *34*, 2014-2017.

(147)   Schuth, F.: Non-siliceous mesostructured and mesoporous materials. *Chem. Mater.* **2001**, *13*, 3184-3195.

(148)   Ciesla, U.; Schuth, F.: Ordered mesoporous materials. *Microporous Mesoporous Mater.* **1999**, *27*, 131-149.

(149)   Yang, P. D.; Zhao, D. Y.; Margolese, D. I.; Chmelka, B. F.; Stucky, G. D.: Generalized syntheses of large-pore mesoporous metal oxides with semicrystalline frameworks. *Nature* **1998**, *396*, 152-155.

(150)   Lu, A. H.; Zhao, D.; Wan, Y.: *Nanocasting: A Versatile Strategy for Creating Nanostructured Porous Materials*; Royal Society of Chemistry, 2010.

(151)   Smatt, J. H.; Weidenthaler, C.; Rosenholm, J. B.; Linden, M.: Hierarchically porous metal oxide monoliths prepared by the nanocasting route. *Chem. Mater.* **2006**, *18*, 1443-1450.

(152)   Lepoutre, S.; Julian-Lopez, B.; Sanchez, C.; Amenitsch, H.; Linden, M.; Grosso, D.: Nanocasted mesoporous nanocrystalline ZnO thin films. *J. Mater. Chem.* **2010**, *20*, 537-542.

(153)   Sayler, F. M.; Grano, A. J.; Smatt, J.-H.; Linden, M.; Bakker, M. G.: Nanocasting of hierarchically porous Co_3O_4, Co, NiO, Ni, and Ag, monoliths: Impact of processing conditions on fidelity of replication. *Microporous Mesoporous Mater.* **2014**, *184*, 141-150.

(154)   Smatt, J.-H.; Schuwer, N.; Jarn, M.; Lindner, W.; Linden, M.: Synthesis of micrometer sized mesoporous metal oxide spheres by nanocasting. *Microporous Mesoporous Mater.* **2008**, *112*, 308-318.

(155)   Tian, B. Z.; Liu, X. Y.; Yang, H. F.; Xie, S. H.; Yu, C. Z.; Tu, B.; Zhao, D. Y.: General synthesis of ordered crystallized metal oxide nanoarrays replicated by microwave-digested mesoporous silica. *Adv. Mater.* **2003**, *15*, 1370-1374.

(156)   Rumplecker, A.; Kleitz, F.; Salabas, E.-L.; Schueth, F.: Hard templating pathways for the synthesis of nanostructured porous Co_3O_4. *Chem. Mater.* **2007**, *19*, 485-496.

(157)   Jiao, F.; Harrison, A.; Jumas, J. C.; Chadwick, A. V.; Kockelmann, W.; Bruce, P. G.: Ordered mesoporous Fe_2O_3 with crystalline walls. *J. Am. Chem. Soc.* **2006**, *128*, 5468-5474.

(158)   Gu, X.; Zhu, W.; Jia, C.; Zhao, R.; Schmidt, W.; Wang, Y.: Synthesis and microwave absorbing properties of highly ordered mesoporous crystalline $NiFe_2O_4$. *Chem. Commun.* **2011**, *47*, 5337-5339.

(159)   Laha, S. C.; Ryoo, R.: Synthesis of thermally stable mesoporous cerium oxide with nanocrystalline frameworks using mesoporous silica templates. *Chem. Commun.* **2003**, 2138-2139.

(160) Roggenbuck, J.; Waitz, T.; Tiemann, M.: Synthesis of mesoporous metal oxides by structure replication: Strategies of impregnating porous matrices with metal salts. *Microporous Mesoporous Mater.* **2008**, *113*, 575-582.

(161) Wang, Y. M.; Wu, Z. Y.; Wang, H. J.; Zhu, J. H.: Fabrication of metal oxides occluded in ordered mesoporous hosts via a solid-state grinding route: The influence of host-guest interactions. *Adv. Funct. Mater.* **2006**, *16*, 2374-2386.

(162) Yue, W.; Zhou, W.: Porous crystals of cubic metal oxides templated by cage-containing mesoporous silica. *J. Mater.Chem.* **2007**, *17*, 4947-4952.

(163) Wang, Y. Q.; Yang, C. M.; Schmidt, W.; Spliethoff, B.; Bill, E.; Schuth, F.: Weakly ferromagnetic ordered mesoporous Co_3O_4 synthesized by nanocasting from vinyl-functionalized cubic Ia3d mesoporous silica. *Adv. Mater.* **2005**, *17*, 53-55.

(164) Zhu, K. K.; Yue, B.; Zhou, W. Z.; He, H. Y.: Preparation of three-dimensional chromium oxide porous single crystals templated by SBA-15. *Chem. Commun.* **2003**, 98-99.

(165) Yang, H. F.; Zhao, D. Y.: Synthesis of replica mesostructures by the nanocasting strategy. *J. Mater. Chem.* **2005**, *15*, 1217-1231.

(166) de Jong, K. P.: *Synthesis of Solid Catalysts*; Wiley, 2009.

(167) Myers, D.: *Surfaces, interfaces and colloids*; Wiley-Vch, New York, 1990.

(168) Jiao, F.; Bruce, P. G.: Mesoporous crystalline beta-MnO_2- a reversible positive electrode for rechargeable lithium batteries. *Adv. Mater.* **2007**, *19*, 657-660.

(169) Imperor-Clerc, M.; Bazin, D.; Appay, M. D.; Beaunier, P.; Davidson, A.: Crystallization of beta-MnO_2 nanowires in the pores of SBA-15 silicas: In situ investigation using synchrotron radiation. *Chem. Mater.* **2004**, *16*, 1813-1821.

(170) Nair, M. M.; Kaliaguine, S.; Kleitz, F.: Nanocast $LaNiO_3$ perovskites as precursors for the preparation of coke-resistant dry reforming catalysts. *ACS Catal.* **2014**, *4*, 3837-3846.

(171) Nair, M. M.; Kleitz, F.; Kaliaguine, S.: Kinetics of methanol oxidation over mesoporous perovskite catalysts. *ChemCatchem* **2012**, *4*, 387-394.

(172) Sun, X.; Shi, Y.; Zhang, P.; Zheng, C.; Zheng, X.; Zhang, F.; Zhang, Y.; Guan, N.; Zhao, D.; Stucky, G. D.: Container effect in nanocasting synthesis of mesoporous metal oxides. *J. Am. Chem. Soc.* **2011**, *133*, 14542-14545.

(173) Taguchi, A.; Schuth, F.: Ordered mesoporous materials in catalysis. *Microporous Mesoporous Mater.* **2005**, *77*, 1-45.

(174) Munnik, P.; Krans, N. A.; de Jongh, P. E.; de Jong, K. P.: Effects of drying conditions on the synthesis of Co/SiO_2 and Co/Al_2O_3 Fischer-Tropsch catalysts. *ACS Catal.* **2014**, *4*, 3219-3226.

(175) Zhu, Y.; Kong, X.; Cao, D.-B.; Cui, J.; Zhu, Y.; Li, Y.-W.: The rise of calcination temperature enhances the performance of Cu catalysts: contributions of support. *ACS Catal.* **2014**, *4*, 3675-3681.

(176) Faungnawakij, K.; Kikuchi, R.; Shimoda, N.; Fukunaga, T.; Eguchi, K.: Effect of Thermal treatment on activity and durability of $CuFe_2O_4$-Al_2O_3 composite catalysts for steam reforming of dimethyl ether. *Angew. Chem. Int. Ed.* **2008**, *47*, 9314-9317.

(177) Lee, S. Y.; Aris, R.: The distribution of active ingredients in supported catalysts prepared by impregnation. *Catal. Rev.* **1985**, *27*, 207-340.

(178) Eggenhuisen, T. M.; Friedrich, H.; Nudelman, F.; Zecevic, J.; Sommerdijk, N. A. J. M.; de Jongh, P. E.; de Jong, K. P.: Controlling the distribution of supported nanoparticles by aqueous synthesis. *Chem. Mater.* **2013**, *25*, 890-896.

(179) Sietsma, J. R. A.; Meeldijk, J. D.; den Breejen, J. P.; Versluijs-Helder, M.; van Dillen, A. J.; de Jongh, P. E.; de Jong, K. P.: The preparation of supported NiO and Co_3O_4 nanoparticles by the nitric oxide controlled thermal decomposition of nitrates. *Angew. Chem. Int. Ed.* **2007**, *46*, 4547-4549.

(180) Eschemann, T. O.; Bitter, J. H.; de Jong, K. P.: Effects of loading and synthesis method of titania-supported cobalt catalysts for Fischer-Tropsch synthesis. *Catal. Today* **2014**, *228*, 89-95.

(181) Campelo, J. M.; Luna, D.; Luque, R.; Marinas, J. M.; Romero, A. A.: Sustainable preparation of supported metal nanoparticles and their applications in catalysis. *ChemSuschem* **2009**, *2*, 18-45.

(182) An, K.; Alayoglu, S.; Musselwhite, N.; Na, K.; Somorjai, G. A.: Designed catalysts from Pt nanoparticles supported on macroporous oxides for selective isomerization of n-Hexane. *J. Am. Chem. Soc.* **2014**, *136*, 6830-6833.

(183) Shen, J.; Ziaei-Azad, H.; Semagina, N.: Is it always necessary to remove a metal nanoparticle stabilizer before catalysis? *J. Mol. Catal. A: Chem.* **2014**, *391*, 36-40.

(184) Naresh, N.; Wasim, F. G. S.; Ladewig, B. P.; Neergat, M.: Removal of surfactant and capping agent from Pd nanocubes (Pd-NCs) using tert-butylamine: its effect on electrochemical characteristics. *J. Mater. Chem. A* **2013**, *1*, 8553-8559.

(185) Thommes, M.: Physical Adsorption Characterization of Nanoporous Materials. *Chem. Ing. Tech.* **2010**, *82*, 1059-1073.

(186) Thommes, M.; Cychosz, K. A.: Physical adsorption characterization of nanoporous materials: progress and challenges. *Adsorption* **2014**, *20*, 233-250.

(187) Horikawa, T.; Do, D. D.; Nicholson, D.: Capillary condensation of adsorbates in porous materials. *Adv. Colloid Interface Sci.* **2011**, *169*, 40-58.

(188) Morishige, K.; Tateishi, N.; Fukuma, S.: Capillary condensation of nitrogen in MCM-48 and SBA-16. *J. Phys. Chem. B* **2003**, *107*, 5177-5181.

(189) Rasmussen, C. J.; Vishnyakov, A.; Thommes, M.; Smarsly, B. M.; Kleitz, F.; Neimark, A. V.: Cavitation in metastable liquid nitrogen confined to nanoscale pores. *Langmuir* **2010**, *26*, 10147-10157.

(190) Neimark, A. V.; Ravikovitch, P. I.: Capillary condensation in MMS and pore structure characterization. *Microporous Mesoporous Mater.* **2001**, *44*, 697-707.

(191) Zeng, Y.; Fan, C.; Do, D. D.; Nicholson, D.: Evaporation from an ink-bottle pore: Mechanisms of adsorption and desorption. *Ind. Eng. Chem. Res.* **2014**, *53*, 15467-15474.

(192) Landers, J.; Gor, G. Y.; Neimark, A. V.: Density functional theory methods for characterization of porous materials. *Colloids and Surfaces A* **2013**, *437*, 3-32.

(193) Ravikovitch, P. I.; Vishnyakov, A.; Neimark, A. V.: Density functional theories and molecular simulations of adsorption and phase transitions in nanopores. *Phys.Rev.E* **2001**, *64,*1-20.

(194) Cullity, B. D.; Stock, S. R.: *Elements of X-ray Diffraction*; Prentice Hall, 2001.

(195) Behrens, M.; Studt, F.; Kasatkin, I.; Kuehl, S.; Haevecker, M.; Abild-Pedersen, F.; Zander, S.; Girgsdies, F.; Kurr, P.; Kniep, B.-L.; Tovar, M.; Fischer, R. W.; Norskov, J. K.; Schloegl, R.: The active site of methanol synthesis over $Cu/ZnO/Al_2O_3$ industrial catalysts. *Science* **2012**, *336*, 893-897.

(196) Gunter, M. M.; Ressler, T.; Bems, B.; Buscher, C.; Genger, T.; Hinrichsen, O.; Muhler, M.; Schlogl, R.: Implication of the microstructure of binary Cu/ZnO catalysts for their catalytic activity in methanol synthesis. *Catal. Lett.* **2001**, *71*, 37-44.

(197)   Amakawa, K.; Sun, L.; Guo, C.; Haevecker, M.; Kube, P.; Wachs, I. E.; Lwin, S.; Frenkel, A. I.; Patlolla, A.; Hermann, K.; Schloegl, R.; Trunschke, A.: How strain affects the reactivity of surface metal oxide catalysts. *Angew. Chem.Int. Ed.* **2013**, *52*, 13553-13557.

(198)   Gai, P. L.; Boyes, E. D.: *Electron Microscopy in Heterogeneous Catalysis*; Taylor & Francis, 2003.

(199)   Niemantsverdriet, J. W.: *Spectroscopy in Catalysis*; Wiley, 2007.

(200)   Gouadec, G.; Colomban, P.: Raman Spectroscopy of nanomaterials: How spectra relate to disorder, particle size and mechanical properties. *Prog. Cryst. Growth Charact. Mater.* **2007**, *53*, 1-56.

(201)   Nottbohm, C. T.; Hess, C.: Investigation of ceria by combined Raman, UV-vis and X-ray photoelectron spectroscopy. *Catal. Commun.* **2012**, *22*, 39-42.

(202)   Choi, Y. M.; Abernathy, H.; Chen, H.-T.; Lin, M. C.; Liu, M.: Characterization of O_2-CeO_2 interactions using in situ Raman spectroscopy and first-principle calculations. *ChemPhysChem* **2006**, *7*, 1957-1963.

(203)   McBride, J. R.; Hass, K. C.; Poindexter, B. D.; Weber, W. H.: Raman and x-ray studies of $Ce_{1-x}Re_xO_{2-y}$, Where Re=La, Pr, Nd, Eu, Gd, and Tb. *J. Appl. Phys.* **1994**, *76*, 2435-2441.

(204)   Kosacki, I.; Petrovsky, V.; Anderson, H. U.; Colomban, P.: Raman spectroscopy of nanocrystalline ceria and zirconia thin films. *J. Am. Ceram. Soc.* **2002**, *85*, 2646-2650.

(205)   Spanier, J. E.; Robinson, R. D.; Zheng, F.; Chan, S. W.; Herman, I. P.: Size-dependent properties of CeO_{2-y} nanoparticles as studied by Raman scattering. *Phys. Rev.B* **2001**, *64,* 1-8.

(206)   Acerbi, N.; Golunski, S.; Tsang, S. C.; Daly, H.; Hardacre, C.; Smith, R.; Collier, P.: Promotion of ceria catalysts by precious metals: Changes in nature of the interaction under reducing and oxidizing conditions. *J. Phys. Chem. C* **2012**, *116*, 13569-13583.

(207)   Liotta, L. F.; Longo, A.; Macaluso, A.; Martorana, A.; Pantaleo, G.; Venezia, A. M.; Deganello, G.: Influence of the SMSI effect on the catalytic activity of a $Pt(1\%)/Ce_{0.6}Zr_{0.4}O_2$ catalyst: SAXS, XRD, XPS and TPR investigations. *Appl.Catal. B* **2004**, *48*, 133-149.

(208)   Acerbi, N.; Tsang, S. C.; Golunski, S.; Collier, P.: A practical demonstration of electronic promotion in the reduction of ceria coated PGM catalysts. *Chem.Commun.* **2008**, 1578-1580.

(209)   Jean, D.; Nohair, B.; Bergeron, J.-Y.; Kaliaguine, S.: Hydrogenolysis of glycerol over Cu/ZnO-based catalysts: Influence of transport phenomena using the madon-boudart criterion. *Ind. Eng. Chem. Res.* **2014**, *53*, 18740-18749.

(210)   Tien-Thao, N.; Zahedi-Niaki, M. H.; Alamdari, H.; Kaliaguine, S.: Effect of alkali additives over nanocrystalline Co-Cu-based perovskites as catalysts for higher-alcohol synthesis. *J. Catal.* **2007**, *245*, 348-357.

(211)   Levasseur, B.; Kaliaguine, S.: Effects of iron and cerium in $La_{1-y}Ce_yCo_{1-x}Fe_xO_3$ perovskites as catalysts for VOC oxidation. *Appl. Catal. B* **2009**, *88*, 305-314.

(212)   Levasseur, B.; Kaliaguine, S.: Methanol oxidation on $LaBO_3$ (B = Co, Mn, Fe) perovskite-type catalysts prepared by reactive grinding. *Appl. Catal. A* **2008**, *343*, 29-38.

(213)   Sarshar, Z.; Sun, Z.; Zhao, D.; Kaliaguine, S.: Development of sinter-resistant core-shell $LaMn_xFe_{1-x}O_3@mSiO_2$ oxygen carriers for chemical looping combustion. *Energy Fuels* **2012**, *26*, 3091-3102.

(214)   Sarshar, Z.; Kleitz, F.; Kaliaguine, S.: Novel oxygen carriers for chemical looping combustion: $La_{1-x}Ce_xBO_3$ (B = Co, Mn) perovskites synthesized by reactive grinding and nanocasting. *Energ. Environ. Sci.* **2011**, *4*, 4258-4269.

(215)   Zhang, R. D.; Villanueva, A.; Alamdari, H.; Kaliaguine, S.: Cu- and Pd-substituted nanoscale Fe-based perovskites for selective catalytic reduction of NO by propene. *J. Catal.* **2006**, *237*, 368-380.

(216)   Wan, Y.; Ma, J. X.; Wang, Z.; Zhou, W.; Kaliaguine, S.: On the mechanism of selective catalytic reduction of NO by propylene over Cu-Al-MCM-41. *Appl.Catal. B* **2005**, *59*, 235-242.

(217)   Lu, A.-H.; Schueth, F.: Nanocasting: A versatile strategy for creating nanostructured porous materials. *Adv. Mater.* **2006**, *18*, 1793-1805.

(218)   Tiemann, M.: Repeated templating. *Chem. Mater.* **2008**, *20*, 961-971.

(219)   Ma, C. Y.; Mu, Z.; Li, J. J.; Jin, Y. G.; Cheng, J.; Lu, G. Q.; Hao, Z. P.; Qiao, S. Z.: Mesoporous Co_3O_4 and Au/Co_3O_4 Catalysts for Low-Temperature Oxidation of Trace Ethylene. *J. Am. Chem. Soc.* **2010**, *132*, 2608-2613.

(220)   Shi, Y.; Guo, B.; Corr, S. A.; Shi, Q.; Hu, Y.-S.; Heier, K. R.; Chen, L.; Seshadri, R.; Stucky, G. D.: Ordered mesoporous metallic MoO_2 materials with highly reversible lithium storage capacity. *Nano Lett.* **2009**, *9*, 4215-4220.

(221)   Ji, X.; Lee, K. T.; Nazar, L. F.: A highly ordered nanostructured carbon-sulphur cathode for lithium-sulphur batteries. *Nat. Mater.* **2009**, *8*, 500-506.

(222)   Cabo, M.; Pellicer, E.; Rossinyol, E.; Castel, O.; Surinach, S.; Baro, M. D.: Mesoporous $NiCo_2O_4$ spinel: Influence of calcination temperature over phase purity and thermal stability. *Cryst. Growth Des.* **2009**, *9*, 4814-4821.

(223)   Sun, Y.; Ji, G.; Zheng, M.; Chang, X.; Li, S.; Zhang, Y.: Synthesis and magnetic properties of crystalline mesoporous $CoFe_2O_4$ with large specific surface area. *J. Mater. Chem.* **2010**, *20*, 945-952.

(224)   Tueysuez, H.; Lehmann, C. W.; Bongard, H.; Tesche, B.; Schmidt, R.; Schueth, F.: Direct imaging of surface topology and pore system of ordered mesoporous silica (MCM-41, SBA-15, and KIT-6) and nanocast metal oxides by high resolution scanning electron microscopy. *J. Am. Chem. Soc.* **2008**, *130*, 11510-11517.

(225)   Luders, U.; Barthelemy, A.; Bibes, M.; Bouzehouane, K.; Fusil, S.; Jacquet, E.; Contour, J.-P.; Bobo, J.-F.; Fontcuberta, J.; Fert, A.: $NiFe_2O_4$: A versatile spinel material brings new opportunities for spintronics. *Adv. Mater.* **2006**, *18*, 1733-1736.

(226)   Vidal-Abarca, C.; Lavela, P.; Tirado, J. L.: The Origin of Capacity Fading in $NiFe_2O_4$ Conversion Electrodes for Lithium Ion Batteries Unfolded by Fe-57 Mossbauer Spectroscopy. *J. Phys. Chem. C* **2010**, *114*, 12828-12832.

(227)   Zhang, R.; Teoh, W. Y.; Amal, R.; Chen, B.; Kaliaguine, S.: Catalytic reduction of NO by CO over $Cu/Ce_xZr_{1-x}O_2$ prepared by flame synthesis. *J. Catal.* **2010**, *272*, 210-219.

(228)   Kleitz, F.; Berube, F.; Guillet-Nicolas, R.; Yang, C.-M.; Thommes, M.: Probing adsorption, pore condensation, and hysteresis behavior of pure fluids in three-dimensional cubic mesoporous KIT-6 silica. *J. Phys. Chem.C* **2010**, *114*, 9344-9355.

(229)   Kleitz, F.; Choi, S. H.; Ryoo, R.: Cubic Ia3d large mesoporous silica: synthesis and replication to platinum nanowires, carbon nanorods and carbon nanotubes. *Chem. Commun.* **2003**, 2136-2137.

(230)   Kim, T.-W.; Chung, P.-W.; Lin, V. S. Y.: Facile Synthesis of Monodisperse Spherical MCM-48 Mesoporous Silica Nanoparticles with Controlled Particle Size. *Chem. Mater.* **2010**, *22*, 5093-5104.

(231)   Na, C. W.; Han, D. S.; Park, J.; Jo, Y.; Jung, M. H.: Ferrimagnetic Mn_2SnO_4 nanowires. *Chem. Commun.* **2006**, 2251-2253.

(232) Lee, H.-W.; Muralidharan, P.; Ruffo, R.; Mari, C. M.; Cui, Y.; Kim, D. K.: Ultrathin spinel LiMn$_2$O$_4$ nanowires as high power cathode materials for Li-ion batteries. *Nano Lett.* **2010**, *10*, 3852-3856.

(233) Liao, Z. M.; Li, Y. D.; Xu, J.; Zhang, J. M.; Xia, K.; Yu, D. P.: Spin-filter effect in magnetite nanowire. *Nano Lett.* **2006**, *6*, 1087-1091.

(234) Djinovic, P.; Batista, J.; Levec, J.; Pintar, A.: Comparison of water-gas shift reaction activity and long-term stability of nanostructured CuO-CeO$_2$ catalysts prepared by hard template and co-precipitation methods. *Appl. Catal. A* **2009**, *364*, 156-165.

(235) Wan, L.; Cui, X.; Chen, H.; Shi, J.: Synthesis of ordered mesoporous CuO/CeO$_2$ composite via co-nanocasting replication method and its improved reactivity towards hydrogen. *Mater. Lett.* **2010**, *64*, 1379-1382.

(236) Ryoo, R.; Joo, S. H.; Jun, S.: Synthesis of highly ordered carbon molecular sieves via template-mediated structural transformation. *J. Phys.Chem. B* **1999**, *103*, 7743-7746.

(237) Yue, W.; Zhou, W.: Synthesis of porous single crystals of metal oxides via a solid-liquid route. *Chem. Mater.* **2007**, *19*, 2359-2363.

(238) Cao, J.-L.; Wang, Y.; Yu, X.-L.; Wang, S.-R.; Wu, S.-H.; Yuan, Z.-Y.: Mesoporous CuO-Fe$_2$O$_3$ composite catalysts for low-temperature carbon monoxide oxidation. *Appl. Catal. B* **2008**, *79*, 26-34.

(239) Zhang, Y.; Liang, H.; Gao, X. Y.; Liu, Y.: Three-dimensionally ordered macro-porous CuO-CeO$_2$ used for preferential oxidation of carbon monoxide in hydrogen-rich gases. *Catal. Commun.* **2009**, *10*, 1432-1436.

(240) Ren, Y.; Ma, Z.; Qian, L.; Dai, S.; He, H.; Bruce, P. G.: Ordered crystalline mesoporous oxides as catalysts for CO oxidation. *Catal. Lett.* **2009**, *131*, 146-154.

(241) Jin, M.; Park, J.-N.; Shon, J. K.; Kim, J. H.; Li, Z.; Park, Y.-K.; Kim, J. M.: Low temperature CO oxidation over Pd catalysts supported on highly ordered mesoporous metal oxides. *Catal. Today* **2012**, *185*, 183-190.

(242) Nilekar, A. U.; Alayoglu, S.; Eichhorn, B.; Mavrikakis, M.: Preferential CO oxidation in hydrogen: reactivity of core-shell nanoparticles. *J. Am. Chem. Soc.* **2010**, *132*, 7418-7428.

(243) Fu, Q.; Li, W.-X.; Yao, Y.; Liu, H.; Su, H.-Y.; Ma, D.; Gu, X.-K.; Chen, L.; Wang, Z.; Zhang, H.; Wang, B.; Bao, X.: Interface-Confined ferrous centers for catalytic oxidation. *Science* **2010**, *328*, 1141-1144.

(244) Tueysuez, H.; Comotti, M.; Schueth, F.: Ordered mesoporous Co$_3$O$_4$ as highly active catalyst for low temperature CO-oxidation. *Chem. Commun.* **2008**, 4022-4024.

(245) Avgouropoulos, G.; Ioannides, T.: Effect of synthesis parameters on catalytic properties of CuO-CeO$_2$. *Appl. Catal. B* **2006**, *67*, 1-11.

(246) Polster, C. S.; Nair, H.; Baertsch, C. D.: Study of active sites and mechanism responsible for highly selective CO oxidation in H$_2$ rich atmospheres on a mixed Cu and Ce oxide catalyst. *J. Catal.* **2009**, *266*, 308-319.

(247) Doi, Y.; Takai, A.; Sakamoto, Y.; Terasaki, O.; Yamauchi, Y.; Kuroda, K.: Tailored synthesis of mesoporous platinum replicas using double gyroid mesoporous silica (KIT-6) with different pore diameters via vapor infiltration of a reducing agent. *Chem. Commun.* **2010**, *46*, 6365-6367.

(248) Tueysuez, H.; Salabas, E. L.; Bill, E.; Bongard, H.; Spliethoff, B.; Lehmann, C. W.; Schueth, F.: Synthesis of hard magnetic ordered mesoporous Co$_3$O$_4$/CoFe$_2$O$_4$ nanocomposites. *Chem. Mater.* **2012**, *24*, 2493-2500.

(249) Jiao, F.; Hill, A. H.; Harrison, A.; Berko, A.; Chadwick, A. V.; Bruce, P. G.: Synthesis of ordered mesoporous NiO with crystalline walls and a bimodal pore size distribution. *J. Am. Chem. Soc.* **2008**, *130*, 5262-5266.

(250) Yen, H.; Seo, Y.; Guillet-Nicolas, R.; Kaliaguine, S.; Kleitz, F.: One-step-impregnation hard templating synthesis of high-surface-area nanostructured mixed metal oxides ($NiFe_2O_4$, $CuFe_2O_4$ and Cu/CeO_2). *Chem. Commun.* **2011**, *47*, 10473-10475.

(251) Strandwitz, N. C.; Stucky, G. D.: Hollow microporous cerium oxide spheres templated by colloidal silica. *Chem. Mater.* **2009**, *21*, 4577-4582.

(252) Giordano, F.; Trovarelli, A.; de Leitenburg, C.; Giona, M.: A model for the temperature-programmed reduction of low and high surface area ceria. *J. Catal.* **2000**, *193*, 273-282.

(253) Bera, P.; Priolkar, K. R.; Sarode, P. R.; Hegde, M. S.; Emura, S.; Kumashiro, R.; Lalla, N. P.: Structural investigation of combustion synthesized Cu/CeO_2 catalysts by EXAFS and other physical techniques: Formation of a $Ce_{1-x}Cu_xO_2$-delta solid solution. *Chem. Mater.* **2002**, *14*, 3591-3601.

(254) Stephens, F. H.; Pons, V.; Baker, R. T.: Ammonia - borane: the hydrogen source par excellence? *Dalton Trans.* **2007**, 2613-2626.

(255) Sutton, A. D.; Burrell, A. K.; Dixon, D. A.; Garner, E. B., III; Gordon, J. C.; Nakagawa, T.; Ott, K. C.; Robinson, P.; Vasiliu, M.: Regeneration of ammonia borane spent fuel by direct reaction with hydrazine and liquid ammonia. *Science* **2011**, *331*, 1426-1429.

(256) Chen, G.; Desinan, S.; Rosei, R.; Rosei, F.; Ma, D.: Hollow ruthenium nanoparticles with small dimensions derived from Ni@Ru core@shell structure: synthesis and enhanced catalytic dehydrogenation of ammonia borane. *Chem. Commun.* **2012**, *48*, 8009-8011.

(257) Chandra, M.; Xu, Q.: A high-performance hydrogen generation system: Transition metal-catalyzed dissociation and hydrolysis of ammonia-borane. *J. Power Sources* **2006**, *156*, 190-194.

(258) Kalidindi, S. B.; Indirani, M.; Jagirdar, B. R.: First row transition metal ion-assisted ammonia-borane hydrolysis for hydrogen generation. *Inorg. Chem.* **2008**, *47*, 7424-7429.

(259) Yamada, Y.; Yano, K.; Xu, Q.; Fukuzumi, S.: Cu/Co_3O_4 nanoparticles as catalysts for hydrogen evolution from ammonia borane by hydrolysis. *J. Phys. Chem. C* **2010**, *114*, 16456-16462.

(260) Kalidindi, S. B.; Sanyal, U.; Jagirdar, B. R.: Nanostructured Cu and Cu@Cu_2O core shell catalysts for hydrogen generation from ammonia-borane. *Phys. Chem. Chem. Phys.* **2008**, *10*, 5870-5874.

(261) Yamada, Y.; Yano, K.; Fukuzumi, S.: Catalytic application of shape-controlled Cu_2O particles protected by Co_3O_4 nanoparticles for hydrogen evolution from ammonia borane. *Energ. Environ. Sci.* **2012**, *5*, 5356-5363.

(262) Kaya, M.; Zahmakiran, M.; Ozkar, S.; Volkan, M.: Copper(0) nanoparticles supported on silica-coated cobalt ferrite magnetic particles: cost effective catalyst in the hydrolysis of ammonia-borane with an exceptional reusability performance. *Acs Appl. Mater. Interfaces* **2012**, *4*, 3866-3873.

(263) Jiang, H.-L.; Akita, T.; Xu, Q.: A one-pot protocol for synthesis of non-noble metal-based core-shell nanoparticles under ambient conditions: toward highly active and cost-effective catalysts for hydrolytic dehydrogenation of NH_3BH_3. *Chem. Commun.* **2011**, *47*, 10999-11001.

(264) Xu, Q.; Chandra, M.: Catalytic activities of non-noble metals for hydrogen generation from aqueous ammonia-borane at room temperature. *J. Power Sources* **2006**, *163*, 364-370.

(265) Yan, J.-M.; Wang, Z.-L.; Wang, H.-L.; Jiang, Q.: Rapid and energy-efficient synthesis of a graphene-CuCo hybrid as a high performance catalyst. *J. Mater. Chem.* **2012**, *22*, 10990-10993.

(266) Shi, J.: On the synergetic catalytic effect in heterogeneous nanocomposite catalysts. *Chem. Rev.* **2013**, *113*, 2139-2181.

(267) Yen, H.; Seo, Y.; Kaliaguine, S.; Kleitz, F.: Tailored mesostructured Copper/Ceria catalysts with enhanced performance for preferential oxidation of CO at low temperature. *Angew. Chem. Int. Ed.* **2012**, *51*, 12032-12035.

(268) Bularzik, J.; Davies, P. K.; Navrotsky, A.: Thermodynamics of solid-solution formation in NiO-CuO. *J. Am. Ceram. Soc.* **1986**, *69*, 453-457.

(269) Davies, P. K.: Investigations of NiO-CuO solid-solutions using transmission electron-microscopy .1. tweed microstructure. *J. Am. Ceram. Soc.* **1986**, *69*, 796-799.

(270) Jobbagy, M.; Soler-Illia, G.; Regazzoni, A. E.; Blesa, M. A.: Synthesis of copper(II)-containing nickel(II) hydroxide particles as precursors of copper(II)-substituted nickel(II) oxides. *Chem. Mater.* **1998**, *10*, 1632-1637.

(271) Kasatkin, I.; Kurr, P.; Kniep, B.; Trunschke, A.; Schloegl, R.: Role of lattice strain and defects in copper particles on the activity of Cu/ZnO/Al$_2$O$_3$ catalysts for methanol synthesis. *Angew. Chem. Int. Ed.* **2007**, *46*, 7324-7327.

(272) Naghash, A. R.; Etsell, T. H.; Xu, S.: XRD and XPS study of Cu-Ni interactions on reduced copper-nickel-aluminum oxide solid solution catalysts. *Chem. Mater.* **2006**, *18*, 2480-2488.

(273) Natile, M. M.; Glisenti, A.: Surface reactivity of NiO: Interaction with methanol. *Chem. Mater.* **2002**, *14*, 4895-4903.

(274) Chandra, M.; Xu, Q.: Room temperature hydrogen generation from aqueous ammonia-borane using noble metal nano-clusters as highly active catalysts. *J. Power Sources* **2007**, *168*, 135-142.

(275) Yan, J.-M.; Zhang, X.-B.; Akita, T.; Haruta, M.; Xu, Q.: One-step seeding growth of magnetically recyclable Au@Co core−shell nanoparticles: highly efficient catalyst for hydrolytic dehydrogenation of ammonia borane. *J. Am. Chem. Soc.* **2010**, *132*, 5326-5327.

(276) Yan, J.-M.; Zhang, X.-B.; Han, S.; Shioyama, H.; Xu, Q.: Iron-Nanoparticle-Catalyzed Hydrolytic Dehydrogenation of Ammonia Borane for Chemical Hydrogen Storage. *Angew. Chem. Int. Ed.* **2008**, *47*, 2287-2289.

(277) Cao, C.-Y.; Chen, C.-Q.; Li, W.; Song, W.-G.; Cai, W.: Nanoporous Nickel spheres as highly active catalyst for hydrogen generation from ammonia borane. *ChemSusChem* **2010**, *3*, 1241-1244.

(278) Xu, Q.; Chandra, M.: Catalytic activities of non-noble metals for hydrogen generation from aqueous ammonia–borane at room temperature. *J. Power Sources* **2006**, *163*, 364-370.

(279) Zahmakıran, M.; Durap, F.; Özkar, S.: Zeolite confined Copper(0) nanoclusters as cost-effective and reusable catalyst in hydrogen generation from the hydrolysis of ammonia-borane. *Inter. J. Hydrogen Energy* **2010**, *35*, 187-197.

(280) Studt, F.; Abild-Pedersen, F.; Bligaard, T.; Sorensen, R. Z.; Christensen, C. H.; Norskov, J. K.: Identification of non-precious metal alloy catalysts for selective hydrogenation of acetylene. *Science* **2008**, *320*, 1320-1322.

(281) Park, J. Y.; Zhang, Y.; Grass, M.; Zhang, T.; Somorjai, G. A.: Tuning of catalytic CO oxidation by changing composition of Rh-Pt bimetallic nanoparticles. *Nano Lett.* **2008**, *8*, 673-677.

(282) Norskov, J. K.; Bligaard, T.; Rossmeisl, J.; Christensen, C. H.: Towards the computational design of solid catalysts. *Nat. Chem.* **2009**, *1*, 37-46.

(283)	Enache, D. I.; Edwards, J. K.; Landon, P.; Solsona-Espriu, B.; Carley, A. F.; Herzing, A. A.; Watanabe, M.; Kiely, C. J.; Knight, D. W.; Hutchings, G. J.: Solvent-free oxidation of primary alcohols to aldehydes using Au-Pd/TiO$_2$ catalysts. *Science* **2006**, *311*, 362-365.

(284)	Kaden, W. E.; Wu, T.; Kunkel, W. A.; Anderson, S. L.: Electronic structure controls reactivity of size-selected Pd clusters adsorbed on TiO$_2$ surfaces. *Science* **2009**, *326*, 826-829.

(285)	Kobayashi, H.; Yamauchi, M.; Kitagawa, H.; Kubota, Y.; Kato, K.; Takata, M.: Atomic-level Pd-Pt alloying and largely enhanced hydrogen-storage capacity in bimetallic nanoparticles reconstructed from core/shell structure by a process of hydrogen absorption/desorption. *J. Am. Chem. Soc.* **2010**, *132*, 5576.

(286)	Wang, H.; Sapi, A.; Thompson, C. M.; Liu, F.; Zherebetskyy, D.; Krier, J. M.; Carl, L. M.; Cai, X.; Wang, L.-W.; Somorjai, G. A.: Dramatically different kinetics and mechanism at solid/liquid and solid/gas interfaces for catalytic isopropanol oxidation over size-controlled Platinum nanoparticles. *J. Am. Chem. Soc.* **2014**, *136*, 10515-10520.

(287)	An, K.; Alayoglu, S.; Musselwhite, N.; Plamthottam, S.; Melaet, G.; Lindeman, A. E.; Somorjai, G. A.: Enhanced CO oxidation rates at the interface of mesoporous oxides and Pt nanoparticles. *J. Am. Chem. Soc.* **2013**, *135*, 16689-16696.

(288)	Kozlov, S. M.; Neyman, K. M.: Catalysis from first principles: Towards accounting for the effects of nanostructuring. *Top. Catal.* **2013**, *56*, 867-873.

(289)	Zhu, X.; Cho, H.-r.; Pasupong, M.; Regalbuto, J. R.: Charge-enhanced dry impregnation: A simple way to improve the preparation of supported metal catalysts. *ACS Catal.* **2013**, *3*, 625-630.

(290)	Munnik, P.; de Jongh, P. E.; de Jong, K. P.: Control and impact of the nanoscale distribution of supported Cobalt particles used in Fischer-Tropsch catalysis. *J. Am. Chem. Soc.* **2014**, *136*, 7333-7340.

(291)	Yeung, C. M. Y.; Yu, K. M. K.; Fu, Q. J.; Thompsett, D.; Petch, M. I.; Tsang, S. C.: Engineering Pt in ceria for a maximum metal-support interaction in catalysis. *J. Am. Chem. Soc.* **2005**, *127*, 18010-18011.

(292)	Singh, S. K.; Xu, Q.: Nanocatalysts for hydrogen generation from hydrazine. *Catal. Sci. Technol.* **2013**, *3*, 1889-1900.

(293)	Manukyan, K. V.; Cross, A.; Rouvimov, S.; Miller, J.; Mukasyan, A. S.; Wolf, E. E.: Low temperature decomposition of hydrous hydrazine over FeNi/Cu nanoparticles. *Appl. Catal. A* **2014**, *476*, 47-53.

(294)	Yen, H.; Kleitz, F.: High-performance solid catalysts for H$_2$ generation from ammonia borane: progress through synergetic Cu-Ni interactions. *J. Mater. Chem.A* **2013**, *1*, 14790-14796.

(295)	Wang, S.; Zhang, D.; Ma, Y.; Zhang, H.; Gao, J.; Nie, Y.; Sun, X.: Aqueous solution synthesis of Pt-M (M = Fe, Co, Ni) bimetallic nanoparticles and their catalysis for the hydrolytic dehydrogenation of ammonia borane. *ACS Appl.Mater. Interfaces* **2014**, *6*, 12429-12435.

(296)	He, L.; Huang, Y.; Wang, A.; Wang, X.; Chen, X.; Jose Delgado, J.; Zhang, T.: A Noble-metal-free catalyst derived from Ni-Al hydrotalcite for hydrogen generation from N$_2$H$_4$ center dot H$_2$O decomposition. *Angew. Chem. Int. Ed.* **2012**, *51*, 6191-6194.

(297)	Xu, Q.; Chandra, M.: A portable hydrogen generation system: Catalytic hydrolysis of ammonia-borane. *J. Alloys Compd.* **2007**, *446*, 729-732.

(298)   Can, H.; Metin, O.: A facile synthesis of nearly monodisperse ruthenium nanoparticles and their catalysis in the hydrolytic dehydrogenation of ammonia borane for chemical hydrogen storage. *Appl. Catal. B* **2012**, *125*, 304-310.

(299)   Wu, C.-T.; Qu, J.; Elliott, J.; Yu, K. M. K.; Tsang, S. C. E.: Hydrogenolysis of ethylene glycol to methanol over modified RANEY catalysts. *Phys. Chem.Chem. Phys.* **2013**, *15*, 9043-9050.

(300)   Lin, J.-H.; Biswas, P.; Guliants, V. V.; Misture, S.: Hydrogen production by water-gas shift reaction over bimetallic Cu-Ni catalysts supported on La-doped mesoporous ceria. *Appl. Catal. A* **2010**, *387*, 87-94.

(301)   Chen, L.-C.; Lin, S. D.: The ethanol steam reforming over Cu-Ni/SiO$_2$ catalysts: Effect of Cu/Ni ratio. *Appl. Catal. B* **2011**, *106*, 639-649.

(302)   Lin, J.-H.; Guliants, V. V.: Hydrogen Production through Water-Gas Shift reaction over supported Cu, Ni, and Cu-Ni nanoparticle catalysts prepared from metal colloids. *ChemCatchem* **2012**, *4*, 1611-1621.

(303)   Studt, F.; Abild-Pedersen, F.; Wu, Q.; Jensen, A. D.; Temel, B.; Grunwaldt, J.-D.; Norskov, J. K.: CO hydrogenation to methanol on Cu-Ni catalysts: Theory and experiment. *J. Catal.* **2012**, *293*, 51-60.

(304)   Gan, L.-Y.; Tian, R.-Y.; Yang, X.-B.; Lu, H.-D.; Zhao, Y.-J.: Catalytic Reactivity of CuNi Alloys toward H$_2$O and CO Dissociation for an Efficient Water-Gas Shift: A DFT Study. *J. Phys. Chem. C* **2012**, *116*, 745-752.

(305)   Kaneda, M.; Tsubakiyama, T.; Carlsson, A.; Sakamoto, Y.; Ohsuna, T.; Terasaki, O.; Joo, S. H.; Ryoo, R.: Structural study of mesoporous MCM-48 and carbon networks synthesized in the spaces of MCM-48 by electron crystallography. *J. Phys. Chem. B* **2002**, *106*, 1256-1266.

(306)   Shin, H. J.; Ryoo, R.; Liu, Z.; Terasaki, O.: Template synthesis of asymmetrically mesostructured platinum networks. *J. Am. Chem. Soc.* **2001**, *123*, 1246-1247.

(307)   Yin, A.; Wen, C.; Guo, X.; Dai, W.-L.; Fan, K.: Influence of Ni species on the structural evolution of Cu/SiO$_2$ catalyst for the chemoselective hydrogenation of dimethyl oxalate. *J. Catal.* **2011**, *280*, 77-88.

(308)   Qiao, Z.-A.; Guo, B.; Binder, A. J.; Chen, J.; Veith, G. M.; Dai, S.: Controlled synthesis of mesoporous carbon nanostructures via a "Silica-Assisted" strategy. *Nano Lett.* **2013**, *13*, 207-212.